Development of Metabolic Autofluorescence Imaging and Analyses to Assess Tumor Microenvironment Heterogeneity

By

Tiffany Marie Heaster

A dissertation submitted in partial fulfillment of

the requirements for the degree of

Doctor of Philosophy

(Biomedical Engineering)

at the

UNIVERSITY OF WISCONSIN-MADISON

2020

Date of oral examination: April 15, 2020

This dissertation is approved by the following members of the Final Oral Committee:

Melissa C. Skala, Associate Professor, Biomedical Engineering

David J. Beebe, Professor, Biomedical Engineering

Kevin W. Eliceiri, Associate Professor, Biomedical Engineering

Paul M. Sondel, Professor, Medical Physics and Biomedical Engineering

Manish S. Patankar, Professor, Obstetrics and Gynecology

ABSTRACT

Cellular heterogeneity in tumors challenges development of effective cancer treatments. Functional profiling methods are often destructive and lack the sensitivity to capture cell-level functional dynamics. The ability to accurately monitor the complex composition and structure of the tumor microenvironment (TME) could provide a fundamental understanding of tumor adaptation and drug resistance. Thus, technologies for single-cell functional assessment are needed to investigate the heterogeneous TME. In this dissertation, metabolic autofluorescence imaging and analyses were developed to identify and investigate sources of TME heterogeneity. Metabolic autofluorescence imaging exploits the endogenous fluorescence of metabolic coenzymes, NAD(P)H and FAD, to observe variations in cell metabolism and function. Fluorescence lifetimes and intensities of NAD(P)H and FAD provide quantitative measurements of heterogeneous metabolic pathway activity and intracellular protein binding. This work demonstrates two-photon metabolic autofluorescence imaging to evaluate spatiotemporal metabolic heterogeneity within *in vitro* and *in vivo* TME models. First, metabolic autofluorescence imaging was developed and validated to assess metabolic heterogeneity in *in vitro*, microscale TME models. Metabolic autofluorescence resolved heterogeneous metabolic changes during macrophage polarization and migration in response to microscale tumor co-culture, modelling dynamic sources of TME heterogeneity. This established metabolic autofluorescence imaging as a unique, non-invasive approach to quantify spatiotemporal heterogeneity in the TME. Improved analytical tools were also generated to characterize this dynamic heterogeneity. Statistical frameworks for quantifying spatial patterns in metabolic autofluorescence measurements across *in vitro* and *in vivo* TME models were designed and used to assess treatment- and model-specific trends in cell-level spatial organization and metabolic activity. This analysis enabled novel quantitative assessment of spatial metabolic dynamics in the TME. Finally, multivariate classification models of metabolic autofluorescence were created to detect tumor cells in states of quiescence, apoptosis, and proliferation to further define tumor cell metabolic heterogeneity. Overall, this dissertation establishes metabolic autofluorescence imaging as robust, label-free method to monitor heterogenous cellular metabolism in the TME.

ACKNOWLEDGMENTS

Thank you to my advisor Dr. Melissa Skala for providing ample opportunities, support and guidance throughout my time as a graduate student. Her direction has led me to accomplishing many research goals and developing my skills as a researcher to take with me in my future career.

Thank you to my committee members Dr. Eliceiri, Dr. Sondel, Dr. Beebe, and Dr. Patankar for providing great insight for the direction of my research and offering support for my success beyond my graduate studies.

Thank you to the scientific collaborators that have contributed greatly to this research: Dr. Bennett Landman, Dr. Scott Hiebert, Dr. Yue Zhao, Dr. Jason Yu, and Mouhita Humayun. I greatly appreciate all the time, effort, and insight to make this work come together.

Thank you to my wonderful lab members that I have had the joy to work with over the years. I couldn't have made it to this point without their endless support, insight, and comic relief. Special thanks to Dan Gil, Maryse, Joe, Amani, Liz, Rupsa, Jose, Tongcheng, and Kayvan for helping me every step of the way.

Thank you to many special friends that have cheered me on as I've pushed on through my graduate studies. I am incredibly lucky to have started at Vanderbilt with such an inspiring cohort of researchers, and overall great people. I'm also extremely fortunate to have a group of amazing friends, ranging from high school to undergrad, who have always been there for me from afar.

Thank you to Dr. Silas Leavesley, Dr. Thomas Rich, and Dr. Peter Favreau for supporting my initial ventures into scientific research and providing advice and inspiration for my journey into (and unpredictably during) graduate research over the years.

Thank you to my loving family for their unwavering support throughout my time in graduate school. I would not have had the courage to pursue and persist in my graduate studies without the continuous encouragement especially from my mom, dad, brother, grandmother, and aunt.

Thank you to my incredible partner in life, Jeremy, for being there for me honestly since Day 1. I never would have gotten this far without his overwhelming support, encouragement, and sacrifice amid his own work. His work and efforts, in and out of science, have inspired me through it all and always will. I couldn't be anymore thankful or grateful for it all.

I also have to thank the baristas at JJ's Market & Cafe and Fair Trade Coffeehouse for keeping me happily caffeinated and offering friendliness and a great atmosphere during my long bouts of research and writing.

TABLE OF CONTENTS

INDEX OF FIGURES AND TABLES

Figure

Table

CHAPTER 1

INTRODUCTION

1.1. Motivation

Tumor progression is largely affected by the complex tumor microenvironment (TME), suggesting that targeting the TME may be a promising approach for advancing cancer therapy[1]. However, cellular heterogeneity within the TME presents a challenge for effective anti-tumor treatment response[2]. Specifically, function, distribution and interaction between tumor, immune, and stromal cell populations within the TME can affect tumor-regulatory functions and drug sensitivity[2]. Furthermore, complex microenvironmental conditions (e.g., gradients of hypoxia, acidosis) can increase the diversity of cell phenotypes, but this remains poorly characterized[3,4]. Standard functional assays (e.g., flow cytometry, ELISA) are limited in their ability to resolve and effectively assess heterogeneous cell populations[5,6]. Single-cell genomic and proteomic technologies have been developed to improve sensitivity to cell heterogeneity[5,7,8]. However, these methods cannot evaluate spatial and temporal effects due to destructive sample processing and labelling[5,6]. Therefore, non-destructive, single-cell imaging and analysis tools are needed to study heterogeneous behavior within the TME.

Metabolic autofluorescence imaging is a powerful method for monitoring heterogeneous interactions within the TME at the single-cell level. This modality enables non-invasive, dynamic imaging of intact, living samples by measuring intrinsic fluorescence from the metabolic co-enzymes NAD(P)H and FAD[9]. Cellular level redox balance is evaluated with the optical redox ratio, defined as the ratio of NAD(P)H to FAD intensity[9–11]. Additionally, NAD(P)H and FAD fluorescence lifetimes report on metabolic enzyme-binding activities[12,13]. Overall, metabolic autofluorescence imaging may provide a versatile, label-free tool for assessing metabolic heterogeneity within the TME.

Spatial and temporal dynamics of cellular activity vary greatly in response to the active TME, contributing to substantial intratumor heterogeneity[14,15]. Metabolic autofluorescence imaging can be translated to assess cellular metabolism in 2D and 3D *in vitro* tumor models and *in vivo* mouse tumors,

providing a more accurate visualization of tumor complexity[16–21]. Multi-photon fluorescence excitation is utilized in metabolic autofluorescence imaging to enable cellular-resolution imaging in thick, scattering samples (≤ 1mm)[22,23]. This circumvents sample dissociation required for most biological assays and allows imaging of conserved local environmental conditions and spatial context of tumor tissue. Thus, metabolic autofluorescence imaging can identify depth-dependent effects on metabolic heterogeneity and visualize changes in TME structure that could alter behavior of the local cellular environment. Additionally, cellular plasticity has been largely attributed to prolonged and variable stimulation by the TME[24–26]. However, destructive sample preparation, high toxicity, and short half-life of exogenous labels limit longitudinal analysis of the TME[5,6]. Metabolic autofluorescence imaging can non-destructively monitor metabolic changes over time in live, intact samples[18,19,21,27,28]. This has been previously demonstrated for capturing altered cell metabolism across 3D models (e.g., organoids, microfluidic platforms) after sustained exposure to various stimuli (e.g., drug, cytokine treatment)[18,19,21,29]. Overall, metabolic autofluorescence imaging uniquely captures spatiotemporal information about single-cell function, offering advantages over standard biological techniques.

Novel analytical tools for autofluorescence images can further identify multiple cell sub-populations within intact, heterogeneous samples[17,30–32]. Quantitative analyses of spatiotemporal cellular heterogeneity can inform on dynamic cellular function and organization in biological samples[33–35]. Adapting these techniques for assessing metabolic autofluorescence in live tumor models may reveal unique patterns in phenotype and metabolism of tumor-infiltrating populations across the TME. Ultimately, development of metabolic autofluorescence imaging and analysis may be significant for enabling non-destructive characterization of cell-level spatial and temporal dynamics in response to the TME.

The goal of this dissertation is to develop and validate metabolic autofluorescence imaging and analysis tools for label-free monitoring of heterogeneous cellular activity in the 3D TME. These tools can resolve heterogeneous cell populations and investigate cell-level functional dynamics to discover key relationships between the TME landscape and tumor progression.

1.2 Dissertation outline

The works of this dissertation are presented as follows:

Chapter 1 provides the study motivation for the research highlighted in this dissertation.

Chapter 2 discusses the significance of TME heterogeneity in the development of treatment resistance and highlights key factors contributing to this heterogeneity[36]. Standard biological assays and imaging techniques for assessing heterogeneity are described, followed by limitations in their application across TME models. The concept of metabolism as a biomarker of cellular heterogeneity is introduced, plus metabolic autofluorescence imaging and analyses as technologies to quantify these metabolic biomarkers[36,37].

Chapter 3 presents metabolic autofluorescence imaging as a tool for measuring spatial and temporal dynamics of macrophage heterogeneity in 2D culture and 3D microfluidic tumor co-cultures. Sensitivity of NAD(P)H and FAD autofluorescence to temporal macrophage heterogeneity was assessed by measuring metabolic changes in 2D cytokine-stimulated macrophages during time-courses of macrophage polarization. Combination of autofluorescence imaging and 3D microscale tumor co-cultures are demonstrated for monitoring spatiotemporal dynamics of metabolic heterogeneity during tumor-mediated macrophage polarization and migration. This study was submitted for preprint at *biorxiv* and is currently under review at *Cancer Research*[38].

Chapter 4 details the creation of an analytical tool to quantify spatial heterogeneity of cell metabolism within *in vitro* and *in vivo* models of TME. The goal of this study was to characterize the spatial distribution of tumor cells with distinct cell metabolism using multivariate spatial statistical tools. Autofluorescence images of tumors *in vivo* and in 3D culture revealed spatial patterns of cell metabolism specific to drug response and resistance. This quantitative analysis framework provides a unique platform to assess the spatial effects of cell-level heterogeneity in tumor progression and treatment response. This work was published in *Frontiers in Oncology* (2019)[39].

Chapter 5 describes development of a classification model to identify heterogeneity in tumor cell-cycle status based on autofluorescence imaging of NAD(P)H and FAD fluorescence intensities and lifetimes. A multivariate model based on autofluorescence measurements was developed to classify tumor cells as quiescent, proliferative, or apoptotic with high accuracy. These tools contribute to the application of metabolic autofluorescence imaging to examine the role of heterogeneous tumor cell function in cancer drug development and treatment planning. This study was published in *Journal of Biophotonics* (2018)[40].

Chapter 6 summarizes the innovation and significant contributions of the dissertation research and provides outlooks on further development and application of the technologies presented.

1.3 References

1. Roma-Rodrigues C, Mendes R, Baptista P V, Fernandes AR. Targeting Tumor Microenvironment for Cancer Therapy. *Int J Mol Sci*. 2019;20(4):840. doi:10.3390/ijms20040840
2. Laplagne C, Domagala M, Le Naour A, et al. Latest Advances in Targeting the Tumor Microenvironment for Tumor Suppression. *Int J Mol Sci*. 2019;20(19):4719. doi:10.3390/ijms20194719
3. Davies AE, Albeck JG. Microenvironmental Signals and Biochemical Information Processing: Cooperative Determinants of Intratumoral Plasticity and Heterogeneity. *Front cell Dev Biol*. 2018;6:44. doi:10.3389/fcell.2018.00044
4. Quail DF, Joyce JA. Microenvironmental regulation of tumor progression and metastasis. *Nat Med*. 2013;19(11):1423-1437. doi:10.1038/nm.3394
5. Chattopadhyay PK, Gierahn TM, Roederer M, Love JC. Single-cell technologies for monitoring immune systems. *Nat Immunol*. 2014;15(2):128-135. doi:10.1038/ni.2796
6. Bendall SC, Nolan GP, Roederer M, Chattopadhyay PK. A deep profiler's guide to cytometry. *Trends Immunol*. 2012;33(7):323-332. doi:https://doi.org/10.1016/j.it.2012.02.010
7. Nishida-Aoki N, Gujral TS. Emerging approaches to study cell–cell interactions in tumor microenvironment. *Oncotarget*. 2019;10(7):785.
8. Hu P, Zhang W, Xin H, Deng G. Single Cell Isolation and Analysis. *Front cell Dev Biol*. 2016;4:116. doi:10.3389/fcell.2016.00116
9. Heikal AA. Intracellular coenzymes as natural biomarkers for metabolic activities and mitochondrial anomalies. *Biomark Med*. 2010;4(2):241-263. doi:10.2217/bmm.10.1
10. Chance B, Schoener B, Oshino R, Itshak F, Nakase Y. Oxidation-reduction ratio studies of mitochondria in freeze-trapped samples. NADH and flavoprotein fluorescence signals. *J Biol Chem*. 1979;254(11):4764-4771.
11. Georgakoudi I, Quinn KP. Optical Imaging Using Endogenous Contrast to Assess Metabolic State. *Annu Rev Biomed Eng*. 2012;14(1):351-367. doi:10.1146/annurev-bioeng-071811-150108

12. Lakowicz JR, Szmacinski H, Nowaczyk K, et al. Fluorescence lifetime imaging of free and protein-bound NADH. *Proc Natl Acad Sci U S A*. 1992;89(4):1271-1275. doi:10.1073/pnas.89.4.1271

13. Skala MC, Squirrell JM, Vrotsos KM, et al. Multiphoton microscopy of endogenous fluorescence differentiates normal, precancerous, and cancerous squamous epithelial tissues. *Cancer Res*. 2005;65(4):1180-1186. doi:10.1158/0008-5472.CAN-04-3031

14. Sun X, Yu Q. Intra-tumor heterogeneity of cancer cells and its implications for cancer treatment. *Acta Pharmacol Sin*. 2015;36(10):1219-1227. doi:10.1038/aps.2015.92

15. Goto T, Hirotsu Y, Amemiya K, Mochizuki H, Omata M. Understanding intratumor heterogeneity and evolution in nsclc and potential new therapeutic approach. *Cancers (Basel)*. 2018;10(7):212.

16. Quinn KP, Sridharan G V., Hayden RS, Kaplan DL, Lee K, Georgakoudi I. Quantitative metabolic imaging using endogenous fluorescence to detect stem cell differentiation. *Sci Rep*. 2013;3. doi:10.1038/srep03432

17. Walsh AJ, Skala MC. Optical metabolic imaging quantifies heterogeneous cell populations. *Biomed Opt Express*. 2015;6(2):559-573. doi:10.1364/BOE.6.000559

18. Walsh AJ, Cook RS, Sanders ME, et al. Quantitative optical imaging of primary tumor organoid metabolism predicts drug response in breast cancer. *Cancer Res*. 2014;74(18):5184-5194. doi:10.1158/0008-5472.CAN-14-0663

19. Shah AT, Heaster TM, Skala MC. Metabolic Imaging of Head and Neck Cancer Organoids. Sobol RW, ed. *PLoS One*. 2017;12(1):e0170415. doi:10.1371/journal.pone.0170415

20. Alfonso-García A, Smith TD, Datta R, et al. Label-free identification of macrophage phenotype by fluorescence lifetime imaging microscopy. *J Biomed Opt*. 2016;21(4):46005. doi:10.1117/1.JBO.21.4.046005

21. Sharick JT, Jeffery JJ, Karim MR, et al. Cellular Metabolic Heterogeneity In Vivo Is Recapitulated in Tumor Organoids. *Neoplasia*. 2019;21(6):615-626. doi:10.1016/j.neo.2019.04.004

22. Pawley JB, Masters BR. Handbook of Biological Confocal Microscopy, Third Edition. *J Biomed Opt*. 2008;13(2):029902. doi:10.1117/1.2911629

23. Vrana NE, Iniewski K. *Cell and Material Interface : Advances in Tissue Engineering, Biosensor, Implant, and Imaging Technologies*. CRC Press; 2016.

24. Hanahan D, Weinberg RA. Hallmarks of cancer: the next generation. *Cell*. 2011;144(5):646-674.

25. Yuan Y, Jiang YC, Sun CK, Chen QM. Role of the tumor microenvironment in tumor progression and the clinical applications (Review). *Oncol Rep*. 2016;35(5):2499-2515. doi:10.3892/or.2016.4660

26. Yuan S, Norgard R, Stanger B. Cellular Plasticity in Cancer. *Cancer Discov*. April 2019. doi:10.1158/2159-8290.CD-19-0015

27. Walsh AJ, Cook RS, Manning HC, et al. Optical metabolic imaging identifies glycolytic levels, subtypes, and early-treatment response in breast cancer. *Cancer Res*. 2013;73(20):6164-6174. doi:10.1158/0008-5472.CAN-13-0527

28. Shah AT, Diggins KE, Walsh AJ, Irish JM, Skala MC. In Vivo Autofluorescence Imaging of Tumor Heterogeneity in Response to Treatment. *Neoplasia*. 2015;17(12):862-870.

doi:10.1016/j.neo.2015.11.006

29. Ayuso JM, Gillette A, Lugo-Cintrón K, et al. Organotypic microfluidic breast cancer model reveals starvation-induced spatial-temporal metabolic adaptations. *EBioMedicine*. 2018;37:144-157. doi:10.1016/j.ebiom.2018.10.046

30. Liu Z, Pouli D, Alonzo CA, et al. Mapping metabolic changes by noninvasive, multiparametric, high-resolution imaging using endogenous contrast. *Sci Adv*. 2018;4(3). doi:10.1126/sciadv.aap9302

31. Walsh AJ, Skala MC. An automated image processing routine for segmentation of cell cytoplasms in high-resolution autofluorescence images. In: Periasamy A, So PTC, König K, eds. Vol 8948. International Society for Optics and Photonics; 2014:89481M. doi:10.1117/12.2040644

32. Yuan Y, Failmezger H, Rueda O, et al. Quantitative Image Analysis of Cellular Heterogeneity in Breast Tumors Complements Genomic Profiling Yinyin Yuan et al . *Sci Transl Med*. 2012;143(157):157ra143-157ra143. doi:10.1126/scitranslmed.3004330

33. Gough A, Stern AM, Maier J, et al. Biologically Relevant Heterogeneity: Metrics and Practical Insights. *SLAS Discov Adv life Sci R D*. 2017;22(3):213—237. doi:10.1177/2472555216682725

34. Spagnolo DM, Al-Kofahi Y, Zhu P, et al. Platform for quantitative evaluation of spatial intratumoral heterogeneity in multiplexed fluorescence images. *Cancer Res*. 2017;77(21):e71-e74. doi:10.1158/0008-5472.CAN-17-0676

35. Pécot T, Zengzhen L, Boulanger J, Salamero J, Kervrann C. A quantitative approach for analyzing the spatio-temporal distribution of 3D intracellular events in fluorescence microscopy. Akhmanova A, ed. *Elife*. 2018;7:e32311. doi:10.7554/eLife.32311

36. Heaster TM. Optical Imaging of Cell Cycle-driven Tumor Heterogeneity. Vanderbilt University; 2016.

37. Datta R, Heaster TM, Sharick JT, Gillette AA, Skala MC. Fluorescence lifetime imaging microscopy (FLIM): fundamentals and advances in instrumentation, analysis, and applications. *In Review*. 2020.

38. Heaster T, Humayun M, Yu J, Beebe DJ, Skala M. Autofluorescence imaging of 3D tumor-macrophage microscale cultures resolves spatial and temporal dynamics of macrophage metabolism. *bioRxiv*. January 2020:2020.03.12.989301. doi:10.1101/2020.03.12.989301

39. Heaster TM, Landman BA, Skala MC. Quantitative spatial analysis of metabolic heterogeneity across *in vivo* and *in vitro* tumor models. *Front Oncol*. 2019;9:1144.

40. Heaster TM, Walsh AJ, Zhao Y, Hiebert SW, Skala MC. Autofluorescence imaging identifies tumor cell-cycle status on a single-cell level. *J Biophotonics*. 2018;11(1):e201600276. doi:10.1002/jbio.201600276

CHAPTER 2

BACKGROUND

2.1 Tumor Heterogeneity in Treatment Response

Tumor heterogeneity contributes to poor cellular response to standard cancer therapies. Sub-populations of malignant and non-malignant cells comprise the bulk tumor mass, and each cell type exhibits unique function. Large proportions of tumor cells typically respond to treatment and are eliminated upon administration of first line therapy (Figure 2.1)[1,2]. However, select tumor sub-populations can evade treatment through functional adaptations that prevent therapy-induced cell death and redirect non-malignant populations to further promote evasive behavior (Figure 2.1). The residual cells can then repopulate the tumor site, generating a new mass abundant in drug-resistant cells (Figure 2.1)[3]. Subsequent treatment regimens become ineffective and allow survival and spread of the tumor. Though this relationship between tumor heterogeneity and treatment resistance has been identified, molecular mechanisms regulating heterogeneity within tumors and their microenvironment are poorly understood, limiting approaches to improve treatment response.

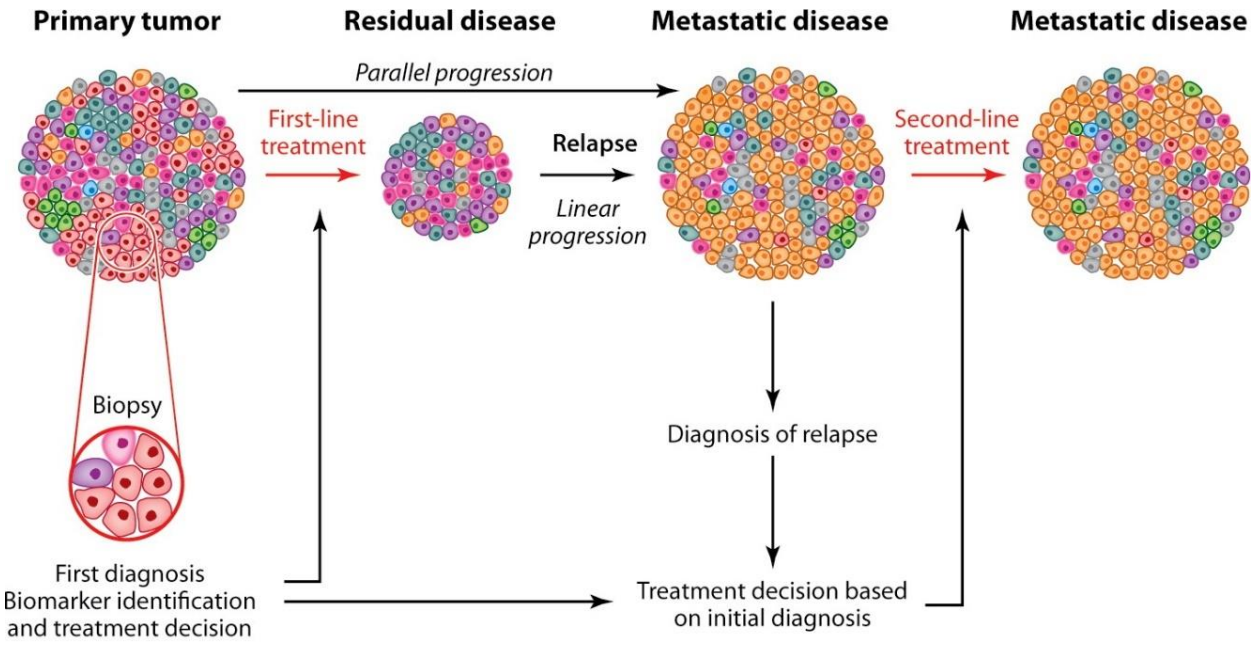

Figure 2.1: Heterogeneity in the TME can cause resistance to successive therapy, tumor recurrence, and spread. The TME is comprised of several heterogeneous cell populations with variable response to treatment. Treatment decisions are made from biopsies that only capture a portion of the heterogeneity, thus only a fraction of tumor cells will respond to treatment. Residual cell populations will continue to proliferate and produce local and/or distant recurrence that are resistant to subsequent treatment. Reprinted with permission under CC BY-4.0 from[3].

2.2 Sources of Heterogeneity in the Tumor Microenvironment

The TME is a complex ecosystem made up of several heterogeneous components, including tumor, immune cells, stroma, extracellular matrix (ECM), vasculature. These heterogeneous populations and their effects on the local tissue environment (e.g., gradients of oxygen, nutrients) can confer tumor treatment resistance. Thus, characterizing sources of heterogeneity has become essential to resolving mechanisms of drug resistance. Several factors contributing to tumor heterogeneity have been established, but their collective role in governing tumor behavior is unclear (Figure 2.2)[4]. For example, genetic mutations influence development of tumor sub-populations with unique function from the bulk tumor and alters cellular sensitivity to cancer treatments[5,6]. Tumor cells also regulate biochemical activity to modulate cell function and drug sensitivity and enhance heterogeneity (e.g., tumor aggression, invasiveness, cell-cycle state)[7]. Functional differences between tumor cell populations (e.g., cell signaling, metabolic programs and secretory profiles) alter treatment efficacy by redirecting function of neighboring cells within the tumor and TME[8,9]. Additionally, several unique cellular components (e.g., immune cells, stroma, vasculature) are present in the microenvironment and compound overall tumor heterogeneity[5,10]. The capacity for both malignant and non-malignant cell populations to reorganize according to environmental stimuli contributes to unique spatial structure and cell-cell interactions, yielding yet another source of heterogeneity[11–13]. Characterization of these diverse sources of tumor heterogeneity is necessary for understanding development of resistant populations and discovering novel targets of drug resistance mechanisms.

2.2.1 Tumor cell heterogeneity

Diverse tumor cell populations can arise within a single tumor due to several intrinsic biological changes. Genetic variation within tumor cell populations has been widely proposed to govern tumor heterogeneity [14,15]. Often, several clonal populations can be identified within a single tumor, each displaying unique phenotypic and functional behavior determined by the genetic profile[8,16]. This is compounded by improper gene synthesis and expression[15]. Deficient DNA damage repair and mitotic structure assembly mechanisms can lead to greater mutation of tumor cells[17,18]. Additionally, cell mutation rate is positively correlated with rate of cell division, suggesting that cell-cycle regulation may contribute to tumor genetic heterogeneity[5,19,20]. Ultimately, evaluating gene-regulated processes may provide fundamental insight into dynamics of tumor heterogeneity.

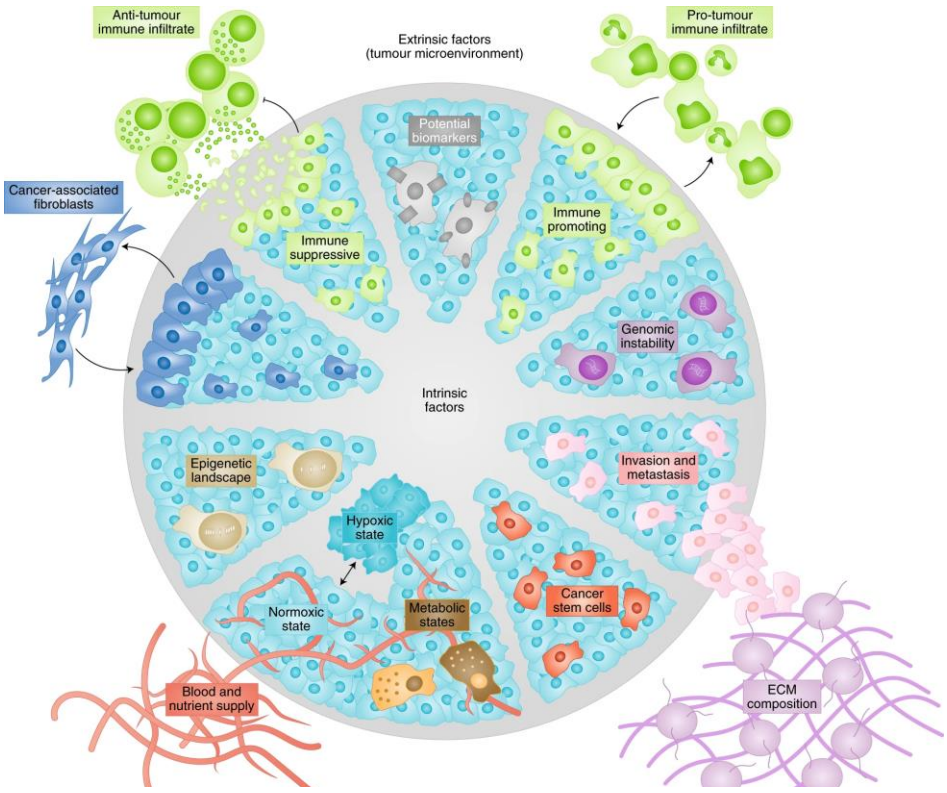

Figure 2.2: Intra- and extra-cellular factors driving heterogeneity within the TME. Various sources of TME heterogeneity are highlighted, ranging from intracellular changes in genetic and epigenetic modifications to extracellular cues (e.g., nutrient supply, tumor-immune/stromal crosstalk). Reprinted with permission under CC BY-4.0 from[4].

Epigenetic alterations have also been largely implicated in increasing tumor heterogeneity. Addition of functional groups (e.g., methyl, acetyl groups) directly to DNA or transcriptional machinery can regulate gene activity without changing coding sequences[21]. This contributes to genetic diversity across cell populations by selectively preventing transcription and expression of target genes[22]. Epigenetic modification enzymes are frequently mutated in cancer, often leading to dysregulation of tumor suppressor genes and hyperactivity of oncogenes[23]. Additionally, cell-cycle regulation plays a significant role in promoting increased intra-tumor heterogeneity. Cell-cycle mechanisms are inherently designed to support cell division for normal biogenesis, repair cell damage, and sustain cell viability during environmental stress (e.g., nutrient deprivation)[24,25]. In response to fluctuating environmental conditions, intracellular signals can induce withdrawal from the cell-cycle into quiescence, identified as a reversible lapse in cell division in which cell viability is maintained[24]. Tumor cell populations exploit this cell-cycle transition into quiescence to become less transcriptionally active, confer resistance to proliferation-targeted drugs, and increase genetic diversity through unique genetic profiles compared to proliferative tumor cells[26–29]. Therefore, sources of intracellular tumor heterogeneity, such as genetic regulation and cell-cycle status, should be more thoroughly explored.

2.2.2 Microenvironment heterogeneity

The tumor and TME are characterized by various cell types and structural compartments that contribute to tumor complexity (Figure 2.3). Infiltration and organization of immune cells, fibroblasts, vasculature, and extracellular matrix are uniquely associated with different tumor types and stages of tumor progression[30]. Additionally, TME composition may fluctuate with effective therapeutic response, reflecting susceptibility to treatment[31]. This will change both the tumor architecture and local microenvironmental conditions (e.g., nutrients, oxygen supply), as malignant cells and adjacent non-malignant cells compete for the variable resource supply[32]. Thus, further characterization of heterogeneity within the TME may provide unique insight into intratumoral processes driving tumor advancement and aggressiveness.

The immune system is a significant source of heterogeneity in the TME and influences cancer progression and efficacy of cancer therapies[33,34]. Immune cell populations infiltrating into the tumor and microenvironment encompass macrophages, T cells, natural killer cells, dendritic cells, and B cells[35]. Alone, the diversity of immune cell populations introduces substantial heterogeneity to the tumor via distinct responses to tumor signaling that stimulate changes in cell function and recruit additional immune cells[34–36]. However, these immune cells also adopt multiple functional phenotypes that alter their interaction with tumor cells[37]. Selective pressures within the TME (e.g., nutrient deprivation, hypoxia) can further regulate the tendency for immune cells to enhance or suppress tumor-directed immune responses. This acquired response upon tumor cell recognition can be harnessed to provide novel therapeutic targets and increase overall treatment efficacy[34]. However, there is poor understanding of mechanisms driving these tumor-immune cell interactions, highlighting the need for better evaluation of immune cell heterogeneity.

Macrophages are one of the most abundant and heterogeneous immune populations infiltrating tumors, especially in specific cancer types (e.g., breast, pancreatic cancer)[35,36,38]. This prominence highlight importance of macrophages in tumor immunogenicity, in addition to their extensive tumor-regulatory functions [38–40]. This prevalence of macrophage diversity provides a reliable model of immune cell heterogeneity but is limited by poor understanding of their plasticity. A subset of macrophage classes (i.e., M1-like and M2-like) have been established and associated with distinct functional characteristics that can locally affect the TME[41–44]. M1-like macrophages promote anti-tumor responses by initiating adaptive immune responses, inducing apoptosis and phagocytosis, and competing for nutrients in TME. M2-like macrophages reinforce tumor progression by promoting immune evasion and providing access supplementary nutrients to increase proliferation and metastatic behavior[43,46,47]. However, this M1-M2 dichotomy model is contradicted by detection of intermediate macrophage states within tumor infiltrates, likely a result of varied exposure to tumor-associated stimulatory factors[48,49]. Thus, macrophage

heterogeneity illustrates the challenge for accurately relating immune cell function to cancer progression, highlighting the need for further observation and characterization.

Furthermore, spatial heterogeneity within tumors has been associated with reduced treatment efficacy and patient tumor relapse[50]. Changes in cellular distribution and extracellular matrix structure of specific tumor regions can regulate interactions across tumor compartments and generate environmental gradients[51]. This behavior essentially results in a feedback loop, where both malignant and non-malignant cells functionally adapt to the local environmental pressures and further alter TME conditions[52]. Spatial variations often exist between multiple tumor cell populations where cell phenotypes vary with resource availability, and these phenotypically-distinct populations distribute in specific patterns across the tumor[11,53–55]. This can affect tumor progression and treatment response by preferentially increasing tumor dormancy localized to nutrient-deprived areas, supporting long-term survival of the tumor upon reactivation[11,56]. Tumor cell spatial distribution may also contribute to survival by directing organization of cell populations based on dispersion of administered drugs within TME[57]. Colocalization of tumor cells with immune/stromal components has also been strongly linked to cancer severity[11]. Tumor cells will often outcompete adjacent immune cells for nutrients and suppress the anti-tumor immune response, or use stromal cell secretions as an alternative nutrient source for survival[58]. Overall, exploring the spatial context of the TME may be pivotal in understanding dynamics of tumor development and treatment evasion.

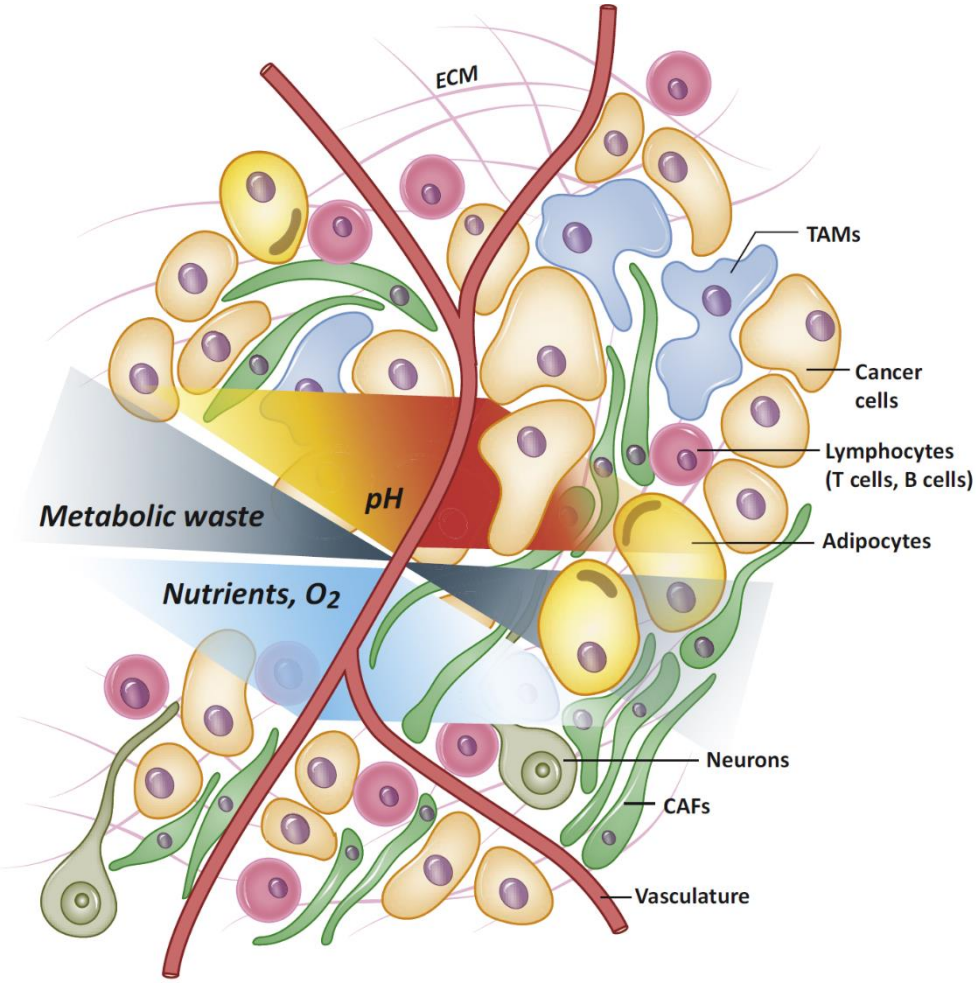

Figure 2.3: Cellular heterogeneity and environment gradients observed in the TME. The diverse landscape of the TME encompasses several immune cell (e.g., macrophages, lymphocytes) and stromal cell (e.g., fibroblasts) populations, as well as structural components such as the ECM and vascular network. Intercellular interactions can cause phenotypic and functional shifts within populations, further driving cellular heterogeneity. Variations in local environmental conditions (e.g., nutrient access, pH, waste accumulation) also affect cell behavior and amplify TME heterogeneity as a whole. Reprinted with permission under CC BY-4.0 from[58].

2.3 Standard Approaches for Assessing Tumor Microenvironment Heterogeneity

Unresolved links between TME heterogeneity and cancer drug resistance have provoked the development of various methods for characterizing heterogeneous cell populations across the TME. Flow cytometry is the current standard for characterizing heterogeneous samples which uses exogenous labelling with fluorescent antibodies or dyes to allow *ex vivo* analysis and sorting of pure cell populations[59]. This technique informs on cell phenotype based on intracellular or cell surface protein expression but provides

limited measures of function, so functional studies are often performed on cell populations post-sorting[60,61]. Exogenous labels can affect cell physiology, impacting the functional analysis of sorted cell populations[62–64]. Additionally, sample processing for flow cytometry prevents preservation of the natural structure of the TME and requires prior knowledge of TME composition to determine appropriate labels for identifying each population[60,65]. Alternatively, biochemical assays, such as enzyme-linked immunosorbent assays (ELISAs), mass cytometry, and protein microarrays, can provide high-throughput assessment of intra- and extra-cellular protein production corresponding to specific cell behaviors[60,66–68]. However, these techniques exhibit sensitivity primarily to the bulk population activity and have limited resolution of function from heterogeneous sub-populations present within a sample[60,66,67]. These assays have been adapted for single-cell analysis, but require tumor dissociation and processing which disregards the spatial structure[60,66,67]. Genomic analyses are also commonly used to determine changes in biological function but typically only reflect relative changes in gene expression aggregated across all cell types within a sample[69]. Advancements in genetic profiling, such as single-cell sequencing, have extended gene expression analyses for characterizing individual cells within heterogeneous samples[70,71]. Similarly to single-cell proteomic analyses, this involves intricate sample processing to isolate individual cells, which can introduce alterations to cellular gene signatures[72]. These methods are widely applicable for evaluating heterogeneity across tumor compartments (e.g., tumor sub-populations, immune cells, stroma), but are unfavorable for preserving the evolving environmental conditions and spatial networks needed to accurately reflect sources of heterogeneity in the TME.

Variations in cell spatial distributions also influences global tumor heterogeneity, but few analytical methods exist to examine tumor spatial structure[11]. Development of mathematical models have attempted simulation of intratumor dynamics, but typically do not reflect all possible sources of environmental variability[73]. Furthermore, descriptive distribution metrics (e.g., measures of proximity, clustering, and autocorrelation) have been used to characterize relative cell locations and their effect on cell phenotype and functional diversity[74–76]. These techniques have been mostly used in histology or immunofluorescence imaging studies to qualitatively assess multi-cellular spatial organization and relationships with bulk

functional measures[76–81]. Like the single-cell tools described above, these techniques require destructive processing and only offer a static representation of tumor organization, ignoring region-specific effects on tumor diversity. Preservation of both the spatial context and viability of experimental tumor models is crucial for development of methods to assess cell-level heterogeneity within the 3D TME.

Identifying and characterizing cell sub-populations within intact, heterogeneous tumor models would better inform on intercellular dynamics promoting heterogeneity in the TME. For example, assessing interactions between tumor cells and blood vessels, extracellular matrix, immune cells, or stromal cells could inform on mechanisms driving aggressive, drug-resistant tumor cell populations by mapping their relative distribution in intact, viable tumor tissue. Also, tumor excision and dissociation required for performing standard biological assays limit observation of dynamic changes in live tumor models over time. Therefore, these drawbacks of standard measures become increasingly prohibitive for translating heterogeneity analyses to more complex models (e.g., 3D *in vitro, in vivo* tumor models). Thus, novel approaches for identifying tumor cell sub-populations within live, intact tissue and monitoring their dynamic function over time could complement standard functional measures to comprehensively evaluate the landscape of tumor heterogeneity.

2.4 Metabolism as a Marker of Cellular Heterogeneity

Metabolism is a principal regulator of function across cell compartments (e.g., tumor, stroma). Accordingly, changes in metabolic products are correlated with changes in cell phenotype and function (Figure 2.4A)[82,83]. Reduced nicotinamide adenine dinucleotide (NADH) and flavin adenine dinucleotide (FAD) are intracellular coenzymes that regulate cell-level metabolic processes[84]. Both serve as essential catalysts in reactions across primary metabolic pathways, as either electron donors or acceptors (Figure 2.4B)[85]. Specifically, cells under abnormal physiological conditions use glycolytic processes to supply ATP, resulting in greater NADH levels[86]. Similarly, FAD redox state is directly correlated with eukaryotic cellular respiration processes (e.g., citric acid cycle, oxidative phosphorylation)[84].

Both NADH and FAD can directly affect mitochondrial activity and intracellular energy production,

leading to changes in tumor cell function (e.g., maturation, cell death). For example, actively proliferating tumor cells upregulate production of glycolytic metabolite production during progression through different cell-cycle phases[87,88]. Similarly, previous studies report variation in intracellular NADH levels associated with changes in tumor cell growth rate[82,83]. In contrast, decreased NADH levels are observed with reduced proliferation (i.e., quiescence), which is associated with increased oxidative metabolism[83]. Environmental changes (e.g., oxidative stress, acidosis) also regulate oxidation and reduction states to appropriately sustain cellular production of ATP and other essential metabolites, yielding shifts in NADH and FAD concentration and binding affinity[89,90]. Thus, monitoring NADH and FAD activity may provide correlative readouts of local changes in tumor oxygen and nutrient supply.

Increased heterogeneity in immune cell populations has also been correlated with metabolic switching (Figure 2.4A)[91]. Sensitivity to metabolic changes in immune cells could reflect heterogeneous immune cell subsets and functional diversity within subsets. Macrophages are one of the dominant immune cell populations infiltrating the TME and provide a reliable model of heterogeneity in immune cell phenotype and function, due to their highly plastic nature[92]. Corresponding to the M1-M2 phenotype paradigm described earlier, these diverse macrophage classes present unique energy demands and metabolic preferences[49]. M1-like macrophages are associated with high production of reactive oxygen species (ROS) to signal tumor cell cytotoxicity and secondary immune recruitment, requiring increased dependence on production of metabolic co-enzyme, NADPH, via the pentose phosphate pathway (PPP)[93]. Homeostatic ROS levels are also maintained by exploiting the NADPH and PPP for macrophage antioxidant production[94]. Increased glycolysis and NADH production also enable survival of M1-like macrophages in nutrient-deprived conditions[95]. In contrast, M2-like macrophages upregulate fatty acid oxidation to produce Acetyl-CoA and NADH for increased oxidative phosphorylation, supporting tumor cell proliferation, angiogenesis, and immunosuppression in the TME[91,96–99]. Extensive studies have established this association between cell metabolism and function across numerous cell types, strongly supporting the utility of cell metabolites such as NADH and FAD as biomarkers of cellular activity and local environmental

pressures in the TME.

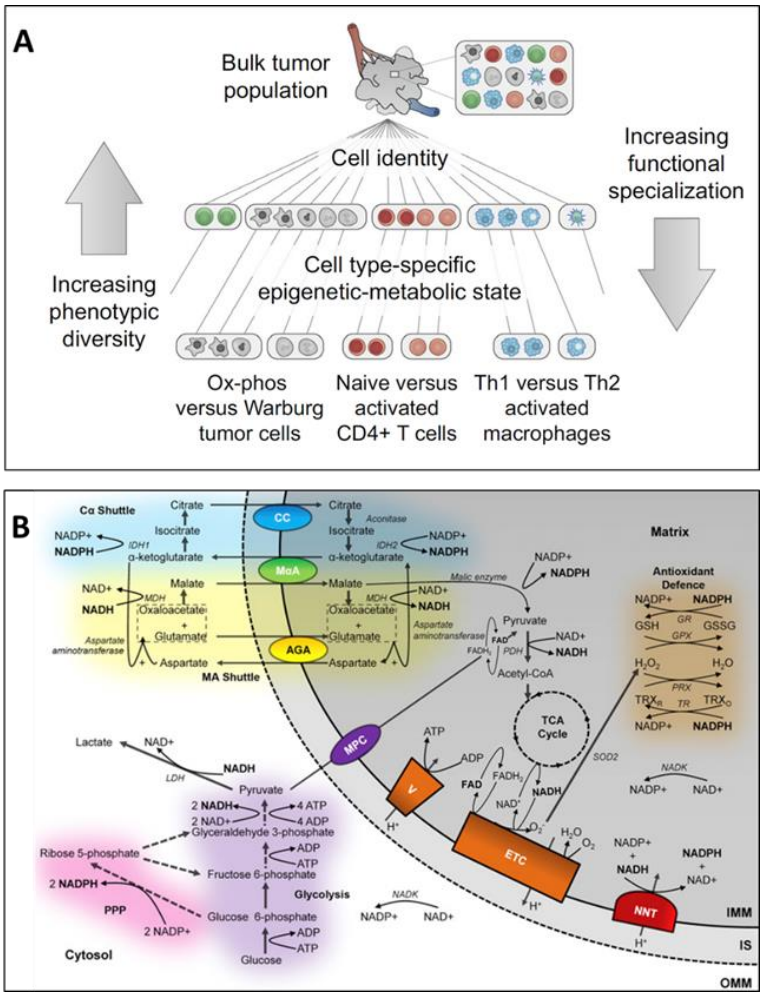

Figure 2.4: Cellular metabolism is linked to phenotypic and functional heterogeneity in cell populations within the TME. A) Bulk tumors are comprised of several heterogeneous cell populations, with each cell population exhibiting unique genetic and metabolic characteristics. Metabolic activity can further distinguish cell subsets within each identified population. Adapted with permission from[68]. B) Primary intracellular metabolic pathways involving NADH and FAD oxidation-reduction reactions. Adapted with permission under CC BY-4.0 from[129].

2.5 Imaging Methods to Capture Heterogeneity in Cancer

2.5.1 Medical imaging modalities

Imaging methods offer non-invasive, non-destructive characterization of heterogeneity in TME models. Several macroscale imaging techniques currently exist for monitoring structural and functional changes in tumor tissue, such as positron emission tomography (PET), ultrasound (US), computed tomography (CT), and magnetic resonance imaging (MRI) (Table 2.1). PET uses contrast

from radioisotope-labelled functional molecules to trace transport and accumulation in specific tissue regions[100]. This can visualize the distribution and enzymatic processing of functional molecules (e.g., 2-deoxy-glucose, thymidine, acetate) or labeled drugs within tumors and relate it to physiological behavior such as biogenesis, nutrient availability, metabolic activity, and overall drug efficacy[101,102]. Combined CT/PET imaging is frequently used to provide complementary information about macroscale structure to determine distribution of PET tracers relative to the tumor mass or other anatomy[103]. CT traditionally relies on X-ray absorption of tissues and bone to provide contrast from the surrounding environment, though radioagents have been introduced to enhance contrast due to low signal from soft tissue[104–107]. For example, ^{18}F-FDG and ^{11}C-acetate PET/CT are commonly used to probe glucose uptake and oxidative metabolic activity, respectively[108]. Ultrasound imaging captures reflected high-frequency sound waves to visualize *in vivo* tissue structure but also has poor soft tissue contrast, similarly requiring additional contrast agents[104,107]. Additionally, MRI is advantageous for imaging structural changes in tumors as it exploits endogenous contrast through high water content of tissues or exogenous contrast from paramagnetic tracers, overcoming the need for use of ionizing radiation[101,109]. Here, the generation of magnetic fields are used direct proton alignment, then radiofrequency pulses are introduced to change the proton orientation[109]. Aligned protons will then relax back to their original alignment after the pulse ceases. The relaxation rate is reflective of the tissue composition or contrast agent accumulation, enabling discrimination of intact tissue regions[109]. MRI can also exhibit sensitivity to metabolic changes by using hyperpolarized metabolites (e.g.,^{13}C-pyruvate/lactate, ^{1}H-choline)[108]. PET/CT and MRI are well-suited to measure tissue-level spatial variations in phenotype and function but lack the spatial resolution to identify and map individual cells within the tissue[108,110]. These modalities have also been adapted to detect diverse tumor cell and immune compartments within the entire mass, but similarly, resolution limits only enable representation of the bulk organization and function of these cell populations[111]. Thus, functional imaging approaches with cellular resolution are needed to comprehensively visualize TME heterogeneity.

2.5.2 Optical imaging modalities

Several optical imaging modalities have also been developed to monitor heterogeneous structure and function in the tumor microenvironment (Table 2.1). Histological and immunofluorescence imaging are standard techniques that use tissue sections from excised tumors for fixation and staining or fluorescent labeling of cell types, structural components, and genes or proteins associated with cell function[112,113]. Microscopy images are collected from select regions or across the entire processed sample, and patterns of cell-specific staining or fluorescence are quantified to determine the presence of multiple, functionally-distinct cell populations in the tissue[112,113]. These techniques have been combined with spatial analyses to determine associations between relative location of diverse cell types and macroscale tumor behavior[77–81]. For example, immune cell and fibroblast infiltration and colocalization with tumor cells within tissue sections are frequently correlated with disease prognosis, though the significance of cell spatial relationships is poorly understood[78,114]. Alternatively, innovation in optical imaging technologies for monitoring heterogeneity in the tumor microenvironment have been steadily progressing. Structural imaging techniques, such as optical coherence and photoacoustic tomography or second- and third-generation microscopy, use contrast from scattering, thermal expansion, or molecular orientation of specific tissue structures to visualize the 3D tumor structure deep within the tissue (mm – cm deep)[107,115–119]. However, these methods provide limited information about the function of cells and tissue. Molecular imaging approaches, such as bioluminescence and Fourier transform infrared imaging, can resolve functional activity in tumor tissue by detecting luminescent functional molecules or endogenous changes in light transmission spectra corresponding to tissue molecular composition[104,105,120–122]. However, these techniques have variable cellular specificity and resolution *in vivo*[104,105,120–122]. Furthermore, numerous fluorescence-based methods exist to characterize intensity and lifetimes of endogenous fluorophores, fluorescent reporters, dyes, and particles reflecting phenotype, function, and distribution of particular cells and structures from 2D images or 3D image volumes[104–107,123,124]. In particular, multiphoton fluorescence using near-infrared excitation is well-equipped for tissue imaging due to high spatial confinement of fluorescence excitation and reduced scattering for deeper penetration into densely-packed tissue[125].

Fluorescent metabolite probes (e.g., 2-NBDG glucose, Peredox NADH-NAD+ sensors) can also enable assessment of tissue metabolism using these optical imaging approaches[126]. These techniques have been used individually and in combination to image 3D tumor-tumor and tumor-stroma interactions within intact tumors. Overall, optical imaging is attractive for studies of TME heterogeneity.

Table 2.1: Comparison of imaging approaches for assessing models of tumor microenvironment. Adapted with permission under CC BY-4.0 from[111].

Imaging modality			Resolution			Contrast agent
			In-plane	Coverage/ depths	Temporal per frame	
Optical	Bioluminescence imaging[104,105]	BLI	>3-5 µm	1-2 cm	>1 s to min	Reporter genes
	Fluorescence imaging[104,105]	FLI	2-3 µm	<1 cm	>1 s to min	Fluorophores, fluorescent nanoparticles
	Fluorescence lifetime microscopy[123]	FLIM	nm range	~1000 µm	>1 s to min	Endogenous, fluorophores, fluorescent nanoparticles
	Fluorescence molecular tomography[107,124]	FMT	<1 mm	1- 2 mm	>1 s to min	NIRF dyes, quantum dots, reporter genes
	Fourier transform infrared imaging[120-122]	FTIR	>3-5 µm	<20 µm	>1 ms to min	Endogenous
	Near-infrared fluorescence imaging[123]	NIRF	~200 µm	<3-4 cm	50-800 ms	NIRF dyes, quantum dots, reporter genes
	Optical coherence tomography[115]	OCT	< 7.5 µm	2-3 mm	<1 s	Endogenous
	Photoacoustic imaging (tomography)[107,116-118]	PAI (PAT)	100 µm	<5-6 cm	>1 s to min	Fluorophores, nanoparticles, quantum dots
	Second-harmonic generation microscopy[119]	SHG	< 1 µm	≤1 mm	>10 s	Endogenous
	Third-harmonic generation microscopy[119]	THG	<1 µm	≤1 mm	>10 s	Endogenous
X-ray	Computed tomography[104,105,124]	CT	~50-200 µm	Whole body	>20 s	Water-soluble, iodinated probes
Magnetic resonance	Magnetic resonance imaging[104,105, 107, 109, 124]	MRI	~25-300 µm	Whole body	>2 min	Endogenous; injected marker or metabolic substrates
	Magnetic resonance spectroscopic imaging[109]	MRSI	mm range	Whole body	min to h	Endogenous; injected marker or metabolic substrates
Nuclear	Positron emission tomography[104,105,124]	PET	1-2 mm	Whole body	>10 s to min	Radiolabeled substrates (nutrients, antibodies, antibody fragments), activatable probes
	Single photon emission computed tomography[104,124]	SPECT	1-2 mm	Whole body	min	Radiolabeled antibodies, antibody fragments, and antigens
Ultrasound	Ultrasound imaging[104,124]	US	50-500 µm	mm to cm	>1 s to min	Endogenous; targeted microbubbles

Imaging modalities are color-coded separating optical, X-ray,magnetic resonance-, nuclear-, (radioactivity-), and ultrasound-based imaging methods

2.6 Autofluorescence Imaging of Cellular Metabolism

Metabolic autofluorescence imaging can exploit endogenous fluorescence of metabolic coenzymes NADH and FAD to monitor metabolic pathway activity in live cells (Figure 2.5)[84,127,128]. NADH and FAD autofluorescence display unique spectral characteristics, enabling separation based on their excitation and emission (NADH Ex/Em maxima: 350nm/460nm; FAD Ex/Em maxima: 435nm/535 nm)[84]. Due to the overlap in excitation and emission characteristics of NADH and NADPH, metabolic autofluorescence imaging similarly demonstrates sensitivity to both NADH and NADPH redox states[127–130]. The increased abundance and quantum yield of NADH suggests our signal primarily reflects NADH

activity[130], though the notation NAD(P)H used onwards indicates this overlap. NAD(P)H and FAD fluorescence intensities can inform on their respective intra-cellular concentrations[127–129]. Furthermore, calculation of the optical redox ratio, defined as the ratio of NAD(P)H intensity to FAD intensity, provides a global measurement of metabolism related to intracellular reduction or oxidation[127,128,131–133]. This metric has been shown to correlate with standard measures of metabolism such as liquid chromatography mass spectrometry and extracellular flux, validating the sensitivity of the optical redox ratio to intracellular metabolic activity[133,134].

Fluorescence lifetime imaging microscopy (FLIM) of NAD(P)H and FAD can contribute additional information specific to protein binding activity[130,131,133,135,136]. Fluorescence lifetime is defined as the time of electron relaxation to the ground energy state following photon absorption and electron

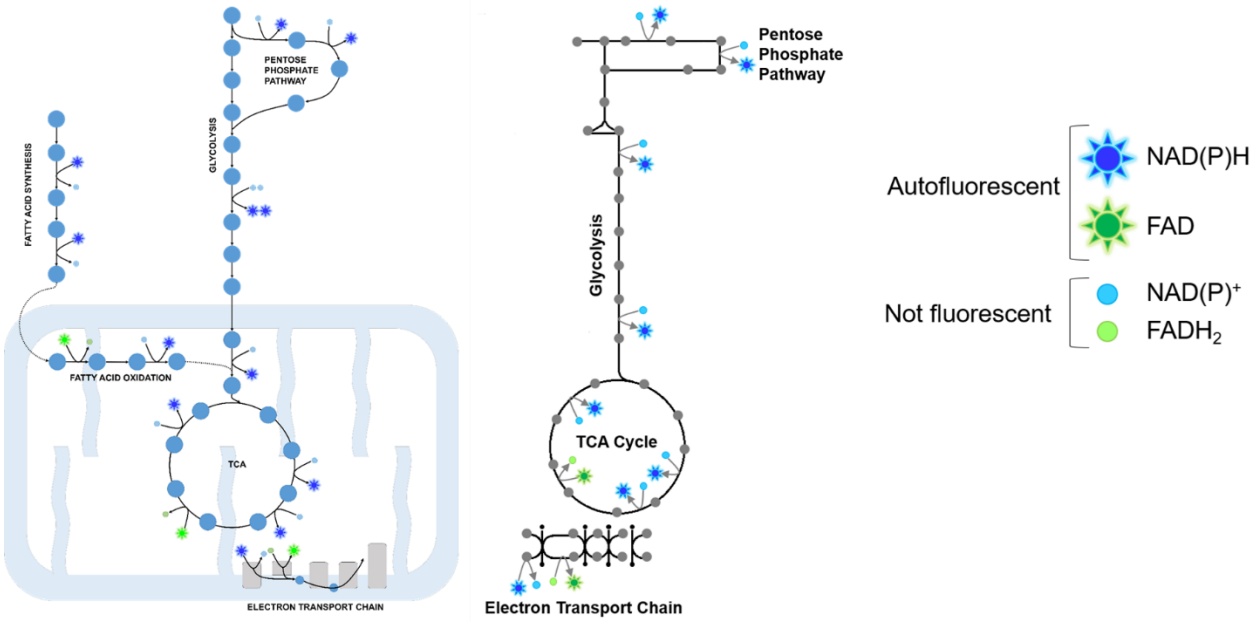

Figure 2.5: Autofluorescent NAD(P)H and FAD provide label-free biomarkers of metabolic pathway activity. Metabolic coenzymes, NAD(P)H and FAD, are utilized in reactions for metabolite production across several metabolic processes, including glycolysis, pentose phosphate pathway, fatty acid oxidation, and oxidative phosphorylation. These coenzymes exhibit endogenous fluorescence, enabling label-free observation of active metabolic processes within cells.

transition to higher energy states[137]. Two-photon excitation of fluorescence lifetime uses focused near-infrared laser pulses to cause nonlinear excitation of electrons via interaction of two, low-energy photons equivalent to the energy required for single photon excitation (Figure 2.6A)[138,139]. The spatial confinement

of two-photon excitation reduces out-of-plane fluorescence and minimizes photodamage, while maximizing resolution and photon detection[138]. Additionally, the use of near-infrared excitation pulses increases depth of penetration, which is ideal for imaging thick, scattering biological samples[125]. Lifetime measurements can distinguish between free and protein-bound forms of NAD(P)H and FAD, characterized by distinct molecular conformations that affect fluorescence quenching[133,135,136]. Fluorescence lifetime measurements detect free and bound NAD(P)H and FAD within each pixel using time-correlated single photon counting (TCSPC). In TCSPC, each photon is assigned to a time bin within a lifetime histogram[140]. Histograms are fit to multi-exponential decay functions corresponding to free and bound coenzyme, which are described in the following equation:

$$I(t) = \sum_i a_i e^{-t/\tau_i}, \quad (1)$$

where I represents fluorescence intensity, t represents time, a_i represents the fractional contribution of each fluorescent species, and τ_i represents the lifetime of each species[138]. An instrument response function (IRF) is measured from a sample with an instantaneous lifetime (e.g., a second harmonic sample for two-photon microscopy) to account for the temporal response of the optical system[140]. FLIM analysis requires some prior assumptions, including the number of lifetime components, temporal offset of detected signals, and sources of background fluorescence[140]. The multi-component exponential decay estimate is then convolved with the IRF and compared to the experimentally-measured lifetime decay curve (Figure 2.6B)[140]. The chi-squared (χ^2) goodness-of-fit test is used to evaluate agreement between the fit and the measured data. Parameters of the model (a_i, τ_i) are iterated to achieve a chi-squared value closest to 1, indicating the best model fit to the experimental data[140]. These lifetime parameters can then inform on NAD(P)H and FAD binding activity. Specifically, unbound NADH exhibits partial quenching of its adenine side chain, resulting in a faster rate of fluorescence decay than in the unquenched, bound form[135]. In contrast, bound FAD exhibits adenine quenching and thus yields a faster fluorescence decay than free FAD[141]. Additional limitations of autofluorescence lifetime hinder application of this technique, including reduced sensitivity to endogenous fluorophores with similar fluorescence characteristics (e.g., NAD(P)H and NADH) and lack

of specificity for all known autofluorescent enzyme reactions (e.g., ~300 different NADH binding sites)[129,149,192]. However, analysis of NAD(P)H and FAD fluorescence lifetime can overall inform on the dynamics of intracellular metabolic activity and environmental stimulation within the TME.

Metabolic autofluorescence provides quantitative, functional information on the single-cell level, demonstrating the capability to evaluate heterogeneity within biological systems[142–144]. NAD(P)H and FAD autofluorescence intensities can reflect substantial changes in active cell metabolic pathways and metabolite

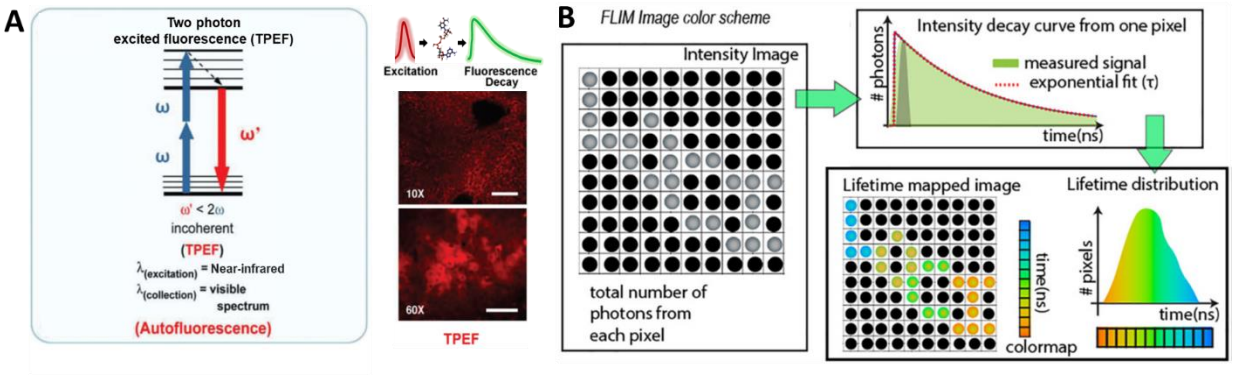

Figure 2.6: Two-photon imaging of autofluorescence lifetimes can inform on activity of biological fluorophores. A) Two-photon excited fluorescence (TPEF) relies on interaction of two photons to cause electronic excitation and corresponding relaxation (emission) equivalent to excitation with a single photon of twice the energy. The total time to electron relaxation is the fluorescence lifetime. Adapted with permission from[139]. B) Per-pixel photon counts are collected and binned according to photon detection time to build up per-pixel fluorescence decay curves. Fluorescence lifetime decay variables (α_i, τ_i) are determined by fitting experimental data with an estimated decay function convolved with the measured IRF. Upon optimization of decay fits, heterogeneity of per-pixel lifetime values can be visualized by lifetime maps or frequency distributions. Adapted with permission from[149].

production[84,127]. Furthermore, variations in fluorescence lifetime can be correlated to environmental changes within biological samples[135]. Previous studies have established that NAD(P)H and FAD autofluorescence intensity and lifetimes can distinguish heterogeneous populations based on tumor and immune phenotypes, treatment response, and cell function[133,135,136,144–148]. Ultimately, sensitivity of metabolic autofluorescence imaging to functionally distinct sub-populations across *in vitro* and *in vivo* tumor models supports further development to investigate the full spectrum of TME heterogeneity.

2.7 Analytical Techniques for Assessing Autofluorescence Heterogeneity

Quantitative analysis of autofluorescence images provides insights into cell function, structure-function relationships, and spatial heterogeneity that are not apparent with qualitative observations of the images. Analytical tools for image segmentation and heterogeneity analysis are introduced in this section. Innovations in these areas are ongoing, and new image analysis tools are frequently adopted from disparate disciplines. The prevalence of intercellular heterogeneity in tumors and limited cell-level sensitivity of standard imaging and biological assays highlight the importance of novel single-cell analysis methods for thorough characterization of the TME.

2.7.1 Heterogeneity analysis of autofluorescence measurements

2.7.1.1 Pixel-level analysis

Pixel-level analysis of autofluorescence intensities and lifetimes can inform on sub-cellular and cell-level heterogeneity within a sample. Lifetime histograms provide a useful quality check of curve fitting from TCSPC pixels, confirm the presence of distinct fluorescence lifetimes, and/or confirm expected changes in lifetime values from an experimental condition or FRET interaction (Figure 2.6B)[149]. Distributions of pixels can also be visualized in phasor space to provide complementary information on the identity of fluorophores in the sample and lifetime changes throughout an experiment [149,150]. Pixel-level FLIM analysis has been previously used to quantify lipid membrane integrity and heterogeneity, immune cell heterogeneity, cell development, protein conformation and organization, and other phenomena[148,151–155].

2.7.1.2 Cell-level analysis

Cell segmentation

Cell-level analysis provides a biological context for interpreting FLIM images by averaging intensity or lifetime values across all pixels within a single cell[137]. This approach quantifies diversity across cells in a similar manner to established techniques such as flow cytometry or colony counting. Segmentation is required for cell-level analysis. However, segmentation of autofluorescence images is challenging due to

low signal-to-noise ratio and poor spatial specificity of the fluorescence signal. CellProfiler has been used to isolate cells, nuclei, and cytoplasms from two-photon NAD(P)H autofluorescence images[156]. This approach identifies nuclei within a specified size range by thresholding pixels above the background fluorescence but below cytoplasmic fluorescence values. Whole cell masks are defined by propagating from nuclear masks. Nuclear masks are subtracted from cell masks to isolate cytoplasmic areas. Various cell segmentation frameworks have been developed to improve single-cell analysis of fluorescence lifetime data, but many of these are only optimized for high SNR, fluorescently labeled images[157–159]. Application of cell segmentation techniques for autofluorescence images would improve quantitative assessment of live, cell-level metabolic changes.

Population distributions of cells

Histograms of intensity and lifetime values can be plotted across numerous cells for population distribution analysis. This approach visualizes heterogeneity within cell classes under basal conditions or in response to perturbations. Histograms can be fit with population density models to summarize the distribution of cells and to identify distinct cell sub-populations. Gaussian mixture modeling is a common population density modeling approach where multiple Gaussian probability density functions are iteratively fit to each frequency histogram (Figure 2.7A)[144,160]. Goodness of fit is assessed by the minimum Akaike Information Criterion (AIC)[160,161]. However, this approach is limited by assumptions about the number of populations within the data and the Gaussian distribution of the data[162,163]. Approaches have been developed to circumvent these assumptions, including density-based clustering[164]. Density-based clustering defines sub-populations within data such that the highest density datapoints define the cluster for the nearest remaining points[164]. Previous studies have shown that population distribution analysis of autofluorescence measurements can classify cell types, drug response, and disease state [131,137,142–144,165]. Additionally, lifetime distributions can identify objects without prior segmentation. Variations in lifetime distributions have identified other molecular features such as tagged neurons in *C.* elegans and metabolic activities within tumors [166,167]. Overall, population distribution analysis provides unique insights into sample heterogeneity.

Quantitative metrics of autofluorescence heterogeneity

Heterogeneity in autofluorescence measurements is commonly quantified from coefficients of variation (CV)[168–171]. The CV is the standard deviation divided by the mean of a measurement, which enables comparisons of variability between samples. However, the CV does not define whether distinct sub-populations exist within the lifetime data. Alternatively, quantitative metrics of heterogeneity (e.g., H-index, wH-index) can be derived from population density models so that the behavior of sub-populations can be compared between conditions[142,143]. Collectively, these studies show that quantitative metrics of fluorescence lifetime heterogeneity provide powerful tools to study diversity in biological systems.

2.7.2 Analysis of autofluorescence spatial distributions

Both qualitative and quantitative analyses have been developed for evaluating spatial heterogeneity of autofluorescence measurements. False-colored intensity and fluorescence lifetime images can be generated from integration of curve fitting parameters (e.g., τ_1, τ_2, α_1, α_2) or phasor values (e.g., g, s)[149,150]. These images are used for qualitative assessments of molecular distribution in biological samples. For example, FLIM images can map lifetime sensors of intracellular molecules (e.g., magnesium, calcium, chromatin, myoglobin, antigens), pH, oxygen, or temperature[172–174]. Intensity and lifetime images of endogenous fluorophores provide qualitative information on the distribution of subcellular and cellular metabolism, biogenesis, and structure[129,145,148,149,169,175–178]. Furthermore, tissue-level autofluorescence images can distinguish cellular compartments across diverse tissue types (e.g., stroma, endothelium, epithelium, cancerous tissue)[153,179–182]. Methods to quantify spatial variations in intracellular fluorescence have been also reported, though these have not been translated for autofluorescence data (Figure 2.7B)[183–185]. For example, QuantEv is one existing platform to evaluate the localization of fluorescently-tagged proteins as a function of the global structure of a cell[184], and a similar approach was designed for spatial analysis of GFP-expressing plant Golgi proteins[185]. Novel analytical approaches to assess autofluorescence spatial distributions will be critical to exploit the wealth of information in autofluorescence images.

2.7.3 Multiparametric analysis of autofluorescence data

Autofluorescence images usually have multiple variables per pixel (e.g., lifetime curve fit parameters, fluorescence intensity) that can be used in multivariate classification models to identify distinct cell subsets or function (Figure 2.7C). Previous studies used discriminant analysis of fluorescence intensity, lifetime, and morphological parameters to classify cell types (keratinocytes, adipocytes, myoblasts, cardiomyocytes, stem cells) in response to metabolic perturbations (growth factor and nutrient starvation/supplementation, environmental stimuli) [186]. Multivariate FLIM analysis can also use more complex models including nonlinear classifiers (e.g., logistic regression, random forests) and convolutional neural networks. These models also achieve high accuracy for multi-group classification based on autofluorescence lifetimes, specifically for T cell subtypes and activation states (e.g., quiescent/activated, CD3/CD4/CD8 co-expression)[187,188]. These studies illustrate the strength of multivariate classification models based on autofluorescence data, which provides robust separation of cell types and cell function.

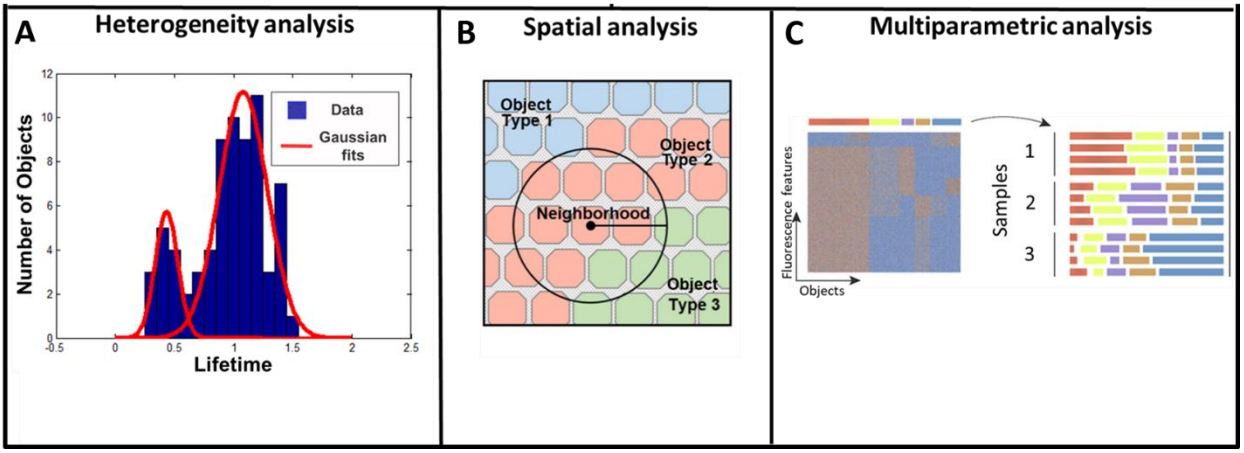

Figure 2.7: Analytical approaches for assessing heterogeneity in cellular autofluorescence. A) Histograms of lifetimes per object are fit to distribution models to describe sub-populations and variability in the data. B) Spatial statistical analyses can quantify spatial heterogeneity in autofluorescence data. For example, relative proximity measurements can define pixel/cell spatial distributions within specified neighborhoods. Adapted with permission from[183]. C) Multiparametric analysis provides models that describe defined classes within the data using all recorded measurements. Adapted with permission from[68].

Proposed relationships between tumor development, treatment response, and heterogeneity within the TME warrants improved methods for assessing the various sources of TME heterogeneity. Metabolic autofluorescence imaging and image analysis are well-established tools for quantifying heterogeneous single-cell function in live, intact samples. As mentioned previously, metabolic autofluorescence imaging has been demonstrated for observing spatial and temporal changes in cell metabolism across *in vivo* and 3D *in vitro* tumor models[131,142,146,147,179,181,189–191]. Current functional assays and imaging techniques have limited ability to resolve these cell-level transitions, supporting further development of metabolic autofluorescence imaging and analysis for characterizing heterogeneity in the TME. Thus, the work presented in this dissertation will focus on advancements in metabolic autofluorescence imaging applications and novel analytical tools to inform on mechanisms driving TME heterogeneity to affect tumor progression.

2.8 References

1. Thakkar S, Sharma D, Kalia K, Tekade RK. Tumor microenvironment targeted nanotherapeutics for cancer therapy and diagnosis: A review. *Acta Biomater*. 2019.
2. Hendrix MJC, Seftor EA, Margaryan N V, Seftor REB. Heterogeneity and Plasticity of Melanoma: Challenges of Current Therapies. In: *Cutaneous Melanoma: Etiology and Therapy [Internet]*. Codon Publications; 2017.
3. Almendro V, Cheng YK, Randles A, et al. Inference of tumor evolution during chemotherapy by computational modeling and in situ analysis of genetic and phenotypic cellular diversity. *Cell Rep*. 2014;6(3):514-527. doi:10.1016/j.celrep.2013.12.041
4. Lawson DA, Kessenbrock K, Davis RT, Pervolarakis N, Werb Z. Tumour heterogeneity and metastasis at single-cell resolution. *Nat Cell Biol*. 2018;20(12):1349-1360. doi:10.1038/s41556-018-0236-7
5. Davies AE, Albeck JG. Microenvironmental Signals and Biochemical Information Processing: Cooperative Determinants of Intratumoral Plasticity and Heterogeneity. *Front cell Dev Biol*. 2018;6:44. doi:10.3389/fcell.2018.00044
6. Ahmed F, Haass NK. Microenvironment-Driven Dynamic Heterogeneity and Phenotypic Plasticity as a Mechanism of Melanoma Therapy Resistance . *Front Oncol* . 2018;8:173. https://www.frontiersin.org/article/10.3389/fonc.2018.00173.
7. Jolly MK, Celià-Terrassa T. Dynamics of Phenotypic Heterogeneity Associated with EMT and Stemness during Cancer Progression. *J Clin Med*. 2019;8(10):1542.
8. Hanahan D, Weinberg RA. Hallmarks of cancer: the next generation. *Cell*. 2011;144(5):646-674.

9. Sever R, Brugge JS. Signal transduction in cancer. *Cold Spring Harb Perspect Med*. 2015;5(4):a006098.

10. Roma-Rodrigues C, Mendes R, Baptista P V, Fernandes AR. Targeting Tumor Microenvironment for Cancer Therapy. *Int J Mol Sci*. 2019;20(4):840. doi:10.3390/ijms20040840

11. Yuan Y. Spatial Heterogeneity in the Tumor. *Cold Spring Harb Perspect Med*. 2017;6(8):a026583-a026583.

12. McQuerry JA, Chang JT, Bowtell DDL, Cohen A, Bild AH. Mechanisms and clinical implications of tumor heterogeneity and convergence on recurrent phenotypes. *J Mol Med*. 2017:1167-1178. doi:10.1007/s00109-017-1587-4

13. Shembrey C, Huntington ND, Hollande F. Impact of tumor and immunological heterogeneity on the anti-cancer immune response. *Cancers (Basel)*. 2019;11(9):1217.

14. Tellez-Gabriel M, Ory B, Lamoureux F, Heymann M-F, Heymann D. Tumour Heterogeneity: The Key Advantages of Single-Cell Analysis. *Int J Mol Sci*. 2016;17(12):2142. doi:10.3390/ijms17122142

15. Greaves M, Maley CC. Clonal evolution in cancer. *Nature*. 2012;481(7381):306.

16. Negrini S, Gorgoulis VG, Halazonetis TD. Genomic instability—an evolving hallmark of cancer. *Nat Rev Mol cell Biol*. 2010;11(3):220-228.

17. Torgovnick A, Schumacher B. DNA repair mechanisms in cancer development and therapy. *Front Genet*. 2015;6:157.

18. Ramón y Cajal S, Sesé M, Capdevila C, et al. Clinical implications of intratumor heterogeneity: challenges and opportunities. *J Mol Med*. 2020;98(2):161-177. doi:10.1007/s00109-020-01874-2

19. Salk JJ, Fox EJ, Loeb LA. Mutational heterogeneity in human cancers: origin and consequences. *Annu Rev Pathol*. 2010;5:51-75. doi:10.1146/annurev-pathol-121808-102113

20. Noble R, Burley J, Sueur C, Hochberg M. *When, Why and How Clonal Diversity Predicts Future Tumour Growth*.; 2019. doi:10.1101/2019.12.17.879270

21. Esteller M. Epigenetics in cancer. *N Engl J Med*. 2008;358(11):1148-1159.

22. Flavahan WA, Gaskell E, Bernstein BE. Epigenetic plasticity and the hallmarks of cancer. *Science*. 2017;357(6348):eaal2380. doi:10.1126/science.aal2380

23. Baxter E, Windloch K, Gannon F, Lee JS. Epigenetic regulation in cancer progression. *Cell Biosci*. 2014;4(1):45.

24. So W-K, Cheung TH. Molecular regulation of cellular quiescence: a perspective from adult stem cells and its niches. In: *Cellular Quiescence*. Springer; 2018:1-25.

25. Soufi A, Dalton S. Cycling through developmental decisions: how cell cycle dynamics control pluripotency, differentiation and reprogramming. *Development*. 2016;143(23):4301-4311.

26. Kwon JS, Everetts NJ, Wang X, et al. Controlling depth of cellular quiescence by an Rb-E2F network switch. *Cell Rep*. 2017;20(13):3223-3235.

27. Baxevanis CN, Perez SA. Cancer dormancy: a regulatory role for endogenous immunity in establishing and maintaining the tumor dormant state. *Vaccines*. 2015;3(3):597-619.

28. Bragado P, Sosa MS, Keely P, Condeelis J, Aguirre-Ghiso JA. Microenvironments dictating tumor

cell dormancy. In: *Minimal Residual Disease and Circulating Tumor Cells in Breast Cancer*. Springer; 2012:25-39.

29. Rybinski B, Yun K. Addressing intra-tumoral heterogeneity and therapy resistance. *Oncotarget*. 2016;7(44):72322.

30. Balkwill FR, Capasso M, Hagemann T. The tumor microenvironment at a glance. 2012.

31. Anari F, Ramamurthy C, Zibelman M. Impact of tumor microenvironment composition on therapeutic responses and clinical outcomes in cancer. *Futur Oncol*. 2018;14(14):1409-1421.

32. Marusyk A, Polyak K. Tumor heterogeneity: causes and consequences. *Biochim Biophys Acta*. 2011;1805(1):1-28. doi:10.1016/j.bbcan.2009.11.002.Tumor

33. Payne KK, Toor AA, Wang X-Y, Manjili MH. Immunotherapy of Cancer: Reprogramming Tumor-Immune Crosstalk. *Clin Dev Immunol*. 2012;2012:1-8. doi:10.1155/2012/760965

34. Zahreddine H, Borden KLB. Mechanisms and insights into drug resistance in cancer. *Front Pharmacol*. 2013;4:28. doi:10.3389/fphar.2013.00028

35. Gajewski TF, Schreiber H, Fu Y-X. Innate and adaptive immune cells in the tumor microenvironment. doi:10.1038/ni.2703

36. Lee H-W, Choi H-J, Ha S-J, Lee K-T, Kwon Y-G. Recruitment of monocytes/macrophages in different tumor microenvironments. *Biochim Biophys Acta - Rev Cancer*. 2013;1835(2):170-179. doi:10.1016/J.BBCAN.2012.12.007

37. Seager RJ, Hajal C, Spill F, Kamm RD, Zaman MH. Dynamic interplay between tumour, stroma and immune system can drive or prevent tumour progression. *Converg Sci Phys Oncol*. 2017;3(3):34002. doi:10.1088/2057-1739/aa7e86

38. Panni RZ, Linehan DC, DeNardo DG. Targeting tumor-infiltrating macrophages to combat cancer. *Immunotherapy*. 2013;5(10):1075-1087. doi:10.2217/imt.13.102

39. De Palma M, Lewis CE. Macrophage Regulation of Tumor Responses to Anticancer Therapies. *Cancer Cell*. 2013;23(3):277-286. doi:10.1016/j.ccr.2013.02.013

40. Quail DF, Joyce JA. Molecular Pathways: Deciphering Mechanisms of Resistance to Macrophage-Targeted Therapies. *Clin Cancer Res*. 2017;23(4):876-884. doi:10.1158/1078-0432.CCR-16-0133

41. Murray PJ. Macrophage Polarization. *Annu Rev Physiol*. 2017;79(1):541-566. doi:10.1146/annurev-physiol-022516-034339

42. Liu YC, Zou XB, Chai YF, Yao YM. Macrophage Polarization in Inflammatory Diseases. *Int J Biol Sci*. 2014;10(5):520-529. doi:10.7150/ijbs.8879

43. Jagannathan N, Ramanathan S. Tumor Associated Macrophage: A Review on the Phenotypes, Traits and Functions. *Iran J Cancer Prev Iran J Cancer Prev*. 2014;7(71):1-81. https://www.ncbi.nlm.nih.gov/pmc/articles/PMC4142950/pdf/IJCP-07-001.pdf. Accessed April 23, 2018.

44. Biswas SK. Tumor Microenvironment and. 2017. doi:10.1101/cshperspect.a026781

45. Biswas SK, Mantovani A. Macrophage plasticity and interaction with lymphocyte subsets: cancer as a paradigm. *Nat Immunol*. 2010;11(10):889-896. doi:10.1038/ni.1937

46. Biswas SK, Sica A, Lewis CE. Plasticity of macrophage function during tumor progression:

regulation by distinct molecular mechanisms. *J Immunol*. 2008;180(4):2011-2017.

47. Martinez FO, Gordon S. The M1 and M2 paradigm of macrophage activation: time for reassessment. *F1000Prime Rep*. 2014;6:13. doi:10.12703/P6-13

48. Chávez-Galán L, Olleros ML, Vesin D, Garcia I. Much More than M1 and M2 Macrophages, There are also CD169(+) and TCR(+) Macrophages. *Front Immunol*. 2015;6:263. doi:10.3389/fimmu.2015.00263

49. Verdeguer F, Aouadi M. Macrophage heterogeneity and energy metabolism. *Exp Cell Res*. 2017;360(1):35-40. doi:10.1016/J.YEXCR.2017.03.043

50. Gallaher JA, Enriquez-Navas PM, Luddy KA, Gatenby RA, Anderson ARA. Spatial Heterogeneity and Evolutionary Dynamics Modulate Time to Recurrence in Continuous and Adaptive Cancer Therapies. *Cancer Res*. 2018;78(8):2127-2139. doi:10.1158/0008-5472.CAN-17-2649

51. Ruprecht V, Monzo P, Ravasio A, et al. How cells respond to environmental cues – insights from bio-functionalized substrates. *J Cell Sci*. 2017;130(1):51 LP - 61. doi:10.1242/jcs.196162

52. Quail DF, Joyce JA. Microenvironmental regulation of tumor progression and metastasis. *Nat Med*. 2013;19(11):1423-1437. doi:10.1038/nm.3394

53. Lloyd MC, Cunningham JJ, Bui MM, Gillies RJ, Brown JS, Gatenby RA. Darwinian Dynamics of Intratumoral Heterogeneity: Not Solely Random Mutations but Also Variable Environmental Selection Forces. *Cancer Res*. 2016;76(11):3136-3144. doi:10.1158/0008-5472.CAN-15-2962

54. Fridman WH, Pagès F, Sautès-Fridman C, Galon J. The immune contexture in human tumours: impact on clinical outcome. *Nat Rev Cancer*. 2012;12(4):298-306. doi:10.1038/nrc3245

55. Nawaz S, Heindl A, Koelble K, Yuan Y. Erratum: Beyond immune density: critical role of spatial heterogeneity in estrogen receptor-negative breast cancer. *Mod Pathol*. 2015;28(12):1621. doi:10.1038/modpathol.2015.133

56. Junttila MR, de Sauvage FJ. Influence of tumour micro-environment heterogeneity on therapeutic response. *Nature*. 2013;501(7467):346-354. doi:10.1038/nature12626

57. Alfarouk KO, Stock C-M, Taylor S, et al. Resistance to cancer chemotherapy: failure in drug response from ADME to P-gp. *Cancer Cell Int*. 2015;15(1):71.

58. Lyssiotis CA, Kimmelman AC. Metabolic interactions in the tumor microenvironment. *Trends Cell Biol*. 2017;27(11):863-875.

59. Hu P, Zhang W, Xin H, Deng G. Single Cell Isolation and Analysis. *Front cell Dev Biol*. 2016;4:116. doi:10.3389/fcell.2016.00116

60. Chattopadhyay PK, Gierahn TM, Roederer M, Love JC. Single-cell technologies for monitoring immune systems. *Nat Immunol*. 2014;15(2):128-135. doi:10.1038/ni.2796

61. Basu S, Campbell HM, Dittel BN, Ray A. Purification of specific cell population by fluorescence activated cell sorting (FACS). *J Vis Exp*. 2010;(41):1546. doi:10.3791/1546

62. Traenkle B, Rothbauer U. Under the microscope: Single-domain antibodies for live-cell imaging and super-resolution microscopy. *Front Immunol*. 2017;8:1030.

63. Stadler C, Rexhepaj E, Singan VR, et al. Immunofluorescence and fluorescent-protein tagging show high correlation for protein localization in mammalian cells. *Nat Methods*. 2013;10(4):315.

64. Snapp EL. Fluorescent proteins: a cell biologist's user guide. *Trends Cell Biol*. 2009;19(11):649-655.

65. Brooks D, Gadalla R, Noamani B, et al. Validation of CyTOF against flow cytometry for immunological studies and monitoring of human cancer clinical trials. *Front Oncol*. 2019;9:415.

66. Huang W, Luo S, Burgess R, Yi Y-H, Huang GF, Huang R-P. New insights into the tumor microenvironment utilizing protein array technology. *Int J Mol Sci*. 2018;19(2):559.

67. Nishida-Aoki N, Gujral TS. Emerging approaches to study cell–cell interactions in tumor microenvironment. *Oncotarget*. 2019;10(7):785.

68. Smith EA, Hodges HC. The Spatial and Genomic Hierarchy of Tumor Ecosystems Revealed by Single-Cell Technologies. *Trends in cancer*. 2019.

69. Vallejos CA, Richardson S, Marioni JC. Beyond comparisons of means: understanding changes in gene expression at the single-cell level. *Genome Biol*. 2016;17:70. doi:10.1186/s13059-016-0930-3

70. Choi YH, Kim JK. Dissecting cellular heterogeneity using single-cell RNA sequencing. *Mol Cells*. 2019;42(3):189.

71. Tang X, Huang Y, Lei J, Luo H, Zhu X. The single-cell sequencing: new developments and medical applications. *Cell Biosci*. 2019;9(1):53.

72. González-Silva L, Quevedo L, Varela I. Tumor Functional Heterogeneity Unraveled by scRNA-seq Technologies. *Trends in Cancer*. 2020.

73. Anderson ARA, Weaver AM, Cummings PT, Quaranta V. Tumor Morphology and Phenotypic Evolution Driven by Selective Pressure from the Microenvironment. *Cell*. 2006;127(5):905-915. doi:10.1016/j.cell.2006.09.042

74. Sokal RR, Oden NL. Spatial autocorrelation in biology: 1. Methodology. *Biol J Linn Soc*. 1978;10(2):199-228. doi:10.1111/j.1095-8312.1978.tb00013.x

75. Ward MD, Skrede Gleditsch K. An introduction to spatial regression models in the social sciences. 2007:87.

76. Heindl A, Nawaz S, Yuan Y. Mapping spatial heterogeneity in the tumor microenvironment: A new era for digital pathology. *Lab Investig*. 2015;95(4):377-384. doi:10.1038/labinvest.2014.155

77. Krüger JM, Wemmert C, Sternberger L, et al. Combat or surveillance? Evaluation of the heterogeneous inflammatory breast cancer microenvironment. *J Pathol*. 2013;229(4):569-578. doi:10.1002/path.4150

78. Yuan Y, Failmezger H, Rueda O, et al. Quantitative Image Analysis of Cellular Heterogeneity in Breast Tumors Complements Genomic Profiling. *Sci Transl Med*. 2012;143(157):157ra143-157ra143. doi:10.1126/scitranslmed.3004330

79. Setiadi AF, Ray NC, Kohrt HE, et al. Quantitative, architectural analysis of immune cell subsets in tumor-draining lymph nodes from breast cancer patients and healthy lymph nodes. *PLoS One*. 2010;5(8). doi:10.1371/journal.pone.0012420

80. Bindea G, Mlecnik B, Tosolini M, et al. Spatiotemporal dynamics of intratumoral immune cells reveal the immune landscape in human cancer. *Immunity*. 2013;39(4):782-795. doi:10.1016/j.immuni.2013.10.003

81. Chang AY, Bhattacharya N, Mu J, et al. Spatial organization of dendritic cells within tumor draining lymph nodes impacts clinical outcome in breast cancer patients. *J Transl Med*. 2013;11(1):1. doi:10.1186/1479-5876-11-242

82. Vander Heiden MG, Cantley LC, Thompson CB. Understanding the Warburg effect: the metabolic requirements of cell proliferation. *Science*. 2009;324(5930):1029-1033. doi:10.1126/science.1160809

83. Hosios AM, Vander Heiden MG. The redox requirements of proliferating mammalian cells. *J Biol Chem*. 2018;293(20):7490-7498. doi:10.1074/jbc.TM117.000239

84. Heikal AA. Intracellular coenzymes as natural biomarkers for metabolic activities and mitochondrial anomalies. *Biomark Med*. 2010;4(2):241-263. doi:10.2217/bmm.10.1

85. Valeur B. Molecular Fluorescence. *Digit Encycl Appl Phys*. December 2009:477-531. doi:doi:10.1002/3527600434.eap684

86. Fadaka A, Ajiboye B, Ojo O, Adewale O, Olayide I, Emuowhochere R. Biology of glucose metabolization in cancer cells. *J Oncol Sci*. 2017;3(2):45-51. doi:https://doi.org/10.1016/j.jons.2017.06.002

87. Cai L, Tu BP. Driving the Cell Cycle Through Metabolism. *Annu Rev Cell Dev Biol*. 2012;28(1):59-87. doi:10.1146/annurev-cellbio-092910-154010

88. Saudemont A, Quesnel B. In a model of tumor dormancy, long-term persistent leukemic cells have increased B7-H1 and B7.1 expression and resist CTL-mediated lysis. *Blood*. 2004;104(7):2124-2133. doi:10.1182/blood-2004-01-0064

89. Handy DE, Loscalzo J. Redox regulation of mitochondrial function. *Antioxid Redox Signal*. 2012;16(11):1323-1367. doi:10.1089/ars.2011.4123

90. He Y, Gao M, Tang H, Cao Y, Liu S, Tao Y. Metabolic Intermediates in Tumorigenesis and Progression. *Int J Biol Sci*. 2019;15(6):1187-1199. doi:10.7150/ijbs.33496

91. Ghesquière B, Wong BW, Kuchnio A, Carmeliet P. Metabolism of stromal and immune cells in health and disease. *Nature*. 2014;511(7508):167-176. doi:10.1038/nature13312

92. Qian B-Z, Pollard JW. Macrophage diversity enhances tumor progression and metastasis. *Cell*. 2010;141(1):39-51. doi:10.1016/j.cell.2010.03.014

93. Koo S, Garg NJ. Metabolic programming of macrophage functions and pathogens control. *Redox Biol*. 2019;24:101198. doi:https://doi.org/10.1016/j.redox.2019.101198

94. Tan H-Y, Wang N, Li S, Hong M, Wang X, Feng Y. The Reactive Oxygen Species in Macrophage Polarization: Reflecting Its Dual Role in Progression and Treatment of Human Diseases. Venditti P, ed. *Oxid Med Cell Longev*. 2016;2016:2795090. doi:10.1155/2016/2795090

95. Viola A, Munari F, Sánchez-Rodríguez R, Scolaro T, Castegna A. The Metabolic Signature of Macrophage Responses. *Front Immunol*. 2019;10:1462. doi:10.3389/fimmu.2019.01462

96. Renner K, Singer K, Koehl GE, et al. Metabolic Hallmarks of Tumor and Immune Cells in the Tumor Microenvironment. *Front Immunol*. 2017;8:248. doi:10.3389/fimmu.2017.00248

97. Pearce EL, Pearce EJ. Metabolic Pathways in Immune Cell Activation and Quiescence. *Immunity*. 2013;38(4):633-643. doi:10.1016/J.IMMUNI.2013.04.005

98. Mehta MM, Weinberg SE, Chandel NS. Mitochondrial control of immunity: beyond ATP. *Nat Rev*

Immunol. 2017;17(10):608-620. doi:10.1038/nri.2017.66

99. O'Neill LAJ, Kishton RJ, Rathmell J. A guide to immunometabolism for immunologists. *Nat Rev Immunol*. 2016;16(9):553-565. doi:10.1038/nri.2016.70

100. Bar-Shalom R, Valdivia AY, Blaufox MD. PET imaging in oncology. *Semin Nucl Med*. 2000;30(3):150-185. doi:https://doi.org/10.1053/snuc.2000.7439

101. Asselin M-C, O'Connor JPB, Boellaard R, Thacker NA, Jackson A. Quantifying heterogeneity in human tumours using MRI and PET. *Eur J Cancer*. 2012;48(4):447-455. doi:https://doi.org/10.1016/j.ejca.2011.12.025

102. Sharma R, Aboagye E. Development of radiotracers for oncology–the interface with pharmacology. *Br J Pharmacol*. 2011;163(8):1565-1585.

103. Ganeshan B, Miles KA. Quantifying tumour heterogeneity with CT. *Cancer Imaging*. 2013;13(1):140-149. doi:10.1102/1470-7330.2013.0015

104. Youn H, Hong K-J. In vivo non invasive molecular imaging for immune cell tracking in small animals. *Immune Netw*. 2012;12(6):223-229. doi:10.4110/in.2012.12.6.223

105. Zhou ZN, Boimel PJ, Segall JE. Tumor-stroma: In vivo assays and intravital imaging to study cell migration and metastasis. *Drug Discov Today Dis Models*. 2011;8(2-3):95-112. doi:10.1016/j.ddmod.2011.07.003

106. Sevick-Muraca EM, Kwon S, Rasmussen JC. Emerging lymphatic imaging technologies for mouse and man. *J Clin Invest*. 2014;124(3):905-914. doi:10.1172/JCI71612

107. Ehling J, Lammers T, Kiessling F. Non-invasive imaging for studying anti-angiogenic therapy effects. *Thromb Haemost*. 2013;109(3):375-390. doi:10.1160/TH12-10-0721

108. Sengupta D, Pratx G. Imaging metabolic heterogeneity in cancer. doi:10.1186/s12943-015-0481-3

109. Yankeelov TE, Arlinghaus LR, Li X, Gore JC. The role of magnetic resonance imaging biomarkers in clinical trials of treatment response in cancer. *Semin Oncol*. 2011;38(1):16-25. doi:10.1053/j.seminoncol.2010.11.007

110. Mu W, Gillies RJ, Aerts HJWL, Napel S, Jardim-Perassi B V. Quantitative imaging of cancer in the postgenomic era: Radio(geno)mics, deep learning, and habitats. *Cancer*. 2018;124(24):4633-4649. doi:10.1002/cncr.31630

111. Ramamonjisoa N, Ackerstaff E. Characterization of the Tumor Microenvironment and Tumor-Stroma Interaction by Non-invasive Preclinical Imaging. *Front Oncol*. 2017;7:3. doi:10.3389/fonc.2017.00003

112. Duraiyan J, Govindarajan R, Kaliyappan K, Palanisamy M. Applications of immunohistochemistry. *J Pharm Bioallied Sci*. 2012;4(Suppl 2):S307-S309. doi:10.4103/0975-7406.100281

113. He L, Long LR, Antani S, Thoma GR. Histology image analysis for carcinoma detection and grading. *Comput Methods Programs Biomed*. 2012;107(3):538-556. doi:https://doi.org/10.1016/j.cmpb.2011.12.007

114. Galon J, Costes A, Sanchez-Cabo F, et al. Type, Density, and Location of Immune Cells Within Human Colorectal Tumors Predict Clinical Outcome. *Science (80-)*. 2006;313(5795):1960 LP - 1964. http://science.sciencemag.org/content/313/5795/1960.abstract.

115. Dhawan AP, D'Alessandro B, Fu X. Optical Imaging Modalities for Biomedical Applications. *IEEE Rev Biomed Eng*. 2010;3:69-92. doi:10.1109/RBME.2010.2081975

116. Xu HN, Zheng G, Tchou J, Nioka S, Li LZ. Characterizing the metabolic heterogeneity in human breast cancer xenografts by 3D high resolution fluorescence imaging. *Springerplus*. 2013;2(1):1-9. doi:10.1186/2193-1801-2-73

117. Wu D, Huang L, Jiang MS, Jiang H. Contrast agents for photoacoustic and thermoacoustic imaging: a review. *Int J Mol Sci*. 2014;15(12):23616-23639. doi:10.3390/ijms151223616

118. Mallidi S, Luke GP, Emelianov S. Photoacoustic imaging in cancer detection, diagnosis, and treatment guidance. *Trends Biotechnol*. 2011;29(5):213-221. doi:10.1016/j.tibtech.2011.01.006

119. Strupler M, Pena A-M, Hernest M, et al. Second harmonic imaging and scoring of collagen in fibrotic tissues. *Opt Express*. 2007;15(7):4054-4065. doi:10.1364/OE.15.004054

120. Noreen R, Chien C-C, Chen H-H, et al. FTIR spectro-imaging of collagen scaffold formation during glioma tumor development. *Anal Bioanal Chem*. 2013;405(27):8729-8736. doi:10.1007/s00216-013-7337-8

121. Bhargava R. Infrared spectroscopic imaging: the next generation. *Appl Spectrosc*. 2012;66(10):1091-1120. doi:10.1366/12-06801

122. Lasch P, Naumann D. Spatial resolution in infrared microspectroscopic imaging of tissues. *Biochim Biophys Acta - Biomembr*. 2006;1758(7):814-829. doi:https://doi.org/10.1016/j.bbamem.2006.06.008

123. Provenzano PP, Eliceiri KW, Keely PJ. Multiphoton microscopy and fluorescence lifetime imaging microscopy (FLIM) to monitor metastasis and the tumor microenvironment. *Clin Exp Metastasis*. 2009;26(4):357-370. doi:10.1007/s10585-008-9204-0

124. Stuker F, Ripoll J, Rudin M. Fluorescence molecular tomography: principles and potential for pharmaceutical research. *Pharmaceutics*. 2011;3(2):229-274. doi:10.3390/pharmaceutics3020229

125. Miller DR, Jarrett JW, Hassan AM, Dunn AK. Deep Tissue Imaging with Multiphoton Fluorescence Microscopy. *Curr Opin Biomed Eng*. 2017;4:32-39. doi:10.1016/j.cobme.2017.09.004

126. Hung YP. Single Cell Imaging of Metabolism with Fluorescent Biosensors. 2012.

127. Chance B, Schoener B, Oshino R, Itshak F, Nakase Y. Oxidation-reduction ratio studies of mitochondria in freeze-trapped samples. NADH and flavoprotein fluorescence signals. *J Biol Chem*. 1979;254(11):4764-4771.

128. Blacker TS, Marsh RJ, Duchen MR, Bain AJ. Activated barrier crossing dynamics in the non-radiative decay of NADH and NADPH. *Chem Phys*. 2013;422:184-194. doi:10.1016/j.chemphys.2013.02.019

129. Blacker TS, Duchen MR. Investigating mitochondrial redox state using NADH and NADPH autofluorescence. *Free Radic Biol Med*. 2016;100:53-65.

130. Skala MC, Squirrell JM, Vrotsos KM, et al. Multiphoton Microscopy of Endogenous Fluorescence Differentiates Normal, Precancerous, and Cancerous Squamous Epithelial Tissues. *Cancer Res*. 2005;65(4):1180 LP - 1186. http://cancerres.aacrjournals.org/content/65/4/1180.abstract.

131. Walsh AJ, Cook RS, Manning HC, et al. Optical metabolic imaging identifies glycolytic levels, subtypes, and early-treatment response in breast cancer. *Cancer Res*. 2013;73(20):6164-6174.

doi:10.1158/0008-5472.CAN-13-0527

132. Quinn KP, Sridharan G V., Hayden RS, Kaplan DL, Lee K, Georgakoudi I. Quantitative metabolic imaging using endogenous fluorescence to detect stem cell differentiation. *Sci Rep*. 2013;3. doi:10.1038/srep03432

133. Georgakoudi I, Quinn KP. Optical Imaging Using Endogenous Contrast to Assess Metabolic State. *Annu Rev Biomed Eng*. 2012;14(1):351-367. doi:10.1146/annurev-bioeng-071811-150108

134. Hou J, Wright HJ, Chan NS-K, et al. Correlating two-photon excited fluorescence imaging of breast cancer cellular redox state with seahorse flux analysis of normalized cellular oxygen consumption. *J Biomed Opt*. 2016;21(6):1-3. https://doi.org/10.1117/1.JBO.21.6.060503.

135. Lakowicz JR, Szmacinski H, Nowaczyk K, Johnson ML. Fluorescence lifetime imaging of free and protein-bound NADH. *Proc Natl Acad Sci U S A*. 1992;89(4):1271-1275. doi:10.1073/PNAS.89.4.1271

136. Quinn KP, Sridharan G V., Hayden RS, Kaplan DL, Lee K, Georgakoudi I. Quantitative metabolic imaging using endogenous fluorescence to detect stem cell differentiation. *Sci Rep*. 2013;3(1):3432. doi:10.1038/srep03432

137. Berezin MY, Achilefu S. Fluorescence lifetime measurements and biological imaging. *Chem Rev*. 2010;110(5):2641-2684. doi:10.1021/cr900343z

138. Lakowicz JR. *Principles of Fluorescence Spectroscopy*. Springer Science & Business Media; 2013.

139. Gailhouste L, Grand Y Le, Odin C, et al. Fibrillar collagen scoring by second harmonic microscopy: A new tool in the assessment of liver fibrosis. *J Hepatol*. 2010;52(3):398-406. doi:10.1016/j.jhep.2009.12.009

140. Becker W. *The Bh TCSPC Handbook*. Becker & Hickl; 2014.

141. van den Berg PAW, Feenstra KA, Mark AE, Berendsen HJC, Visser AJWG. Dynamic Conformations of Flavin Adenine Dinucleotide: Simulated Molecular Dynamics of the Flavin Cofactor Related to the Time-Resolved Fluorescence Characteristics. *J Phys Chem B*. 2002;106(34):8858-8869. doi:10.1021/jp020356s

142. Sharick JT, Jeffery JJ, Karim MR, et al. Cellular Metabolic Heterogeneity In Vivo Is Recapitulated in Tumor Organoids. *Neoplasia*. 2019;21(6):615-626. doi:10.1016/j.neo.2019.04.004

143. Shah AT, Diggins KE, Walsh AJ, Irish JM, Skala MC. In Vivo Autofluorescence Imaging of Tumor Heterogeneity in Response to Treatment. *Neoplasia*. 2015;17(12):862-870. doi:10.1016/j.neo.2015.11.006

144. Walsh AJ, Skala MC. Optical metabolic imaging quantifies heterogeneous cell populations. *Biomed Opt Express*. 2015;6(2):559-573. doi:10.1364/BOE.6.000559

145. Stuntz E, Gong Y, Sood D, et al. Endogenous Two-Photon Excited Fluorescence Imaging Characterizes Neuron and Astrocyte Metabolic Responses to Manganese Toxicity. *Sci Rep*. 2017;7(1):1041. doi:10.1038/s41598-017-01015-9

146. Walsh AJ, Cook RS, Sanders ME, et al. Quantitative optical imaging of primary tumor organoid metabolism predicts drug response in breast cancer. *Cancer Res*. 2014;74(18):5184-5194. doi:10.1158/0008-5472.CAN-14-0663

147. Shah AT, Heaster TM, Skala MC. Metabolic Imaging of Head and Neck Cancer Organoids. Sobol RW, ed. *PLoS One*. 2017;12(1):e0170415. doi:10.1371/journal.pone.0170415

148. Alfonso-García A, Smith TD, Datta R, et al. Label-free identification of macrophage phenotype by fluorescence lifetime imaging microscopy. *J Biomed Opt*. 2016;21(4):46005. doi:10.1117/1.JBO.21.4.046005

149. Chacko J V, Eliceiri KW. Autofluorescence lifetime imaging of cellular metabolism: Sensitivity toward cell density, pH, intracellular, and intercellular heterogeneity. *Cytom Part A*. 2019;95(1):56-69.

150. Ranjit S, Malacrida L, Jameson DM, Gratton E. Fit-free analysis of fluorescence lifetime imaging data using the phasor approach. *Nat Protoc*. 2018;13(9):1979-2004. doi:10.1038/s41596-018-0026-5

151. Gratton E, Parasassi T. Fluorescence lifetime distributions in membrane systems. *J Fluoresc*. 1995;5(1):51-57.

152. Stöckl M, Plazzo AP, Korte T, Herrmann A. Detection of lipid domains in model and cell membranes by fluorescence lifetime imaging microscopy of fluorescent lipid analogues. *J Biol Chem*. 2008;283(45):30828-30837.

153. Rico-Jimenez JJ, Serafino MJ, Shrestha S, et al. Automated detection of superficial macrophages in atherosclerotic plaques using autofluorescence lifetime imaging. *Atherosclerosis*. 2019;285:120-127. doi:10.1016/j.atherosclerosis.2019.04.223

154. Cho KWY, Ma N, de Mochel NR, Pham PDA, Yoo TY, Digman MA. Label-free assessment of preimplantation embryo quality by the Fluorescence Lifetime Imaging Microscopy (FLIM)-phasor approach. *Reprod Biomed Online*. 2019;38:e34-e35.

155. Krishnamoorthy G. Fluorescence Lifetime Distribution Brings Out Mechanisms Involving Biomolecules While Quantifying Population Heterogeneity. In: *Reviews in Fluorescence 2017*. Springer; 2018:75-98.

156. Walsh AJ, Skala MC. An automated image processing routine for segmentation of cell cytoplasms in high-resolution autofluorescence images. In: Periasamy A, So PTC, König K, eds. Vol 8948. International Society for Optics and Photonics; 2014:89481M. doi:10.1117/12.2040644

157. Arena ET, Rueden CT, Hiner MC, Wang S, Yuan M, Eliceiri KW. Quantitating the cell: turning images into numbers with ImageJ. *Wiley Interdiscip Rev Dev Biol*. 2017;6(2):e260.

158. Hall M, Frank E, Holmes G, Pfahringer B, Reutemann P, Witten IH. The WEKA data mining software: an update. *ACM SIGKDD Explor Newsl*. 2009;11(1):10-18.

159. Sommer C, Straehle C, Koethe U, Hamprecht FA. Ilastik: Interactive learning and segmentation toolkit. In: *2011 IEEE International Symposium on Biomedical Imaging: From Nano to Macro*. IEEE; 2011:230-233.

160. Pan W, Lin J, Le CT. Model-based cluster analysis of microarray gene-expression data. *Genome Biol*. 2002;3(2):RESEARCH0009. http://www.ncbi.nlm.nih.gov/pubmed/11864371. Accessed April 23, 2018.

161. Akaike H. A new look at the statistical model identification. In: *Selected Papers of Hirotugu Akaike*. Springer; 1974:215-222.

162. Haney SA. Rapid Assessment and Visualization of Normality in High-Content and Other Cell-

Level Data and Its Impact on the Interpretation of Experimental Results. *J Biomol Screen*. 2014;19(5):672-684. doi:10.1177/1087057114526432

163. Huang S. Non-genetic heterogeneity of cells in development: more than just noise. *Development*. 2009;136(23):3853-3862.

164. Rodriguez A, Laio A. Clustering By Fast Search and Find of Desity Peaks. *Science (80-)*. 2014;344(6191):1492-1496.

165. Cannon TM, Shah AT, Skala MC. Autofluorescence imaging captures heterogeneous drug response differences between 2D and 3D breast cancer cultures. *Biomed Opt Express*. 2017;8(3):1911-1925.

166. Akers W, Lesage F, Holten D, Achilefu S. In vivo resolution of multiexponential decays of multiple near-infrared molecular probes by fluorescence lifetime-gated whole-body time-resolved diffuse optical imaging. *Mol Imaging*. 2007;6(4):2007-7290.

167. Ramanujan VK, Zhang J-H, Biener E, Herman BA. Multiphoton fluorescence lifetime contrast in deep tissue imaging: prospects in redox imaging and disease diagnosis. *J Biomed Opt*. 2005;10(5):1-11. https://doi.org/10.1117/1.2098753.

168. Berge ES, Favreau P, Heaster TM, Shah AT, Skala MC. Fluorescence lifetime imaging of unstained, fixed FaDu tumor slides. In: *Label-Free Biomedical Imaging and Sensing (LBIS) 2019*. Vol 10890. International Society for Optics and Photonics; 2019:108901D.

169. Dysli C, Wolf S, Zinkernagel MS. Autofluorescence Lifetimes in Geographic Atrophy in Patients With Age-Related Macular Degeneration. *Invest Ophthalmol Vis Sci*. 2016;57(6):2479-2487. doi:10.1167/iovs.15-18381

170. Katika KM, Pilon L, Dipple K, Levin S, Blackwell J, Berberoglu H. In vivo time-resolved autofluorescence measurements on human skin. In: *Photonic Therapeutics and Diagnostics II*. Vol 6078. International Society for Optics and Photonics; 2006:60780L.

171. Esposito A, Gerritsen HC, Wouters FS. Fluorescence lifetime heterogeneity resolution in the frequency domain by lifetime moments analysis. *Biophys J*. 2005;89(6):4286-4299. doi:10.1529/biophysj.104.053397

172. Sargenti A, Candeo A, Farruggia G, et al. Fluorescence lifetime imaging of intracellular magnesium content in live cells. *Analyst*. 2019;144(6):1876-1880.

173. Penjweini R, Andreoni A, Rosales T, et al. Intracellular oxygen mapping using a myoglobin-mCherry probe with fluorescence lifetime imaging. *J Biomed Opt*. 2018;23(10):107001.

174. Pliss A, Zhao L, Ohulchanskyy TY, Qu J, Prasad PN. Fluorescence lifetime of fluorescent proteins as an intracellular environment probe sensing the cell cycle progression. *ACS Chem Biol*. 2012;7(8):1385-1392.

175. Bird DK, Yan L, Vrotsos KM, et al. Metabolic mapping of MCF10A human breast cells via multiphoton fluorescence lifetime imaging of the coenzyme NADH. *Cancer Res*. 2005;65(19):8766-8773.

176. Bower AJ, Li J, Chaney EJ, Marjanovic M, Spillman DR, Boppart SA. High-speed imaging of transient metabolic dynamics using two-photon fluorescence lifetime imaging microscopy. *Optica*. 2018;5(10):1290-1296.

177. Chang C-W, Mycek M-A. Precise fluorophore lifetime mapping in live-cell, multi-photon

excitation microscopy. *Opt Express*. 2010;18(8):8688-8696.

178. König K, So PTC, Mantulin WW, Tromberg BJ, Gratton E. Two-photon excited lifetime imaging of autofluorescence in cells during UV A and NIR photostress. *J Microsc*. 1996;183(3):197-204.

179. Jones JD, Ramser HE, Woessner AE, Quinn KP. In vivo multiphoton microscopy detects longitudinal metabolic changes associated with delayed skin wound healing. *Commun Biol*. 2018;1(1):198.

180. Hato T, Winfree S, Day R, et al. Two-photon intravital fluorescence lifetime imaging of the kidney reveals cell-type specific metabolic signatures. *J Am Soc Nephrol*. 2017;28(8):2420-2430.

181. Skala MC, Riching KM, Gendron-Fitzpatrick A, et al. In vivo multiphoton microscopy of NADH and FAD redox states, fluorescence lifetimes, and cellular morphology in precancerous epithelia. *Proc Natl Acad Sci*. 2007;104(49):19494-19499.

182. Gorpas D, Phipps J, Bec J, et al. Autofluorescence lifetime augmented reality as a means for real-time robotic surgery guidance in human patients. *Sci Rep*. 2019;9(1):1187.

183. Stoltzfus CR, Filipek J, Gern BH, et al. CytoMAP: a spatial analysis toolbox reveals features of myeloid cell organization in lymphoid tissues. *CELL-REPORTS-D-19-04536*. 2019.

184. Pécot T, Zengzhen L, Boulanger J, Salamero J, Kervrann C. A quantitative approach for analyzing the spatio-temporal distribution of 3D intracellular events in fluorescence microscopy. Akhmanova A, ed. *Elife*. 2018;7:e32311. doi:10.7554/eLife.32311

185. Biot E, Crowell E, Burguet J, Höfte H, Vernhettes S, Andrey P. Strategy and software for the statistical spatial analysis of 3D intracellular distributions. *Plant J*. 2016;87(2):230-242. doi:10.1111/tpj.13189

186. Liu Z, Pouli D, Alonzo CA, et al. Mapping metabolic changes by noninvasive, multiparametric, high-resolution imaging using endogenous contrast. *Sci Adv*. 2018;4(3). doi:10.1126/sciadv.aap9302

187. Walsh A, Mueller K, Jones I, et al. Label-free Method for Classification of T cell Activation. *bioRxiv*. 2019:536813.

188. Wang ZJ, Walsh AJ, Skala MC, Gitter A. Classifying T cell activity in autofluorescence intensity images with convolutional neural networks. *bioRxiv*. January 2019:737346. doi:10.1101/737346

189. Szulczewski JM, Inman DR, Entenberg D, et al. In Vivo Visualization of Stromal Macrophages via label-free FLIM-based metabolite imaging. *Sci Rep*. 2016;6(1):25086. doi:10.1038/srep25086

190. Ayuso JM, Gillette A, Lugo-Cintrón K, et al. Organotypic microfluidic breast cancer model reveals starvation-induced spatial-temporal metabolic adaptations. *EBioMedicine*. 2018;37:144-157. doi:10.1016/j.ebiom.2018.10.046

191. Xylas J, Varone A, Quinn KP, et al. Noninvasive assessment of mitochondrial organization in three-dimensional tissues reveals changes associated with cancer development. *Int J cancer*. 2015;136(2):322-332. doi:10.1002/ijc.28992

192. Sharick JT, Favreau PF, Gillette AA, Sdao SM, Merrins MJ, Skala MC. Protein-bound NAD(P)H Lifetime is Sensitive to Multiple Fates of Glucose Carbon. *Sci Rep*. 2018;8(1):5456. doi:10.1038/s41598-018-23691-x

CHAPTER 3

AUTOFLUORESCENCE IMAGING OF 3D TUMOR-MACROPHAGE MICROSCALE CULTURES RESOLVES SPATIAL AND TEMPORAL DYNAMICS OF MACROPHAGE METABOLISM

3.1 Abstract

Macrophages within the tumor microenvironment (TME) exhibit a spectrum of pro-tumor and anti-tumor functions, yet it is unclear how the TME regulates this macrophage heterogeneity. Standard methods to measure macrophage heterogeneity require destructive processing, limiting spatiotemporal studies of function within the live, intact 3D TME. Here, we demonstrate two-photon autofluorescence imaging of NAD(P)H and FAD to non-destructively resolve spatiotemporal metabolic heterogeneity of individual macrophages within 3D microscale TME models. Fluorescence lifetimes and intensities of NAD(P)H and FAD were acquired at 24, 48, and 72 hours post-stimulation for mouse macrophages (RAW 264.7) stimulated with IFN-γ or IL-4 plus IL-13 in 2D culture, validating that autofluorescence measurements capture known metabolic phenotypes. To quantify metabolic dynamics of macrophages within the TME, mouse macrophages or human monocytes (RAW264.7 or THP-1) were cultured alone or with breast cancer cells (mouse PyVMT or primary human IDC) in 3D microfluidic platforms. Human monocytes and mouse macrophages in tumor co-cultures exhibited significantly different FAD mean lifetimes and greater migration than monocultures at 24, 48, and 72 hours post-seeding. In co-cultures with primary human cancer cells, actively-migrating monocyte-derived macrophages had greater redox ratios (NAD(P)H/FAD intensity) compared to passively-migrating monocytes at 24 and 48 hours post-seeding, reflecting metabolic heterogeneity in this sub-population of monocytes. Genetic analyses further confirmed this metabolic heterogeneity. These results establish label-free autofluorescence imaging to quantify dynamic metabolism, polarization, and migration of macrophages at single-cell resolution within 3D microscale models. This combined culture and imaging system provides unique insights into spatiotemporal tumor-immune crosstalk within the 3D TME.

3.2 Introduction

Immune cells are a critical component of the tumor microenvironment (TME) and regulate tumor initiation, progression, and therapeutic response[1]. The phenotype and function of immune cells surrounding or infiltrating the tumor are crucial to tumor fate[1–3]. Macrophages are a subset of immune cells with diverse function that are abundant within numerous tumor types, especially breast and pancreatic tumors[1,2,4]. This prevalence suggests that macrophages may serve as important immune mediators of tumor behavior, yet macrophage activity is complex and not well understood. For example, multiple macrophage phenotypes have been identified, each with unique functional and stimulatory activity that influence the surrounding cellular environment[5–7]. Two well-characterized classes of macrophages, M1-like and M2-like macrophages, exhibit distinct responses to tumors[7,8]. M1-like macrophages promote anti-tumor activity through apoptotic or phagocytic signaling, secondary immune stimulation via cytokine secretion and antigen presentation, and nutrient deprivation of tumors[7,9,10]. M2-like macrophages support tumor growth by suppressing immune recognition and promoting cancer cell proliferation, motility, and vessel growth[7,9,10]. However, intermediate macrophage states have also been observed within tumors, suggesting a more complex model of macrophage heterogeneity than this M1-M2 dichotomy[11,12]. This heterogeneity within macrophage populations presents a substantial challenge for effective treatments, emphasizing the need to characterize cell-level macrophage function within the 3D TME.

Cell function has been correlated with metabolism across numerous cell types, including macrophages[13]. Therefore, monitoring metabolic preferences within macrophages could reveal heterogeneity in macrophage phenotype and function. Metabolic demands greatly differ between M1-like and M2-like macrophage classes[7,9]. M1-like macrophages generate nitrogen oxide to induce tumor cell death and recruit additional monocytes to the tumor. This increases the production of the metabolic co-enzyme, NADH, via glycolysis and sustains the viability of M1-like macrophages within tumors[14–16]. Conversely, elevated fatty acid oxidation and oxidative phosphorylation in M2-like macrophages support angiogenesis and tumor growth[14–19]. Here, fatty acid oxidation generates acetyl-CoA and NADH, driving downstream oxidative phosphorylation[17,19]. Microenvironmental changes can regulate these distinct

metabolic demands and produce diverse macrophage phenotypes[20,21]. This highlights a continuum of metabolic activity related to macrophage function that is provoked by complex stimuli from the TME[20–22]. Therefore, monitoring macrophage metabolic heterogeneity improve understanding of tumor-macrophage crosstalk.

3D tumor models provide reliable models of tumor structure and TME conditions that influence immune cell function. The key advantages of microscale models include controllable features that can be easily tuned to simulate the TME and designs enabling various combinations of culture conditions that support high-throughput assessment[23,24]. Combined tumor and immune cell culture within an extracellular matrix (ECM) further enables paracrine signaling between cell layers and protein-protein interactions necessary for cell motility[25,26]. These microscale platforms also provide a simple approach to recapitulate *in vivo* tumor-associated environmental conditions (e.g., hypoxia, nutrient availability) that regulate both macrophage phenotype and function[23–25,27]. These representative 3D tumor models provide attractive systems to evaluate macrophage heterogeneity in response to spatiotemporal changes in the microenvironment.

The destructive nature of most standard biological assays highlights the need for non-invasive tools to monitor macrophage heterogeneity within intact samples. Flow cytometry requires single-cell tumor dissociation that destroys the native tumor spatial context, followed by fixation and antibody-labeling that can alter cell function[28]. Standard functional assays (e.g., plate reader-based ELISA) only provide bulk cell measurements that cannot capture cell-level heterogeneity[28]. Whole body imaging (e.g., PET/CT, MRI) can track macrophages in 3D but have poor cellular resolution[29,30]. Therefore, the limitations of standard measurements prohibit monitoring spatiotemporal macrophage heterogeneity within the complex 3D TME. This highlights a need for new non-invasive techniques and *in vitro* models to characterize macrophage heterogeneity.

Autofluorescence imaging has previously quantified cellular heterogeneity *in vivo* and in 3D cultures using label-free two-photon microscopy[31–42]. Specifically, autofluorescence imaging can quantify

the endogenous fluorescence of metabolic coenzymes NADH and FAD, which are both used across several cellular metabolic processes[43–47]. NADH and NADPH have overlapping fluorescence properties, and are collectively referred to as NAD(P)H [48]. Fluorescence intensity measurements can inform on the intra-cellular concentrations of NAD(P)H and FAD. The optical redox ratio, defined as the ratio of NAD(P)H intensity to FAD intensity, provides a measure of the relative oxidation-reduction state of the cell[32,35,44]. Fluorescence lifetime imaging microscopy (FLIM) of NAD(P)H and FAD provide additional information specific to protein binding activity[49]. Lifetime measurements can distinguish between free and protein-bound forms of NAD(P)H and FAD, characterized by distinct molecular conformations that affect fluorescence quenching[49]. Previous studies have shown that metabolic autofluorescence imaging detects spatial and temporal changes in stromal cells across *in vivo* and 3D *in vitro* models[31,38,39,42,50–55]. Thus, metabolic autofluorescence imaging of microscale 3D models was demonstrated to quantify metabolic activity and visualize macrophage heterogeneity within the 3D TME using primary human cancer, human cell lines, and mouse cell lines

3.3 Methods

3.3.1 2D cell culture

RAW 264.7 murine macrophages (ATCC TIB-71) were maintained in culture medium composed from standard RPMI 1640 (Gibco), 10% fetal bovine serum, and 1% penicillin:streptomycin. RAW macrophages were seeded in 35 mm glass bottom dishes (MatTek) for imaging experiments. All imaging samples were plated at a density of $1x10^5$ cells per dish and incubated at 37 ºC and 5% CO2, for 24 hours to allow cell adhesion. Separate cultures of macrophages polarized with M1-like (IFN-γ) or M2-like (IL-4/IL-13) cytokines were generated by standard media substitution with 2 mL cytokine-supplemented media and incubated between 24-72 hours. Media for M(IFN-γ) stimulation consisted of RPMI 1640 supplemented with 10 ng/ml interferon-γ (IFN-γ; R&D systems), and media for M(IL4/IL13) stimulation consisted of RPMI 1640 with 20 ng/ml interleukin 4 (IL-4; Invitrogen) and 20 ng/ml interleukin 13 (IL-13; Gibco).

3.3.2 Microdevice design and fabrication

Description of the Stacks microfluidic platform is previously described in detail[27]. 24-well polystyrene microdevices (dimensions: 75 mm x 50 mm) were fabricated by injection molding and sterilized via sonication in isopropanol. Collagen hydrogels (2.0 mg/ml) were prepared and a 4.5 µL volume was suspended within each microwell of the device (thickness ~1.2 mm), creating an open-air culture system compatible for two-photon imaging. The hydrogel was generated from a mixture of 6 µL 10X PBS, 14 µL sterile water, 6 µL NaOH (Sigma), 160 µL Bovine collagen type I (PureCol, Advanced BioMatrix), 3 µL fibronectin (Sigma) and 50 µL cell type-specific medium (RPMI1640 – mouse; complete DMEM/F12 (Gibco) – human). Collagen hydrogels were polymerized by incubation at 37ºC for at least 6 hours, prior to sequential seeding of breast carcinoma cells and macrophages (~1000 cells/µL each) on the opposing ends of the collagen layer.

3.3.3 3D microdevice culture

The 3D microfluidic platform was used for co-cultures of primary and immortalized macrophages and breast carcinoma of both mouse and human origin. PyVMT (established from FVB MMTV-PyVmT mouse tumors) and MDA-MB-231 (ATCC HTB-26) human breast cancer cells were cultured in medium composed from standard Dulbecco's Modified Eagle Medium (DMEM, Gibco), 10% fetal bovine serum, and 1% penicillin:streptomycin. RAW 264.7 macrophages (ATCC TIB-71) and THP-1 human monocytes (ATCC TIB-202) were cultured in RPMI 1640 medium supplemented with 10% fetal bovine serum and 1% penicillin:streptomycin. Patient-derived invasive breast carcinoma cells (IDC; 171881-019-R-J1-PDC, Passages 7-12) were obtained upon request from the NCI Patient-Derived Models Repository (NCI PDMR)[56]. Culture of patient-derived cells required specialized media consisting of 1X Advanced DMEM/F12 (Gibco) supplemented with 5% Fetal Bovine Serum, 1.1 µM Hydrocortisone (Sigma), 1.61 nM EGF Recombinant Human Protein (Invitrogen), 0.178 mM Adenine (Sigma), 1% penicillin:streptomycin, 2 mM L-Glutamine (Invitrogen), and 0.01 mM Y-27632 dihydrochloride (Tocris)[56]. Well conditions included macrophages incubated with and without tumor cells over 72 hours. For gene expression analysis, tumor cells and macrophages were cultured on separate Stacks layers to

prevent cell type cross-contamination. An additional Stacks layer with wells only containing 10 µL culture medium was placed on top of each Stacks layer with cells. These layers were then overlaid form a four-layer Stacks setup (media layer-macrophage layer-media layer-tumor layer). Media changes were performed daily by aspirating old media from each well and replacing with 10 µL of fresh culture media during incubation between imaging experiments.

3.3.4 Autofluorescence imaging

FLIM images were acquired with an Ultima two-photon imaging system (Bruker) composed of an ultrafast tunable laser source (Insight DS+, Spectra Physics) coupled to a Nikon Ti-E inverted microscope equipped with time correlated single photon counting electronics (SPC 150, Becker & Hickl GmbH). The ultrafast tunable laser source enabled excitation of NAD(P)H (750 nm) and FAD (890 nm) fluorescence. For 2D macrophage imaging, NAD(P)H and FAD fluorescence were excited sequentially, and their respective emission was isolated using 440/80 and 550/100 bandpass filters (Chroma). Laser power at the sample for NAD(P)H and FAD excitation was approximately 11.3 mW and 11.5 mW, respectively. Simultaneous excitation of NAD(P)H (750 nm) and FAD (895 nm) was performed for all 3D samples by wavelength mixing of 750 nm and 1040 nm laser lines to virtually generate a 895 nm excitation effect as described previously[57]. Approximate laser power at the sample during wavelength mixing was 10.7 mW at 750 nm and 16.3 mW at 1040nm. NAD(P)H and FAD emission during wavelength mixing were isolated using a 466/40 and a 540/24 nm bandpass filter (Chroma), respectively. All samples were illuminated through a 40X/1.15 NA objective (Nikon), with 2X optical zoom for wavelength mixing to capture fluorescence emission only from pixels with efficient mixing. Emission was detected with GaAsP photomultiplier tubes (Hamamatsu 7422PA-40). Per-pixel lifetime decay curves were collected by scanning the field of view (256x256 pixels; 300µm X 300 µm) over 60 seconds with a 4.8 microsecond pixel dwell time. To prevent photobleaching within the sample, photon count rates were maintained at ~1-3×10^5 photons/second. The instrument response function was generated from second harmonic signal of urea crystals excited at 900 nm, with a full width at half maximum of 240 picoseconds. A fluorescence lifetime standard measurement was collected daily by imaging a YG fluorescent bead (Polysciences Inc), measured

as 2.1±0.09 nanoseconds consistent with reported lifetime values[58,59]. Autofluorescence images were captured for each 2D polarization condition at 24, 48, and 72 hours post-stimulation, with a minimum of four representative fields of view per sample (~1000-2000 cells). For 3D cultures, autofluorescence lifetime volumes were acquired across 2- 3 wells for each macrophage monoculture and co-culture condition for at least 3 separate devices (i.e., 6 to 9 wells per condition). Image volumes captured images at 3 μm z-steps starting at the macrophage seeding plane and ending at the leading edge of the macrophage layer (~1000-3000 cells). Z-stack image depths ranged from 24 to 210 μm.

3.3.5 Image analysis

Per-pixel fluorescence lifetimes of free and protein-bound NAD(P)H and FAD were calculated from fitting fluorescence decays to the following bi-exponential model: $I(t) = \alpha_1 e^{-t/\tau_1} + \alpha_2 e^{-t/\tau_2} + C$ [49]. Fluorescence intensity images were generated by integrating photon counts over the per-pixel fluorescence decays. The per-pixel ratio of NAD(P)H fluorescence intensity to FAD intensity was calculated to determine optical redox ratio. A customized CellProfiler pipeline was used to segment individual cell cytoplasms[60]. Cytoplasm masks were applied to all images to determine single-cell redox ratio and NAD(P)H and FAD fluorescence lifetime variables. Fluorescence lifetime variables consist of the mean lifetime ($\tau_m = \tau_1\alpha_1 + \tau_2\alpha_2$), free- and protein-bound lifetime components (τ_1, τ_2), and their fractional contributions (α_1 and α_2; where $\alpha_1 + \alpha_2 = 1$) for each cell cytoplasm. Nine total variables were analyzed for each cell cytoplasm: NAD(P)H τ_m, FAD τ_m, NAD(P)H τ_1, FAD τ_1, NAD(P)H τ_2, FAD τ_2, NAD(P)H α_1, FAD α_1, and optical redox ratio.

3.3.6 Metabolic inhibition

To validate that metabolic changes were specific to macrophage polarization, 2D polarized macrophages were treated with a panel of metabolic inhibitors with known activity and imaged post-treatment. RAW264.7 macrophages were stimulated to glycolytic M(IFN-γ) or M(IL4/IL13) phenotype for 72 hours[61–64]. Next, glycolysis was inhibited with media + 10 mM 2-deoxyglucose (2DG; Sigma), FAO was inhibited with media + 100 nM etomoxir (ETO; Sigma), or OXPHOS was inhibited with media + 4mM

sodium cyanide (NACN; Sigma)[65–67]. Autofluorescence imaging was performed immediately before adding inhibitor and after treatment for 5 mins (NaCN), 1 hour (2DG), or 24 hours (ETO).

3.3.7 Immunofluorescence staining and imaging

Following autofluorescence imaging, unstimulated and cytokine-stimulated 2D cultures of RAW264.7 macrophages were stained according to supplier instructions with both PE-conjugated CD86 antibody (Tonbo Biosciences) and FITC-conjugated CD206 antibody (BioRad) to confirm macrophage polarization. Conjugated antibodies were diluted to 1:30 in PBS+goat serum. 2D immunofluorescence images were acquired using the two-photon microscope setup described above. CD206-FITC fluorescence intensity was excited at 890 nm and collected with a 550/100 nm bandpass filter, while CD86-PE fluorescence was excited at 1050 nm and collected with a 650/47 nm filter.

3.3.8 mRNA Isolation, cDNA Synthesis and real time-quantitative PCR (RT-qPCR)

To assess heterogeneity in macrophage polarization and confirm expected functional phenotypes, expression levels of genes specific to broad macrophage classes (i.e., M1-like, M2-like, mixed phenotypes) were analyzed by qPCR. For 2D cultures, separate cultures of M0, M(IFN-γ), M(IL4/IL13) RAW 264.7 macrophages were maintained in 6-well plates prior to mRNA extraction. For 3D cultures, RAW264.7 macrophages or THP-1 monocytes were cultured alone or with breast cancer cells in the 3D Stacks microfluidic platform. For all experiments, mRNA was extracted at 24, 48 and 72 hours using a Dynabeads™ mRNA DIRECT™ Purification Kit (Thermo Fisher, 61012). Purified mRNA was quantified using a Qubit fluorometer (Thermo Fisher) and a Qubit™ RNA BR Assay Kit (Thermo Fisher, Q10210). mRNA was reverse transcribed using RT² PreAMP cDNA synthesis kit (Qiagen, 330451). The prepared cDNA was preamplified using the RT² PreAMP Primer Mix for Human and Mouse PCR Array (Qiagen, PBH-181Z). cDNA was analyzed by RT-qPCR using a Qiagen RT2 profiler custom panel (Qiagen, PAHS-181Z, CLAM3313, CLAH36077) following supplier instructions. Gene lists for mouse and human experiments are reported in Table A.2.

3.3.9 Population density modeling

Population density modeling of single-cell metabolism was used to observe differences in macrophage heterogeneity across 2D polarized cultures and 3D tumor-macrophage cultures over time. Frequency histograms were generated based on single-cell metabolic autofluorescence measurements across samples. Multiple Gaussian probability density functions were fit to each distribution histogram to identify the presence of sub-populations with distinct metabolic activity[37]. Accurate sub-population identification was evaluated by iteratively increasing the number of fitted Gaussian curves and calculating the Akaike Information Criterion (AIC) for each iteration[37,68]. The number of fitted Gaussians yielding the lowest AIC value indicate the optimal fit conditions and number of sub-populations per sample[37,68].

3.3.10 Statistics

Tukey's tests for non-parametric, unpaired comparisons were performed to assess differences in autofluorescence variables between 2D cytokine-stimulated cultures and 3D monoculture and co-culture conditions over 72 hours. Multiple student's t-tests were performed to assess significance of fold change differences represented as volcano plots for redox ratio changes in 2D macrophage populations in response to metabolic inhibitors and gene expression changes with respect to M0 conditions for 2D mouse macrophages or monoculture for 3D mouse and human macrophages. Coefficient of variation was calculated to evaluate variability across 3D mouse monocultures and co-cultures over 72 hours. The non-parametric, squared-ranks test was performed to assess the equality of coefficients of variation between monoculture and co-culture groups (MATLAB, SquaredRanksTest)[69,70]. Metabolic autofluorescence results are represented as line plots, dot plots, or bar graphs plotted in GraphPad. Heatmaps of autofluorescence variables with respect to depth were generated in MATLAB.

3.4 Results

3.4.1 Microscale 3D co-culture and metabolic autofluorescence imaging provide innovative and complementary tools to monitor 3D changes in macrophage metabolism within the TME

Autofluorescence imaging can non-destructively monitor live, single-cell metabolism and 3D migration, while 3D microscale co-cultures reliably model tumor complexity with selective environmental

control and high-throughput capabilities. Specifically, the Stacks 3D microfluidic system enables multi-cellular cultures with minimal biological material, flexible configuration, and well-characterized environmental gradients[27]. The Stacks system was combined with metabolic autofluorescence imaging to monitor tumor-mediated changes in macrophage metabolism and migration (Figure 3.1A)[27]. Microscale 3D co-cultures of tumor cells and macrophages were established in the Stacks 3D system using primary human cancer cells, and cell lines from mouse and human origin (Figure 3.1A). A collagen-based ECM was polymerized within each well, then monocytes/macrophages were seeded with (co-culture) or without (monoculture) breast cancer cells at the opposing end of the ECM layer (Figure 3.1A). Both the metabolic autofluorescence and microfluidic culture technologies were validated by imaging macrophages in 2D culture with standard stimulation techniques and in 3D co-cultures of macrophages alone in the Stacks 3D system (Figure 3.1B). Finally, the metabolic dynamics of tumor-stimulated macrophages were characterized by collecting NAD(P)H and FAD autofluorescence image volumes of monocytes/macrophages migrating across the ECM at 24, 48, and 72 hours (Figure 3.1C). Overall, this approach provides unique, quantitative imaging of macrophage spatiotemporal dynamics in the TME that cannot be achieved with conventional assessments that lack single-cell resolution, 3D complexity, and/or non-destructive monitoring capability.

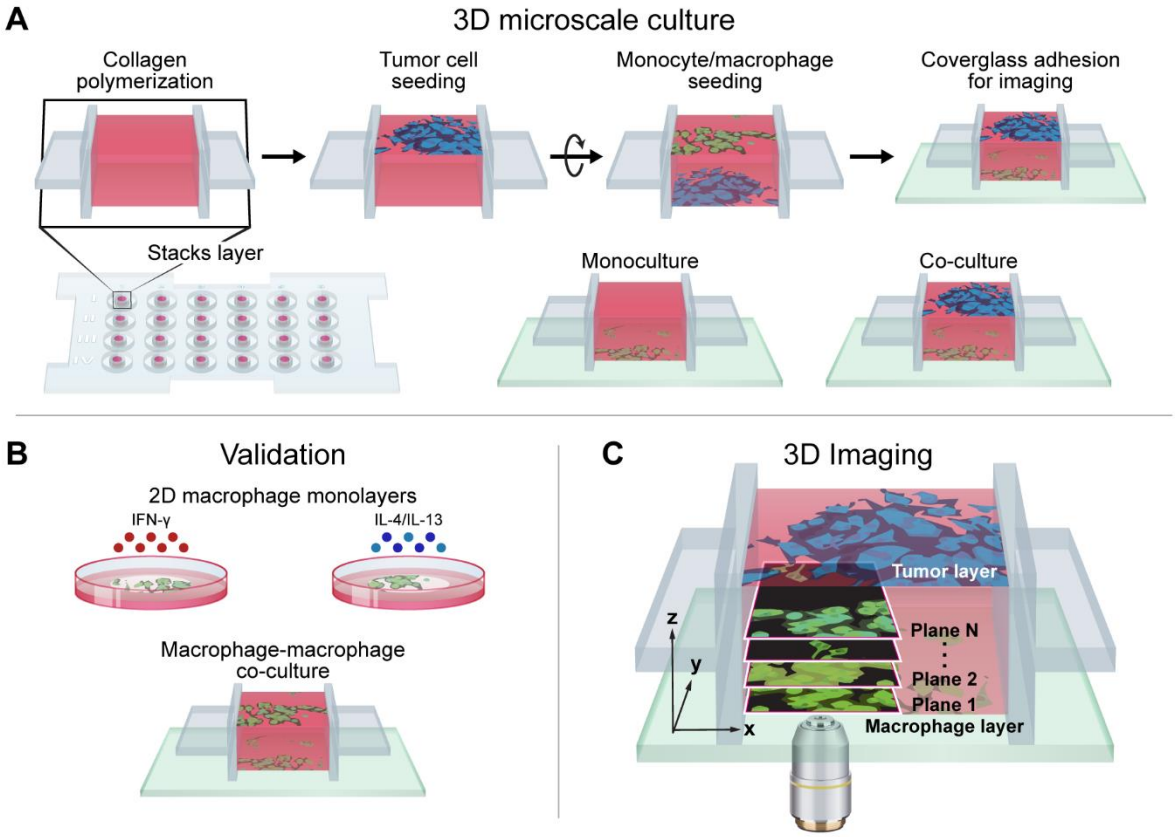

Figure 3.1: Metabolic autofluorescence imaging of macrophages in the Stacks 3D microscale co-culture system. Illustration of experimental workflow showing (A) design of the Stacks 3D co-culture of macrophages/monocytes and tumor cells from primary patient samples, along with cell lines of mouse and human origin, (B) validation of metabolic autofluorescence imaging in 2D culture with standard stimulations and in Stacks 3D microscale system with macrophages alone, and (C) metabolic autofluorescence imaging of 3D migration and single-cell metabolism for macrophages in the Stacks 3D microscale co-culture system.

3.4.2 Metabolic imaging validation: macrophage stimulation in 2D in vitro culture

To establish the sensitivity of metabolic autofluorescence imaging to distinct macrophage phenotypes, metabolic autofluorescence measurements were first validated in 2D cultures of RAW264.7 mouse macrophages stimulated with IFN-γ (M(IFN-γ): anti-tumor M1-like phenotype), IL-4/IL-13 (M(IL4/IL13): pro-tumor M2-like phenotype), or without cytokine stimulation (M0: naïve macrophages). Macrophages were maintained in cytokine-supplemented media and imaged over 24-72 hours. Autofluorescence imaging of NAD(P)H and FAD demonstrates time-dependent differences in M(IFN-γ) and M(IL4/IL13) macrophages (Figure 3.2A). M(IFN-γ) macrophages have increased redox ratio compared

to M(IL4/IL13) macrophages, with the greatest redox ratio differences at 72 hours post-polarization (Figure 3.2A). Individual M(IFN-γ) and M(IL4/IL13) macrophages have heterogeneous NAD(P)H and FAD lifetimes across fields-of view at all timepoints. A flattened, cuboid structure was observed for M(IFN-γ) macrophages, whereas M(IL4/IL13) macrophages extended outward with spindle projections, consistent with reported morphology of polarized macrophages (Figure 3.2A)[71]. These known subset-specific morphological changes become more pronounced over time (Figure 3.2A). Staining for common M1-like and M2-like surface proteins (CD86 and CD206, respectively) show increasing CD86 expression in M(IFN-γ) macrophages across the 72 hour time course, while M(IL4/IL13) macrophages have stronger CD206 expression (Figure 3.2A).

Quantitative autofluorescence measurements were then compared between M0, M(IFN-γ) and M(IL4/IL13) macrophages over the 72 hour time course to determine whether metabolic autofluorescence can distinguish macrophage polarization states. The redox ratio was significantly different ($p<0.0001$) between M0, M(IFN-γ) and M(IL4/IL13) macrophages at 48 and 72 hours post-polarization (Figure 3.2B). M(IFN-γ) macrophages had decreased ($p<0.0001$) NAD(P)H mean lifetime (τ_m) at 24 and 72 hours compared with M0 and M(IL4/IL13) macrophages (Figure 3.2C). However, at 48 hours, M(IFN-γ) and M(IL4/IL13) macrophages had similar NAD(P)H τ_m ($p>0.05$). Significant differences in FAD τ_m across all three macrophage conditions were only observed at 24 hours post-stimulation ($p<0.05,0.001$) (Figure 3.2D). The short (τ_1) and long lifetimes (τ_2) and their relative contribution (α_1) for NAD(P)H and FAD influence changes in τ_m over the time course (Figure A.1A-F).

Metabolic inhibitors were used to confirm observed autofluorescence differences between M(IFN-γ) and M(IL4/IL13) macrophages. Glycolysis, oxidative phosphorylation, and fatty acid oxidation were inhibited with 2-deoxyglucose, sodium cyanide, and etomoxir, respectively. Fold changes in redox ratio with respect to untreated controls with the same stimulation are shown in Figure 3.2E. Inhibition of glycolysis decreased the redox ratio of M(IFN-γ) macrophages to a greater degree than M(IL4/IL13) macrophages (Figure 3.2E), consistent with published studies that show increased reliance on glycolysis for these anti-tumor, M1-like macrophages compared to pro-tumor, M2-like macrophages[14–16]. Conversely,

M(IL4/IL13) macrophages showed greater increases in redox ratio than M(IFN-γ) macrophages with inhibition of oxidative phosphorylation and fatty acid oxidation (Figure 3.2E). This is consistent with prior studies that show increased reliance on oxidative phosphorylation and fatty acid oxidation in M2-like macrophages compared to M1-like macrophages[14–19]. Fold changes are statistically significant between control and inhibitor-treated conditions across all treatments (Table A.1). Fold change of both NAD(P)H and FAD mean lifetimes with inhibitors are shown in Figure A.1. These findings agree with previous studies reporting upregulation of glycolysis in M1-like macrophages, while M2-like macrophages preferentially shift towards a more oxidative metabolic state[5,6,12,14,19]. Collectively, these results demonstrate that metabolic autofluorescence imaging can assess macrophage phenotype and metabolism.

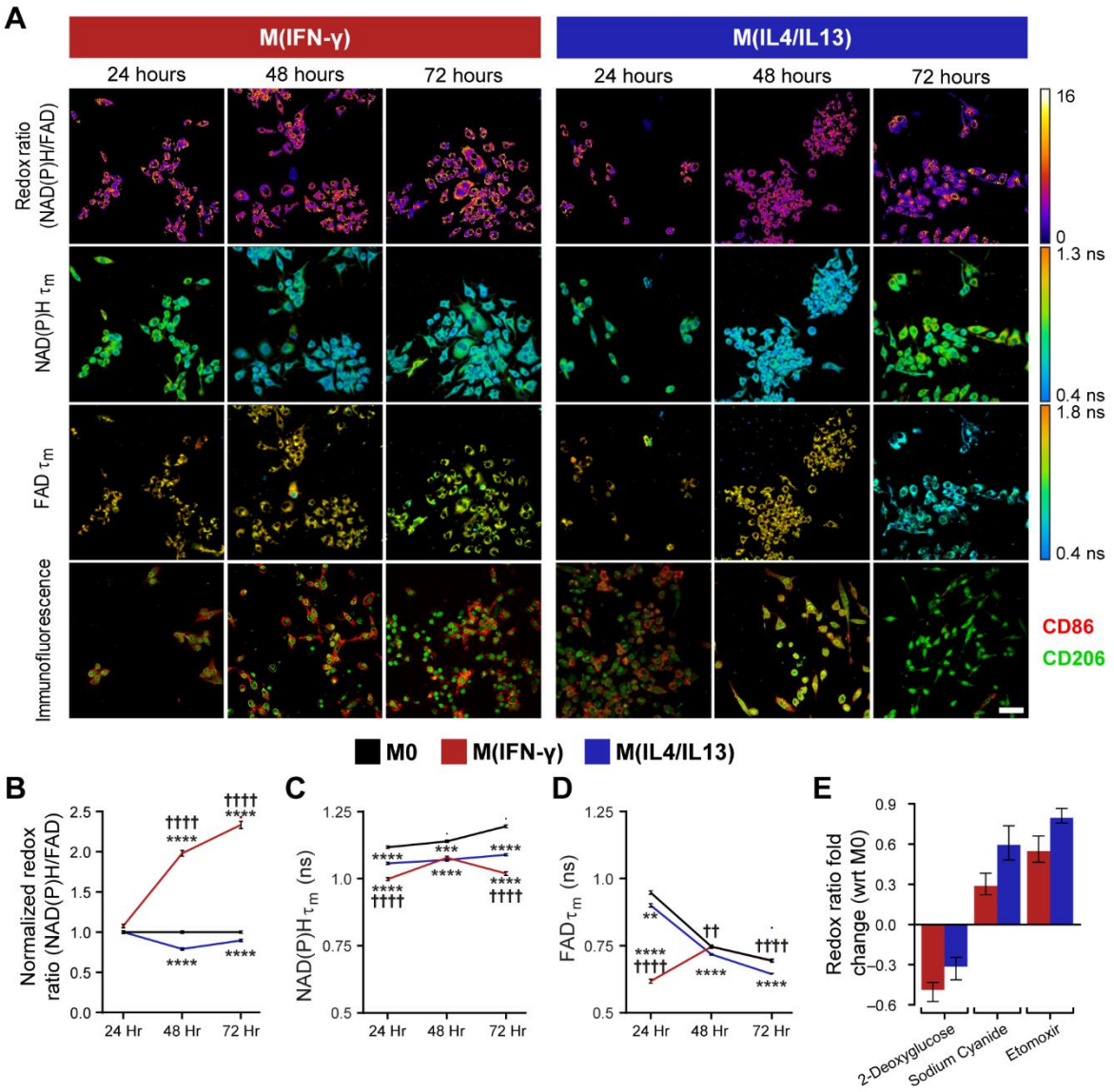

Figure 3.2: Metabolic autofluorescence imaging is sensitive to temporal changes in macrophage metabolism in 2D culture. A) Representative optical redox ratio, NAD(P)H and FAD mean lifetime (τ_m) images of RAW 264.7 macrophages cytokine-stimulated to M(IFN-γ) (anti-tumor M1-like phenotype), M(IL4/IL13) (pro-tumor M2-like phenotype), or unstimulated (M0 naïve phenotype). Representative immunofluorescence images show surface expression of known M1-like and M2-like macrophage markers (CD86, CD206). Scale Bar = 50 μm. Quantitative analysis of B) redox ratio and mean lifetimes (τ_m) of C) NAD(P)H and D) FAD show dynamic metabolic changes during continued exposure to cytokines. **,***, ****p<0.01,0.001, 0.0001 vs. M0; ††, †††† p<0.01,0.0001 vs. M(IL4/IL13). Metabolic characterization was performed via inhibition with E) 2-deoxyglucose (2DG, glycolysis inhibitor), etomoxir (ETO, fatty acid oxidation inhibitor), and sodium cyanide (NaCN, oxidative phosphorylation inhibitor). Reported values are fold change of redox ratio with respect to M0 control under the same polarization conditions.

Population density modeling of single-cell redox ratios was performed to determine whether metabolic autofluorescence imaging can resolve macrophage heterogeneity. Population density curves revealed heterogeneous metabolic sub-populations of macrophages across conditions and time points (Figure 3.3A-C). All stimulation conditions and time points have a narrow population of cells with similarly low redox ratio along with a second population of cells with a broad range of higher redox ratios (Figure 3.3A-C). These distributions illustrate the heterogeneous metabolic state of macrophages on a single-cell level. Population distributions overlap between M0, M(IFN-γ), and M(IL4/IL13) conditions, which highlights a continuum of metabolic activity between conditions. M(IFN-γ) and M(IL4/IL13) macrophages also exhibited greater variability compared to M0 macrophages at 24 and 72 hours (Table A.3). Increasing numbers of sub-populations are observed from population distribution analysis of single-cell NAD(P)H and FAD τ_m during macrophage stimulation, highlighting substantial heterogeneity in enzyme binding activity (Figure A.1M-R).

Heterogeneity in macrophage function within stimulation conditions (M(IFN-γ) or M(IL4/IL13)) was further assessed from gene and protein expression. Immunofluorescence was quantified from images of M(IFN-γ) and M(IL4/IL13) macrophages stained for CD86 and CD206 expression (Figure 3.3D). Both stimulation conditions have basal expression of these markers that fluctuate during polarization[72]. Thus, the ratio of CD86 to CD206 expression was used to assess protein changes associated with macrophage polarization[73]. The CD86:CD206 ratio increased significantly in M(IFN-γ) compared with M(IL4/IL13) conditions by 72 hours, while heterogenous expression was observed at earlier time points (Figure 3.3D). Gene expression of cytokines and other mediators of inflammation (Table A.2) were also measured with qPCR to assess macrophage function across 24-72 hours of stimulation (Figure 3.3E-F). Ccl2 and Ccl5 expression and downregulation of IL10 and Ptgs2 in M(IFN-γ) conditions at 72 hours indicates polarization towards M1-like phenotype (Fig 3.3E). IFN-γ stimulation at 72 hours also upregulated mixed phenotype Il12b, IL6, Ccl22 and Nos2 and M2-like gene, Stat3. Accordingly, IL-4/IL-13 stimulation gradually upregulated IL10 and Ptgs2 while Il1b and Vegfa were significantly downregulated by 72 hours, confirming M2-like polarization (Figure 3.3F). Variability in expression of M1-like, M2-like, and mixed phenotype

genes at 24- and 48-hours of stimulation suggests incomplete polarization at earlier time points (Figure 3.3E-F).

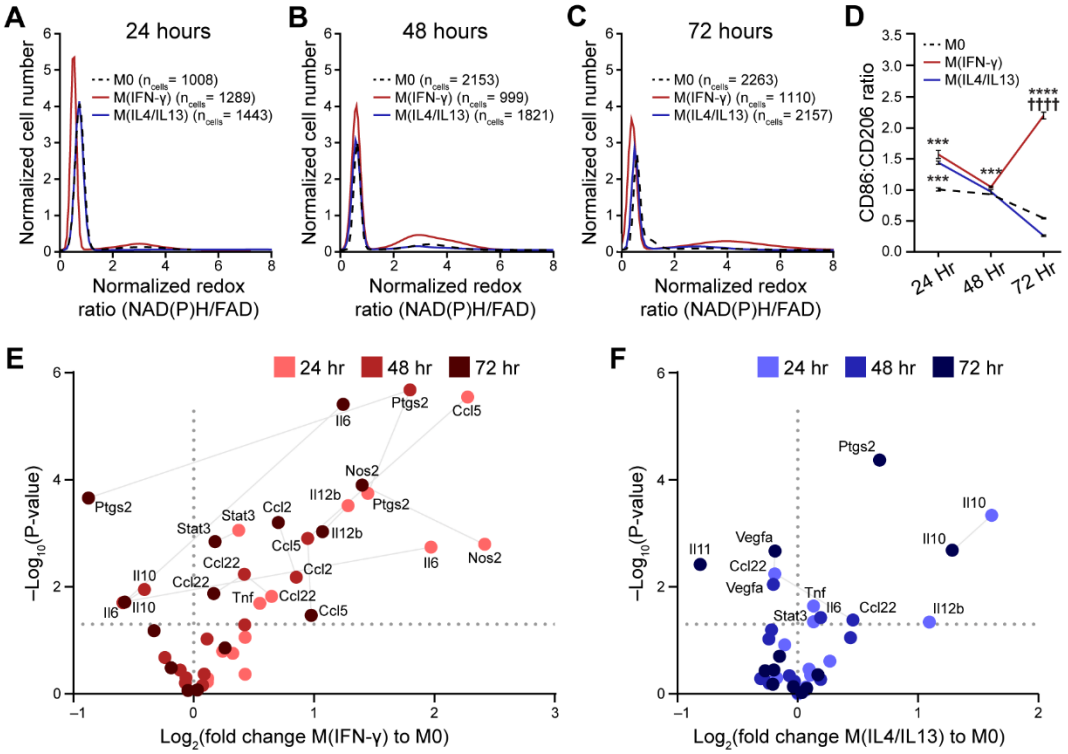

Figure 3.3: Metabolic autofluorescence measurements resolve metabolic heterogeneity linked to heterogeneous 2D cytokine-stimulated macrophage polarization. Population density modeling of redox ratios per cell illustrates heterogeneous macrophage metabolism at A) 24 hours, B) 48 hours, and C) 72 hours of stimulation. Two distinct sub-populations of cell metabolism are present for each time point and stimulation condition. Expression levels of known M1-like and M2-like macrophage markers (CD86, CD206) were quantified for M0, M(IFN-γ), and M(IL4/IL13) macrophages at D) 24 hours, 48 hours and 72 hours; ** p<0.01, ***p<0.001. Expression levels of M1-like and M2-like genetic markers for E) M(IFN-γ), and F) M(IL4/IL13) conditions were evaluated with qPCR at 24 hours, 48 hours, and 72 hours following stimulation.

3.4.3 Evaluating non-specific effects of 3D Stacks co-culture system on macrophage metabolism and migration

The Stacks system was previously characterized for diffusion gradients and cell viability, survival, and recruitment[27]. To determine non-specific changes in metabolism within the Stacks system, metabolic activity of macrophages 1 hour after seeding was assessed for RAW264.7 macrophage monocultures and RAW264.7+PyVMT mouse breast carcinoma co-cultures. Autofluorescence measurements were not

significantly different between monocultured macrophages and co-cultured macrophages, confirming that macrophages were similar for both conditions at the time of seeding (Figure A.2A-C). Additionally, RAW264.7 macrophages were seeded on both ends of the ECM layer to account for non-specific macrophage migration in the 3D Stacks system without tumor stimulation. Minimal change in macrophage migration was detected over 72 hours within macrophage-macrophage cultures (Figure A.2D-F). Overall, this data suggests that changes in macrophage migration and metabolism in co-culture at later time-points are due to tumor-specific signaling.

3.4.4 Mouse macrophage metabolism and migration using 3D metabolic imaging and tumor microscale Stacks system

Next, metabolic autofluorescence was characterized in microfluidic cultures of mouse Polyoma-Middle T Virus (PyVMT) mammary carcinoma and mouse RAW264.7 macrophages over a 72 hour time-course. Redox ratio, NAD(P)H τ_m and FAD τ_m of co-cultured macrophages from a representative z-plane (migration distance = 6 μm) are visually distinct from monocultured macrophages at the same z-plane as early as 24 hours post-seeding (Figure 3.4A). Morphological differences also emerge between monocultured and co-cultured macrophages over the 72 hour time course. Co-cultured macrophages were larger than monocultured macrophages and adopted a mixture of flat, cuboidal or elongated, spindle-like morphologies, commonly observed for polarized macrophage states (Figure 3.4A)[71]. Quantitative autofluorescence measurements more clearly capture metabolic changes across 3D macrophage cultures. Significant differences in NAD(P)H τ_m and FAD τ_m were observed between monocultured and co-cultured macrophages at 24, 48 and 72 hours, while the redox ratio of co-cultured macrophages significantly decreased only at 72 hours compared to monoculture conditions (Figure 3.4C-E). The redox ratio gradually decreased over 72 hours of co-culture with tumor cells (Figure 3.4C), while NAD(P)H and FAD τ_m did not significantly change over time (Figure 3.4D&E). Further changes in NAD(P)H and FAD lifetime components were also observed over the co-culture time course (Figure A.3A-F).

Genetic heterogeneity between macrophages within 3D co-cultures was evaluated by qPCR for a gene panel associated with M1-like, M2-like, and mixed macrophage phenotypes (Table A.2)[74]. Minimal

changes in gene expression of select M1-like, M2-like, and mixed phenotype genes were observed between monocultured and co-cultured macrophages at early time points (Figure 3.4B). However, 72 hours of co-culture resulted in significantly increased expression across Ccl2, Ccl5, and IL23a (M1-like), Vegfa and Stat3 (M2-like), and IL6 (mixed phenotype) (Figure 3.4B). Additionally, Il12b was significantly downregulated in co-cultured macrophages at 72 hours (Figure 3.4B). Heterogeneity during RAW264.7 macrophage polarization in response to PyVMT tumor cell co-culture was also quantified with population density modeling of cell-level metabolic autofluorescence over the 72-hour imaging time course (Figure 3.4F-H). Two distinct redox ratio sub-populations of macrophages are present in co-culture at the 24 hour and 72 hour time points, and in monoculture at 24 and 48 hours (Figure 3.4F&H). Variability in redox ratio of macrophage monocultures is less than co-cultures at all time points (Table A.3). Heterogeneity in enzyme binding activity is reflected in single-cell NAD(P)H and FAD τ_m distributions, which also detect macrophage sub-populations during stimulation (Figure A.3G-L). These results demonstrate that this 3D tumor co-culture can stimulate heterogeneous changes in macrophage gene expression (Figure 3.4B) that may contribute to the metabolic heterogeneity between individual macrophages that is exclusively captured with metabolic autofluorescence measurements (Figure 3.4F-H).

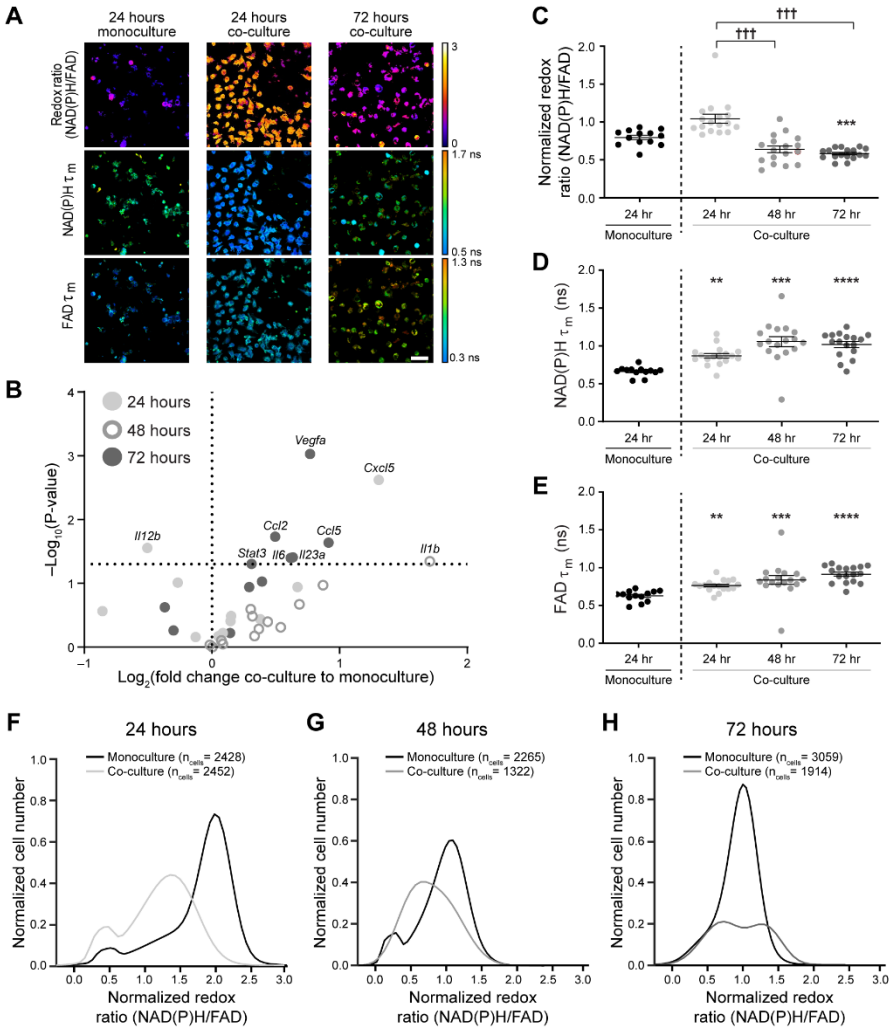

Figure 3.4: Metabolic autofluorescence imaging of mouse macrophages within 3D Stacks tumor co-cultures. A) Representative autofluorescence images (z-plane distance: 6 µm) demonstrate qualitative differences in the redox ratio, NAD(P)H and FAD mean lifetimes (τ_m) of RAW264.7 macrophages in co-culture with PyVMT mouse mammary tumor cells. Scale bar = 50 µm. B) Gene expression levels of M1-like and M2-like markers were evaluated for monocultured and co-cultured macrophages at 24, 48, and 72 hours using qPCR. Upregulation of both M1-like and M2-like genes were observed in co-cultures by 72 hours, demonstrating heterogeneity in macrophage polarization in response to tumor stimulation. Quantitative analysis of C) redox ratio, D) NAD(P)H τ_m, and E) FAD τ_m highlight dynamic metabolic changes in macrophages during prolonged tumor-macrophage co-culture. Monocultured macrophages were not significantly different ($p>0.05$) across time points, so only the 24 hour monoculture is shown above. Significant differences in NAD(P)H and FAD τ_m are observed between monocultures and co-cultures, as early as 24 hours post-seeding. Additionally, macrophage co-cultures exhibit a gradual decline in redox ratio over time, consistent with transition to a more oxidized state; **,***,**** $p<0.01,0.001,0.001$ vs. monoculture, ††† $p<0.001$. Population density curves of single-cell redox ratios in monocultures and co-cultures at F) 24 hours, G) 48 hours, and H) 72 hours demonstrate variable cellular-level heterogeneity in co-cultured macrophages over time in monocultures.

Next, mouse macrophage metabolism was monitored during migration toward the tumor layer within 3D co-cultures by acquiring volumes of metabolic autofluorescence images spanning the macrophage layer. Heatmaps of optical redox ratio at each z-plane show that macrophage metabolism and migratory distance vary over the 72 hour time course (Figure 3.5A). Heatmaps of NAD(P)H τ_m and FAD τ_m with migration distance are represented in Figure A.3. The number of macrophages within each z-plane (depth increments of 3 μm) was divided by the total number of macrophages within each image volume to quantify the migration distance of macrophages over time (Figure 3.5B-D). Monocultured macrophages exhibited minimal migration from the seeding plane, whereas co-cultured macrophages migrated further into the ECM toward the tumor layer especially at 24 and 48 hours (Figure 3.5B&C). Therefore, the maximum migration distance for the monoculture condition was used to threshold passive from active macrophage migration at each time point (Figure 3.5B-D)[75]. Actively-migrating macrophages in co-culture have lower redox ratio at all time points, suggesting that these macrophages shift towards oxidative metabolism to enhance migration in the tumor microenvironment (Figure 3.5E). Additionally, NAD(P)H τ_m decreases in actively-migrating macrophages at 24 and 48 hours, while FAD τ_m increases significantly at 72 hours (Figure 3.5F&G). These results highlight the combination of metabolic autofluorescence imaging and 3D Stacks co-culture to reveal novel relationships between metabolic activity and macrophage migration.

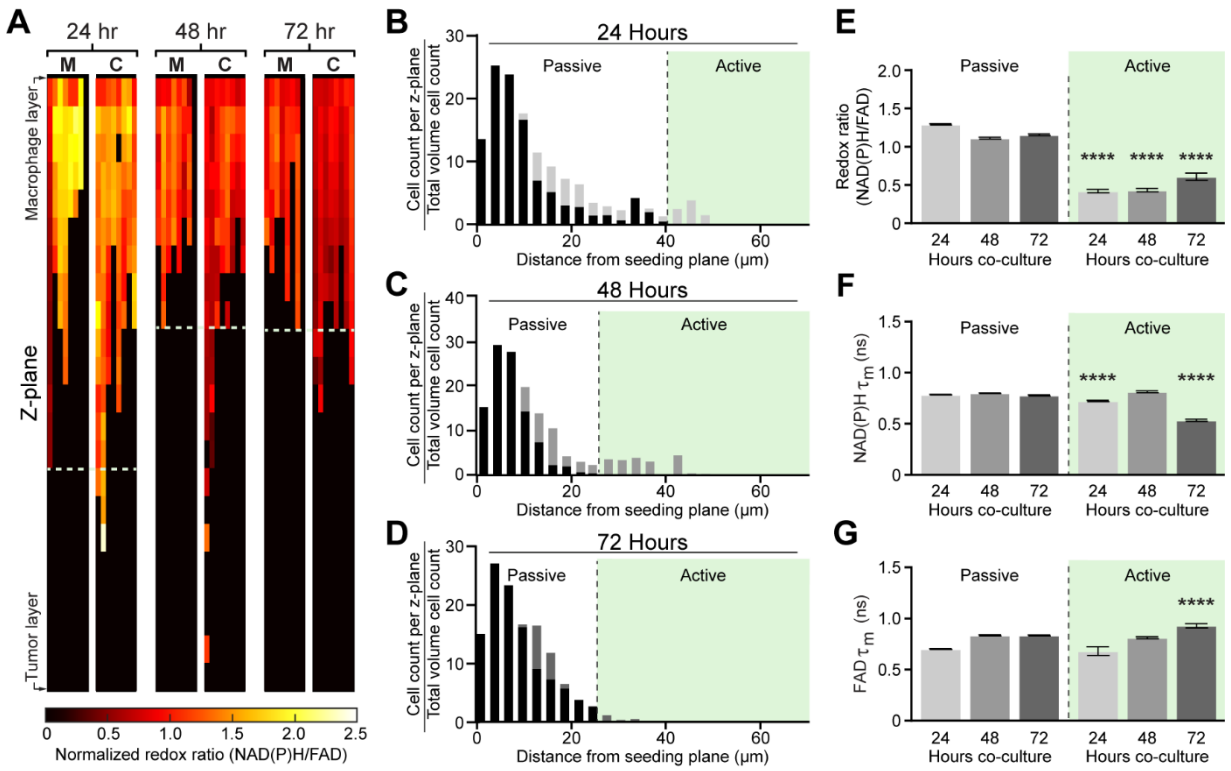

Figure 3.5: Microscale tumor co-cultures regulate mouse macrophage metabolism and migration over time. A) Representative heatmaps show changes in optical redox ratio with z-plane and time within monocultured, "M", and co-cultured, "C", macrophages. Cell density distributions of migration distance identify a distinct sub-population of actively-migrating RAW264.7 macrophages in the PyVMT mouse mammary tumor co-culture condition at B) 24 hours, C) 48 hours, and D) 72 hours. Passively- and actively- migrating macrophage populations were defined in co-cultures over 72 hours to observe time-dependent relationships between E) redox ratio, F) NAD(P)H τ_m and G) FAD τ_m and migratory activity. Actively-migrating populations exhibit lower redox ratio than passive-migrating populations at all time points, suggesting macrophages undergo a metabolic switch during migration;****$p<0.0001$ vs passive migration.

3.4.5 Human macrophage metabolism and 3D migration in response to patient-derived breast cancer cells

THP-1 human monocytes were cultured alone or with patient-derived IDC cells, and metabolic autofluorescence changes were measured over 72 hours. Qualitative redox images from a representative z-plane (migration distance = 12 μm) highlight cell-level heterogeneity in redox ratio and lifetimes for co-cultures compared to monoculture (Figure 3.6A). Increased cell and nucleus size are observed in co-cultured cells, consistent with reported morphological differences between human monocytes and activated macrophages (Figure 3.6A)[76]. Expression of M1-like and M2-like macrophage signature genes demonstrate

heterogeneity in macrophage phenotype for human co-cultures [77,78]. 24 hours of co-culture significantly upregulated only IL1B, while expression of TNF and PTGS2 significantly decreased in 48 hour co-cultures (Figure 3.6B). Mixed phenotype genes were variably expressed at both 24 and 48 hours (Figure 3.6B). Conversely, mixed phenotype IL12B, TGFB1, CSF1, NOS2, IL10 was upregulated after 72 hours co-culture with patient-derived tumor cells (Figure 3.6B). IL1B, TNF (M1-like) and CCL22, VEGFA, PTGS2 (M2-like) were also significantly increased by 72 hours (Figure 3.6B). Quantitative autofluorescence measurement showed monocyte-derived macrophages in co-culture have significantly higher redox ratio at 48 hours (Figure 3.6C), no change in NAD(P)H τ_m at any time point (Figure 3.6D), and significantly lower FAD τ_m at all time points compared to monoculture (Figure 3.6E). NAD(P)H and FAD lifetime components were also affected by tumor co-culture (Figure A.4A-F). In contrast, the time course of autofluorescence changes in THP-1 human monocytes in co-culture with a triple negative breast cancer cell line (MDA-MB-231, Figure A.5) substantially differs from patient-derived IDC co-cultures (Figure 3.6), highlighting breast cancer cell origin as a source of variability in monocyte-derived macrophage metabolism. These findings demonstrate variation in tumor-mediated monocyte activation and macrophage polarization across species, culture in 2D vs. 3D, and breast tumor sub-types, which highlights the unique insights enabled by combining 3D Stacks and autofluorescence imaging technologies.

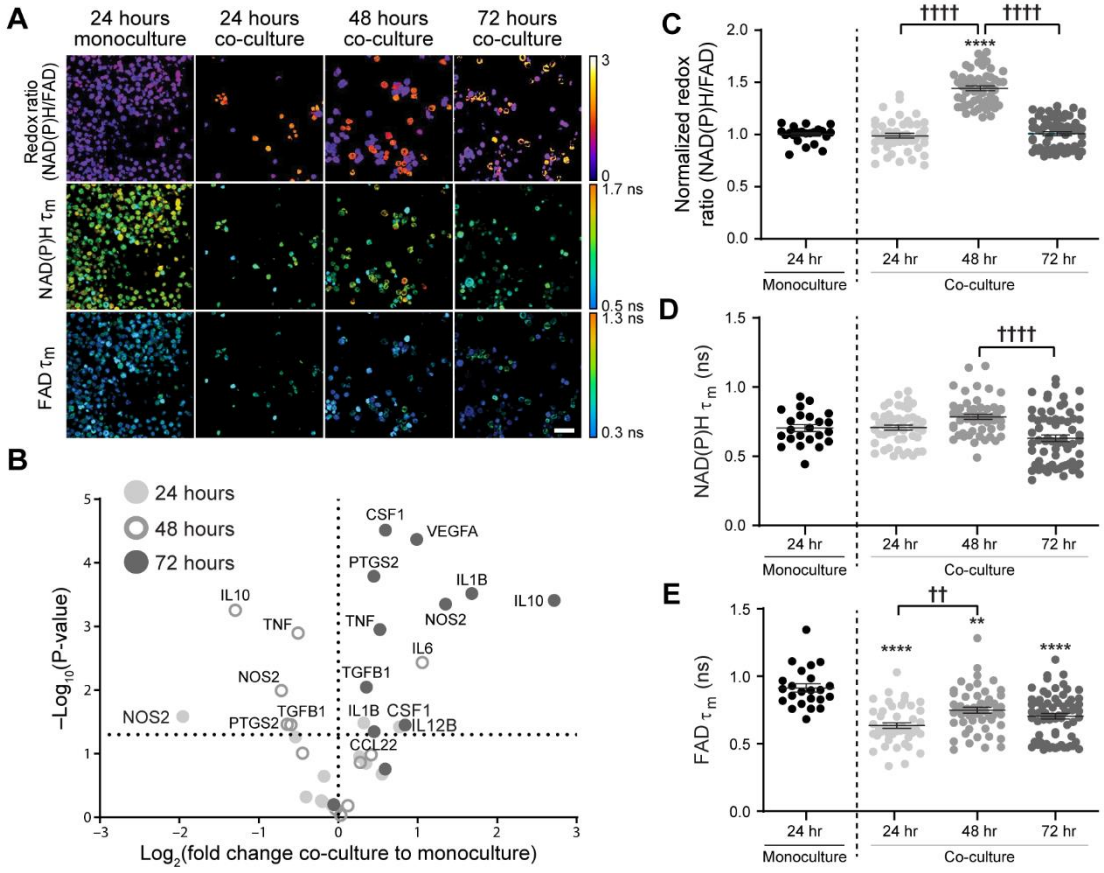

Figure 3.6: Metabolic autofluorescence imaging captures human monocyte-derived macrophage metabolism in 3D Stacks co-cultures with primary human invasive ductal carcinoma. A) Representative images (z-plane distance: 12µm) display qualitative changes in redox ratio, NAD(P)H τ_m, and FAD τ_m between monoculture and co-cultures over 72 hours. Scale bar = 50 µm. B) Gene expression changes in co-cultured monocyte-derived macrophages over 24, 48, and 72 hours measured from qPCR. Changes are reported as log fold change with respect to the average of the monoculture condition for each measurement and time point. Metabolic changes in human THP-1 monocytes were quantified following co-culture with primary human IDC: C) Redox ratio, D) NAD(P)H τ_m, and E) FAD τ_m. **,**** $p<0.01,0.0001$ vs. monoculture; ††, †††† $p<0.01,0.0001$.

Tumor-mediated migration was also assessed in 3D co-cultures of primary IDC and THP-1 monocytes. Heatmaps of redox ratio changes with z-plane show increased migration in co-culture conditions and decreased redox ratio in macrophages localized closer to the tumor at 72 hours (Figure 3.7A), similar to the behavior of RAW264.7 cells (Figure 3.5A). NAD(P)H and FAD τ_m of macrophages also vary with time and z-plane (Figure A.4G-H). Monocyte-derived macrophages stimulated in co-culture exhibited substantial migration towards the tumor layer at all time points, in contrast to monocytes in

monoculture (Figure 3.7B-D). Passively- and actively-migrating macrophages were then defined based on monoculture migration distances at each time point (Figure 3.7B-D). Both the redox ratio and FAD τ_m of actively-migrating macrophages co-culture were higher at early time points compared to passively-migrating macrophages, but gradually declined over 72 hours (Figure 3.7E&G). Actively-migrating macrophages in co-culture also have decreased NAD(P)H τ_m at 24 and 72 hours (Figure 3.7F). Overall, these results establish the versatility of the platform to address the challenge of evaluating dynamic macrophage function in the human TME.

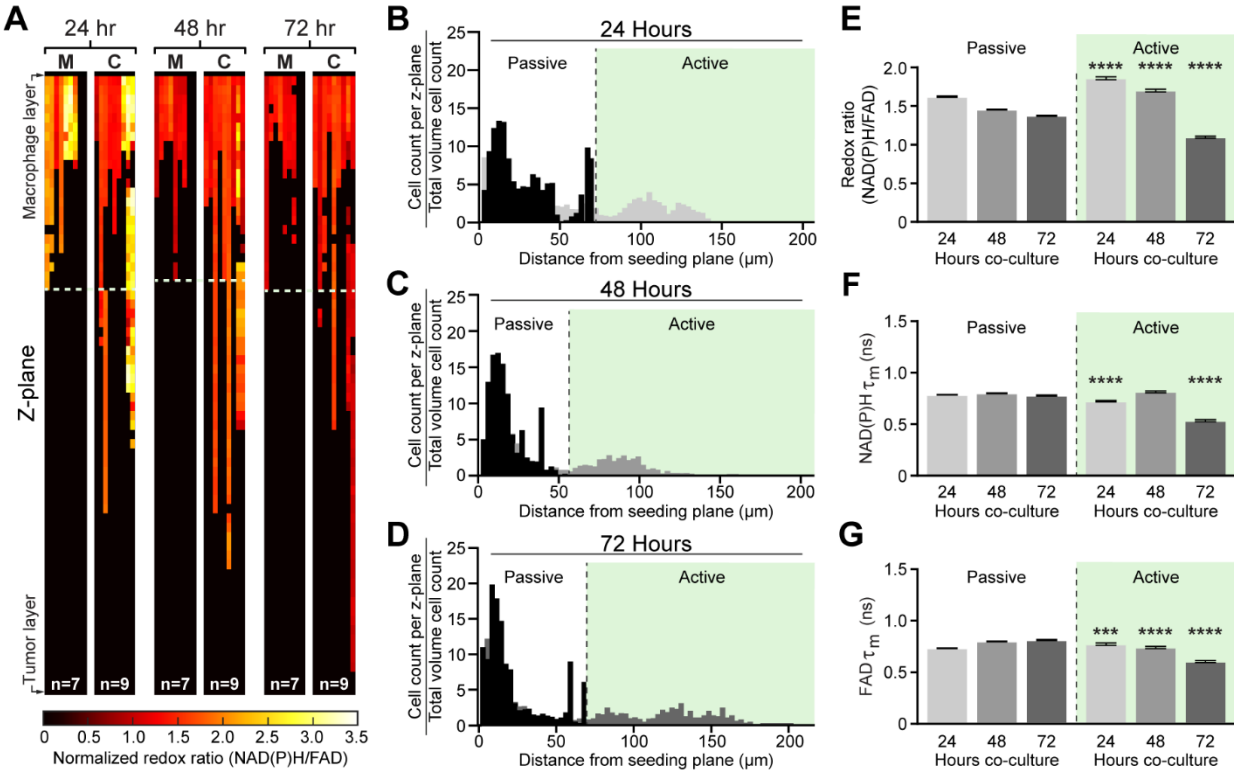

Figure 3.7: Spatial and temporal metabolic changes of human monocyte-derived macrophages in co-culture with primary human invasive ductal carcinoma. A) Representative heatmaps depicting changes in redox ratio with z-plane. Co-cultured macrophages, "C", exhibit greater migratory activity and gradual decreases in redox ratio over time compared to monocultured macrophages, "M". Representative cell density distributions reveal significant monocyte-derived macrophage migration in response to tumor co-culture, with a large population of actively-migrating macrophages at B) 24 hours, C) 48 hours, and D) 72 hours. Differences in E) redox ratio, F) NAD(P)H τ_m, and G) FAD τ_m between actively- and passively-migrating populations were quantified at each time point. ***,**** $p<0.001,0.0001$ vs. passive migration.

3.5 Discussion

Macrophage plasticity leads to frequent shifts in function and metabolism in the TME, resulting in heterogeneous tumor-associated macrophage populations[14,21,79]. Here, we show that metabolic autofluorescence imaging can monitor macrophage heterogeneity during polarization and migration within a 3D microfluidic model of the TME. Metabolic autofluorescence imaging enables non-destructive monitoring of metabolic changes in individual, live cells within 3D *in vitro* cultures and *in vivo* tumors[31,33,34,39–42,50,51,80]. Additionally, 3D microfluidic culture systems, such as the Stacks microfluidic device used in this study, provide simple platforms to recapitulate dynamic environmental conditions that characterize *in vivo* tumors (e.g., hypoxia, acidosis, nutrient starvation) and are powerful to study primary human cells in an *in vivo*-like environment[81–86]. Previous studies have shown that metabolic autofluorescence can identify macrophages in 2D cultures and *in vivo* but have not explored spatiotemporal heterogeneity in macrophage metabolism within the TME [34,41,42,53]. This is the first study to monitor cell-level macrophage metabolism in microfluidic models of intact TME. Here, we quantify metabolic heterogeneity of macrophages in the Stacks 3D microdevice platform using autofluorescence imaging to provide novel insights into spatiotemporal heterogeneity of macrophages in the TME.

Temporal changes in microenvironment conditions affect macrophage metabolism and function, so this study quantified time-dependent changes in macrophage autofluorescence within microfluidic 3D tumor co-cultures. This study first confirmed that metabolic autofluorescence imaging can quantify changes in macrophage metabolism and distinguish macrophage sub-populations within intact, living samples. Differences in NAD(P)H and FAD autofluorescence were first observed in 2D cytokine-stimulated macrophages over 72 hours and reflected the expected metabolic shifts for M(IFN-γ) and M(IL4/IL13) macrophages (Figure 3.2)[87–89]. This result is consistent with previous metabolic flux and metabolite accumulation studies showing increased glycolysis in LPS- or IFN-γ+TNF-α-stimulated (M1-like) macrophages and increased TCA cycle in IL-4-stimulated (M2-like) macrophages, as well as NAD(P)H lifetime studies distinguishing -γ/LPS-treated and IL-4/IL-13 treated mouse bone marrow-derived macrophages (BMDMs)[41]. Next, RAW264.7 macrophages co-cultured in 3D with PyVMT breast cancer

displayed changes in redox ratio consistent with metabolic changes from tumor stimulation in previous studies (Figure 3.4A&C)[90]. Differences in redox ratio and fluorescence lifetime measurements were observed between RAW264.7 macrophages in cytokine-stimulated 2D cultures (Figure 3.2B-D) and tumor-stimulated 3D cultures (Figure 3.4C-E), consistent with reported differences in intracellular metabolite concentration and metabolic flux based on stimulation condition (e.g., cytokines, tumor conditioned media) and culture in 2D vs. 3D[91,92]. Additionally, 3D co-cultured RAW264s exhibited heterogeneous cell-level autofluorescence and pooled gene expression (Figure 3.4B, F-H). This is consistent with reported time courses of metabolic and genetic changes in co-cultures of tumor cells and monocytes or macrophages[93]. Furthermore, the genetic and metabolic heterogeneity observed here is supported by recent studies that similarly show tumor-associated macrophages adopt a mixture of M1-like and M2-like characteristics and functions[94–98]. This reinforces a model of tumor-associated macrophages with diverse phenotypes[99], which can be further explored using the methods demonstrated here. Ultimately, these studies show that metabolic autofluorescence imaging is sensitive to heterogeneity in macrophage function and metabolism within 3D models of the TME.

Microfluidic culture is also attractive for mimicking the 3D spatial structure of the TME. Accordingly, multi-photon excitation of metabolic autofluorescence enables cellular-resolution imaging in thick, scattering samples to monitor environmental gradients and spatial heterogeneity in 3D tumor models[47,100]. Therefore, we measured metabolic heterogeneity of RAW264 macrophages with 3D migration during co-culture with PyVMT tumor cells (Figure 3.5). Macrophages in co-culture exhibited greater migration across the ECM layer over 72 hours compared to monocultured macrophages, which was shown to be a tumor-specific behavior (Figure 3.5A-D, Figure A.2D-F,3M-N). Previous studies suggest that mouse macrophages often exhibit random migration during chemotaxis[101]. This is consistent with our observations of mouse macrophage migration (Figure 3.5A-D). Prior studies have also shown that M2-like macrophages are typically more migratory, which is consistent with the oxidative metabolic shift in mouse macrophages localized closest to the tumor layer (actively-migrating) (Figure 3.5E-G)[102,103]. Overall, metabolic

autofluorescence imaging and microfluidic models of 3D microenvironment illustrate tumor-driven spatiotemporal changes in macrophage metabolism.

An important advantage of the Stacks system is the use of primary human cells for studies of human tumor-immune interactions. We highlighted this advantage with 3D co-cultures of primary IDC and THP-1 monocytes (Figure 3.6). Previous studies have shown that human THP-1 monocytes will differentiate and preferentially polarize to M2-like macrophages as early as 48 hours after treatment with tumor-conditioned media[104–106]. This is consistent with redox ratio changes of THP-1s in co-culture with primary tumor cells (Figure 3.6C). The late oxidative, M2-like switch captured by the redox ratio is also consistent with previous reports of 2D differentiated THP-1 cells exposed to IL-4 (M2-like) cytokine stimulation[34]. Co-cultured THP-1s also migrated farther across the ECM than monocultures over 72 hours (Figure 3.7A-D). Human macrophages and monocytes exhibit strong directional migration toward chemotactic gradients (Figure 3.7B-D), consistent with our observations of human macrophage and monocyte migration[107]. The redox ratio of actively-migrating human macrophages increased at 24 hours and gradually declined over 72 hours (Figure 3.7E-G), consistent with reports of upregulated glycolytic metabolism prior to oxidative shifts in human macrophages during chemoattractant-induced migration[108]. These studies indicate that metabolic autofluorescence imaging in human tumor-macrophage microfluidic cultures provides a valuable platform to characterize novel spatiotemporal dynamics of macrophage metabolism within the human TME.

Overall, we have established a novel, single-cell imaging and 3D microfluidic culture platform to monitor the spatial and temporal dynamics of macrophage metabolism within the TME. Autofluorescence imaging of 3D tumor-macrophage co-cultures characterized metabolic heterogeneity with tumor-mediated macrophage polarization and migration. This approach could be used to evaluate metabolic heterogeneity in more complex 3D microscale cultures with additional immune cells, stromal cells, and vasculature. Furthermore, direct manipulation of environmental gradients (e.g., oxygen, nutrients, pH) during culture and imaging could assess the relationship between environmental pressures and macrophage metabolism, function, and organization. Ultimately, these tools may improve our understanding of cellular heterogeneity and metabolism in the TME, and their effects on tumor progression and treatment response.

3.6 Acknowledgments

We would like to thank Rupsa Datta and Jose Ayuso for their valuable input on the experimental design and manuscript composition. We acknowledge Jens Eickoff for his guidance in statistical analysis of the reported data. We also acknowledge for Matthew Stefely for input on design of scientific diagrams and data representation.

3.7 References

1. Gajewski TF, Schreiber H, Fu Y-X. Innate and adaptive immune cells in the tumor microenvironment. doi:10.1038/ni.2703

2. Lee HW, Choi HJ, Ha SJ, Lee KT, Kwon YG. Recruitment of monocytes/macrophages in different tumor microenvironments. *Biochim Biophys Acta - Rev Cancer*. 2013;1835(2):170-179. doi:10.1016/J.BBCAN.2012.12.007

3. Zahreddine H, Borden KLB. Mechanisms and insights into drug resistance in cancer. *Front Pharmacol*. 2013;4:28. doi:10.3389/fphar.2013.00028

4. Panni RZ, Linehan DC, DeNardo DG. Targeting tumor-infiltrating macrophages to combat cancer. *Immunotherapy*. 2013;5(10):1075-1087.

5. Murray PJ. Macrophage Polarization. *Annu Rev Physiol*. 2017;79(1):541-566. doi:10.1146/annurev-physiol-022516-034339

6. Liu Y-C, Zou X-B, Chai Y-F, Yao Y-M. Macrophage Polarization in Inflammatory Diseases. *Int J Biol Sci*. 2014;10(5):520-529. doi:10.7150/ijbs.8879

7. Jagannathan N, Ramanathan S. Tumor Associated Macrophage: A Review on the Phenotypes, Traits and Functions. *Iran J Cancer Prev Iran J Cancer Prev*. 2014;7(71):1-81. https://www.ncbi.nlm.nih.gov/pmc/articles/PMC4142950/pdf/IJCP-07-001.pdf. Accessed April 23, 2018.

8. Biswas SK, Mantovani A. Macrophage plasticity and interaction with lymphocyte subsets: cancer as a paradigm. *Nat Immunol*. 2010;11(10):889-896. doi:10.1038/ni.1937

9. Biswas SK. Tumor Microenvironment and. 2017. doi:10.1101/cshperspect.a026781

10. Martinez FO, Gordon S. The M1 and M2 paradigm of macrophage activation: time for reassessment. *F1000Prime Rep*. 2014;6:13. doi:10.12703/P6-13

11. Chávez-Galán L, Olleros ML, Vesin D, Garcia I. Much More than M1 and M2 Macrophages, There are also CD169(+) and TCR(+) Macrophages. *Front Immunol*. 2015;6:263. doi:10.3389/fimmu.2015.00263

12. Verdeguer F, Aouadi M. Macrophage heterogeneity and energy metabolism. *Exp Cell Res*. 2017;360(1):35-40. doi:10.1016/J.YEXCR.2017.03.043

13. Netea-Maier RT, Smit JWA, Netea MG. Metabolic changes in tumor cells and tumor-associated macrophages: A mutual relationship. *Cancer Lett*. 2018;413:102-109. doi:10.1016/J.CANLET.2017.10.037

14. Ghesquière B, Wong BW, Kuchnio A, Carmeliet P. Metabolism of stromal and immune cells in health and disease. *Nature*. 2014;511(7508):167-176. doi:10.1038/nature13312

15. Renner K, Singer K, Koehl GE, et al. Metabolic Hallmarks of Tumor and Immune Cells in the Tumor Microenvironment. *Front Immunol*. 2017;8:248. doi:10.3389/fimmu.2017.00248

16. Pearce EL, Pearce EJ. Metabolic Pathways in Immune Cell Activation and Quiescence. *Immunity*. 2013;38(4):633-643. doi:10.1016/J.IMMUNI.2013.04.005

17. Mehta MM, Weinberg SE, Chandel NS. Mitochondrial control of immunity: beyond ATP. *Nat Rev Immunol*. 2017;17(10):608-620. doi:10.1038/nri.2017.66

18. Ajmal H, Rehman S, Farooq U, Ain QU, Riaz F, Hassan A. Convolutional neural network based image segmentation: a review. In: *Proc.SPIE*. Vol 10649. ; 2018. https://doi.org/10.1117/12.2304711.

19. O'Neill LAJ, Kishton RJ, Rathmell J. A guide to immunometabolism for immunologists. *Nat Rev Immunol*. 2016;16(9):553-565. doi:10.1038/nri.2016.70

20. Van den Bossche J, O'Neill LA, Menon D. Macrophage Immunometabolism: Where Are We (Going)? *Trends Immunol*. 2017;38(6):395-406. doi:10.1016/J.IT.2017.03.001

21. Biswas SK, Mantovani A. Orchestration of Metabolism by Macrophages. *Cell Metab*. 2012;15(4):432-437. doi:10.1016/J.CMET.2011.11.013

22. Zhu L, Zhao Q, Yang T, Ding W, Zhao Y. Cellular Metabolism and Macrophage Functional Polarization. *Int Rev Immunol*. 2015;34(1):82-100. doi:10.3109/08830185.2014.969421

23. Montanez-Sauri SI, Sung KE, Berthier E, Beebe DJ. Enabling screening in 3D microenvironments: probing matrix and stromal effects on the morphology and proliferation of T47D breast carcinoma cells. *Integr Biol*. 2013;5(3):631. doi:10.1039/c3ib20225a

24. Montanez-Sauri SI, Beebe DJ, Sung KE. Microscale screening systems for 3D cellular microenvironments: platforms, advances, and challenges. *Cell Mol Life Sci*. 2015;72(2):237-249. doi:10.1007/s00018-014-1738-5

25. McWhorter FY, Smith TD, Luu TU, Rahim MK, Haun JB, Liu WF. Macrophage secretion heterogeneity in engineered microenvironments revealed using a microwell platform. *Integr Biol (Camb)*. 2016;8(7):751-760. doi:10.1039/c6ib00053c

26. Kim S-H, Turnbull J, Guimond S. Extracellular matrix and cell signalling: the dynamic cooperation of integrin, proteoglycan and growth factor receptor. *J Endocrinol*. 2011;209(2):139-151. doi:10.1530/JOE-10-0377

27. Yu J, Berthier E, Craig A, et al. Reconfigurable open microfluidics for studying the spatiotemporal dynamics of paracrine signalling. *Nat Biomed Eng*. 2019;3(10):830-841. doi:10.1038/s41551-019-0421-4

28. Chattopadhyay PK, Gierahn TM, Roederer M, Love JC. Single-cell technologies for monitoring immune systems. *Nat Immunol*. 2014;15(2):128-135. doi:10.1038/ni.2796

29. Ottobrini L, Martelli C, Trabattoni DL, Clerici M, Lucignani G. In vivo imaging of immune cell trafficking in cancer. *Eur J Nucl Med Mol Imaging*. 2011;38(5):949-968. doi:10.1007/s00259-010-1687-7

30. Laing RE, Nair-Gill E, Witte ON, Radu CG. Visualizing cancer and immune cell function with metabolic positron emission tomography. doi:10.1016/j.gde.2009.10.008

31. Walsh AJ, Cook RS, Manning HC, et al. Optical metabolic imaging identifies glycolytic levels, subtypes, and early-treatment response in breast cancer. *Cancer Res*. 2013;73(20):6164-6174. doi:10.1158/0008-5472.CAN-13-0527

32. Skala MC, Squirrell JM, Vrotsos KM, et al. Multiphoton microscopy of endogenous fluorescence differentiates normal, precancerous, and cancerous squamous epithelial tissues. *Cancer Res*. 2005;65(4):1180-1186. doi:10.1158/0008-5472.CAN-04-3031

33. Walsh A, Mueller K, Jones I, et al. Label-free Method for Classification of T cell Activation. *bioRxiv*. 2019:536813.

34. Smokelin IS, Mizzoni C, Erndt-Marino J, Kaplan D, Georgakoudi I. Optical changes in THP-1 macrophage metabolism in response to pro- and anti-inflammatory stimuli reported by label-free two-photon imaging. *J Biomed Opt*. 2020;25(1):1-14. https://doi.org/10.1117/1.JBO.25.1.014512.

35. Georgakoudi I, Quinn KP. Optical Imaging Using Endogenous Contrast to Assess Metabolic State. *Annu Rev Biomed Eng*. 2012;14(1):351-367. doi:10.1146/annurev-bioeng-071811-150108

36. Quinn KP, Sridharan G V., Hayden RS, Kaplan DL, Lee K, Georgakoudi I. Quantitative metabolic imaging using endogenous fluorescence to detect stem cell differentiation. *Sci Rep*. 2013;3(1):3432. doi:10.1038/srep03432

37. Walsh AJ, Skala MC. Optical metabolic imaging quantifies heterogeneous cell populations. *Biomed Opt Express*. 2015;6(2):559-573. doi:10.1364/BOE.6.000559

38. Walsh AJ, Cook RS, Sanders ME, et al. Quantitative optical imaging of primary tumor organoid metabolism predicts drug response in breast cancer. *Cancer Res*. 2014;74(18):5184-5194. doi:10.1158/0008-5472.CAN-14-0663

39. Shah AT, Heaster TM, Skala MC. Metabolic Imaging of Head and Neck Cancer Organoids. Sobol RW, ed. *PLoS One*. 2017;12(1):e0170415. doi:10.1371/journal.pone.0170415

40. Heaster TM, Walsh AJ, Zhao Y, Hiebert SW, Skala MC. Autofluorescence imaging identifies tumor cell-cycle status on a single-cell level. *J Biophotonics*. 2018;11(1):1-15. doi:10.1002/jbio.201600276

41. Alfonso-García A, Smith TD, Datta R, et al. Label-free identification of macrophage phenotype by fluorescence lifetime imaging microscopy. *J Biomed Opt*. 2016;21(4):46005. doi:10.1117/1.JBO.21.4.046005

42. Szulczewski JM, Inman DR, Entenberg D, et al. In Vivo Visualization of Stromal Macrophages via label-free FLIM-based metabolite imaging. *Sci Rep*. 2016;6(1):25086. doi:10.1038/srep25086

43. Heikal AA. Intracellular coenzymes as natural biomarkers for metabolic activities and mitochondrial anomalies. *Biomark Med*. 2010;4(2):241-263. doi:10.2217/bmm.10.1

44. Chance B, Schoener B, Oshino R, Itshak F, Nakase Y. Oxidation-reduction ratio studies of mitochondria in freeze-trapped samples. NADH and flavoprotein fluorescence signals. *J Biol Chem*. 1979;254(11):4764-4771.

45. Blacker TS, Marsh RJ, Duchen MR, Bain AJ. Activated barrier crossing dynamics in the non-radiative decay of NADH and NADPH. *Chem Phys*. 2013;422:184-194. doi:10.1016/j.chemphys.2013.02.019

46. Sharick JT, Favreau PF, Gillette AA, Sdao SM, Merrins MJ, Skala MC. Protein-bound NAD(P)H Lifetime is Sensitive to Multiple Fates of Glucose Carbon. *Sci Rep*. 2018;8(1):5456.

doi:10.1038/s41598-018-23691-x

47. Mulligan SJ, Macvicar BA. Two-Photon Fluorescence Microscopy: Basic Principles, Advantages and Risks. https://pdfs.semanticscholar.org/cdf1/24284c19218d3478ceafa77f4c11222c9e3d.pdf. Accessed May 8, 2018.

48. Blacker TS, Duchen MR. Investigating mitochondrial redox state using NADH and NADPH autofluorescence. *Free Radic Biol Med*. 2016;100:53-65.

49. Lakowicz JR, Szmacinski H, Nowaczyk K, Johnson ML. Fluorescence lifetime imaging of free and protein-bound NADH. *Proc Natl Acad Sci U S A*. 1992;89(4):1271-1275. doi:10.1073/PNAS.89.4.1271

50. Sharick JT, Jeffery JJ, Karim MR, et al. Cellular Metabolic Heterogeneity In Vivo Is Recapitulated in Tumor Organoids. *Neoplasia*. 2019;21(6):615-626. doi:10.1016/j.neo.2019.04.004

51. Shah AT, Demory Beckler M, Walsh AJ, Jones WP, Pohlmann PR, Skala MC. Optical Metabolic Imaging of Treatment Response in Human Head and Neck Squamous Cell Carcinoma. *PLoS One*. 2014;9(3):1-10. doi:10.1371/journal.pone.0090746

52. Ayuso JM, Gillette A, Lugo-Cintrón K, et al. Organotypic microfluidic breast cancer model reveals starvation-induced spatial-temporal metabolic adaptations. *EBioMedicine*. 2018;37:144-157. doi:10.1016/j.ebiom.2018.10.046

53. Li Y, Liu T-M. Discovering Macrophage Functions Using In Vivo Optical Imaging Techniques. *Front Immunol*. 2018;9:502. doi:10.3389/fimmu.2018.00502

54. Jones JD, Ramser HE, Woessner AE, Quinn KP. In vivo multiphoton microscopy detects longitudinal metabolic changes associated with delayed skin wound healing. *Commun Biol*. 2018;1(1):198.

55. Xylas J, Varone A, Quinn KP, et al. Noninvasive assessment of mitochondrial organization in three-dimensional tissues reveals changes associated with cancer development. *Int J cancer*. 2015;136(2):322-332. doi:10.1002/ijc.28992

56. NCI-Frederick, Frederick National Laboratory for Cancer Research, Frederick M. The NCI Patient-Derived Models Repository (PDMR).

57. Mahou P, Zimmerley M, Loulier K, et al. Multicolor two-photon tissue imaging by wavelength mixing. *Nat Methods*. 2012;9(8):815.

58. Skala MC, Riching KM, Gendron-Fitzpatrick A, et al. In vivo multiphoton microscopy of NADH and FAD redox states, fluorescence lifetimes, and cellular morphology in precancerous epithelia. *Proc Natl Acad Sci*. 2007;104(49):19494-19499.

59. Bird DK, Yan L, Vrotsos KM, et al. Metabolic mapping of MCF10A human breast cells via multiphoton fluorescence lifetime imaging of the coenzyme NADH. *Cancer Res*. 2005;65(19):8766-8773.

60. Walsh AJ, Skala MC. An automated image processing routine for segmentation of cell cytoplasms in high-resolution autofluorescence images. In: Periasamy A, So PTC, König K, eds. Vol 8948. International Society for Optics and Photonics; 2014:89481M. doi:10.1117/12.2040644

61. He C, Carter AB. The Metabolic Prospective and Redox Regulation of Macrophage Polarization. *J Clin Cell Immunol*. 2015;6(6). doi:10.4172/2155-9899.1000371

62. Galván-Peña S, Neill LAJO', Dileepan KN, Shen B. Metabolic reprograming in macrophage polarization. 2014. doi:10.3389/fimmu.2014.00420

63. El Kasmi KC, Stenmark KR. Contribution of metabolic reprogramming to macrophage plasticity and function. *Semin Immunol*. 2015;27(4):267-275. doi:10.1016/j.smim.2015.09.001

64. Venter G, Oerlemans FTJJ, Wijers M, et al. Glucose Controls Morphodynamics of LPS-Stimulated Macrophages. 2014. doi:10.1371/journal.pone.0096786

65. Freemerman AJ, Johnson AR, Sacks GN, et al. Metabolic reprogramming of macrophages: Glucose Transporter (GLUT1)-mediated glucose metabolism drives a pro-inflammatory phenotype*. doi:10.1074/jbc.M113.522037

66. Bost F, Decoux-Poullot A-G, Tanti J, Clavel S. Energy disruptors: rising stars in anticancer therapy? *Nat Publ Gr*. 2015;46. doi:10.1038/oncsis.2015.46

67. Ley K, Pramod AB, Croft M, Ravichandran KS, Ting JP. How Mouse Macrophages Sense What Is Going On. *Front Immunol*. 2016;7:204. doi:10.3389/fimmu.2016.00204

68. Akaike H. A new look at the statistical model identification. In: *Selected Papers of Hirotugu Akaike*. Springer; 1974:215-222.

69. Edward Miller G. Use of the squared ranks test to test for the equality of the coefficients of variation. *Commun Stat Comput*. 1991;20(2-3):743-750.

70. Levy B. Conover's Two-Sample Squared Ranks Test for Equality of Variance. *MATLAB Cent File Exch*. 2020. https://www.mathworks.com/matlabcentral/fileexchange/4584-conover-s-two-sample-squared-ranks-test-for-equality-of-variance.

71. Rodell CB, Arlauckas SP, Cuccarese MF, et al. TLR7/8-agonist-loaded nanoparticles promote the polarization of tumour-associated macrophages to enhance cancer immunotherapy. *Nat Biomed Eng*. 2018;2:578-588. https://www.ncbi.nlm.nih.gov/pubmed/30345161.

72. Smith TD, Tse MJ, Read EL, Liu WF. Regulation of macrophage polarization and plasticity by complex activation signals. *Integr Biol*. 2016;8(9):946-955.

73. Li Z, Zhao M, Li T, et al. Decidual macrophage functional polarization during abnormal pregnancy due to Toxoplasma gondii: role for LILRB4. *Front Immunol*. 2017;8:1013.

74. Bardi GT, Smith MA, Hood JL. Melanoma exosomes promote mixed M1 and M2 macrophage polarization. *Cytokine*. 2018;105:63-72.

75. Pakshir P, Alizadehgiashi M, Wong B, et al. Dynamic fibroblast contractions attract remote macrophages in fibrillar collagen matrix. *Nat Commun*. 2019;10(1):1-17.

76. Rostam HM, Reynolds PM, Alexander MR, Gadegaard N, Ghaemmaghami AM. Image based machine learning for identification of macrophage subsets. *Sci Rep*. 2017;7(1):1-11.

77. Spiller KL, Wrona EA, Romero-Torres S, et al. Differential gene expression in human, murine, and cell line-derived macrophages upon polarization. *Exp Cell Res*. 2016;347(1):1-13. doi:https://doi.org/10.1016/j.yexcr.2015.10.017

78. Surdziel E, Clay I, Nigsch F, et al. Multidimensional pooled shRNA screens in human THP-1 cells identify candidate modulators of macrophage polarization. *PLoS One*. 2017;12(8):e0183679. https://doi.org/10.1371/journal.pone.0183679.

79. Kelly B, Aj L, Neill O'. Metabolic reprogramming in macrophages and dendritic cells in innate

immunity. *Nat Publ Gr*. 2015;25(25). doi:10.1038/cr.2015.68

80. Liu Z, Pouli D, Alonzo CA, et al. Mapping metabolic changes by noninvasive, multiparametric, high-resolution imaging using endogenous contrast. *Sci Adv*. 2018;4(3). doi:10.1126/sciadv.aap9302

81. Cyril Corbet A, Pinto A, Martherus R, et al. Acidosis Drives the Reprogramming of Fatty Acid Metabolism in Cancer Cells through Changes in Mitochondrial and Histone Acetylation. *Cell Metab*. 2016;24(9):311-323. doi:10.1016/j.cmet.2016.07.003

82. Riemann A, Wußling H, Loppnow H, Fu H, Reime S, Thews O. Acidosis differently modulates the inflammatory program in monocytes and macrophages. *Biochim Biophys Acta - Mol Basis Dis*. 2016;1862(1):72-81. doi:10.1016/J.BBADIS.2015.10.017

83. Colegio OR. Lactic acid polarizes macrophages to a tumor-promoting state. *Oncoimmunology*. 2016;5(3):e1014774. doi:10.1080/2162402X.2015.1014774

84. Heming TA, Tuazon DM, Davé SK, Chopra AK, Peterson JW, Bidani A. Post-transcriptional effects of extracellular pH on tumour necrosis factor-alpha production in RAW 246.7 and J774 A.1 cells. *Clin Sci (Lond)*. 2001;100(3):259-266. doi:10.1042/CS1000259

85. Gerry AB, Leake DS. Effect of low extracellular pH on NF-κB activation in macrophages. *Atherosclerosis*. 2014;233(2):537-544. doi:10.1016/j.atherosclerosis.2014.01.014

86. Raggi F, Pelassa S, Pierobon D, et al. Regulation of human Macrophage M1-M2 Polarization Balance by hypoxia and the Triggering receptor expressed on Myeloid cells-1. *Front Immunol*. 2017;8(SEP):1-18. doi:10.3389/fimmu.2017.01097

87. Seim GL, Britt EC, John S V, et al. Two-stage metabolic remodelling in macrophages in response to lipopolysaccharide and interferon-γ stimulation. *Nat Metab*. 2019;1(7):731-742. doi:10.1038/s42255-019-0083-2

88. Viola A, Munari F, Sánchez-Rodríguez R, Scolaro T, Castegna A. The Metabolic Signature of Macrophage Responses. *Front Immunol*. 2019;10:1462. doi:10.3389/fimmu.2019.01462

89. Tavakoli S, Downs K, Short JD, et al. Characterization of macrophage polarization states using combined measurement of 2-deoxyglucose and glutamine accumulation: implications for imaging of atherosclerosis. *Arterioscler Thromb Vasc Biol*. 2017;37(10):1840-1848.

90. Khabipov A, Kaeding A, Liedtke KR, Freund E, Partecke L-I, Bekeschus S. RAW 264.7 Macrophage Polarization by Pancreatic Cancer Cells–A Model for Studying Tumour-promoting Macrophages. *Anticancer Res*. 2019;39(6):2871-2882.

91. Halbrook CJ, Pontious C, Kovalenko I, et al. Macrophage-Released Pyrimidines Inhibit Gemcitabine Therapy in Pancreatic Cancer. *Cell Metab*. 2019;29(6):1390-1399.e6. doi:https://doi.org/10.1016/j.cmet.2019.02.001

92. Caires HR, Esteves T, Quelhas P, Barbosa MA, Navarro M, Almeida CR. Macrophage interactions with polylactic acid and chitosan scaffolds lead to improved recruitment of human mesenchymal stem/stromal cells: a comprehensive study with different immune cells. *J R Soc Interface*. 2016;13(122):20160570.

93. Hagemann T, Wilson J, Burke F, et al. Ovarian Cancer Cells Polarize Macrophages Toward A Tumor-Associated Phenotype. *J Immunol*. 2006;176(8):5023 LP - 5032. doi:10.4049/jimmunol.176.8.5023

94. Aras S, Raza Zaidi M. TAMeless traitors: Macrophages in cancer progression and metastasis. *Br J Cancer*. 2017;117(11):1583-1591. doi:10.1038/bjc.2017.356

95. Van den Bossche J, Bogaert P, Van Hengel J, et al. Alternatively activated macrophages engage in homotypic and heterotypic interactions through IL-4 and polyamine-induced E-cadherin/catenin complexes. *Blood, J Am Soc Hematol*. 2009;114(21):4664-4674.

96. Jinushi M, Chiba S, Yoshiyama H, et al. Tumor-associated macrophages regulate tumorigenicity and anticancer drug responses of cancer stem/initiating cells. *Proc Natl Acad Sci*. 2011;108(30):12425-12430.

97. Hassanzadeh Ghassabeh G, De Baetselier P, Brys L, et al. Identification of a common gene signature for type II cytokine–associated myeloid cells elicited *in vivo* in different pathologic conditions. *Blood*. 2006;108(2):575-583.

98. Awad RM, De Vlaeminck Y, Maebe J, Goyvaerts C, Breckpot K. Turn Back the TIMe: Targeting Tumor Infiltrating Myeloid Cells to Revert Cancer Progression . *Front Immunol* . 2018;9:1977. https://www.frontiersin.org/article/10.3389/fimmu.2018.01977.

99. Xue J, Schmidt S V, Sander J, et al. Transcriptome-based network analysis reveals a spectrum model of human macrophage activation. *Immunity*. 2014;40(2):274-288. doi:10.1016/j.immuni.2014.01.006

100. Pawley JB, Masters BR. Handbook of Biological Confocal Microscopy, Third Edition. *J Biomed Opt*. 2008;13(2):029902. doi:10.1117/1.2911629

101. Hind LE, Mackay JL, Cox D, Hammer DA. Two-dimensional motility of a macrophage cell line on microcontact-printed fibronectin. *Cytoskeleton (Hoboken)*. 2014;71(9):542-554. doi:10.1002/cm.21191

102. Vogel DYS, Heijnen PDAM, Breur M, et al. Macrophages migrate in an activation-dependent manner to chemokines involved in neuroinflammation. *J Neuroinflammation*. 2014;11:23. doi:10.1186/1742-2094-11-23

103. Hind LE, Lurier EB, Dembo M, Spiller KL, Hammer DA. Effect of M1–M2 polarization on the motility and traction stresses of primary human macrophages. *Cell Mol Bioeng*. 2016;9(3):455-465.

104. Sawa-Wejksza K, Dudek A, Lemieszek M, Kaławaj K, Kandefer-Szerszeń M. Colon cancer–derived conditioned medium induces differentiation of THP-1 monocytes into a mixed population of M1/M2 cells. *Tumor Biol*. 2018;40(9):1010428318797880.

105. Valeta-Magara A, Gadi A, Volta V, et al. Inflammatory Breast Cancer Promotes Development of M2 Tumor-associated Macrophages and Cancer Mesenchymal Cells Through a Complex Cytokine Network. *Cancer Res*. 2019:canres-2158.

106. Zhang F, Wang H, Wang X, et al. TGF-β induces M2-like macrophage polarization via SNAIL-mediated suppression of a pro-inflammatory phenotype. *Oncotarget*. 2016;7(32):52294.

107. Bzymek R, Horsthemke M, Isfort K, et al. Real-time two- and three-dimensional imaging of monocyte motility and navigation on planar surfaces and in collagen matrices: roles of Rho. *Sci Rep*. 2016;6(1):25016. doi:10.1038/srep25016

108. Semba H, Takeda N, Isagawa T, et al. HIF-1α-PDK1 axis-induced active glycolysis plays an essential role in macrophage migratory capacity. *Nat Commun*. 2016;7(1):11635. doi:10.1038/ncomms11635

CHAPTER 4

QUANTITATIVE SPATIAL ANALYSIS OF METABOLIC HETEROGENEITY ACROSS *IN VIVO* AND *IN VITRO* TUMOR MODELS

4.1 Abstract

Metabolic preferences of tumor cells vary within a single tumor, contributing to tumor heterogeneity, drug resistance, and patient relapse. However, the relationship between tumor treatment response and metabolically distinct tumor cell populations is not well-understood. Here, a quantitative approach was developed to characterize spatial patterns of metabolic heterogeneity in tumor cell populations within *in vivo* xenografts and 3D *in vitro* cultures (i.e., organoids) of head and neck cancer. Label-free images of cell metabolism were acquired using two-photon fluorescence lifetime microscopy of the metabolic co-enzymes NAD(P)H and FAD. Previous studies have shown that NAD(P)H mean fluorescence lifetimes can identify metabolically distinct cells with varying drug response. Thus, density-based clustering of the NAD(P)H mean fluorescence lifetime was used to identify metabolic sub-populations of cells, then assessed in control, cetuximab-, cisplatin-, and combination-treated xenografts 13 days post-treatment and organoids 24 h post-treatment. Proximity analysis of these metabolically distinct cells was designed to quantify differences in spatial patterns between treatment groups and between xenografts and organoids. Multivariate spatial autocorrelation and principal components analyses of all autofluorescence intensity and lifetime variables were developed to further improve separation between cell sub-populations. Spatial principal components analysis and Z-score calculations of autofluorescence and spatial distribution variables also visualized differences between models. This analysis captures spatial distributions of tumor cell sub-populations influenced by treatment conditions and model-specific environments. Overall, this novel spatial analysis could provide new insights into tumor growth, treatment resistance, and more effective drug treatments across a range of microscopic imaging modalities (e.g., immunofluorescence, imaging mass spectrometry).

4.2 Introduction

Cancer cells within a single tumor have heterogeneous function and phenotype[1], resulting in unpredictable progression and treatment response[2]. However, the relationship between these diverse cell populations and global tumor activity is not well-understood. Furthermore, treatment response is altered by interactions between tumor cell populations and their microenvironment. Changes in the tumor microenvironment can contribute to increased tumor cell heterogeneity, directing these cells to adapt genetic, epigenetic, and metabolic processes for growth and survival[3]. These cell-level adaptations could include mechanisms of drug resistance, so an understanding of cell-level tumor heterogeneity could provide insight into more effective cancer treatments. Experimental tumor models are crucial for investigating effects of tumor heterogeneity in cancer progression and drug development. Mouse models are commonly used because they are well-characterized and maintain *in vivo* tumor conditions. 3D organotypic cultures (i.e., organoids) are a popular emerging model system because organoids offer increased throughput compared to *in vivo* models, while maintaining key features of the original tumor, including drug response[4]. Both models enable microscopic imaging of tumor cell function and metabolic activity. These models also provide well-defined systems to test new methods for quantifying heterogeneity in tumor cell function. Quantifying spatial functional heterogeneity within *in vivo* mouse models and *in vitro* tumor organoids could establish a link between global tumor drug response and tumor cell heterogeneity, while highlighting differences between *in vivo* and *in vitro* 3D model systems. This link between cell-level behavior and overall tumor response would provide fundamental insight toward developing new treatments that target multiple cell sub- populations, and comparisons between 3D cell culture and *in vivo* systems could inform on the best use of each model system.

Cell-level spatial relationships influence macroscale tumor behavior, but quantitative analysis of tumor microscopic spatial structure has been limited[5]. Mathematical modeling has shown promise in simulating tumor spatial heterogeneity but may not account for all biological adaptions that occur within the tumor[6].Alternatively, spatial analysis of experimental models can account for the physical location of

observations to quantify local distributions and spatial associations within data, including microscopic images[7]. Computational biological image analysis provides quantitative insight into cellular activity (8, 9), and pre-existing data sets provide a readily available source of annotated data to develop and validate these image analysis tools[10–12]. A subset of these methods includes population clustering, which can identify distinct cell populations within images, and proximity measurements, which define cellular organization within and between these distinct cell populations[13]. Spatial autocorrelation also provides a measure of similarity within local cell neighborhoods through comparisons between single cell measurements and averages across neighboring cells, and can be adapted for multivariate assessment[13, 14]. Previous studies have used subsets of these techniques to assess qualitative spatial structure within histology sections or fluorescently-labeled samples to describe the organization of multiple cellular compartments and correlate to genetic profiling and prognosis[15–20]. However, these approaches can only provide a snapshot of the spatial organization at a single point in time, and require sample destruction, fixation, and labeling. Furthermore, previous studies have not investigated spatial patterns of metabolic heterogeneity at the single-cell level within living samples, which may reflect unique sources of microenvironmental stress or drug resistance.

Novel processes governing bulk tumor behavior could be characterized by integrating analytical approaches to assess intra-tumor spatial metabolic heterogeneity based on single-cell analysis of viable tumor models. Tools to assess functional heterogeneity at the cellular level are needed to better understand mechanisms that drive tumor drug response. Metabolic autofluorescence imaging can non- invasively monitor spatial and temporal changes in cellular metabolism across intact, living 3D tumor models. Metabolic autofluorescence imaging uses two-photon microscopy to quantify the fluorescence intensities and lifetimes of NAD(P)H and FAD, which are metabolic co-enzymes involved in several cellular metabolic processes[21–23]. The fluorescence properties of NADH and NADPH overlap, and are referred to collectively as NAD(P)H. The optical redox ratio, defined as the ratio of NAD(P)H intensity to FAD intensity, measures the oxidation-reduction state of the cell and correlates with mass spectrometry measurements of NADH to NAD+ ratios, and inversely correlates to oxygen consumption measurements[23–

[28]. The fluorescence lifetimes of free and enzyme-bound NAD(P)H and FAD are distinct, and thus provide complimentary information to the optical redox ratio, specifically on enzyme binding activity and quenchers in the microenvironment[23, 25, 26, 29, 30]. Previous studies have shown that NAD(P)H lifetimes change depending on the particular enzyme bound to NADH, indicating that that NAD(P)H lifetime reports on shifts in enzyme activity in cells[31]. Also, lifetimes of NAD(P)H correlate with intracellular NADPH to NADH concentration ratios[32]. Metabolic autofluorescence imaging has been previously demonstrated for monitoring heterogeneous changes in cell metabolism with drug treatment in mouse models of cancer *in vivo* and in 3D tumor organoids *in vitro*[30, 33, 34]. Altogether, metabolic autofluorescence imaging generates 3D images at sub-cellular resolution without requiring exogenous labels, sample fixation, or sample sectioning, and thus allows for the 3D spatial context of tumors to be maintained in living samples. Single-cell metabolic autofluorescence measurements can quantify metabolic heterogeneity over time and space within the same living sample and can thus relate microscopic heterogeneity to whole-tumor growth.

Here, we developed a suite of spatial statistical analysis tools to quantify the spatial diversity of tumor cell metabolism based on metabolic autofluorescence measurements. These tools were applied to previously published *in vitro* and *in vivo* metabolic autofluorescence data. Based on previous evidence showing NAD(P)H mean lifetime (τ_m) identifies distinct tumor cell populations, density-based clustering of NAD(P)H τ_m was used here to identify cell populations with distinct metabolic activity within xenografts 13 days post-treatment and organoids 24 hours post-treatment[30, 35, 36]. Maps of the clustered NAD(P)H lifetime populations were created to qualitatively evaluate the organization of sub-populations and visualize connectivity within and between populations. Population proximity calculations provided quantitative metrics to describe the spatial distribution of NAD(P)H lifetime sub-populations within xenografts and organoids. Multivariate spatial autocorrelation was then designed for all metabolic variables to improve separation between metabolic sub-populations based on distinct spatial organization. Finally, z-score calculations and multivariate spatial principal components analysis across all metabolic variables were used to assess sample variability and inter-model comparisons of spatial metabolic trends. This work provides a

novel approach to quantify spatial patterns in cell function across *in vivo* and *in vitro* tumor models with broad applicability to additional single-cell imaging datasets, such as microscopy images using fluorescent probes or imaging mass spectrometry[37–39].

4.3 Materials and Methods

Recurring abbreviations are listed in Table B.1.

4.3.1 Head and Neck Cancer Xenograft Model

Mouse xenografts were grown and treated as previously described (30). Briefly, FaDu human squamous cell carcinoma cells were injected subcutaneously in both flanks of nude mice to generate FaDu xenografts for imaging experiments. Tumor-bearing mice received intraperitoneal injection of vehicle, cetuximab (33 mg/kg)[40, 41], cisplatin (6 mg/kg)[42], or their combination three times per week over 13 days. Tumor growth curves show that cetuximab or cisplatin treatment alone results in stable disease (no change in tumor volume) and their combination results in response (reduction in tumor volume), compared to control over this 13 day treatment time- course[36]. Mice from each treatment group were selected for imaging 13 days post-treatment. Flank tumors in anesthetized mice were exposed by cutting away the skin layer covering the tumor prior to transfer onto the microscope stage for *in vivo* imaging. All animal studies were approved by the Vanderbilt University Animal Care and Use Committee and were designed according to NIH animal welfare guidelines. Mice were isoflurane-anesthetized prior to any reported surgical or imaging procedures.

4.3.2 Organoid Generation

FaDu organoids were generated according to previously reported methods[36]. FaDu tumors from nude mice were excised and dissociated to generate cell suspensions for 3D cultures. Macrosuspensions were combined with Matrigel at a 1:2 ratio by volume and plated in 100 µL droplets on 35 mm glass bottomed imaging dishes (MatTek). Organoids were incubated overnight to solidify, then maintained in fresh media prior to start of treatment. At 24 h prior to imaging, media was replaced with treatment-supplemented media containing 20 nM cetuximab[43], 33 µM cisplatin[44, 45], or their combination. 24 hours of

these treatments results in no significant change in number of cells per organoid or organoid volume. Previous studies demonstrate early treatment response in organoids (1–3 days) is consistent with measured tumor growth at later timepoints (several weeks)[33, 34]. Accordingly, 24 h of treatment in organoids does result in significant decreases in NAD(P)H τ_m for cisplatin, cetuximab, and cisplatin+cetuximab (combination) treatment, which is an early indicator of treatment response consistent with later changes in tumor volume[36].

4.3.3 Metabolic Autofluorescence Image Acquisition

Measurements of fluorescence lifetime (FLIM) and intensity were acquired through a two-photon microscope and collected with a GaAsP photomultiplier tube equipped for time-correlated single photon counting (Becker and Hickl). NAD(P)H (750 nm) and FAD (890 nm) fluorescence were excited with a tunable titanium-sapphire laser (Coherent). Fluorescence emission for NAD(P)H and FAD were collected at 400–480 and 500–600 nm, respectively. Intensity and FLIM images were acquired for each field of view with 256 × 256 pixel resolution. Lifetime decay curves were integrated over a 60 s total scan time with a pixel dwell time of 4.8 microseconds. The photon count rate was maintained at ~2–3 × 10^5 photons/second during imaging for optimal photon counting and minimal photobleaching. Each xenograft or organoid was imaged as previously described[30, 46]. For xenograft experiments, 4–6 representative fields of view were acquired per tumor ~20–40 µm from the tumor surface, with 2–6 tumors per treatment group (~1,000–2,000 cells per treatment group). For organoid experiments, a single image was captured several cell layers from the surface for 4–6 individual organoids within a given treatment group (~200–400 cells per treatment group). These imaging planes were chosen for both *in vivo* and *in vitro* imaging to avoid surface artifacts and sample a viable region away from the necrotic core.

4.3.4 Image Analysis

Fluorescence lifetimes corresponding to free and protein-bound NAD(P)H and FAD were calculated using SPCImage (Becker and Hickl). Measured fluorescence decay curves were deconvolved from the instrument response and fit to the following bi-exponential model[26]. $I(t) = \alpha_1 e^{-t/\tau_1} + \alpha_2 e^{-t/\tau_2} + C$. Second

harmonic generation signal from urea crystals at an incident wavelength of 900 nm was measured to determine the instrument response function (full width at half maximum = 244 ps). From this model, the short and long lifetime components (τ_1, τ_2) and the fractional contributions of each (α_1, α_2) were calculated for individual pixels across NAD(P)H and FAD images. Photon events over a 3 × 3 pixel area were binned to improve photon count. NAD(P)H and FAD intensity images were generated through pixel-by-pixel integration of photon count over fluorescence decay time for respective lifetime images. The per-pixel ratio of NAD(P)H fluorescence intensity to FAD intensity was then calculated to determine the optical redox ratio. A customized CellProfiler pipeline was used to segment individual cell cytoplasms (nucleus excluded)[35]. This mask was applied to all cells per image to compute the redox ratio, mean fluorescence lifetime of NAD(P)H ($\tau_m = \alpha_1\tau_1 + \alpha_2\tau_2$), FAD τ_m, free lifetime (τ_1 for NAD(P)H and τ_2 for FAD), protein-bound lifetime (τ_2 for NAD(P)H and τ_1 for FAD) and fractional contributions of the lifetimes (α_1 and α_2) for each cell cytoplasm per image[33]. Note that $\alpha_1 + \alpha_2 = 1$ so the fraction can be determined from α_1 only. Therefore, "metabolic variables" include 9 total variables: redox ratio, NAD(P)H τ_m, τ_1, τ_2, α_1, and FAD τ_m, τ_1, τ_2, α_1.

4.3.5 Quantitative Spatial Analysis

Analytical tools were developed to quantify spatial distributions of metabolic sub-populations based on metabolic variables within *in vitro* and *in vivo* tumor models. These tools quantified the effects of treatment on the spatial diversity of tumor cell metabolism. Through this approach, clustering techniques identified functionally distinct cell populations in metabolic autofluorescence data. Additionally, spatial statistical analysis of metabolic autofluorescence data revealed patterns in their spatial organization. Analysis steps are briefly outlined in Figure 4.1 and discussed in detail below.

4.3.5.1 Single Variable Analysis of NAD(P)H τ_m Images

Cell sub-population assignment and mapping

Previous studies have shown that NAD(P)H τ_m can predict drug sensitivity in FaDu tumors and organoids, where low NAD(P)H τ_m indicates response to treatment and high NAD(P)H τ_m indicates

resistance[30, 36]. Therefore, the single variable analysis here focuses on NAD(P)H τ_m. In the current study, NAD(P)H τ_m measurements were aggregated across all cells per condition prior to clustering. Kernel density estimation of the data distribution was first used to visualize the presence of multiple cell populations based on NAD(P)H τ_m (Figure 4.1A, black line; "ksdensity" in MATLAB)[47]. Density-based clustering methods were then used to detect multiple cell populations within images ("densityClust" in MATLAB)[48]. Cell clusters were determined from single-cell NAD(P)H τ_m measurements[36]. Similarity matrices were calculated from pairwise differences between NAD(P)H τ_m values (picoseconds) across all cells within an aggregated dataset. A local density per cell and similarity threshold between cells was calculated as described in Rodriguez and Laio[48]. Cluster centers were defined as cells with a high local density and large pairwise difference from the nearest high density cell. Each cell was then assigned to a cluster matching the cluster assignment of the nearest high density cell. Color- coded frequency distribution histograms visualized the bins containing cluster centers (Figure 4.1A, green bars) and separation of populations (Figure 4.1A, red and blue bars). Clusters with lowest NAD(P)H τ_m were designated as a "responsive" cell population while clusters with highest NAD(P)H τ_m were designated as a "resistant" cell population based on previous studies relating drug response to NAD(P)H τ_m values[30, 36]. Density-based clustering analysis was validated by comparing class assignments of two lines of breast carcinoma cells to expert cell classification based on morphology [expert classification described in[35]]. Confusion matrices and classification accuracy (≥93%, Figure B.1) confirm the accuracy of density-based clustering.

Spatial proximity analysis

Proximity measures were quantified to assess the spatial distribution of cell populations within individual images. Two cells with an inter-cellular physical distance less than the average cell diameter ($d_{cell\_diameter}$) were defined as connected neighbors and given a weight of 1, while two cells with inter-cellular distances greater than $d_{cell\_diameter}$ (non-neighboring cells) were weighted as 0. Weights were calculated pairwise across all cells within an image. To incorporate population assignments from density-based clustering, weights were kept as 1 if the cell neighbor was defined as responsive or weighted as 2 if the neighbor was defined as resistant. These weights were also defined pairwise for each cell-neighbor

combination. Distance matrices were generated to assess the physical distance between neighbors with identical and dissimilar population assignments (i.e., responsive or resistant). The minimum intra-population and inter-population physical distances (i.e., intra- and inter-population proximity) were then determined for each cell, representing the distance to the nearest cell of identical and dissimilar population assignment (Figures 4.1C,D). Intra-population and inter-population distances were averaged across all cells for a given treatment for both model systems. To account for difference in scale between xenografts and organoids, xenograft distance measurements were normalized to the width of the imaging field of view, while organoid measurements were normalized to the organoid diameter. Additionally, centroids were calculated for each organoid sample ("regionprops" in MATLAB) to evaluate physical distance from each cell to the organoid center. Distance to organoid centers (i.e., organoid centricity) was independently assessed for responsive and resistant cell populations (Figure 4.1E).

4.3.5.2 Multivariate Spatial Analysis of All Metabolic Variable Images

Multivariate analyses were used to determine cellular spatial organization across all metabolic variables (redox ratio, NAD(P)H τ_m, τ_1, τ_2, α_1, and FAD τ_m, τ_1, τ_2, α_1) for improved separation between responsive and resistant cells.

Multivariate spatial autocorrelation

Spatial autocorrelation of all metabolic variables was evaluated at the global and local scale for all samples (xenografts and organoids). Moran's I (Figure 4.1F) was used to determine macroscale spatial similarity for each metabolic variable per image (ape package in R)[49]. Moran's I was defined as:

$$I = \frac{N}{W}\frac{\sum_i^{i=m}\sum_j^{j=n} w_{ij}(x_i - \bar{x})(x_j - \bar{x})}{\sum_i^{i=m}(x_i - \bar{x})^2} \quad (1),$$

where w_{ij} represents the weight (0 or 1) indicating connection (1) or no connection (0) between a pair of cells, x_i, x_j represent the metabolic variable value at a given cell location, x represents the metabolic variable average across the image, N represents the number of cells in the image, and W represents the total sum of the weight matrix ($w_{m,n}$)[14].

The range of Moran's I values extended between −1 and 1. An image containing cells surrounded by cells with similar metabolic variable values is represented by I values approaching 1, while an image with cells surrounded by cells with dissimilar metabolic variable values is represented by I values approaching −1. Images with cells that are surrounded by cells with both similar and dissimilar metabolic variable values (i.e., random organization) is represented by I values near 0. All spatial autocorrelation analysis was implemented in R (ape, ade4 packages in R)[49, 50].

Local indicators of spatial association (LISA) were used to visualize the similarity of metabolic variables within local cell neighborhoods as a function of model system (xenograft or organoid), treatment condition, and drug response (responsive or resistant)[51]. For each metabolic variable, individual cell measurements (Figure 4.1F, x-axis) were correlated with the measurement average of its "neighbors" (cells within one cell diameter) (Figure 4.1F, y-axis). A cell was defined as "high" or "low" if the metabolic variable value for the cell was above or below the mean across all cells within an image, respectively (Figure 4.1F, vertical line). Similarly, a neighborhood (defined as all the neighbors of a given cell) was defined as "high" or "low" if the mean metabolic variable for the neighborhood was above or below the mean across all neighborhoods within an image, respectively (Figure 4.1F, horizontal line)[51]. Individual cells and their neighbors with identical definitions (high/low) for a given metabolic variable were designated as homogeneous cell neighborhoods (Figure 4.1F, upper right and lower left quadrants). High prevalence of homogeneous cell neighborhoods indicated metabolic activity was largely dependent on spatial organization of cells.

Spatial principal components analysis

Spatial principal components analysis (spatial PCA) was applied by modifying standard principal components analysis to account for spatial structure based on Moran's I statistics (adespatial package, R)[34, 35]. All metabolic variables and spatial parameters collectively were referred to as "variables." Lag matrices were created from the product of spatial weights matrices ($w_{m,n}$, Equation 1) and corresponding variable matrices. Covariance between the variable matrix and lagged variable matrix was then assessed to define the principal component axes. The spatial principal component loadings were determined, representing each

variable's contribution to a linear combination maximizing both the variance and Moran's I across the data. Loading vectors were plotted to observe the magnitude and direction of each variable projected onto the spatial principal component axes (Figure 4.1G, red arrows)[52]. Principal component scores per image were determined by averaging linear combinations of the product of each variable and the corresponding component loadings across all cells (Figure 4.1G, black dots). Similarly, lagged scores were determined by averaged linear combinations of the lag matrix weighted by the spatial principal component loadings (Figure 4.1G, arrowheads). Vectors connecting principal component scores and lagged scores demonstrated the average difference in measurements between cells and their neighbors for a given condition.

Z-score standardization

The magnitude of differences between xenografts and organoids was assessed by compiling variables (metabolic variables and spatial parameters) across all experimental groups to compare Z-scores across models. Z-score transformation for all variables per image was performed by subtracting the variable average and dividing by the variable standard deviation of the corresponding control or treated organoid condition (53). Z-score heatmaps were generated across all treatment conditions and model systems to demonstrate differences between models (gplots package, R) (54).

4.3.6 Statistical Analysis

Student's t-tests and Tukey's multiple comparison statistical tests for non-parametric, unpaired comparisons were performed to assess differences across organoid and xenograft treatment conditions[53]. Error bars indicate the mean ± standard deviation. Measurements with an alpha value <0.5 considered statistically significant. Cohen's d values were also computed to determine effect size[53]. Local constant non-parametric regression was used to assess significant relationships between treatment condition and Moran's I for each metabolic variable[55, 56]. Xenograft or organoid treatment condition and corresponding standard error of Moran's I values served as explanatory variables evaluated for effects on the dependent variable, Moran's I.

4.4 Results

4.4.1 Spatial Clustering Based on NAD(P)H τ_m

To distinguish spatial differences in heterogeneous cell populations with respect to treatment, we first implemented spatial clustering based on a single metabolic variable, specifically NAD(P)H τ_m. This was assessed on a previously published dataset of images from control and cetuximab-, cisplatin-, and combination-treated FaDu xenografts and organoids after 13 days and 24 hours, respectively. Published studies of this dataset include standard measurements of organoid and *in vivo* treatment response, which are consistent with studies showing agreement between early treatment response in organoids and long-term tumor volume measurements[33,34,36]. NAD(P)H τ_m was chosen for this analysis as decreases in NAD(P)H τ_m with treatment *in vivo* and in organoids correlate with later decreases in FaDu tumor volume[30]. Cells with high NAD(P)H τ_m were treatment resistant, whereas cells with low NAD(P)H τ_m were responsive to treatment in these previous studies. Later analysis (Figures 4.4–4.6) defined multivariate spatial heterogeneity across all 9 metabolic variables.

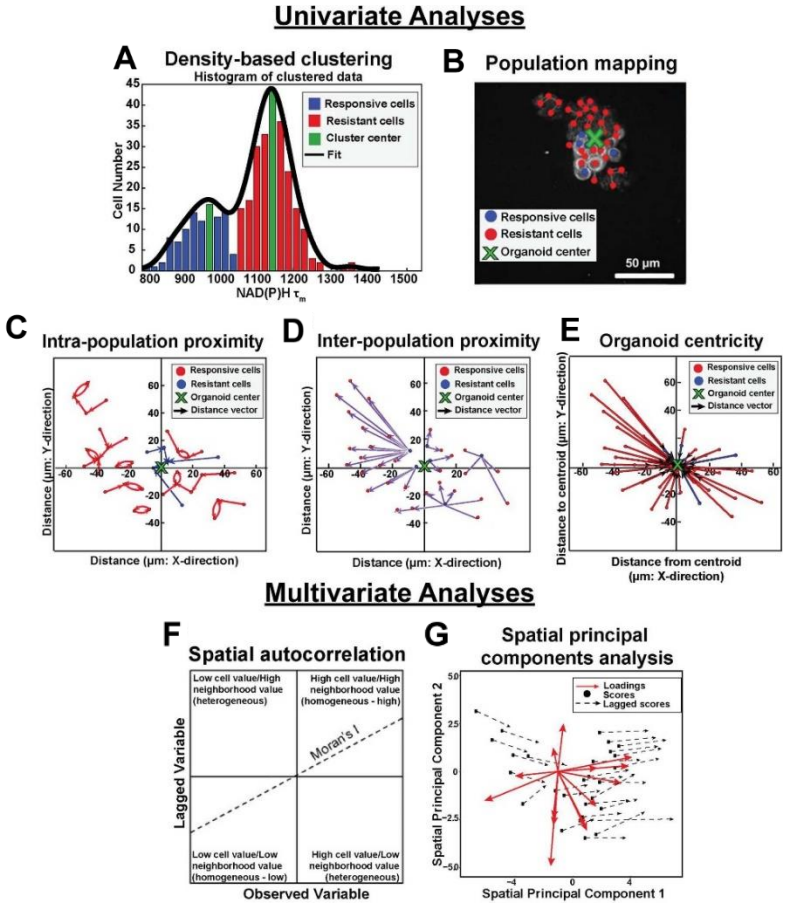

Figure 4.1. Population density analysis and spatial statistical analysis quantify spatial heterogeneity of cell metabolism. Single variable analyses using NADH τ_m data is outlined in (A–E). (A) Frequency histograms of single-cell NAD(P)H τ_m values (blue, green, red bars) are fit with kernel density fitting (black line) to represent the data distribution. Density-based clustering analysis of NAD(P)H τ_m identifies sub-populations based on cluster centers (green bins). Cells are assigned to the nearest cluster with higher local density (responsive cluster, blue bins; resistant cluster, red bins). (B) Population spatial maps of NAD(P)H τ_m-defined clusters include markers of responsive cells (blue dots), resistant cells (red dots), and organoid centroid (green x) on top of the original NAD(P)H intensity image (gray). (C) Intra-population proximity is defined as the distance between cells within a population (responsive or resistant), represented by the average length of the blue (responsive) or red (resistant) arrows in the plot. (D) Inter-population proximity is defined as the distances between cells belonging to separate populations (responsive or resistant), represented by the average length of the purple arrows in the plot for the responsive (blue) cells. (E) Organoid centricity is defined as the distance from the organoid center to each cell within a class (responsive or resistant), represented by the average length of the blue (responsive) or red (resistant) arrows in the plot. Multivariate analyses performed across all metabolic variables is described in (F,G). (F) Multivariate spatial autocorrelation assesses the similarity of a local cluster by plotting each metabolic variable for each cell (observed variable) against the average of its neighboring cells (lagged variable). The slope of the data represents the Moran's I, a global measure of spatial autocorrelation. (G) Multivariate spatial principal components analysis illustrates variation between xenografts and organoids as a function of treatment group and cell population (responsive or resistant). Loadings vectors represent the contribution of each metabolic or spatial variable to each spatial principal component (x- and y- axes). Scores for each image are calculated from a linear combination of each variable weighted by their loadings. Lagged scores correspond to the combination of weighted variables for neighbors within an image. Vector lengths represent the average magnitude of difference between cell scores and neighbor (lagged) scores.

Population distributions were used to visualize the presence of multiple cell populations with either high (resistant) or low (responsive) NAD(P)H τ_m in response to treatment (Figure 4.2). Sub-population analysis also demonstrated the extent of heterogeneity across models and treatment groups (Figures 4.2A,B). For example, multiple populations are only present in cetuximab-treated organoids but are present in both cetuximab- and cisplatin-treated xenografts, suggesting xenografts may exhibit increased heterogeneity in response to single agent treatment (Figures 4.2A,B). Density-based clustering was performed to classify treatment response on a single-cell level. Density-based classification using NAD(P)H τ_m was validated with high accuracy (≥93%; Figure B.1) compared to expert classification in 2D cultures of cell lines. Following validation, this method was used to classify responsive and resistant cells within xenografts and organoids. Population assignments for each cell were mapped back to the images to display the spatial organization of responsive and resistant populations (Figures 4.2C,D). Population maps qualitatively demonstrate low dispersion of cell populations and their macroscale organization. Overall, visualization of cell organization revealed spatial clustering patterns of resistant and responsive cell populations, which are unique to specific treatment and microenvironmental conditions.

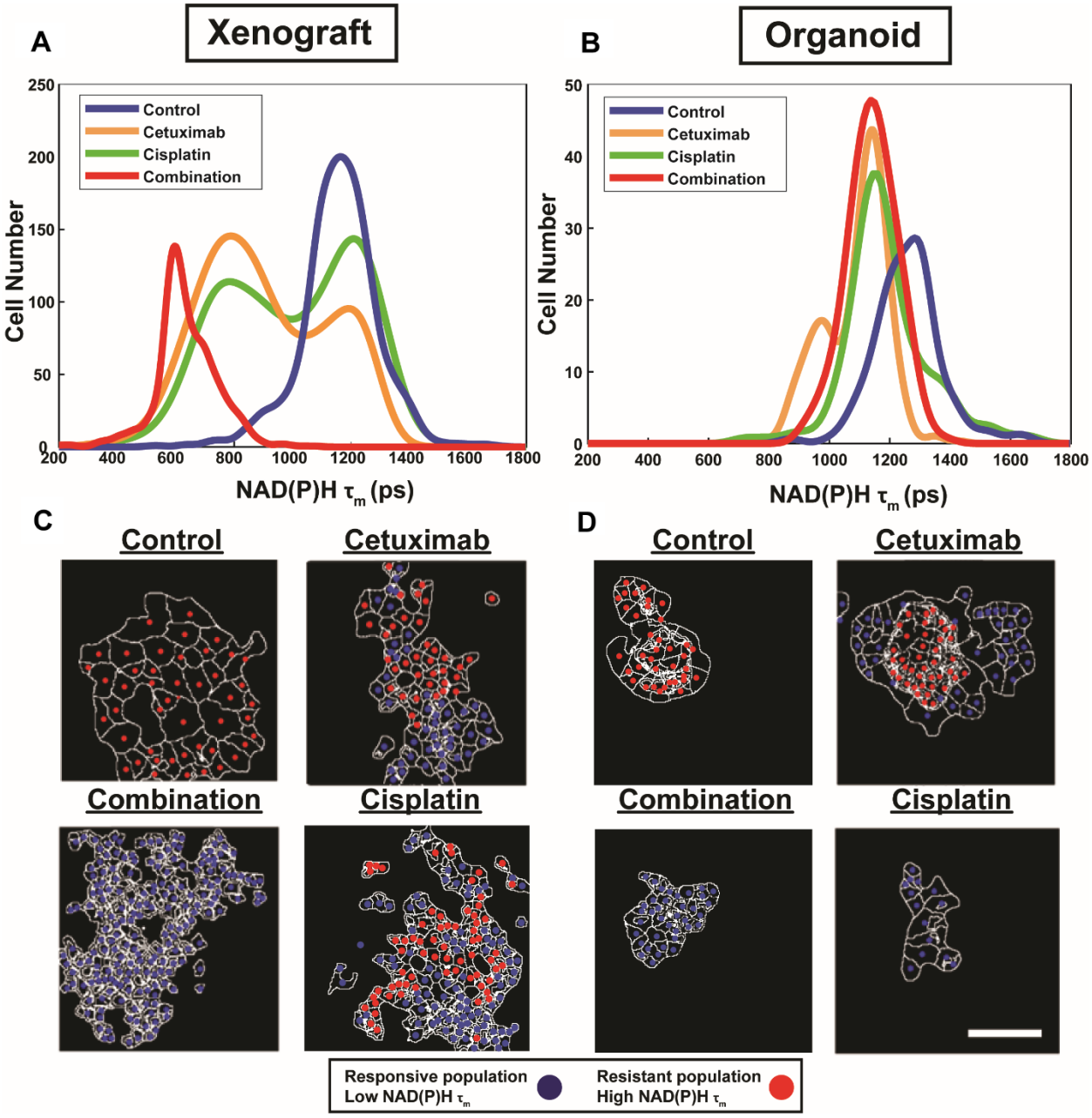

Figure 4.2. Sub-population distributions and population mapping visualize treatment-dependent spatial heterogeneity within FaDu xenografts and organoids. Population density modeling of single cell measurements of NAD(P)H τ_m in FaDu (A) xenografts and (B) organoids reveal heterogeneous cell populations within control, cetuximab-treated, cisplatin-treated, or cetuximab and cisplatin-treated (combination) groups. Representative population maps of control and treated (C) xenografts and (D) organoids demonstrate spatial organization of cell populations with differing treatment response. Individual cells are color-coded based on the population assignment determined from density-based clustering analysis. Responsive populations, corresponding to low NAD(P)H τ_m, are coded red, and resistant populations, corresponding to high NAD(P)H τ_m, are coded blue. Cell outlines are in white. Scale bar = 50 µm.

Next, quantitative metrics were developed to directly compare the spatial distributions of responsive and resistant cell populations that were defined by NAD(P)H τ_m and evaluated on control and drug-treated FaDu xenograft and organoid images (Figure 4.3). Clustering percentages informed on mixing between responsive and resistant cells, providing an objective comparison of cell dispersion across treatment conditions and model systems (Figures 4.3A,B). For example, xenografts 13 days post-treatment displayed considerable segregation between responsive and resistant cells, with >90% of cell neighbors belonging to the same population in conditions with both cell classes (cetuximab and cisplatin groups; Figure 4.3A), while 24 hours treated organoids yielded lower clustering (~80%) of responsive and resistant cell populations (cetuximab group only, Figure 4.3B).

Intra-population proximity measurements demonstrated density of cell packing within each population (Figures 4.3C,D). Highly compact cell organization was represented by low intra- population distances, demonstrated by the single, responsive cell population in combination-treated xenografts (Figure 4.3C, $p < 0.0001$). Conversely, high intra-population distances illustrated sparse cell organization, reflected through increased distances in cisplatin-treated organoid populations compared to control, cetuximab, and combination populations (Figure 4.3D, $p < 0.0001$). Responsive populations in cetuximab-treated xenografts formed denser clusters than resistant populations ($p < 0.05$), while no significant differences were observed between responsive and resistant cells with cisplatin treatment (Figure 4.3C). However, cisplatin-resistant cell populations had more compact cell organization than resistant cells in control xenografts ($p < 0.001$). Additionally, cisplatin treatment resulted in closer proximity within resistant xenograft populations than cetuximab treatment (Figure 4.3C, $p < 0.001$). Intra-population proximity measurements also provided comparisons of both density and uniformity of population clusters, most distinct between cetuximab and cisplatin organoids (Figure 4.3D, $p < 0.05$). Spatial organization of cell sub-populations appeared to be independent of sample size, as significant differences in organoid diameter measurements were only observed between control and cetuximab-treated organoids despite unique spatial organization across all groups (Figure B.2). Inter-population distances quantified localization of cell

populations relative to each other, comparable across treatment groups with multiple cell populations (Figure 4.3E). Inter-population distances were not significantly different between xenograft and organoid cells treated with cetuximab, suggesting that cell populations organize similarly in cetuximab-treated organoids and xenografts (Figure 4.3E). However, cisplatin-treated xenografts had decreased inter-population distances compared to cetuximab-treated xenografts (Figure 4.3E, $p < 0.001$).

Additionally, organoid centricity measurements provided assessment of cell organization relative to central and peripheral organoid regions (Figure 4.3F). This served as a complementary measure of cell packing in organoids with only one cell population (control, cisplatin, and combination groups), indicating similar packing across these conditions (Figure 4.3F, $p > 0.05$). Furthermore, organoid centricity measurements showed resistant populations within cetuximab-treated organoids aggregated closer to organoid centers than responsive cells (Figure 4.3F, $p < 0.0001$). Responsive populations in cetuximab-treated organoids localized further from the organoid center compared to responsive populations in cisplatin and combination organoids, demonstrating a change in distribution of responsive cells when multiple sub-populations are present (Figure 4.3F, $p < 0.0001$). Heatmaps comparing spatial parameters between resistant and responsive populations across treatment conditions demonstrate direction of change, significance, and effect size (Figure B.3).

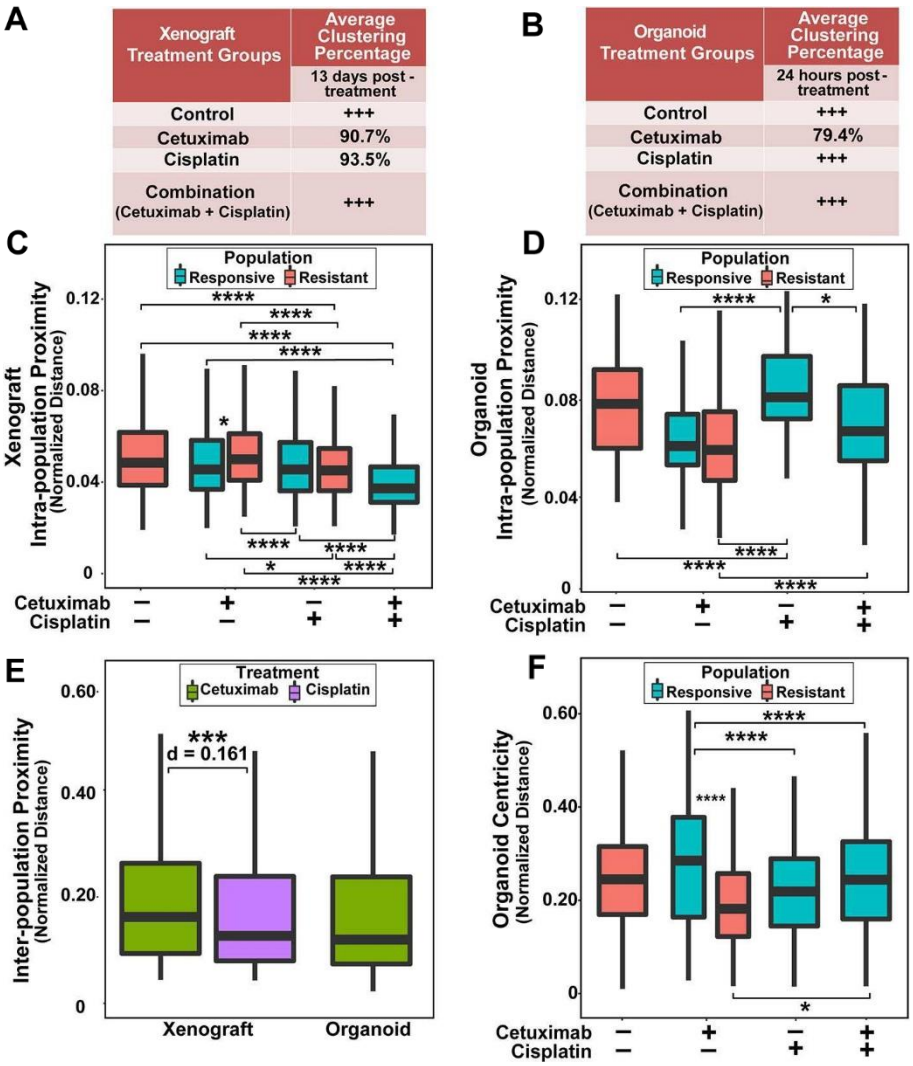

Figure 4.3. Spatial clustering and proximity based on NAD(P)H τ_m for responsive and resistant cell populations. (A) Clustering percentage in xenografts after 13 days of treatment. Control and combination-treated xenografts have only one population of cells each, indicated by +++. (B) Clustering percentage in organoids after 24 hours of treatment. Only cetuximab treatment yields multiple cell populations in organoids. (C) Average distance between cells within a single population (intra-population proximity) in xenografts. (D) Intra-population proximity in organoids. (E) Average distance between responsive and resistant cells (inter-population proximity) in xenografts and organoids for treatments that have 2 populations. (F) Average distance to organoid centers (organoid centricity). (*, ***, ****$p < 0.05$, 0.001, 0.0001; Tukey-HSD test).

4.4.2 Spatial Clustering Based on Multivariate Analysis of All 9 Metabolic Variables

Distinct clustering was demonstrated for responsive and resistant cell populations defined by a single variable, NAD(P)H τ_m (Figure 4.3). However, multivariate analysis was used to determine spatial patterns of the 8 other metabolic variables (redox ratio, NAD(P)H τ_1, τ_2, α_1, and FAD τ_m, τ_1, τ_2, α_1) in attempt

to improve separation between responsive and resistant tumor cell populations. Multivariate measures of spatial autocorrelation for all metabolic variables were quantified to comprehensively assess metabolic relationships between single cells and their surrounding neighbors. Macroscale clustering for each metabolic variable was determined by calculating global Moran's I per metabolic variable for control and treated FaDu xenograft and organoid images.

Moran's I was first calculated for each metabolic variable across all treatment conditions, then non-parametric regression was performed to determine which metabolic variables yielded Moran's I values with significant dependence on treatment condition (Tables 4.1, 4.2). Regression analysis identified NAD(P)H and FAD τ_2 as significant variables for FaDu xenografts and redox ratio, NAD(P)H and FAD α_1 for FaDu organoids. Similarity in clustering patterns within treatment groups was represented by low variability in Moran's I, observed for all metabolic variables across all xenografts per treatment group (Figures 4.4A,B, Figure B.4). Conversely, organoids demonstrated greater variability of Moran's I within treatment groups (Figures 4.5A–C, Figure B.7). Positive spatial autocorrelation indicated increased cluster formation, displayed in virtually all xenograft treatment groups across all metabolic variables (Figures 4.4A,B, Figure B.4). Overall, combination treatment demonstrated the highest Moran's I values for τ_2 measurements, while control xenografts were characterized by low Moran's I (Figures 4.4A,B). Random organization of metabolic activity was illustrated by Moran's I values near zero, reflected in redox ratio, NAD(P)H α_1 and FAD α_1 of cisplatin-treated organoids (Figures 4.5A–C). Conversely, cetuximab treatment resulted in the greatest Moran's I of these variables, indicating clusters of homogenous metabolic activity within cetuximab-treated organoids (Figures 4.5A–C). Furthermore, cisplatin treatment consistently yielded Moran's I near zero across all metabolic variables, while other organoid treatment conditions displayed varied response (Figure B.7).

Table 4.1. P-values from non-parametric regression between treatment condition and Moran's I in xenografts

Variable	*P*-value	Variable	*P*-value
Redox Ratio	0.11	FAD τ_m	0.383
NAD(P)H τ_m	0.323	FAD τ_1	0.707
NAD(P)H τ_1	0.183	**FAD τ_2**	**0.015**
NAD(P)H τ_2	**0.043**	FAD α_1	0.378
NAD(P)H α_1	0.246	FAD Intensity	0.155
NAD(P)H Intensity	0.178		

Bold values represents $p < 0.05$.

Table 4.2. P-values from non-parametric regression between treatment condition and Moran's I in organoids

Variable	*P*-value	Variable	*P*-value
Redox Ratio	**0.005**	FAD τ_m	0.331
NAD(P)H τ_m	0.398	FAD τ_1	0.248
NAD(P)H τ_1	0.301	FAD τ_2	0.494
NAD(P)H τ_2	0.627	**FAD α_1**	**0.005**
NAD(P)H α_1	**0.008**	FAD Intensity	0.175
NAD(P)H Intensity	0.266		

Bold values represents $p < 0.05$.

LISA provided complementary information to Moran's I by describing the relationship between single cells and their local neighborhood (description in Figure 4.1F). Metabolic variables per cell (observed variable) were directly compared with the average of surrounding cells (lagged variable). Cell clusters within xenografts predominantly had τ_2 values that were homogeneously high (control group) or homogeneously low (combination group), represented by cells within the upper right and lower left quadrants, respectively (Figures 4.4C,D). Additionally, cisplatin- and combination-treated organoids were both predominantly composed of low redox ratio and FAD α_1 clusters (Figures 4.5D,F). Higher frequency of cells in the upper left and lower right LISA quadrants demonstrated greater heterogeneity in metabolic

variables within cell clusters, observed for τ_2 measurements in cisplatin- and cetuximab-treated xenografts and redox and FAD α_1 measurements in cetuximab-treated organoids (Figures 4.4C,D, 4.5D, F). NAD(P)H α_1 clusters similarly exhibit substantial heterogeneity across control and treated organoids (Figure 4.5E). Metabolic variables not significantly dependent on treatment yielded variable clustering in xenografts and organoids, with some treatment groups primarily restricted to one quadrant (Figures B.5, B.8).

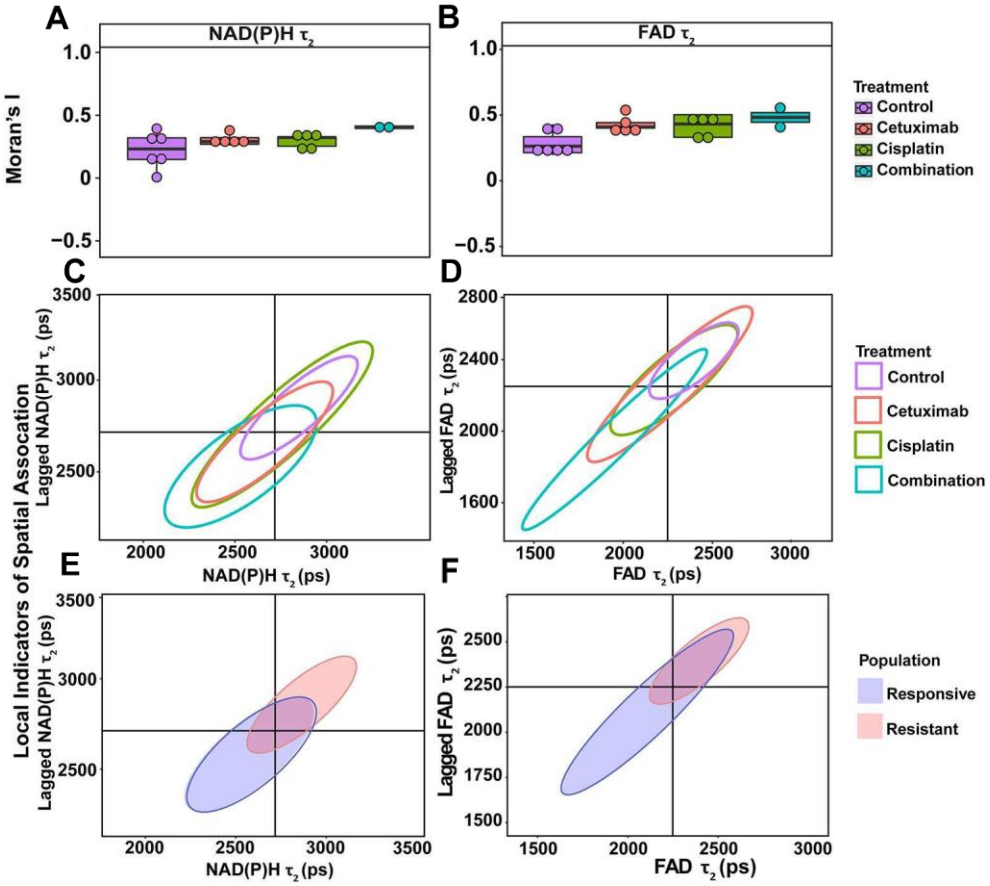

Figure 4.4. Spatial clustering patterns of metabolic variables in FaDu xenografts. Moran's I based on (A) NAD(P)H τ_2 and (B) FAD τ_2 measurements is plotted across control and treated xenografts. (C–F) Ellipses represent the distribution of cell clusters, with cells falling in the upper right (homogeneously high value clusters) and lower left quadrants (homogeneously low value clusters). Clustering is plotted for each treatment group for (C) NAD(P)H τ_2 and (D) FAD τ_2. Clustering is similarly plotted for responsive and resistant cells for (E) NAD(P)H τ_2 and (F) FAD τ_2.

LISA were also used to assess distinct clustering of metabolic variables based on treatment response. In xenografts, resistant populations form clusters of high NAD(P)H and FAD τ_2 (Figures 4.4E,F). In contrast, responsive populations predominantly organize into clusters with low τ_2 (Figures 4.4E,F). Responsive populations are also characterized by clusters of lower NAD(P)H and FAD τ_m and τ_2, and higher NAD(P)H and FAD α_1 compared with resistant cells (Figure B.6). Responsive and resistant cells in organoids also had distinct clustering patterns (Figures 4.5G–I). Responsive cells in organoids were characterized by low redox ratio clusters (Figure 4.5G). Resistant cells conversely had clusters of higher NAD(P)H and FAD α_1 compared to responsive cells (Figures 4.5H,I). Responsive and resistant populations demonstrated variable clustering across other metabolic variables (Figure B.9).

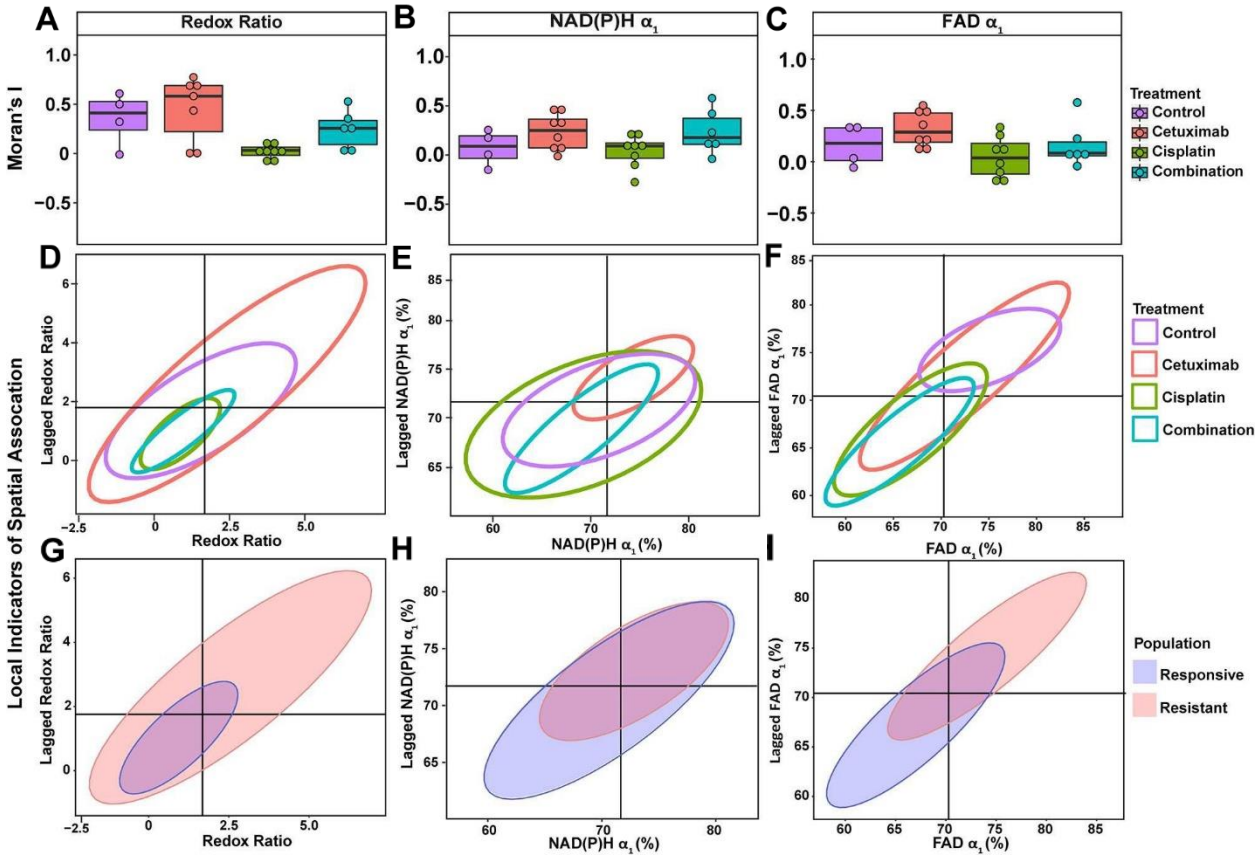

Figure 4.5. Spatial clustering patterns of metabolic parameters in FaDu organoids. Moran's I based on (A) redox ratio, (B) NAD(P)H α_1, and (C) FAD α_1 measurements for control and treated organoids. (D–F) Ellipses represent the distribution of cell clusters, with cells falling in the upper right (homogeneously high value clusters) and lower left quadrants (homogeneously low value clusters). Clustering is plotted for each treatment group for (D) redox ratio, (E) NAD(P)H α_1, and (F) FAD α_1. Cluster patterns of responsive and resistant cells are plotted for (G) redox ratio, (H) NAD(P)H α_1, and (I) FAD α_1.

4.4.3. Metabolic and Spatial Variability in Xenograft and Organoid Models

Spatial principal components analysis (spatial PCA) was used to relate multivariate measurements of cell metabolism with spatial trends across models and treatment conditions (Figure 4.6A)[57]. Briefly, multivariate metabolic and spatial data was weighted by a binary matrix indicating neighbors for each cell (i.e., cell neighborhood) prior to standard calculation of principal components. FAD τ_1, τ_2, τ_m, and intra-population distances had the highest positive loadings along spatial principal component 1, which reflects their dominant contribution to overall variability within organoids and xenografts (Figure 4.6A). Both NAD(P)H and FAD α_1 had the largest negative loadings along spatial principal component 1, which also reflects their dominant, yet opposing contribution to overall variability within organoids and xenografts. NAD(P)H τ_1, τ_2, τ_m, all intensity-based measurements, and two spatial metrics (clustering percentage, inter-population proximity) had stronger projection along the second principal axis. Variable vectors with similar directionality and magnitude are correlated. As expected, NAD(P)H τ_1, τ_2, τ_m and separately, FAD τ_1, τ_2, τ_m exhibited strong positive correlation ($\tau_m = \alpha_1\tau_1 + \alpha_2\tau_2$). The redox ratio [defined as NAD(P)H/FAD intensity] was positively correlated with NAD(P)H intensity, but negatively correlated with FAD intensity. Inter-population proximity was closely related to redox ratio and NAD(P)H intensity, while intra-population proximity was closely related to FAD τ_1 but not highly correlated with the other two spatial metrics (clustering percentage, inter-population proximity). In contrast, clustering percentage was inversely correlated with inter-population proximity.

Mean spatial PCA scores were then plotted for both responsive and resistant cells within each control and treatment group for both xenografts and organoids to observe similarities across models (Figure 4.6B). Each point represents the mean spatial PCA score for an organoid (filled) or xenograft (hollow), and points were plotted on the same axes as Figure 4.6A. The location of each dot can be correlated with metabolic variables on the same axes in Figure 4.6A. Xenografts were generally correlated with variables in the upper left quadrant of Figure 4.6A [e.g., NAD(P)H α_1, clustering percentage] compared to organoids, which correlate with NAD(P)H and FAD τ_1, τ_2, and τ_m (blue vs. red ellipse, Figure 4.6B).

Vectors extending from points on spatial PCA plots described the response of cell neighborhoods within the organoid or xenograft (arrows, Figure 4.6B). The location of the arrowhead represents differences between the average cell response and the average cell neighborhood response. Of note, fewer xenografts were imaged per treatment group, and thus clustering and correlation of cell neighborhoods were less defined compared to the more high-throughput organoid analysis. Mean spatial PCA scores of both cells and their neighborhoods in responsive organoid populations are predominantly correlated within the combination treatment group. Conversely, resistant cells within cetuximab and control organoids are not correlated. Spatial PCA maps at the cellular level across treatments and models (organoids and xenografts) also help to visualize the organization of cell neighborhoods (Figure B.10).

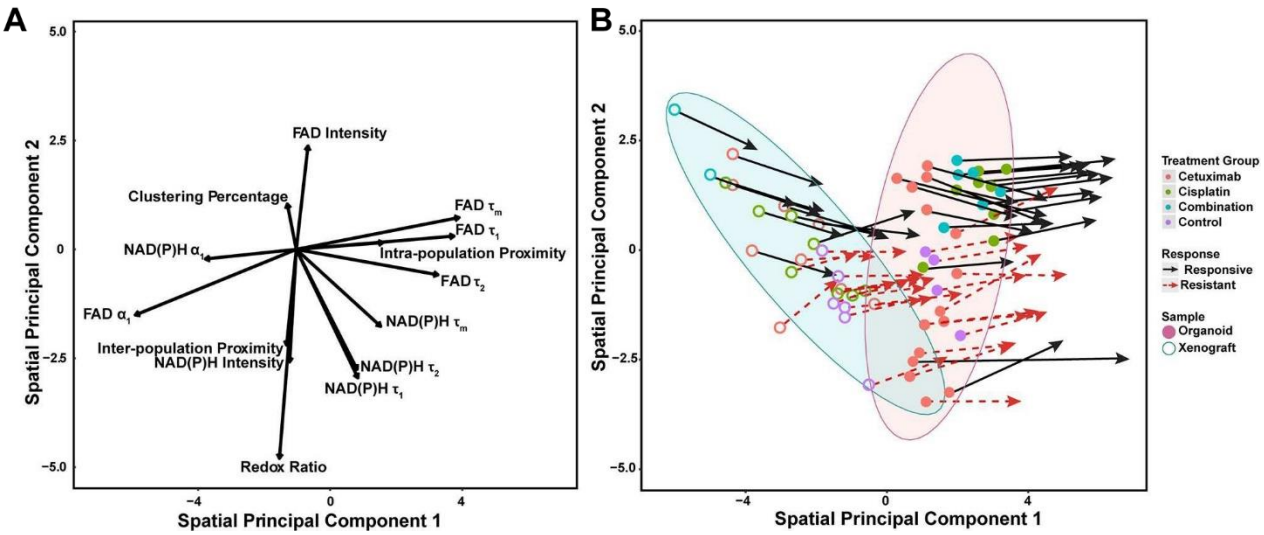

Figure 4.6. Multivariate analyses of metabolic activity and spatial organization in xenografts and organoids. (A) Loading vectors for all treatment conditions across both organoids and xenografts. (B) The same spatial PCA plot as (A), with treatment groups and model systems plotted to observe spatial clustering patterns. Points correspond to the spatial PCA score for a single organoid (filled circle) or xenograft (open circle). Arrows represent differences between average spatial PCA scores of an organoid or xenograft and the average spatial PCA score of their cell neighborhood.

Heatmaps of Z-scores for metabolic variables and spatial parameters were generated for further comparison between treatment groups and model systems (Figure 4.7). Z-scores were calculated relative to the mean and standard deviation of the corresponding organoid condition to visualize differences between models for each treatment group. Xenografts consistently exhibited higher FAD α_1 and lower FAD τ_m, τ_1,

and τ_2 compared with organoids, regardless of treatment condition. Intensity measurements were generally increased in control xenografts compared to control organoids. Additionally, control xenografts exhibited shorter intra-population distances within resistant populations. Organoids and xenografts showed substantial differences in response to combination treatment. Specifically, combination-treated xenografts yielded higher α_1 and lower τ_m, τ_1, and τ_2 for both NAD(P)H and FAD. This trend was also observed between models in response to cetuximab treatment. Spatial measurements displayed contrast between cisplatin-treated xenografts and organoids due to the presence of two populations in xenografts, compared to a single population in organoids. Cisplatin treatment also caused increased redox ratio and NAD(P)H α_1 in xenografts compared to organoids. Heatmaps of Z-scores within xenograft and organoid conditions are shown in Figure B.11.

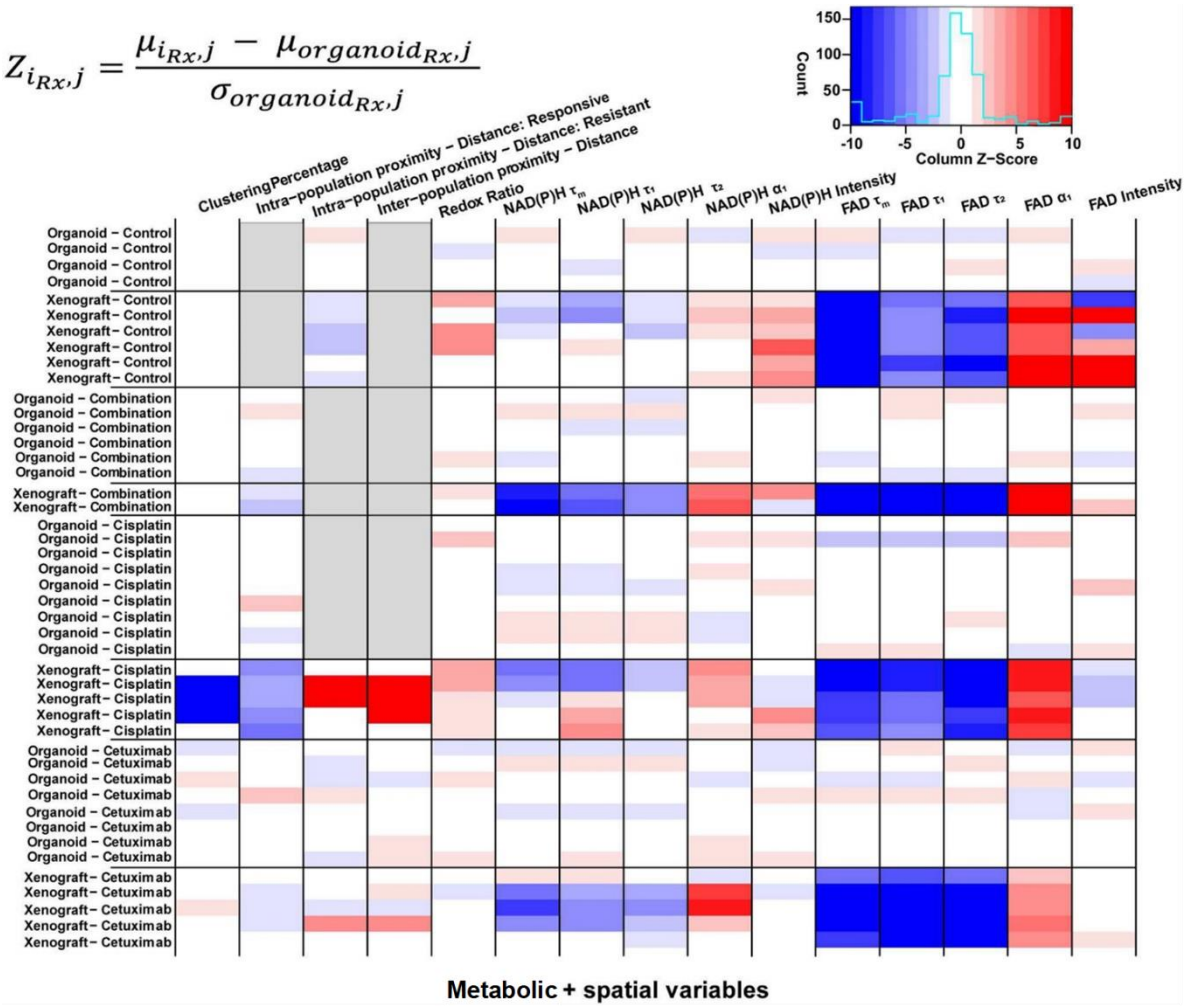

Figure 4.7. Z-scores of metabolic and spatial variables in control and treated xenografts and organoids. Heatmap of Z-scores across treatment groups and model systems (organoid and xenograft). Each Z-score is calculated for each sample of a given treatment group (i_{Rx}) and variable (j) as the difference between the mean variable per sample and the mean variable across all organoids of the corresponding treatment group ($organoid_{Rx}$) divided by the standard deviation of the organoid treatment group. Z-score differences within a single treatment group represent variability across samples. Gray boxes indicate samples without a value for a given variable, specific to xenograft and organoid treatment groups with a single population.

4.5 Discussion

Spatial heterogeneity within tumors contributes to poor therapeutic response and tumor recurrence. However, to characterize intra-tumor heterogeneity at the cellular level and its effect on disease progression have been limited to destructive methods that require tumor dissociation, and thus removal from the host. Here, we have combined metabolic autofluorescence imaging with spatial statistical methods to quantify organization of multiple cell sub-populations within intact, heterogeneous samples[35, 47]. Previous studies have established that metabolic autofluorescence imaging can resolve phenotypic differences within 2D and 3D *in vitro* tumor models, and *in vivo* mouse tumors[23, 24, 27, 30, 33, 36, 58].

However, these previous studies did not thoroughly assess spatial distributions of metabolic cell sub-populations, which is important for monitoring cell-cell interactions in tumors[59]. We have developed novel analytical methods to quantify cell-level heterogeneity in tumor models by combined metabolic autofluorescence imaging and density-based clustering (Figure 4.1A)[29, 30, 43–45]. Density-based clustering methods promote robust identification of distinct, rare populations by exclusively considering distances between data points, circumventing assumptions about the data distribution typically necessary for clustering[48]. Spatial statistical analysis of data clustered by a single variable [NAD(P)H τ_m, previously shown to separate drug-responsive and -resistant cells[12, 26]] provides unique metrics for the organization of heterogeneous cell populations within samples (Figures 4.1B–E). Finally, multivariate analyses of spatial organization across all metabolic variables enables greater separation between responsive and resistant cells to compare spatial trends within a sample (Figures 4.1F,G). In the future, metabolic autofluorescence imaging and quantitative metrics of cellular connectivity could guide the development of novel therapies that target drug-resistant tumor microenvironments for improved therapeutic outcomes.

This is the first study to combine label-free, live cell imaging, and spatial statistical techniques to assess treatment-dependent changes in tumor cell function. Previous studies have used microscopic spatial analyses to determine the organization of phenotypically distinct cell populations within fixed, stained tumor tissue sections[16–20]. For example, distributions of tumor and stromal cells at the time of biopsy or surgery have been correlated with clinical outcome, but these studies disregard both heterogeneity within cell types and treatment-specific cell organization[17,60]. Otherwise, previous microscopic work has focused on spatial patterns of genetic expression rather than functional (e.g., metabolic) heterogeneity[61–64]. Macroscopic heterogeneity in metabolite concentration and uptake *in vivo* has been previously investigated by PET and MRI, but these techniques lack the spatial resolution to detect cell-level heterogeneity[62,65]. Notably, endogenous metabolic fluorescence imaging has previously evaluated macroscale spatial distributions of the redox ratio *in vivo* and *in vitro*[63]. These studies observed higher redox ratio and NAD(P)H intensity tumor regions, but low FAD regions localized at the periphery of untreated mouse breast carcinoma xenografts. Interestingly, we observed the same trend in centrally-located resistant cell populations across organoids (Figures 4.3F, 4.5G, Figure B.9). Unlike these previous studies, our current study quantified cell-level spatial distributions of distinct metabolic sub-populations (Figure 4.3) and the clustering patterns of these metabolic sub-populations (Figures 4.4, 4.5), which varied with respect to treatment and drug response in live, intact, unstained samples.

The spatial distribution of metabolically-distinct cell populations was quantified for samples with distinct treatment and drug response because cell metabolism is both a therapeutic target and a route of tumor evasion[66]. Responsive cells were previously shown to exhibit lower NAD(P)H τ_m with cetuximab or cisplatin treatment compared to resistant cells, which often emerge from the selective pressures of cancer treatment[30, 36, 67]. Clustering percentage (Figures 4.3A,B), intra-population distances (Figures 4.3C,D), and inter-population distances (Figure 4.3E) represented the relative organization of NAD(P)H τ_m-defined populations in xenografts and organoids. These results showed that cells with similar treatment response (i.e., responsive/resistant) pack together closely, and that cells formed single, uniform clusters of responsive

or resistant cells, as opposed to several small, dispersed clusters. Spatial analysis of all metabolic variables indicated high intercellular dissimilarity and more random cluster patterns in organoids compared to xenografts (Figures 4.4, 4.5, B.5–B.8), in contrast to clustering based on NAD(P)H τ_m alone (Figures 4.2D, 4.3D–F), which indicates that spatial analysis of all metabolic variables together captures different metabolic features than NAD(P)H τ_m individually. However, spatial heterogeneity was low in control and combination-treated groups compared to single-agent treatment for both xenografts and organoids (Figures 4.4C,D, 4.5D–F, B.5, B.8). Though spatial patterns were only quantified for single plane images at defined time points in this study, this analysis can be translated to data acquired over multiple sample depths and treatment time points to determine their influence on cellular spatial organization. Overall, this spatial analysis highlights substantial differences in the local metabolic landscape of combination and single agent treatments across tumor models. Notably, NAD(P)H lifetime can be modulated in response to alternative metabolic and environmental changes, highlighting the complexity associated with functional readouts of cell metabolism[32, 68, 69]. Cellular response to treatment can also modulate several subcellular metabolic processes, collectively reflected by changes in NAD(P)H lifetime[70]. Consequently, further development of this analysis to incorporate environmental and functional measurements would be valuable for resolving biological mechanisms driving spatial changes in cellular behavior. For example, proximity to vasculature could be inferred from metabolic autofluorescence images as blood vessels appear as dark, branch-like regions. Biomarkers of local environmental conditions (e.g., oxygen/pH sensors, metabolic enzyme assays) could be correlated with spatial patterns in metabolic autofluorescence data. Future work can also integrate our spatial metabolic analysis with microfluidic models of microenvironmental gradients to disentangle relationships between nutrient availability, environmental stressors, and treatment response[71]. Collectively, integration of this spatial analysis with complementary biological data could provide additional insight into mechanisms altering NAD(P)H lifetime and associated drug sensitivity, leading to more effective treatment regimens[72].

Previous studies confirm that xenografts and organoids have consistent treatment response across multiple model systems, using standard measures of response (e.g., tumor volume, cell viability)[73–77]. Published studies also show that NAD(P)H τ_m decreases with cetuximab or cisplatin treatment in both FaDu xenografts and organoids[30,36]. The current paper develops spatial analysis to quantify differences in cellular spatial organization between models and treatment conditions. In these datasets, xenografts had decreased FAD τ_m, τ_1, τ_2 and increased FAD α_1 compared to organoids, regardless of spatial distribution (Figure 4.7). This difference in FAD lifetimes averaged across all cells could be due to a number of factors, including different imaging time-points post-treatment, although organoids provide an early measure of response (1–3 days post-treatment) that agrees with later tumor volume (weeks post-treatment), which motivated the imaging time points used in this study[33,34]. Differences in FAD lifetimes could also be due to shifts in metabolic flux, enzyme binding activity, temperature, oxygenation, and/or pH *in vivo* compared to *in vitro*[74–76].

We also demonstrate that spatial analysis can capture differences in the distribution of cellular drug response between *in vivo* and *in vitro* systems. Specifically, responsive populations defined by NAD(P)H τ_m in xenografts were more densely clustered than resistant populations, while the opposite trend was observed in organoids (Figures 4.3C,D). Also, the spherical geometry of organoids maintains responsive cells on the periphery and resistant cells clustered in the core (Figure 4.3G), consistent with previous reports[78]. The observed differences in the distribution of cell metabolism between models are likely due to distinct methods of drug delivery between organoids (diffusion) and xenografts (vascular delivery). Organoids require drug diffusion from the outer to inner cell layers, which act as a physical barrier limiting penetration of both small and large molecule drugs (~100 Da−1 kDa) and cause gradations in drug dose and metabolic activity[79]. In contrast, poor vascularity and inefficient tumor microvessels in xenografts result in a complete lack of drug dosing for some cells *in vivo*[80]. This poor vascularity could contribute to segregation of cell populations with distinct metabolic activity *in vivo* (Figures 4.4A–C, B.5). Spatial patterns of cellular drug response could be correlated with drug diffusion to assess the influence of drug

accessibility on cellular metabolic distributions. Overall, these differences in drug delivery between models highlight the utility of each model for studies of drug efficacy and drug delivery. Notably, organoids are useful for high- throughput and time-course measurements of drug efficacy at early time-points using numerous drugs, whereas xenografts can model both drug delivery and treatment effects. Although drug delivery in xenografts may only partially reflect drug delivery *in vivo* human tumors, xenografts still serve as a useful first approach[81,82].

The methods developed in this study establish the combination of metabolic autofluorescence imaging and spatial statistical analysis to quantify the spatial heterogeneity of tumor cell metabolism. We have shown that cell-level spatial organization of metabolism is altered by treatment and model system. These methods could be translated to metabolic autofluorescence data acquired over an entire organoid volume or a superficial tumor volume to characterize 3D distributions of metabolism and drug response. In addition, this analytical approach could integrate complementary metrics from autofluorescence images including cell morphology, intracellular metabolic changes, and other endogenous fluorophores. Furthermore, this approach can be extended to or combined with other single cell imaging approaches probing as gene (e.g., RNA or DNA-FISH) and protein expression (e.g., immunofluorescence)[83,84]. Overall, cell-level functional imaging and quantitative analysis of spatial heterogeneity could significantly improve understanding of tumor growth and treatment resistance.

4.6 Acknowledgments

The authors would like to thank A. Shah, C. Walsh, D. Gil, P. Favreau, G. Deane for valuable discussions on study design and statistical analysis. This work was supported by the National Science Foundation Graduate Research Fellowship [DGE-1256259 to T.H.]; the National Science Foundation [CBET-1642287]; Stand Up to Cancer [SU2C-AACR-IG-08-16, SU2C-AACR-PS-18]; and the National Institutes of Health [R01 CA185747, R01 CA205101, R01 CA211082, R21 CA224280, U01 TR002383].

4.7 References

1. Marusyk A, Almendro V, Polyak K. Intra-tumour heterogeneity: a looking glass for cancer? Nat Rev Cancer. (2012) 12:323–34. doi: 10.1038/nrc3261

2. Marusyk A, Polyak K. Tumor heterogeneity: causes and consequences. Biochim Biophys Acta. (2011) 1805:1–28. doi: 10.1016/j.bbcan.2009.11.002

3. Yuan Y, Jiang YC, Sun CK, Chen QM. Role of the tumor microenvironment in tumor progression and the clinical applications. Oncol Rep. (2016) 35:2499– 515. doi: 10.3892/or.2016.4660

4. Fang Y, Eglen RM. Three-dimensional cell cultures in drug discovery and development. SLAS Discov. (2017) 22:456–72. doi: 10.1177/1087057117696795

5. Yuan Y. Spatial heterogeneity in the tumor. Cold Spring Harb Perspect Med. (2017) 6:a026583. doi: 10.1101/cshperspect.a026583

6. Anderson ARA, Weaver AM, Cummings PT, Quaranta V. Tumor morphology and phenotypic evolution driven by selective pressure from the microenvironment. Cell. (2006) 127:905–15. doi: 10.1016/j.cell.2006.09.042

7. Anselin L. Interactive Techniques and Exploratory Spatial Data Analysis. (1999). p. 253–66.

8. Nelson CJ, Jackson PTG, Obara B. Combining mathematical morphology and the Hilbert transform for fully automatic nuclei detection in fluorescence microscopy. In: International Symposium on Mathematical Morphology and Its Applications to Signal and Image Processing. Springer (2019). p. 532–43.

9. Stegmaier J, Otte JC, Kobitski A, Bartschat A, Garcia A, Nienhaus GU, et al. Fast segmentation of stained nuclei in terabyte-scale, time resolved 3D microscopy image stacks. PLoS ONE. (2014) 9:e90036. doi: 10.1371/journal.pone.0090036

10. Ljosa V, Sokolnicki KL, Carpenter AE. Annotated high-throughput microscopy image sets for validation. Nat Methods. (2012) 9:637. doi: 10.1038/nmeth.2083

11. Zaritsky A. Sharing and reusing cell image data. Mol Biol Cell. (2018) 29:1274– 80. doi: 10.1091/mbc.E17-10-0606

12. Meijering E, Carpenter AE, Peng H, Hamprecht FA, Olivo-Marin JC. Imagining the future of bioimage analysis. Nat Biotechnol. (2016) 34:1250–5. doi: 10.1038/nbt.3722

13 Sokal RR, Oden NL. Spatial autocorrelation in biology: 1. methodology. Biol J Linn Soc. (1978) 10:199–228. doi: 10.1111/j.1095-8312.1978.tb00013.x

14. Ward MD, Skrede Gleditsch K. An introduction to spatial regression models in the social sciences (2007) 87. doi: 10.4135/9781412985888

15. Heindl A, Nawaz S, Yuan Y. Mapping spatial heterogeneity in the tumor microenvironment: a new era for digital pathology. Lab Investig. (2015) 95:377–84. doi: 10.1038/labinvest.2014.155

16. Krüger JM, Wemmert C, Sternberger L, Bonnas C, Dietmann G, Gançarski P, et al. Combat or surveillance? Evaluation of the heterogeneous inflammatory breast cancer microenvironment. J Pathol. (2013) 229:569–78. doi: 10.1002/path.4150

17. Yuan Y, Failmezger H, Rueda O, Ali H, Graf S, Chin S, et al. Quantitative image analysis of cellular heterogeneity in breast tumors complements genomic profiling. Sci Transl Med. (2012) 143:157ra143. doi: 10.1126/scitranslmed.3004330

18. Setiadi AF, Ray NC, Kohrt HE, Kapelner A, Carcamo-Cavazos V, Levic EB, et al. Quantitative, architectural analysis of immune cell subsets in tumor- draining lymph nodes from breast cancer patients and healthy lymph nodes. PLoS ONE. (2010) 5:e12420. doi: 10.1371/journal.pone.0012420

19. Bindea G, Mlecnik B, Tosolini M, Kirilovsky A, Waldner M, Obenauf AC, et al. Spatiotemporal dynamics of intratumoral immune cells reveal the immune landscape in human cancer. Immunity. (2013) 39:782–95. doi: 10.1016/j.immuni.2013.10.003

20. Chang AY, Bhattacharya N, Mu J, Setiadi AF, Carcamo-Cavazos V, Lee GH, et al. Spatial organization of dendritic cells within tumor draining lymph nodes impacts clinical outcome in breast cancer patients. J Transl Med. (2013) 11:1. doi: 10.1186/1479-5876-11-242

21. Chance B, Schoener B, Oshino R, Itshak F, Nakase Y. Oxidation-reduction ratio studies of mitochondria in freeze-trapped samples. NADH and flavoprotein fluorescence signals. J Biol Chem. (1979) 254:4764–71.

22. Heikal AA. Intracellular coenzymes as natural biomarkers for metabolic activities and mitochondrial anomalies. Biomark Med. (2010) 4:241–63. doi: 10.2217/bmm.10.1

23. Walsh AJ, Cook RS, Manning HC, Hicks DJ, Lafontant A, Arteaga CL, et al. Optical metabolic imaging identifies glycolytic levels, subtypes, and early-treatment response in breast cancer. Cancer Res. (2013) 73:6164–74. doi: 10.1158/0008-5472.CAN-13-0527

24. Skala MC, Squirrell JM, Vrotsos KM, Eickhoff JC, Gendron-Fitzpatrick A, Eliceiri KW, et al. Multiphoton microscopy of endogenous fluorescence differentiates normal, precancerous, and cancerous squamous epithelial tissues. Cancer Res. (2005) 65:1180–6. doi: 10.1158/0008-5472.CAN-04-3031

25. Georgakoudi I, Quinn KP. Optical imaging using endogenous contrast to assess metabolic state. Annu Rev Biomed Eng. (2012) 14:351–67. doi: 10.1146/annurev-bioeng-071811-150108

26. Lakowicz JR, Szmacinski H, Nowaczyk K, Johnson ML. Fluorescence lifetime imaging of free and protein-bound NADH. Proc Natl Acad Sci USA. (1992) 89:1271–5. doi: 10.1073/pnas.89.4.1271

27. Quinn KP, Sridharan GV, Hayden RS, Kaplan DL, Lee K, Georgakoudi I. Quantitative metabolic imaging using endogenous fluorescence to detect stem cell differentiation. Sci Rep. (2013) 3:3432. doi: 10.1038/srep03432

28. Hou J, Wright HJ, Chan NS-K, Tran RDH, Razorenova OV, Potma EO, et al. Correlating two-photon excited fluorescence imaging of breast cancer cellular redox state with seahorse flux analysis of normalized cellular oxygen consumption. J Biomed Opt. (2016) 21:1–3. doi: 10.1117/1.JBO.21.6.060503

29. Liu Z, Pouli D, Alonzo CA, Varone A, Karaliota S, Quinn KP, et al. Mapping metabolic changes by noninvasive, multiparametric, high- resolution imaging using endogenous contrast. Sci Adv. (2018) 4:eaap9302. doi: 10.1126/sciadv.aap9302

30. Shah AT, Diggins KE, Walsh AJ, Irish JM, Skala MC. In vivo autofluorescence imaging of tumor heterogeneity in response to treatment. Neoplasia. (2015) 17:862–70. doi: 10.1016/j.neo.2015.11.006

31. Sharick JT, Favreau PF, Gillette AA, Sdao SM, Merrins MJ, Skala MC. Protein- bound NAD(P)H lifetime is sensitive to multiple fates of glucose carbon. Sci Rep. (2018) 8:5456. doi: 10.1038/s41598-018-23691-x

32. Blacker TS, Mann ZF, Gale JE, Ziegler M, Bain AJ, Szabadkai G, et al. Separating NADH and NADPH fluorescence in live cells and tissues using FLIM. Nat Commun. (2014) 5:3936. doi: 10.1038/ncomms4936

33. Walsh AJ, Cook RS, Sanders ME, Aurisicchio L, Ciliberto G, Arteaga CL, et al. Quantitative optical imaging of primary tumor organoid metabolism predicts drug response in breast cancer. Cancer Res. (2014) 74:5184–94. doi: 10.1158/0008-5472.CAN-14-0663

34. Sharick JT, Jeffery JJ, Karim MR, Walsh CM, Esbona K, Cook RS, et al. Cellular metabolic heterogeneity *in vivo* is recapitulated in tumor organoids.vNeoplasia. (2019) 21:615–26. doi: 10.1016/j.neo.2019.04.004

35. Walsh AJ, Skala MC. Optical metabolic imaging quantifies heterogeneous cell populations. Biomed Opt Express. (2015) 6:559–73. doi: 10.1364/BOE.6.000559

36. Shah AT, Heaster TM, Skala MC. Metabolic imaging of head and neck cancer organoids. PLoS ONE. (2017) 12:e0170415. doi: 10.1371/journal.pone.0170415

37. de Back W, Zerjatke T, Roeder I. Statistical and mathematical modeling of spatiotemporal dynamics of stem cells. Methods Mol Biol. (2019)2017:219–43. doi: 10.1007/978-1-4939-9574-5_17

38. Cassese A, Ellis SR, Ogrinc Potocnik N, Burgermeister E, Ebert M, Walch A, et al. Spatial autocorrelation in mass spectrometry imaging. Anal Chem. (2016) 88:5871–8. doi: 10.1021/acs.analchem.6b00672

39. Alexandrov T, Chernyavsky I, Becker M, von Eggeling F, Nikolenko S. Analysis and interpretation of imaging mass spectrometry data by clustering mass- to-charge images according to their spatial similarity. Anal Chem. (2013) 85:11189–95. doi: 10.1021/ac401420z

40. Tijink BM, Neri D, Leemans CR, Budde M, Dinkelborg LM, Stigter-van Walsum M, et al. Radioimmunotherapy of head and neck cancer xenografts using 131I-labeled antibody L19-SIP for selective targeting of tumor vasculature. J Nucl Med. (2006) 47:1127–35. doi: 10.1001/archotol.132.8.886-a

41. Skvortsova I, Skvortsov S, Raju U, Stasyk T, Riesterer O, Schottdorf E- M, et al. Epithelial-to-mesenchymal transition and c-myc expression are the determinants of cetuximab-induced enhancement of squamous cell carcinoma radioresponse. Radiother Oncol. (2010) 96:108–15. doi: 10.1016/j.radonc.2010.04.017

42. Cividalli A, Ceciarelli F, Livdi E, Altavista P, Cruciani G, Marchetti P, et al. Radiosensitization by oxaliplatin in a mouse adenocarcinoma: influence of treatment schedule. Int J Radiat Oncol Biol Phys. (2002) 52:1092–8. doi: 10.1016/S0360-3016(01)02792-4

43. Li X, Fan Z. The epidermal growth factor receptor antibody cetuximab induces autophagy in cancer cells by downregulating HIF-1α and Bcl-2 and activating the beclin 1/hVps34 complex. Cancer Res. (2010) 70:5942–52. doi: 10.1158/0008-5472.CAN-10-0157

44. Robbins KT, Varki NM, Storniolo AM, Hoffman H, Hoffman RM. Drug response of head and neck tumors in native-state histoculture. Arch Otolaryngol Neck Surg. (1991) 117:83–6. doi: 10.1001/archotol.1991.01870130089022

45. Levitt JM, Baldwin A, Papadakis A, Puri S, Xylas J, Münger K, et al. Intrinsic fluorescence and redox changes associated with apoptosis of primary human epithelial cells. J Biomed Opt. (2006) 11:64012. doi: 10.1117/1.2401149

46. Freemerman AJ, Johnson AR, Sacks GN, Milner JJ, Kirk EL, Troester MA, et al. Metabolic reprogramming of macrophages: Glucose Transporter (GLUT1)- mediated glucose metabolism drives a pro-inflammatory phenotype. J Biol Chem. (2014) 289:7884–96. doi: 10.1074/jbc.M113.522037

47. Heaster TM, Walsh AJ, Landman BA, Skala MC. Density-based clustering analyses to identify heterogeneous cellular sub-populations. In: Skala MC, Campagnola PJ, editors. Proceedings Volume 10043, Diagnosis and Treatment of Diseases in the Breast and Reproductive System. San Francisco, CA: International Society for Optics and Photonics (2017). p. 100430X.

48. Rodriguez A, Laio A. Clustering by fast search and find of desity peaks. Science. (2014) 344:1492–6. doi: 10.1126/science.1242072

49. Paradis E, Claude J, Strimmer K. APE : analyses of phylogenetics and evolution in R language. Bioinformatics. (2004) 20:289–90. doi: 10.1093/bioinformatics/btg412

50. Dray S, Dufour AB. The ade4 package: implementing the duality diagram for ecologists. J Stat Softw. (2007) 22. doi: 10.18637/jss.v022.i04

51. Anselin L. Local Indicators of Spatial Association—LISA. Geogr Anal. (1995) 27:93–115. doi: 10.1111/j.1538-4632.1995.tb00338.x

52. Dray S, Bauman D, Blanchet G, Borcard D, Clappe S, Guenard G, et al. Adespatial: Multivariate Multiscale Spatial Analysis (2018).

53. Dray S, Jombart T. Revisiting Guerry's data: introducing spatial constraints in multivariate analysis. Ann Appl Stat. (2011) 5:2278–99. doi: 10.1214/10-AOAS356

54. Wadsworth HM. Handbook of Statistical Methods for Engineers and Scientists, 2nd ed (1997).

55. Warnes G, Ingelheim B, Magnusson A. Package 'gtools' (2005).

56. Racine J, Li Q. Nonparametric estimation of regression functions with both categorical and continuous data. J Econom. (2004) 119:99–130. doi:10.1016/S0304-4076(03)00157-X

57. Racine JS, Hart J, Li Q. Testing the significance of categorical predictor variables in nonparametric regression models. Econom Rev. (2006) 25:523–44. doi: 10.1080/07474930600972590

58. Jombart T, Devillard S, Dufour AB, Pontier D. Revealing cryptic spatial patterns in genetic variability by a new multivariate method. Heredity. (2008) 101:92–103. doi: 10.1038/hdy.2008.34

59. Heaster TM, Walsh AJ, Zhao Y, Hiebert SW, Skala MC. Autofluorescence imaging identifies tumor cell-cycle status on a single-cell level. J Biophotonics. (2018) 11:e201600276. doi: 10.1002/jbio.201600276

60. Gough A, Stern AM, Maier J, Lezon T, Shun TY, Chennubhotla C, et al. Biologically Relevant Heterogeneity: Metrics and Practical Insights. SLAS Discov Adv life Sci R D. 2017 Mar;22(3):213—237.

61. Galon J, Costes A, Sanchez-Cabo F, Kirilovsky A, Mlecnik B, Lagorce-Pagès C, et al. Type, Density, and Location of Immune Cells Within Human Colorectal Tumors Predict Clinical Outcome. Science. 2006 Sep 29;313(5795):1960 LP – 1964.

62. Pan W, Lin J, Le CT. Model-based cluster analysis of microarray gene- expression data. Genome Biol. (2002) 3:RESEARCH0009.

63. McQuerry JA, Chang JT, Bowtell DDL, Cohen A, Bild AH. Mechanisms and clinical implications of tumor heterogeneity and convergence on recurrent phenotypes. J Mol Med . 2017;1167–78.

64. Sengupta D, Pratx G. Imaging metabolic heterogeneity in cancer. Mol Can. 2016;2(1):1-9.

65. Xu HN, Zheng G, Tchou J, Nioka S, Li LZ. Characterizing the metabolic heterogeneity in human breast cancer xenografts by 3D high resolution fluorescence imaging. Springerplus. 2013;2(1):1–9.

66. Almendro V, Cheng YK, Randles A, Itzkovitz S, Marusyk A, Ametller E, et al. Inference of tumor evolution during chemotherapy by computational modeling and in situ analysis of genetic and phenotypic cellular diversity. Cell Rep. 2014;6(3):514–27.

67. Mu W, Gillies RJ, Aerts HJWL, Napel S, Jardim-Perassi B V. Quantitative imaging of cancer in the postgenomic era: Radio(geno)mics, deep learning, and habitats. Cancer. 2018;124(24):4633–49.

68. Hammoudi N, Ahmed KBR, Garcia-Prieto C, Huang P. Metabolic alterations in cancer cells and therapeutic implications. Chin J Cancer. 2011;30(8):508–25.

69. De Lartigue J. Tumor heterogeneity: A central foe in the war on cancer. JCSO. 2018.

70. Schaefer PM, Kalinina S, Rueck A, von Arnim CAF, von Einem B. NADH Autofluorescence—A Marker on its Way to Boost Bioenergetic Research. Cytom Part A. 2019;95(1):34–46.

71. Chacko J V, Eliceiri KW. Autofluorescence lifetime imaging of cellular metabolism: Sensitivity toward cell density, pH, intracellular, and intercellular heterogeneity. Cytom Part A. 2019;95(1):56-69.

72. Zaal EA, Berkers CR. The Influence of Metabolism on Drug Response in Cancer. Front Oncol . 2018 Nov 2;8:500. Available from: https://www.ncbi.nlm.nih.gov/pubmed/30456204

73. Ayuso JM, Gillette A, Lugo-Cintrón K, Acevedo-Acevedo S, Gomez I, Morgan M, et al. Organotypic microfluidic breast cancer model reveals starvation-induced spatial-temporal metabolic adaptations. EBioMedicine . 2018 Nov 1;37:144–57.

74. Muz B, de la Puente P, Azab F, Azab AK. The role of hypoxia in cancer progression, angiogenesis, metastasis, and resistance to therapy. Hypoxia. 2015;3:83–92.

75. Schütte M, Risch T, Abdavi-Azar N, Boehnke K, Schumacher D, Keil M, et al. Molecular dissection of colorectal cancer in pre-clinical models identifies biomarkers predicting sensitivity to EGFR inhibitors. Nat Commun . 2017 Feb 10;8:14262.

76. Sachs N, de Ligt J, Kopper O, Gogola E, Bounova G, Weeber F, et al. A Living Biobank of Breast Cancer Organoids Captures Disease Heterogeneity. Cell. 2018;172(1):373-386.e10.

77. Tanaka N, Osman AA, Takahashi Y, Lindemann A, Patel AA, Zhao M, et al. Head and neck cancer organoids established by modification of the CTOS method can be used to predict *in vivo* drug sensitivity. Oral Oncol . 2018;87:49–57.

78. Huang L, Bockorny B, Paul I, Akshinthala D, Gandarilla O, Bose A, et al. Pancreatic tumor organoids for modeling *in vivo* drug response and discovering clinically-actionable biomarkers. bioRxiv. 2019.

79. Rosa R, Monteleone F, Zambrano N, Bianco R. *In vitro* and *in vivo* models for analysis of resistance to anticancer molecular therapies. Curr Med Chem. 2014;21(14):1595–606.

80. Hubert CG, Rivera M, Spangler LC, Wu Q, Mack SC, Prager BC, et al. A three-dimensional organoid culture system derived from human glioblastomas recapitulates the hypoxic gradients and cancer stem cell heterogeneity of tumors found *in vivo*. Cancer Res. 2016;76(8):2465–77.

81. Jo Y, Choi N, Kim K, Koo HJ, Choi J, Kim HN. Chemoresistance of cancer cells: Requirements of tumor microenvironment-mimicking *in vitro* models in anti-cancer drug development.

Theranostics. 2018;8(19):5259–75.

82. Di Paolo A, Bocci G. Drug distribution in tumors: Mechanisms, role in drug resistance, and methods for modification. Curr Oncol Rep. 2007 Jan;9(2):109–14.

83. Zhu AZ. Quantitative translational modeling to facilitate preclinical to clinical efficacy & toxicity translation in oncology. Futur Sci OA . 2018 Apr 23;4(5):FSO306–FSO306.

84. Combest AJ, Roberts PJ, Dillon PM, Sandison K, Hanna SK, Ross C, et al. Genetically Engineered Cancer Models, But Not Xenografts, Faithfully Predict Anticancer Drug Exposure in Melanoma Tumors. Oncol . 2012 Oct 1;17(10):1303–16

85. Pichon X, Lagha M, Mueller F, Bertrand E. A growing toolbox to image gene expression in single cells: sensitive approaches for demanding challenges. Mol Cell. 2018;71(3):468–80.

86. Ohno M, Karagiannis P, Taniguchi Y. Protein expression analyses at the single cell level. Molecules. 2014;19(9):13932–47.

CHAPTER 5

AUTOFLUORESCENCE IMAGING IDENTIFIES TUMOR CELL-CYCLE STATUS ON A SINGLE-CELL LEVEL

5.1 Abstract

The goal of this study is to validate fluorescence intensity and lifetime imaging of metabolic co-enzymes NAD(P)H and FAD (metabolic autofluorescence imaging) as a method to quantify cell-cycle status of tumor cells. Heterogeneity in tumor cell-cycle status (e. g. proliferation, quiescence, apoptosis) increases drug resistance and tumor recurrence. Cell-cycle status is closely linked to cellular metabolism. Thus, this study applies cell-level metabolic imaging to distinguish proliferating, quiescent, and apoptotic populations. Two-photon microscopy and time-correlated single photon counting are used to measure optical redox ratio (NAD(P)H fluorescence intensity divided by FAD intensity), NAD(P)H and FAD fluorescence lifetime parameters. Redox ratio, NAD(P)H and FAD lifetime parameters alone exhibit significant differences ($p < 0.05$) between population means. To improve separation between populations, linear combination models derived from partial least squares - discriminant analysis (PLS-DA) are used to exploit all measurements together. Leave-one-out cross validation of the model yielded high classification accuracies (92.4 and 90.1% for two and three populations, respectively). Metabolic autofluorescence imaging and PLS-DA also identifies each sub-population within heterogeneous samples. These results establish single-cell analysis with metabolic autofluorescence imaging and PLS-DA as a label-free method to distinguish cell-cycle status within intact samples. This approach could be used to incorporate cell-level tumor heterogeneity in cancer drug development.

5.2 Introduction

The metabolism, drug response, and genetic expression of cells are heterogeneous within a single tumor, which affects cancer progression and response to treatment[1]. Specifically, quiescent cancer cells lack responsiveness to standard chemotherapies, introducing a major challenge to efficacy of cancer treatment[2,3]. Quiescent cell sub-populations promote tumor dormancy, which results in therapeutic resistance and later

tumor recurrence. However, the mechanisms responsible for the emergence of quiescent cell populations and interactions between quiescent cells and the tumor or metastatic microenvironment are not well understood. This is largely due to the inability to distinguish quiescent cell populations from the bulk, proliferating population. Furthermore, quiescent cells can re-enter the cell-cycle after years of remission, and initiate tumor recurrence[3]. Thus, it is essential to avoid misidentification of quiescent cells as apoptotic, despite their similarly reduced metabolic activity[3]. Robust methods to identify quiescent cells within the heterogeneous tumor mass are needed to develop improved cancer therapies that target these dormant, yet lethal, cell populations.

Flow cytometry is a standard measure of cell function, and is used to identify quiescent and resistant cancer cells in heterogeneous tumors. Flow cytometry applications are constrained to exogenous labelling using fluorescent antibodies or dyes to allow *ex vivo* sorting into pure cell populations. The use of these fluorescent labels is highly disruptive to cell physiology, limiting the applicability of flow cytometry[4]. Additionally, flow cytometry requires the dissociation of the sample into a single cell suspension *ex vivo*, and thus loses the microenvironmental and spatial context of each sub-population. Identifying and characterizing cell sub-populations within intact, heterogeneous tumors would inform on spatial relationships with supporting cells in the microenvironment. For example, interactions between dormant tumor cells and blood vessels, extracellular matrix, immune cells, and fibroblasts could be compared to those interactions with proliferating tumor cells within intact samples. Also, the use of flow cytometry prevents the study of dynamic changes in live tumors over time, because tumors must be removed and dissociated for analysis. Thus, a technology that could monitor dynamic changes over time, and identify tumor cell sub-populations within intact, living samples, could supplement current methods to provide a more complete picture of tumor heterogeneity.

Metabolic autofluorescence imaging measures the autofluorescence intensities and lifetimes of the metabolic co-enzymes NAD(P)H and FAD. Metabolic autofluorescence imaging is attractive for the study of tumor heterogeneity because it is non-invasive, does not use exogenous labels, can monitor dynamic changes within intact samples[5–8], including *in vivo* tumors[9,10], achieves cellular resolution, and is

sensitive to cell metabolism[11]. Metabolic autofluorescence imaging is sensitive to cell malignancy, cancer progression, and provides early measures of tumor cell drug response[5–7]. The fluorescence intensities of NAD(P)H and FAD can be combined into the "optical redox ratio" (fluorescence intensity of NAD(P)H/FAD), which is sensitive to the relative amounts of electron donor and acceptor in a cell[12]. The redox ratio was established by Chance *et al.*[13] and has since been used for an array of applications in cancer, including studies of cancer progression, invasion, and drug response[5–8, 14]. Fluorescence lifetime imaging (FLIM) provides a complementary measurement to the redox ratio[9], and is sensitive to the enzyme binding activities of NAD(P)H and FAD[15]. Specifically, the protein- bound NAD(P)H lifetime is significantly longer than the free NAD(P)H lifetime, due to self- quenching in the free state[15, 19–23]. Conversely, FAD lifetimes are short and long in the protein- bound and free states, respectively[15]. Combined information from the fluorescence intensities and lifetimes of NAD(P)H and FAD provide a measure of the global metabolic activity in individual cells within intact samples[5,13–18,24], specifically on redox balance and enzyme binding activity. Previous studies have established that metabolic autofluorescence imaging is sensitive to cancer progression and drug response[5–7,9].

The goal of this study is to use metabolic autofluorescence imaging to discriminate proliferating, quiescent, and apoptotic cell populations. We hypothesized that populations exhibiting varying cell-cycle activity can be metabolically distinguished based on the NAD(P)H and FAD fluorescence lifetimes and redox ratio. Here, we demonstrate the feasibility of using metabolic autofluorescence imaging to identify sub-populations in an acute myeloid leukemia (AML) model, a well-defined model for observing cell-cycle status. Pure and co-cultured populations of each cell type were evaluated using metabolic autofluorescence imaging. The results illustrate that metabolic autofluorescence imaging can identify proliferating, quiescent, and apoptotic cell populations within heterogeneous samples. Therefore, this approach could be valuable in the development of new cancer therapies that target dormant and treatment-resistant cell sub-populations.

5.3 Materials and Methods

5.3.1 Cell Culture

Kasumi-1 cells (acute myeloid leukemia progenitors; ATCC) were suspended in standard RPMI

1640 culture medium with additives of 10% fetal bovine serum and 1% penicillin:streptomycin. Proliferation, quiescence, and apoptosis was achieved in separate cultures by: (1) refreshing standard RPMI media (no treatment, proliferation group), (2) substituting media supplemented with 250 nM JQ1 (a transcription inhibitor[25–27]; Bradner lab, quiescence group), or (3) substituting media supplemented with 2.1 mM cytarabine (Ara-C, standard chemotherapy [27]; Vanderbilt pharmacy, apoptosis group). Cell seeding density was maintained at 2.5 x 10^4 cells per 35 mm glass bottom dish (MatTek). All imaging samples were overlaid with a coverslip immediately prior to imaging, to reduce motion artifact of suspended cells.

In a separate cohort, cell-cycle activity was validated with flow cytometry for each treatment group. Cell-cycle status was determined for apoptotic and proliferating populations using standard cleaved caspase 3 and Ki67 labeling, respectively. Cell-cycle status of the quiescent group was confirmed upon simultaneous Pyronin Y labeling of RNA content and Hoechst 33342 labeling of DNA content in proliferating and quiescent groups, based on lower RNA levels in quiescent cells compared with cells undergoing active proliferation[29]. Cells from proliferation, quiescence, and apoptosis groups were seeded at a density of 2.5 x10^6 cells per milliliter in 75-T tissue culture flasks. 72 hours after treatment, each culture was labeled with Ki67 antibody conjugated to FITC (proliferation; Life Technologies), cleaved caspase 3 (CC3) antibody conjugated to FITC (apoptosis; Life Technologies), Hoechst 3342 (quiescence; Sigma) and pyronin Y (quiescence; Sigma) to confirm cell-cycle status of each respective culture via flow cytometry. Population fluorescence thresholds, or gates, for cell sorting were established by autofluorescence flow cytometry (no antibody labeling) of cells from each population. Experts in flow cytometry established these gates based on standard practice. Percent of positively stained cells per sample was calculated as the ratio of cells exhibiting fluorescence intensities beyond established thresholds to total cell count.

5.3.2 Verification of metabolism with varied cell-cycle status

The dominant role of oxidative phosphorylation in leukemic progenitor cells was confirmed upon perturbation with cyanide. Proliferating Kasumi-1 cells were plated on 35 mm glass dishes at 2.5 x 10^4

cells per dish after a 72-hour incubation period. Following acquisition of NAD(P)H and FAD images, cell media was replaced with media supplemented with 4 mM NaCN (Sigma) and imaged five minutes after media change[9]. Redox ratio measurements were normalized to untreated proliferating samples for comparison between treatment groups.

Unlike proliferating leukemic cells, quiescent leukemic cells rely on fatty acid oxidation, which is a feeder reaction for oxidative phosphorylation[28,30]. JQ1 is known to induce quiescence in leukemic cells, forcing them to rely on fatty acid oxidation[25–27,30]. To verify the metabolism of JQ1-treated (quiescent) cells, proliferating and quiescent cell groups were resuspended in media supplemented with 100 nM of etomoxir (Sigma), an inhibitor of fatty acid oxidation[30]. Following treatment, cells were incubated for 48 hours and imaged using fluorescence lifetime imaging[30]. As previously discussed, redox ratio comparison between treatment groups was possible following normalization to untreated proliferating samples.

5.3.3 Fluorescence lifetime imaging

FLIM was conducted on a multi-photon fluorescence lifetime microscope (Bruker Nano Inc.) built around a Nikon Ti:E inverted microscope using a 40X (1.3NA) oil-immersion objective. A titanium:sapphire (Chameleon Ultra II, Coherent) laser was used for excitation of NAD(P)H (750 nm) and FAD (890 nm) autofluorescence. A 400–480 nm bandpass filter isolated NAD(P)H fluorescence emission. A 500 nm high pass dichroic mirror and a 500–600 nm bandpass filter isolated FAD fluorescence emission. Both NAD(P)H and FAD fluorescence emission were detected with a GaAsP photo- multiplier tube. Fluorescence lifetime images were acquired using electronics enabling time-correlated single photon counting (TCSPC). Acquisition of 170 x 170 mm (256 x 256 pixels) images required a 60- second integration time and pixel dwell time of 4.8 microseconds. Photobleaching of the sample was avoided during image acquisition by maintaining photon count rates at approximately 1—2 $x10^5$ photons/second. Fields-of-view for NAD(P)H and FAD were the same for each image location within a sample. Four fields-of-view were acquired from each dish, and fields-of-view were selected to control for cell number per field-of-view across all experimental groups. An average of 40–

60 cells were included in each field-of-view, resulting in 150–250 cells from each dish. All reported data represent a single replicate. Three independent replicates were conducted for all experiments, each demonstrating agreement with observed trends in reported data. Average power was measured daily for all experiments and maintained at approximately 6.5–6.9 mW for NAD(P)H excitation and 7.4–7.7 mW for FAD excitation.

5.3.4 Image analysis

Fluorescence lifetime fits were calculated using SPCImage (Becker & Hickl GmbH). Fluorescence contributions from background and cell nuclei were minimized via thresholding. The second harmonic generated signal from urea crystals at 900 nm excitation was used to measure the instrument response function, which was found to have a full width at half maximum of 220 ps. The measured instrument response function was deconvolved from the experimentally measured decay curve prior to curve fitting. All decay curves were fit to a two-component exponential model:

$$I(t) = \alpha_1 e^{-t/\tau_1} + \alpha_2 e^{-t/\tau_2} + C \quad (1)$$

where I(t) is the fluorescence intensity at time t following laser excitation, τ_1 and τ_2 are the short and long fluorescence lifetimes, α_1 and α_2 represent the short and long lifetime component contributions, and C represents background light contribution. A two-component decay curve was used to represent the free and protein-bound conformations of NAD(P)H and FAD[7]. Respective mean lifetimes of NAD(P)H and FAD were calculated as a weighted average of the short and long lifetimes ($\tau_m = \alpha_1\tau_1 + \alpha_2\tau_2$). Fluorescent bead (YG microspheres, Polysciences Inc.) measurements were acquired daily to validate fluorescence lifetime values. Bead lifetime measurements (1.9 ± 0.09 nanoseconds) were consistent with values reported in literature[8,9].

Photon counts from the NAD(P)H and FAD fluorescence lifetime images were integrated over the fluorescence decay time on a per-pixel basis to generate NAD(P)H and FAD intensity images. The redox ratio for each pixel per image was calculated by dividing NAD(P)H fluorescence intensity by FAD fluorescence intensity per pixel. The redox ratio was normalized to redox ratio measurements of a control,

proliferating sample taken each day to account for variations in relative laser powers across days and excitation wavelengths.

A customized CellProfiler pipeline was used to segment individual cell cytoplasms (nucleus excluded). The steps of the pipeline were as follows: (1) threshold the low intensity nucleus from lower intensity background and higher intensity cytoplasm, (2) propagate to identify the cell boundary, and (3) subtract the nucleus from the cell boundary. This mask was applied to all cells in all images to compute a mean redox ratio, NAD(P)H τ_1, τ_2, α_1, τ_m, and FAD τ_1, τ_2, α_1, τ_m, for each cell cytoplasm in each image (9 total variables)[5].

5.3.5 Threshold for classification of individual variables

Thresholds were used to classify cells as apoptotic, proliferating, or quiescent based on each of the 9 individual variables (redox ratio, NAD(P)H τ_m, τ_1, τ_2, and α_1, FAD τ_m, τ_1, τ_2, and α_1). Two thresholds per variable were defined from receiver operator characteristic (ROC) analysis as a value that maximizes the true positive rate while minimizing the false positive rate between the low- and mid-range populations and the mid- and high-range populations. Classification accuracies and confusion matrices were calculated from the number of misclassified cells.

5.3.6 Partial least squares-discriminant analysis

To obtain maximal separation between groups with differing cell-cycle activity, partial least squares – discriminant analysis (PLS-DA)[32] was used to incorporate 7 fluorescence variables (NAD(P)H τ_1, τ_2, α_1; FAD τ_1, τ_2, α_1; redox ratio). This technique performs iterations of linear transformations on a matrix of samples with known classification. These transformations are then projected onto a vector comprised of classification values for each sample. The resultant equation represents an optimal boundary between all classes and provides information about the significance of each variable included in model construction, unlike other classification methods[32]. PLS-DA determines the contribution of each independent variable incorporated into the model, thus NAD(P)H and FAD τ_m were excluded from generation of our model. Weight centering of all groups was applied to minimize

bias in separation boundaries influenced by uneven cell numbers. Weight centering was achieved by calculating the difference between individual values in the data set and the average of means across all groups[33]. Separate models were developed for two-group and three-group classification to overcome skewed weighting criteria by the training data set. In the case of three-group classification, one-vs-all PLS- DA was applied to calculate distinct separation boundaries for all three classes, ensuring appropriate transformation of the known training data set for satisfactory class representation[32,33]. Calculation of the Mahalanobis distance from each class mean to all data points ensured appropriate assignment of separation boundaries[33].

Images were acquired from pure samples of apoptotic, proliferating, or quiescent cells 72 hours post-treatment. Data from all three conditions were combined to form comprehensive datasets for PLS- DA model development and evaluation using leave- one-out cross validation (LOOCV) in the R software package. Each cell within these comprehensive datasets (n samples) was assessed by exclusion prior to PLS-DA analysis, partitioning the 1 excluded cell as the validation sample and the remaining n-1 observations as the training set. The PLS-DA model was then developed based on the n-1 training set data, and model classification performance was evaluated on correct classification of the 1 excluded cell. This approach was repeated n times, to classify all n cells in the comprehensive data set.

PLS-DA was also implemented in the R software package. Linear combination models based on the 7 fluorescence variables were separately generated for the two-group and three-group cases. Weights represent the relative contribution of the variable toward overall covariance of the training dataset in relation to its known class. Confusion matrices representing the number of misclassified cells per class from the validation set were generated, with each matrix column and row corresponding to the true and predicted classes, respectively. Evaluation metrics (i.e., classification accuracy, sensitivity and specificity) were subsequently calculated for each model, based on the validation set. Generated PLS-DA models were evaluated using the posterior probability of class membership, which was calculated for individual

validation set samples.

For experimental demonstration of these models, heterogeneous samples were generated by plating cells from each population at various proportions. Images were acquired immediately following plating. For the two-group demonstration set, proliferating and quiescent cells were plated at the following proportions: 100:0, 30:70, 50:50, 70:30, 0:100 (proliferating : quiescent). The three- group demonstration included plating proportions of 33:33:33, 50:25:25, 25:25:50 (proliferating : quiescent : apoptotic). Two- and three-group PLS-DA models generated from the entire training data sets were applied for single-cell identification within these mixed samples. Color-coded images were produced to demonstrate the model's ability to resolve each population within the co-cultures, with color assignments corresponding to the model-determined cell-cycle status of individual cells. Confirmation of cell-cycle status for each cell in each field-of-view was not feasible in the heterogeneous samples.

5.3.7 Statistical Analysis

A Wilcoxon rank sum test of the redox ratio and lifetime parameters (τ_m, τ_1, τ_2, and α_1) for NAD(P)H and FAD was used to assess significant differences between groups using these 9 individual variables alone. A Tukey multiple comparison test was used to correct for multiple comparisons across cell types. Error bars are representative of the mean ± standard error of the mean. Statistical significance was indicated with an α value less than 0.05.

5.4 Results

5.4.1 Validation of homogeneous populations

Pure populations of apoptotic, quiescent, and proliferating cells were generated by replacing standard cell culture media with media supplemented with cytarabine, the bromodomain and extra terminal (BET) family inhibitor JQ1, or no supplementary agent, respectively. Cell-cycle status for each population was validated by labeling with antibodies or cellular component dyes followed by flow cytometry (see methods). Histogram plots of the apoptotic group show significantly higher FITC-CC3

fluorescence from the labeled population compared to the negative control (unstained cells), and 97.5% of cells in the labeled group were positive for apoptosis (Figure 5.1A). Similar differences in fluorescence signal were observed in the proliferating group for FITC Ki67 labeled vs. negative control, and 99.7% of cells in the labeled group were positive for proliferation (Figure 5.1B). Overlaid dot density plots of the labeled proliferating and quiescent groups show distinct separation between each population based on lower RNA content (Pyronin Y) in quiescent cells as expected, with 93.4% cells in the double-stained quiescent population exhibiting decreased Pyronin Y fluorescence intensity compared to the proliferating population (Figure 5.1C). This is comparable to previous studies reporting elevated Pyronin Y levels in proliferating populations[29]. Similarly, apoptotic populations can be distinguished with this double-staining method as they exhibit extremely low Hoechst and Pyronin Y fluorescence[25]. Additional cohorts of quiescent populations labeled with Ki67 and cleaved caspase-3 yielded less than of 5% of cells positive for either marker, further supporting a quiescent phenotype (data not shown).

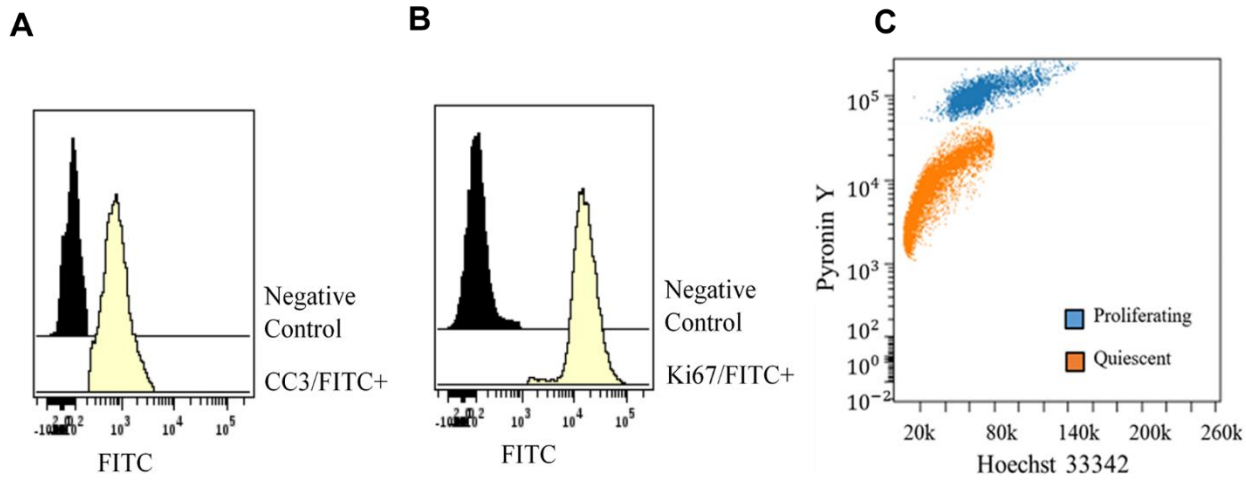

Figure 5.1. Flow cytometry analysis confirms cell-cycle activity associated with apoptotic, proliferating, quiescent and Kasumi-1 cell populations. Pure populations of (A) apoptotic cells individually labeled with cleaved caspase 3 (CC3) con- jugated to FITC, and (B) proliferating cells individually labeled with Ki67 conjugated to FITC. Comparison to unstained controls (negative control, A&B) demonstrate that the stained populations are positive for CC3 (A) and Ki67 (B). (C) Similarly, pure populations of quiescent and proliferating cells were labeled with Pyronin Y (RNA content) and Hoechst 33342 (DNA content) simultaneously to demonstrate separation between the quiescent populations (low RNA content) and proliferating population (high RNA content). In (C) each dot is an individual cell.

5.4.2 Metabolic perturbations in proliferating and quiescent cells

A series of metabolic inhibitors were used to perturb dominant metabolic pathways in proliferating and quiescent leukemia cells. These perturbations verify that our autofluorescence measurements accurately reflect changes in active metabolic pathways in these cells. Cyanide perturbation assessed the metabolism of proliferating human acute myeloid leukemia cells. Cyanide inhibits oxidative phosphorylation, resulting in an abundance of NADH in the cytoplasm. The significant increase in the redox ratio after cyanide treatment (Figure 5.2A) agrees with the reported dominance of oxidative phosphorylation in leukemic cells[28]. Similarly, the reduced NAD(P)H τ_m is consistent with previous studies of cyanide treatment in cancer cells (Figure 5.2B)[5–7]. Trends in FAD τ_m were also comparable to previously reported data (Figure 5.2C)[9]; however, there was not a significant change in the FAD τ_m following addition of cyanide in these cells.

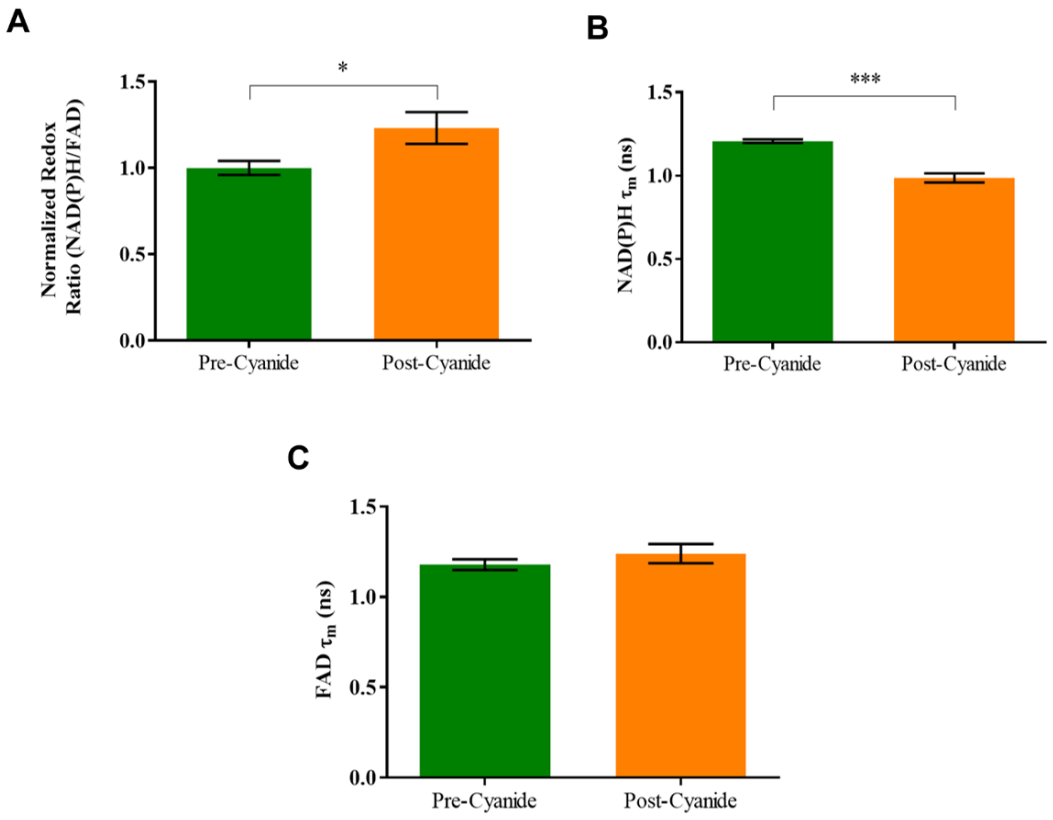

Figure 5.2. Inhibition of oxidative phosphorylation affects proliferating cell metabolism. Quantitative measurement (mean+/-SE) of the (A) redox ratio, (B) NAD(P)H mean lifetime (τ_m), and (C) FAD τ_m for proliferating Kasumi-1 cells (n = 150-250 cells per group) before and five minutes after addition of 4 mM cyanide. (* $p < 0.05$, *** $p < 0.001$).

Quiescent Kasumi-1 cells rely largely on fatty acid oxidation (Figure 5.3). Etomoxir treatment increased the redox ratio of quiescent cells (Figure 5.3B). The increase in the redox ratio after etomoxir treatment in quiescent cells indicates that inhibition of fatty acid oxidation also inhibits downstream oxidative phosphorylation in quiescent cells. No significant change in the redox ratio was observed in proliferating cells treated with etomoxir, which indicates that these proliferating cells have less dependence on fatty acid oxidation[28]. Furthermore, changes in NAD(P)H τ_2 were not statistically different ($p > 0.05$) before vs. after etomoxir treatment in proliferating cells. Significant differences in NAD(P)H τ_m, τ_1, τ_2, and α_1 were observed ($p < 0.05$) between proliferating and quiescent cells prior to etomoxir treatment. Perturbation with etomoxir yielded significant increases in NAD(P)H τ_m, τ_1, τ_2, and α_1 ($p < 0.05$), similarly demonstrating contrast between proliferating and quiescent populations. Etomoxir resulted

in significant decreases in FAD τ_m, τ_1, τ_2, and α_1 following treatment ($p < 0.001$, data not shown).

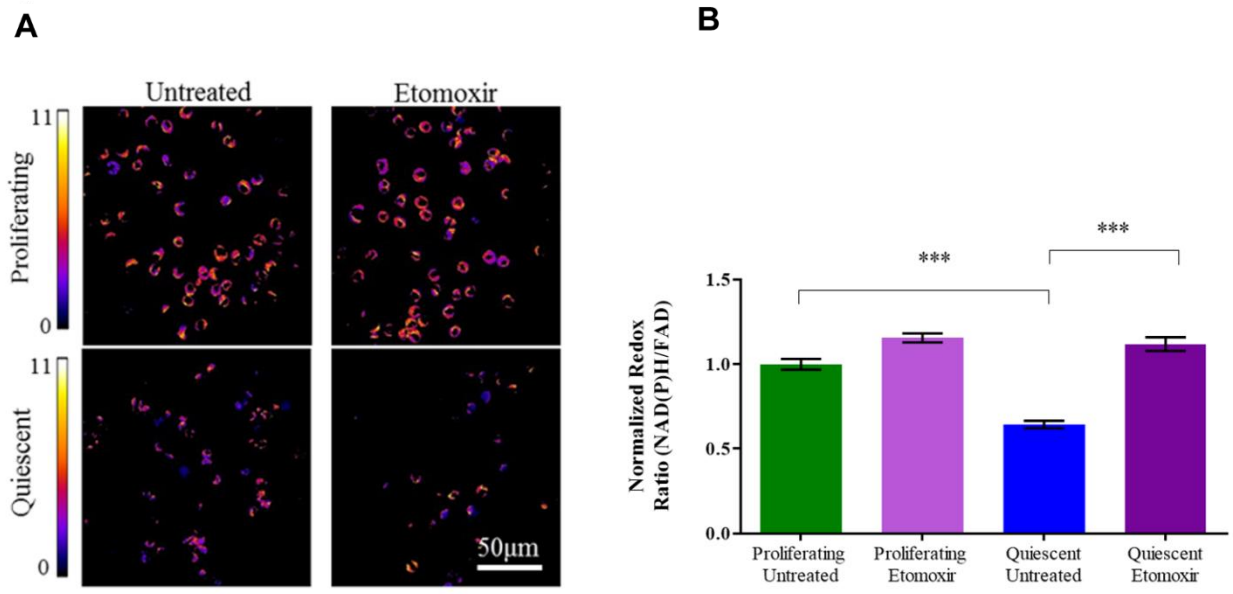

Figure 5.3. Inhibition of fatty acid oxidation affects quiescent cell metabolism. (A) Representative redox ratio images. (B) Quantitative measurement (mean +/-SE) of the redox ratio for untreated proliferating and quiescent Kasumi-1 cells (n = 150-250 cells per group), as well as etomoxir-treated proliferating and quiescent cells (n= 150-250 cells per group). Kasumi- 1 cells were forced into quiescence by treatment with JQ1 (250 nM) 72 hours before etomoxir (100 nM) or vehicle treatment. (***$p < 0.001$).

5.4.3 Metabolic autofluorescence imaging of proliferating, quiescent, and apoptotic cells

Metabolic autofluorescence imaging was performed in acute myeloid leukemia cells forced into apoptotic, proliferating, and quiescent states, to validate metabolic autofluorescence imaging as a method for classifying these cell states. Untreated (proliferating), JQ1- treated (quiescent), and cytarabine-treated (apoptotic) Kasumi-1 cells were imaged at 72 hours post- treatment. Two-photon fluorescence lifetime imaging revealed qualitative differences in the redox ratio, NAD(P)H τ_m, and FAD τ_m within proliferating, quiescent, and apoptotic cell populations (Figure 5.4). Quiescent cells exhibited a distinct decrease in redox ratio across all cells in comparison to both proliferating and apoptotic groups (Figure 5.4). Longer NAD(P)H and FAD mean lifetimes were observed in apoptotic cells than in proliferating and quiescent groups. Cellular morphology can also provide some

discrimination between cells with varied cell-cycle status. In contrast to the apoptotic and quiescent groups, proliferating cells were characterized with a well-defined nuclear area (Figure 5.4). Quiescent cells exhibited a significant decrease in overall cell area (Figure 5.4) compared to apoptotic populations ($p < 0.05$, 72.5 ± 3.99 mm^2 vs. 96 ± 9.06 mm^2) and modest, but not significant, differences compared to proliferating populations (84.5 ± 4.30 mm^2).

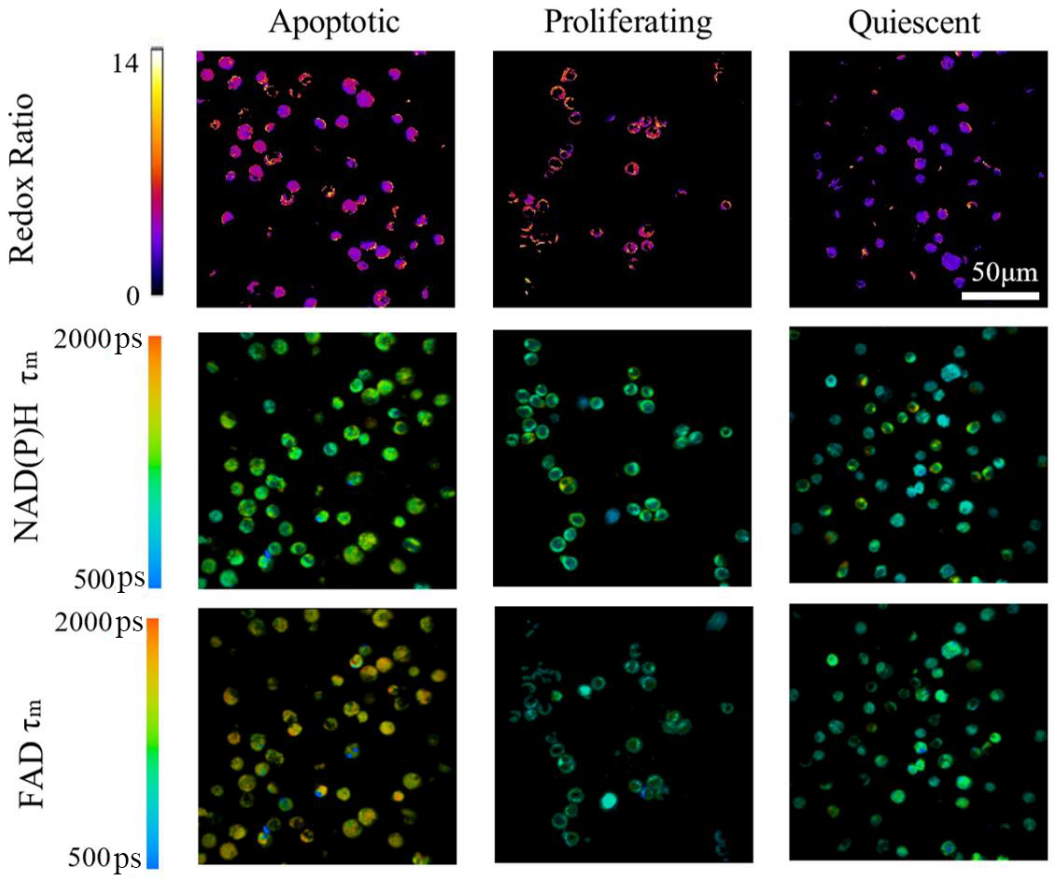

Figure 5.4. Lifetime and redox images. Representative redox ratio, NAD(P)H τ_m, and FAD τ_m images of Kasumi-1 cells forced into apoptotic, proliferating, and quiescent states, 72 hours post-treatment.

Quantitative metabolic autofluorescence analysis can distinguish proliferating, quiescent, and apoptotic samples on a population-level (Figure 5.5). Each cell was treated as an independent measurement, across all 4 FOVs (40-60 cells per FOV) per dish and all 3 replicate dishes per experimental group (proliferating, apoptotic, quiescent). The redox ratio is increased in proliferating cells compared to apoptotic and quiescent cells, and is also increased for apoptotic cells compared to quiescent cells ($p < 0.001$, Figure

5.5A). Both NAD(P)H and FAD τ_m are highest in apoptotic populations ($p<0.001$), but lack significance between proliferating and quiescent cells (Figures 5.5B and C). Proliferating cells exhibited higher NAD(P)H τ_1 and α_1 compared to apoptotic and quiescent cells ($p < 0.001$, Figure 5.5D,F). Like the redox ratio, NAD(P)H τ_2 is significantly different between all three groups ($p<0.001$, Figure 5.5E). FAD τ_1 was only effective in discriminating quiescent cells from the other two conditions ($p < 0.001$, Figure 5.5G). Apoptotic cells exhibited significant differences in FAD τ_2 and α_1 compared to proliferating and quiescent cells ($p<0.05$, $p<0.001$, Figures 5.5H and I). Overall, significant differences exist between cell groups in Figure 5.5A-I, but there is still overlap between apoptotic, proliferating, and quiescent cells at the single-cell level. Furthermore, classification of cells to all three categories (apoptotic, proliferating, quiescent) based on any metabolic variable alone yields poor overall classification accuracy (Table 5.1). Therefore, classification based on a combination of all measured metabolic variables could improve separation between cell groups.

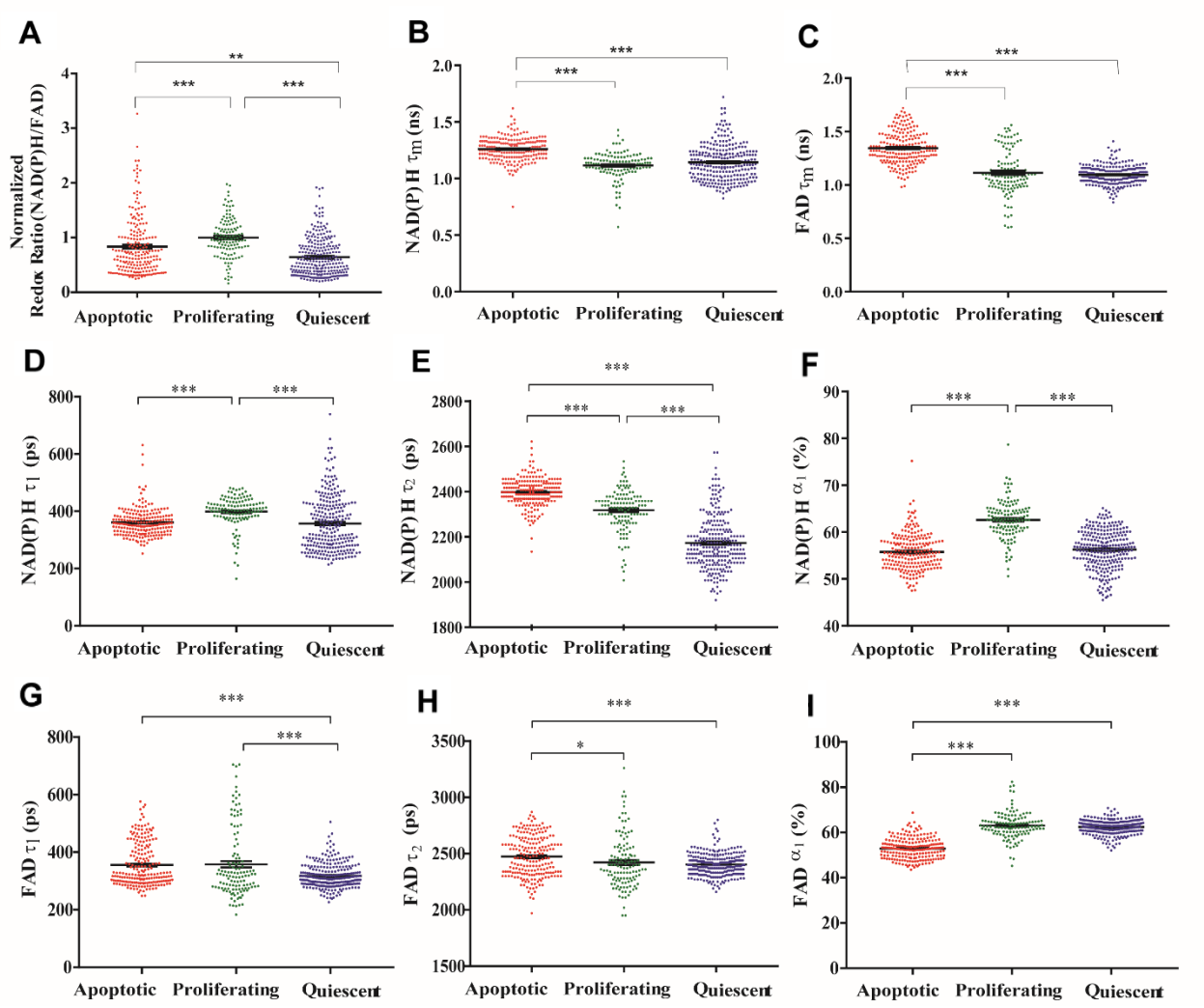

Figure 5.5. Quantitative redox and lifetime measurements. Quantitative measurement (mean +/- SE) of the (A) redox ratio, (B) NAD(P)H τ_m, (C) FAD τ_m, (D) NAD(P)H τ_1, (E) NAD(P)H τ_2, (F) NAD(P)H α_1, (G) FAD τ_1, (H) FAD τ_2, and (I) FAD α_1 at the single-cell level for proliferating, quiescent, and apoptotic (n= 150-250 cells per group) Kasumi-1 cells at 72 hours post-treatment. Each dot is an individual cell. (* $p < 0.05$, **$p< 0.01$, ***$p< 0.001$).

Table 5.1. Overall three-group classification accuracy with individual metabolic autofluorescence variables

Variable	Classification Accuracy
Redox Ratio	43.2%
NAD(P)H τ_m	44.6%
FAD τ_m	66.0%
NAD(P)H τ_1	27.2%
NAD(P)H τ_2	41.0%
NAD(P)H α_1	22.8%
FAD τ_1	31.3%
FAD τ_2	23.6%
FAD α_1	46.1%

5.4.4 Classification model using partial least squares – discriminant analysis (PLS-DA)

PLS-DA was performed to maximize separation between cell-cycle status groups on the single-cell level. The first iteration of PLS-DA aimed to separate proliferating and quiescent cell populations. This two-group PLS-DA model (Table 5.2) was created from an initial training data set, consisting of measurements of individual cells from pure samples of quiescent and proliferating cells (Figure 5.6). The weights of each fluorescence variable (NAD(P)H τ_1, τ_2, α_1; FAD τ_1, τ_2, α_1; redox ratio) included in two-group PLS-DA model based on the entire training data provide a general sense of the influence of each variable (Table 5.2). Cross-validation using the leave-one-out approach demonstrated classification accuracy of 92.4% for the generated model. The two-group PLS-DA showed improved separation of proliferating and quiescent populations (Figure 5.6) compared to any single variable (Figure 5.5). A confusion matrix representing overall classification performance of individual cells shows low rates of misclassification across classes for the two-group model and resulted in a sensitivity and specificity of 96.1% and 84.7%, respectively, for discriminating between both groups (Table 5.3).

Table 5.2. Variable weights for two-group and three-group PLS-DA models

Variable	Redox Ratio	NADH τ_1	NADH τ_2	NADH α_1	FAD τ_1	FAD τ_2	FAD α_1
Two-group PLS-DA weights	0.023	0.00035	0.0017	0.058	-0.000080	0.000073	-0.00092
Three-group PLS-DA weights:							
Proliferating vs. rest	0.011	0.0013	0.00070	0.049	0.00051	-0.00032	0.014
Apoptotic vs. rest	0.013	-0.0027	0.0021	-0.0093	-0.00063	0.00046	-0.025
Quiescent vs. rest	-0.023	0.0014	-0.0028	-0.039	0.00012	-0.00014	0.011

Table 5.3. Confusion matrix: two-group classification

		Actual	
		Proliferating	Quiescent
Predicted	Proliferating	105	6
	Quiescent	19	251

This approach was extended to include all three populations using one-vs-all multiclass PLS-DA, again with measurements of pure samples from apoptotic, proliferating, and quiescent cells for the initial training data set. Variable weights for PLS-DA models based on the entire three-group training data set are also reported (Table 5.2). Similarly, the three-group PLS-DA showed improved separation between proliferating, quiescent, and apoptotic populations on a per-cell basis (Figure 5.7) compared to any single variable (Figure 5.5), yielding classification accuracy of 90.1%. A confusion matrix representing overall classification performance of individual cells shows low rates of misclassification across classes for the three-group model (Table 5.4). Model classification yielded sensitivities of 87.6% (apoptosis), 82.3% (proliferating), and 97.5% (quiescent), and specificities of 97.9% (apoptosis), 95.5% (proliferating), and 93.7% (quiescent) for discriminating indicated populations from all other sample populations.

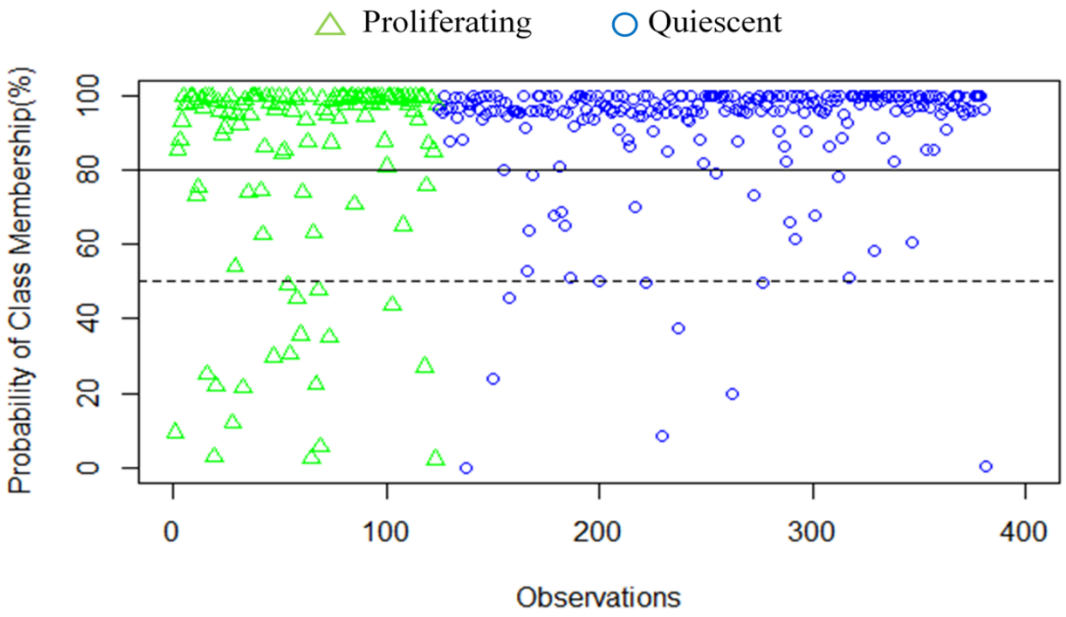

Figure 5.6. Posterior probability of class membership predictions from two-group partial least squares – discriminant analysis. Classification of proliferating (triangles), and quiescent (circles) cells yields an overall classification accuracy of 92.4%. Model classification demonstrated satisfactory sensitivity and specificity for discriminating proliferating and quiescent populations. (sensitivity: 96.1%, specificity: 84.7%). Each symbol is an individual cell.

Table 5.4. Confusion matrix: three-group classification

		Actual		
		Apoptotic	Proliferating	Quiescent
Predicted	Apoptotic	177	6	5
	Proliferating	19	93	1
	Quiescent	6	14	234

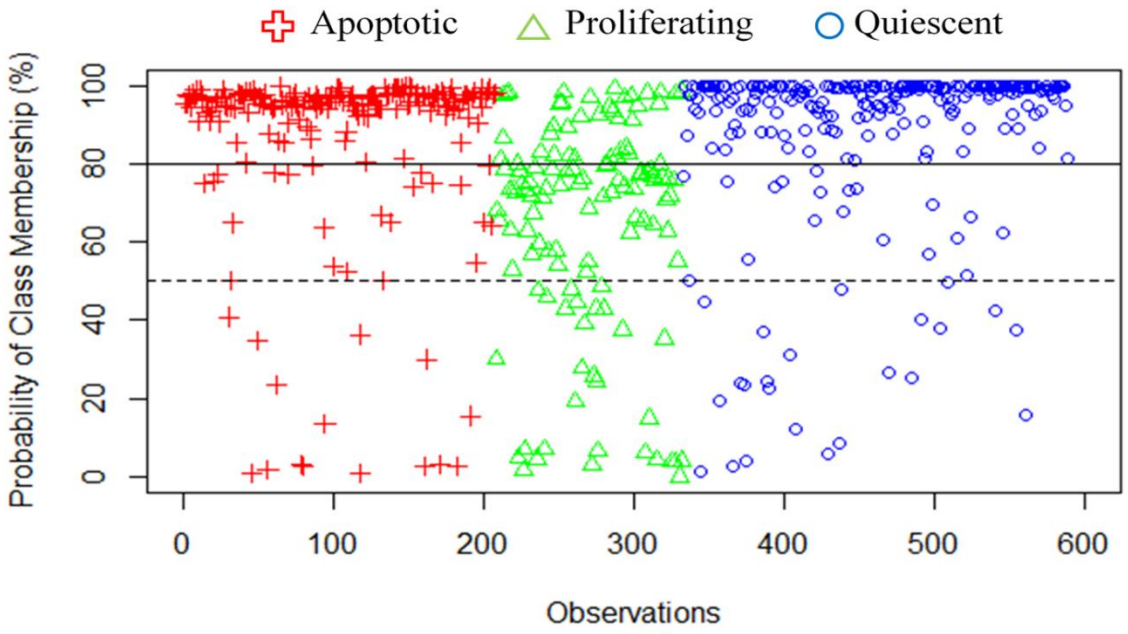

Figure 5.7. Posterior probability of class membership predictions from three-group partial least squares – discriminant analysis. Classification of apoptotic (pluses), proliferating (triangles), and quiescent (circles) cells yields an overall classification accuracy of 90.1%. Model classification demonstrated satisfactory sensitivity/specificity for discriminating each respective population from remaining sample populations. (apoptotic: 87.6%/97.9%; proliferating: 82.3%/95.5%; quiescent: 97.5%/93.7%). Each symbol is an individual cell.

5.4.5 Application of PLS-DA models to two- and three-group co-cultures

The PLS-DA model accurately identified all cells in homogeneous samples of each population not included in initial model training, supporting translation to heterogeneous samples. The two- and three-group PLS-DA were subsequently applied to mixed co-cultures of proliferating, quiescent, and apoptotic cells. Two-group PLS-DA identified proliferating cells and quiescent cells at each plating proportion (Figure 5.8A-E). The proportion of cells classified as proliferating : quiescent (38:62, 46:54, 64:36) are similar to their respective plated proportions (30:70, 50:50, 70:30) (Figure 5.8F).

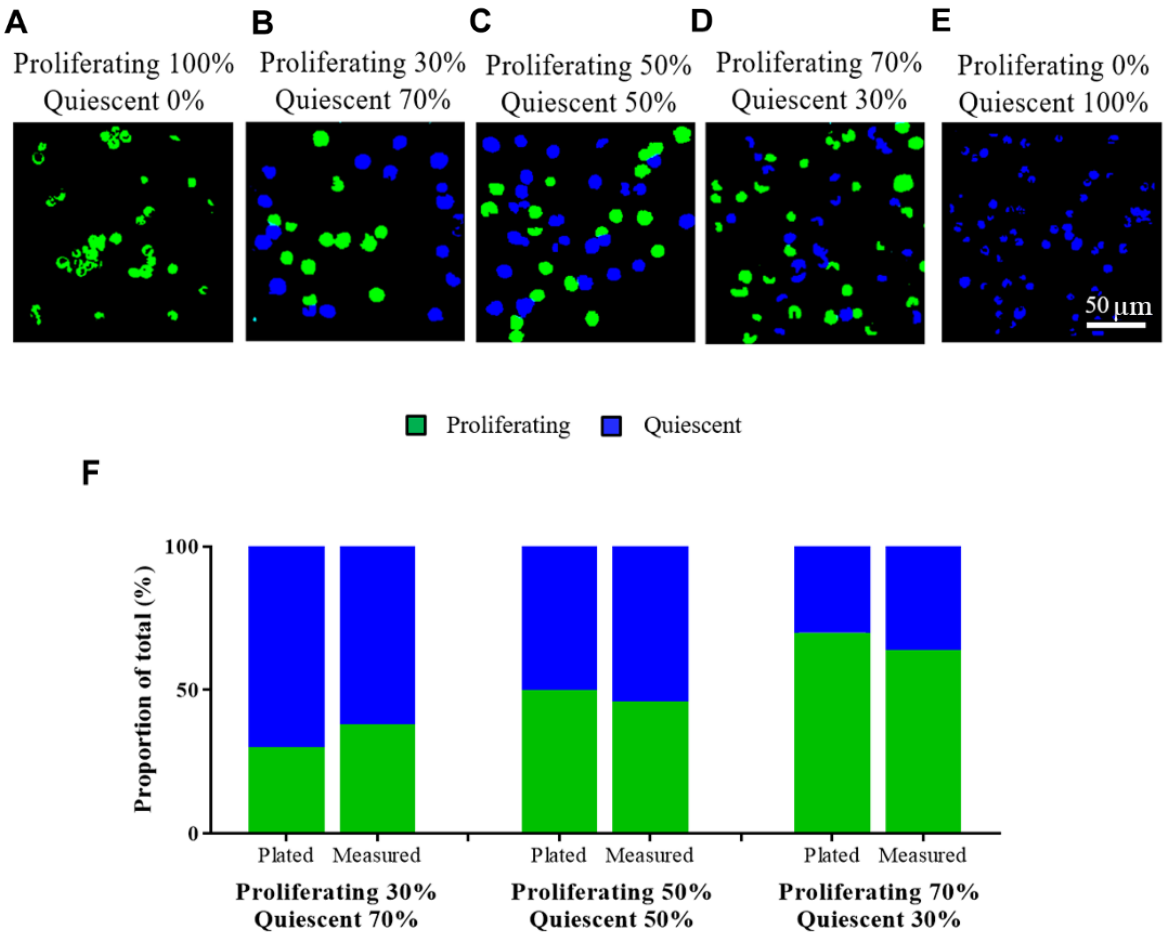

Figure 5.8. Two-Group PLS-DA Model Demonstration. Representative images of heterogeneous mixtures of proliferating (green) and quiescent (blue) populations plated at various proportions (n = 150-250 cells per mixture). (A) 100% proliferating, 0% quiescent, (B) 30% proliferating, 70% quiescent, (C) 50% proliferating, 50% quiescent, (D) 70% proliferating, 30% quiescent (E) 0% proliferating, 100% quiescent. (F) Graphical representation of differences between plated proportions and measured proportions for each mixture sample. These illustrations demonstrate the sensitivity of metabolic autofluorescence imaging to distinguish proliferating and quiescent populations in heterogeneous samples.

Next, the three-group model was demonstrated on mixtures of all three populations (Figure 5.9). The three-group model enabled identification of apoptotic, proliferating, and quiescent populations in mixed samples plated at varied proportions (Figure 5.9A-C). All populations were resolvable regardless of plating proportion. The proportion of cells classified as proliferating : quiescent : apoptotic (35:37:28, 42:31:27, 19:34:47) are similar to their respective plated

proportions (33:33:33, 50:25:25, 25:25:50) (Figure 5.9D).

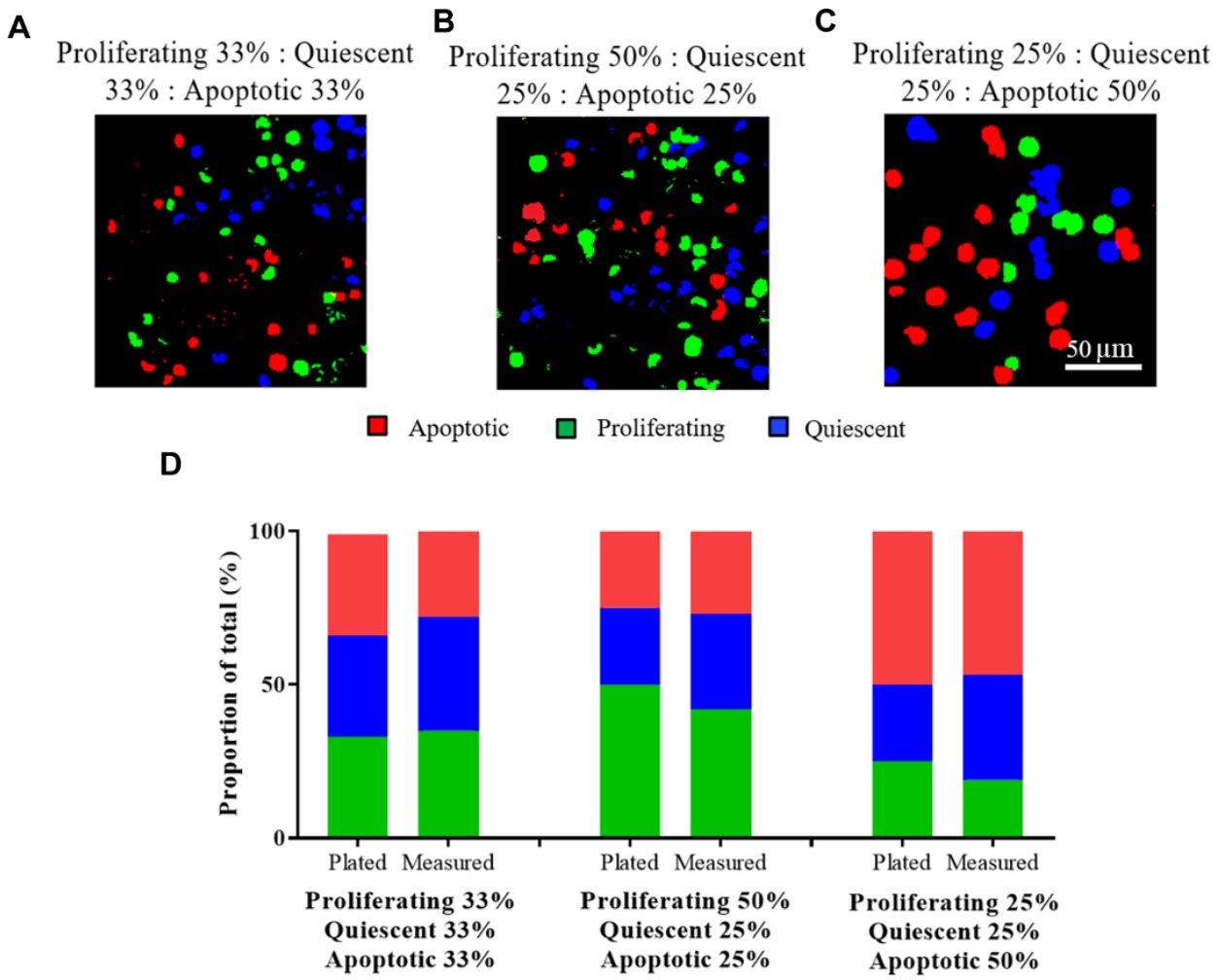

Figure 5.9. Three-Group PLS-DA Model Demonstration. Representative images of heterogeneous mixtures of proliferating (green), quiescent (blue), and apoptotic (red) populations plated at various proportions (n = 150-250 cells per mixture). (A) 33% proliferating, 33% quiescent, 33% apoptotic, (B) 50% proliferating, 25% quiescent, 25% apoptotic, (C) 25% proliferating, 25% quiescent, 50% apoptotic. (D) Graphical representation of differences between plated proportions and measured proportions for each mixture sample. These illustrations demonstrate the sensitivity of metabolic autofluorescence imaging to quiescent populations in the presence of proliferating and apoptotic populations, at varying proportions.

5.5 Discussion

Tumor heterogeneity is a significant challenge in new drug development and treatment planning in cancer[1]. There is a need for methods to assess tumor heterogeneity in intact samples without the use of contrast agents, so that improved therapies can be developed for heterogeneous tumors. Metabolism

is an attractive measure of tumor heterogeneity, due to its fundamental role in malignant transformation and in drug resistance[1,11 14]. Our results demonstrate that metabolic autofluorescence imaging can discriminate cell-cycle status on a single-cell level in cell lines, without the use of contrast agents. Metabolic autofluorescence imaging has been previously used to study single-cell response *in vivo*[5, 9–10, 14] and in live, three-dimensional cultures[8, 34–35]. The current study supports the use of metabolic autofluorescence imaging to quantify cell-cycle heterogeneity within these *in vivo* and three-dimensional *in vitro* samples. Therefore, the proposed methods can provide further insight into strategies to circumvent drug resistance.

To our knowledge, this study is the first to apply label-free imaging techniques and classification algorithms to classify the cell-cycle status of single cells. Previous studies have used fluorescent labels to characterize the metabolism of leukemic cells in different cell-cycle phases. Oxidative phosphorylation was reported as the primary energy source for leukemic progenitor cells, by observing levels of reactive oxygen species produced by these cells[28]. These findings are consistent with our studies, specifically with the increased redox ratio in Kasumi-1 cells upon inhibition of oxidative phosphorylation with cyanide ($p < 0.05$, Figure 5.2). Oxidative phosphorylation is driven by metabolites produced in upstream pathways, which promote these cells to adopt different functional phenotypes. Similarly, analysis of the oxygen consumption of leukemia progenitors in proliferating or quiescent states showed that proliferating leukemic cells use more glycolytic metabolism compared to quiescent cells[30]. Furthermore, perturbation with a fatty acid oxidation inhibitor (etomoxir) eradicated the quiescent cells[27], suggesting these cells rely more heavily on fatty acid oxidation. Our results with the same fatty acid oxidation inhibitor (Figure 5.3) are consistent with these previous findings[30], and validate the reliance of quiescent leukemic cells on fatty acid oxidation (in contrast to proliferating leukemic cells). Additionally, comparisons of the redox ratio, NAD(P)H and FAD lifetime parameters (τ_m, τ_1, τ_2, and α_1) across proliferating, apoptotic, and quiescent cells indicate that metabolism differs with cell-cycle status (Figure 5.5).

The redox ratio, NAD(P)H and FAD lifetime parameters (τ_m, τ_1, τ_2, and α_1) individually demonstrate poor classification accuracy in distinguishing proliferating, apoptotic, and quiescent cells *in vitro* (Table 5.1). To optimize single-cell identification, we applied PLS-DA to generate a linear combination model of 7 measured metabolic variables (NAD(P)H τ_1, τ_2, α_1; FAD τ_1, τ_2, α_1; redox ratio). Our results show that this PLS-DA improves the separation of apoptotic, proliferating, and quiescent cells in pure samples (Figure 5.6 and Figure 5.7). Both the two- and three-group PLS-DA models exhibited increased classification accuracy compared to the classification accuracy with any metabolic variable alone (Tables 5.1, 5.3, and 5.4). These PLS-DA models combined with metabolic autofluorescence imaging enable visualization of tumor heterogeneity on a single-cell level.

The PLS-DA models were applied to metabolic autofluorescence images of mixed cultures of proliferating, apoptotic, and quiescent cells. This mixed-culture sample did result in reduced sensitivity of the PLS-DA model to apoptotic cells compared to the pure samples. This reduced sensitivity is likely due to drug removal from the media for co-culture experiments36. Furthermore, the plated ratio does not directly reflect the imaged ratios of each cell-cycle group within mixed samples. We hypothesize that discrepancies between plating and imaged ratios could be due to secretions from apoptotic cells, which affect the cell-cycle status of other cells in the culture[36]. Additional discrepancies arise from sampling error for the small field-of-view of the microscopy images vs. the overall plated ratio. These discrepancies between plated and imaged ratios in co-culture are consistent with those observed in our previous studies[37], in which cell morphology was used for gold standard classification of individual cells in microscopy images (cell morphology is not sufficient to discriminate the cell-cycle in the current study). These results suggest that metabolic autofluorescence imaging combined with PLS- DA can identify proliferating, apoptotic, and quiescent cells in co-culture (Figures 5.8 and 5.9).

The methods demonstrated here have the potential to contribute to studies of tumor dormancy and drug resistance. Tumor dormancy has been identified as a primary source of resistance to

conventional therapies, because non-proliferating tumor cells lack treatment response[1,2]. There are many theories on the mechanisms driving tumor dormancy. One predominant theory suggests that, at the single-cell level, quiescence within a cell sub-population of the tumor promotes the bulk mass to enter a state of dormancy[2,3, 38,39]. The metabolic autofluorescence imaging and PLS-DA approach used in this paper to identify and monitor quiescent tumor cells in the presence of both proliferating and apoptotic cells could be used to study interactions between dormant, proliferating, and apoptotic tumor cells, and the effect of quiescence on tumor progression. Our methods could also be used to identify extracellular influences that initiate transitions be- tween quiescence, proliferation, and apoptosis. Furthermore, these results support the use of cellular metabolic measurements to study the development of tumor dormancy.

With additional validation, our approach could be applied to universally examine cell-cycle driven tumor heterogeneity. These techniques could be translated to clinical samples, using blood samples for blood cancers, or using organoids derived from solid tumor biopsies. Our group has previously applied metabolic autofluorescence imaging to patient-derived organoids, to guide personalized treatment decisions[8, 34, 35]. The tools developed in this paper could further characterize heterogeneous cell populations within these organoids for more informed treatment planning. These tools could also be used to study tumor dormancy in mouse models of cancer. Overall, we have demonstrated metabolic autofluorescence imaging and PLS-DA as valuable tools for observing cell-cycle status, which can be applied to future studies of tumor dormancy and treatment resistance.

5.6 Acknowledgments

We would like to acknowledge the funding sources, including grants for the National Institutes of Health (R01 CA185747, R01 CA142888), the National Science Foundation (CBET-1554027), Stand Up To Cancer (Innovative Research Grant), and National Science Foundation Graduate Research Fellowship (DGE- 0909667). Furthermore, we acknowledge Dr. Jonathan Irish, Kirsten Diggens, Deon Doxie, and Nalin Leelatin for their guidance in designing flow cytometry experiments. Flow cytometry experiments were performed in the VUMC Flow Cytometry Shared Resource. The VUMC Flow Cytometry Shared

Resource is supported by the Vanderbilt Ingram Cancer Center (P30 CA68485) and the Vanderbilt Digestive Disease Research Center (DK058404).

5.7 References

1. Junttila MR, de Sauvage FJ. Influence of tumour micro-environment heterogeneity on therapeutic response. *Nature*. 2013;501(7467):346-354. doi:10.1038/nature12626

2. Saudemont A, Quesnel B. In a model of tumor dormancy, long-term persistent leukemic cells have increased B7-H1 and B7.1 expression and resist CTL-mediated lysis. *Blood*. 2004;104(7):2124-2133. doi:10.1182/blood-2004-01-0064

3. Sosa MS, Bragado P, Aguirre-Ghiso JA. Mechanisms of disseminated cancer cell dormancy: an awakening field. *Nat Rev Cancer*. 2014;14(9):611-622.

4. Cai L, Tu BP. Driving the Cell Cycle Through Metabolism. *Annu Rev Cell Dev Biol*. 2012;28(1):59-87. doi:10.1146/annurev-cellbio-092910-154010

5. Skala MC, Riching KM, Gendron-Fitzpatrick A, et al. In vivo multiphoton microscopy of NADH and FAD redox states, fluorescence lifetimes, and cellular morphology in precancerous epithelia. *Proc Natl Acad Sci*. 2007;104(49):19494-19499.

6. Walsh A, Cook RS, Rexer B, Arteaga CL, Skala MC. Optical imaging of metabolism in HER2 overexpressing breast cancer cells. *Biomed Opt Express*. 2012;3(1):75-85.

7. Walsh AJ, Poole KM, Duvall CL, Skala MC. Ex vivo optical metabolic measurements from cultured tissue reflect in vivo tissue status. *J Biomed Opt*. 2012;17(11):116015.

8. Walsh AJ, Cook RS, Sanders ME, et al. Quantitative optical imaging of primary tumor organoid metabolism predicts drug response in breast cancer. *Cancer Res*. 2014;74(18):5184-5194. doi:10.1158/0008-5472.CAN-14-0663

9. Walsh AJ, Cook RS, Manning HC, et al. Optical metabolic imaging identifies glycolytic levels, subtypes, and early-treatment response in breast cancer. *Cancer Res*. 2013;73(20):6164-6174. doi:10.1158/0008-5472.CAN-13-0527

10. Shah AT, Diggins KE, Walsh AJ, Irish JM, Skala MC. In Vivo Autofluorescence Imaging of Tumor Heterogeneity in Response to Treatment. *Neoplasia*. 2015;17(12):862-870. doi:10.1016/j.neo.2015.11.006

11. Ganeshan K, Chawla A. Metabolic regulation of immune responses. *Annu Rev Immunol*. 2014;32:609-634.

12. Varone A, Xylas J, Quinn KP, et al. Endogenous two-photon fluorescence imaging elucidates metabolic changes related to enhanced glycolysis and glutamine consumption in precancerous epithelial tissues. *Cancer Res*. 2014;74(11):3067-3075.

13. Chance B, Legallais V, Schoener B. Metabolically linked changes in fluorescence emission spectra of cortex of rat brain, kidney and adrenal gland. *Nature*. 1962;195(4846):1073-1075.

14. Georgakoudi I, Quinn KP. Optical Imaging Using Endogenous Contrast to Assess Metabolic State. *Annu Rev Biomed Eng*. 2012;14(1):351-367. doi:10.1146/annurev-bioeng-071811-150108

15. Conklin MW, Provenzano PP, Eliceiri KW, Sullivan R, Keely PJ. Fluorescence lifetime imaging of endogenous fluorophores in histopathology sections reveals differences between normal and

tumor epithelium in carcinoma in situ of the breast. *Cell Biochem Biophys*. 2009;53(3):145-157.

16. Mayevsky A. Mitochondrial function and energy metabolism in cancer cells: past overview and future perspectives. *Mitochondrion*. 2009;9(3):165-179.

17. Heikal AA. Intracellular coenzymes as natural biomarkers for metabolic activities and mitochondrial anomalies. *Biomark Med*. 2010;4(2):241-263. doi:10.2217/bmm.10.1

18. Eto K, Tsubamoto Y, Terauchi Y, et al. Role of NADH shuttle system in glucose-induced activation of mitochondrial metabolism and insulin secretion. *Science (80-)*. 1999;283(5404):981-985.

19. Varone A, Xylas J, Quinn KP, et al. Endogenous two-photon fluorescence imaging elucidates metabolic changes related to enhanced glycolysis and glutamine consumption in precancerous epithelial tissues. *Cancer Res*. 2014;74(11):3067-3075.

20. Nakashima N, Yoshihara K, Tanaka F, Yagi K. Picosecond fluorescence lifetime of the coenzyme of d-amino acid oxidase. *J Biol Chem*. 1980;255(11):5261-5263.

21. Blacker TS, Mann ZF, Gale JE, et al. Separating NADH and NADPH fluorescence in live cells and tissues using FLIM. *Nat Commun*. 2014;5:3936.

22. Pradhan A, Pal P, Durocher G, et al. Steady state and time-resolved fluorescence properties of metastatic and non-metastatic malignant cells from different species. *J Photochem Photobiol B Biol*. 1995;31(3):101-112.

23. Konig K, Riemann I. High-resolution multiphoton tomography of human skin with subcellular spatial resolution and picosecond time resolution. *J Biomed Opt*. 2003;8(3):432-439.

24. Wu Y, Zheng W, Qu JY. Sensing cell metabolism by time-resolved autofluorescence. *Opt Lett*. 2006;31(21):3122-3124.

25. Filippakopoulos P, Qi J, Picaud S, et al. Selective inhibition of BET bromodomains. *Nature*. 2010;468(7327):1067-1073.

26. Roderick JE, Tesell J, Shultz LD, et al. c-Myc inhibition prevents leukemia initiation in mice and impairs the growth of relapsed and induction failure pediatric T-ALL cells. *Blood, J Am Soc Hematol*. 2014;123(7):1040-1050.

27. Zhang S, Zhao Y, Heaster TM, et al. BET inhibitors reduce cell size and induce reversible cell cycle arrest in AML. *J Cell Biochem*. 2018;(October):1-14. doi:10.1002/jcb.28005

28. Lagadinou ED, Sach A, Callahan K, et al. BCL-2 Inhibition Targets Oxidative Phosphorylation and Selectively Eradicates Quiescent Human Leukemia Stem Cells. *Cell Stem Cell*. 2013;12(3):329-341. doi:https://doi.org/10.1016/j.stem.2012.12.013

29. Qiu L, Liu M, Pan K. A triple staining method for accurate cell cycle analysis using multiparameter flow cytometry. *Molecules*. 2013;18(12):15412-15421.

30. Samudio I, Harmancey R, Fiegl M, et al. Pharmacologic inhibition of fatty acid oxidation sensitizes human leukemia cells to apoptosis induction. *J Clin Invest*. 2010;120(1):142-156.

31. Walsh AJ, Skala MC. An automated image processing routine for segmentation of cell cytoplasms in high-resolution autofluorescence images. In: Periasamy A, So PTC, König K, eds. Vol 8948. International Society for Optics and Photonics; 2014:89481M. doi:10.1117/12.2040644

32. Gromski PS, Muhamadali H, Ellis DI, et al. A tutorial review: Metabolomics and partial least

squares-discriminant analysis–a marriage of convenience or a shotgun wedding. *Anal Chim Acta*. 2015;879:10-23.

33. Brereton RG, Lloyd GR. Partial least squares discriminant analysis: taking the magic away. *J Chemom*. 2014;28(4):213-225.

34. Walsh AJ, Castellanos JA, Nagathihalli NS, Merchant NB, Skala MC. Optical imaging of drug-induced metabolism changes in murine and human pancreatic cancer organoids reveals heterogeneous drug response. *Pancreas*. 2016;45(6):863.

35. Shah AT, Heaster TM, Skala MC. Metabolic Imaging of Head and Neck Cancer Organoids. Sobol RW, ed. *PLoS One*. 2017;12(1):e0170415. doi:10.1371/journal.pone.0170415

36. Geske FJ, Lieberman R, Strange R, Gerschenson LE. Early stages of p53-induced apoptosis are reversible. *Cell Death Differ*. 2001;8(2):182-191.

37. Walsh AJ, Skala MC. Optical metabolic imaging quantifies heterogeneous cell populations. *Biomed Opt Express*. 2015;6(2):559-573. doi:10.1364/BOE.6.000559

38. Bragado P, Sosa MS, Keely P, Condeelis J, Aguirre-Ghiso JA. Microenvironments dictating tumor cell dormancy. In: *Minimal Residual Disease and Circulating Tumor Cells in Breast Cancer*. Springer; 2012:25-39.

39. Baxevanis CN, Perez SA. Cancer dormancy: a regulatory role for endogenous immunity in establishing and maintaining the tumor dormant state. *Vaccines*. 2015;3(3):597-619.

CHAPTER 6

CONCLUSIONS AND FINAL REMARKS

6.1 Summary and conclusions

The goal of this dissertation is to establish metabolic autofluorescence imaging and analysis for characterizing heterogeneous cell-level interactions within the TME. Advances of non-invasive imaging technologies have improved functional assessment of cellular heterogeneity within the TME and overall understanding of tumor progression[1]. Specifically, metabolic autofluorescence imaging provides a method to visualize cell-level metabolic dynamics in live, intact models of the 3D TME by measuring two-photon excited autofluorescence of NAD(P)H and FAD[2–4]. NAD(P)H and FAD fluorescence intensities and lifetimes inform on cellular redox states and metabolic enzyme binding activity[2–7]. This endogenous functional contrast enables dynamic monitoring of heterogenous cell populations in live 2D and 3D TME models, highlighting key advantages for practical use of metabolic autofluorescence imaging.

The work presented in this dissertation demonstrates novel application and development of metabolic autofluorescence imaging and analysis tools to quantify sources of biological heterogeneity that alter the TME landscape. Metabolic autofluorescence imaging quantifies single-cell metabolic changes, demonstrating the capability to evaluate functional heterogeneity within biological systems[8]. Other functional assays or imaging modalities are not equipped to provide cell-level resolution of function without requiring tumor dissociation and destructive processing and labeling. These standard techniques provide limited assessment of heterogeneous cell phenotypes and functions associated with the complex TME. Furthermore, current metabolic autofluorescence applications have not thoroughly explored spatial and temporal metabolic changes in the TME and their relationship with tumor volume. This dissertation shows that metabolic autofluorescence imaging can non-invasively monitor the spatiotemporal behavior of heterogeneous cell populations, and provides novel statistical analysis tools to monitor heterogeneity in the TME.

Chapter 2 contributes fundamental knowledge towards the rationale for the work reported in this dissertation. TME architecture and components of the TME that regulate tumor development and treatment response are discussed. The dynamic behavior and heterogeneity of the TME have been widely studied, but current characterization methods have significant disadvantages that are summarized in Chapter 2. Finally, the principles of metabolic autofluorescence imaging and analyses are described, focused primarily on its application to *in vitro* and *in vivo* cancer models.

Chapter 3 demonstrates metabolic autofluorescence imaging to monitor microenvironmental stimulation of macrophage polarization and migration in 3D human and mouse microscale cultures of the TME. Temporal assessment of macrophage metabolic heterogeneity with metabolic autofluorescence imaging was first validated in 2D cytokine-stimulated macrophage cultures. Following validation, metabolic autofluorescence imaging was performed in macrophage monocultures and tumor co-cultures within the 3D Stacks microscale platform using human and mouse cells. These experiments revealed heterogeneous macrophage metabolism and migration in response to prolonged tumor stimulation. These results were the first to demonstrate spatial and temporal metabolic autofluorescence changes in 3D tumor-macrophage microscale cultures. This work establishes the combined imaging and culture platform as a novel tool for non-invasively monitoring cell-level macrophage dynamics in 3D, *in vitro* TME models.

Chapter 4 reports on a spatial statistical framework to quantify the heterogeneous distribution of cell metabolism across models of the TME. This method combined density-based clustering, descriptive spatial metrics, and multivariate spatial analyses to define sub-populations and quantify local and global spatial relationships in *in vitro* and *in vivo* tumor models. Following validation in 2D breast tumor co-cultures, metabolic sub-populations and their spatial distributions were characterized in control and drug-treated 3D tumor organoids and *in vivo* xenografts of human squamous cell carcinoma (FaDu). This algorithm was the first to quantify spatial distributions of metabolic sub-populations within live, intact tumor models using metabolic autofluorescence. Overall, this analysis of intercellular spatial relationships

provides a novel tool to assess the spatial context of TME heterogeneity and its influence on tumor growth and treatment resistance.

Chapters 3 and 4 show that metabolic autofluorescence imaging can track spatial and temporal heterogeneity in the TME. Chapter 5 investigates the role of tumor cell-cycle status as one source of this heterogeneity, by testing whether metabolic autofluorescence imaging can classify cells in states of proliferation, apoptosis, or quiescence. Here, linear combination models derived from partial least squares - discriminant analysis (PLS-DA) were generated to accurately classify cell-cycle states within mixed cultures based on their autofluorescence intensity and lifetime values. These findings demonstrate single-cell metabolic autofluorescence imaging and multivariate PLS-DA as a reliable method to classify heterogeneous cell sub-populations based on states of proliferation, apoptosis, or quiescence within live, intact samples. These cell-cycle states are one of many sources of cell heterogeneity in the TME, and sensitivity of metabolic autofluorescence imaging to these varied functional states demonstrates its potential for characterizing the broad spectrum of TME heterogeneity.

Overall, this dissertation presents new developments in metabolic autofluorescence imaging and analysis for exploring TME heterogeneity. Metabolic autofluorescence imaging is sensitive to distinct cell phenotypes (e.g., tumor cell receptor status, drug sensitivity, cell-cycle state discussed in Chapters 4 & 5) and changes in cell-specific function (e.g., macrophages with and without tumor stimulation discussed in Chapter 3). Image analysis tools developed in this dissertation capture the behavior of individual cells or populations. These imaging and analysis methods can also be extended to study spatiotemporal heterogeneity across several disease models, highlighting the broad value of these techniques.

6.2 Significant contributions

Metabolic autofluorescence imaging has been previously used in preclinical and clinical studies due to its sensitivity to endogenous, metabolism-linked contrast, which provides a unique biomarker of tissue composition and function. Accordingly, metabolic autofluorescence imaging offers several advantages for evaluating heterogeneity in viable models of the TME. This non-destructive, label-free technique can be performed in intact 2D, 3D *in vitro* and *in vivo* samples[2,9–11] and is sensitive to cell-level

metabolism as a proxy of cell function[3,12]. This dissertation includes developments of metabolic autofluorescence imaging and analysis to better define cell function within the heterogeneous TME.

6.2.1. Single-cell imaging and analysis tools for assessing multi-faceted functional heterogeneity

Metabolic autofluorescence imaging is attractive for monitoring cell heterogeneity, because it achieves cellular resolution and high molecular specificity by exploiting NAD(P)H and FAD autofluorescence[2–4,7,13]. Previous work has established that metabolic autofluorescence imaging can distinguish heterogeneous cell populations based on cell sub-types, functional states, and drug sensitivity[5,6,8,11,14–20]. However, relationships between metabolic autofluorescence and sources of TME heterogeneity have not been exhaustively characterized. The studies reported in Chapters 3-5 develop imaging and analysis tools to resolve cell-level metabolic activity in populations exhibiting distinct functions (e.g., tumor cell-cycle state, treatment response, and macrophage function), to ultimately establish a versatile imaging tool that is sensitive to multiple sources of TME heterogeneity. The development of cell-level analysis methods, such as population density modeling (Chapters 3 & 4) and single-cell classification (Chapter 5), improved discrimination across these diverse cell populations based on their metabolic variability, further enhancing the ability of metabolic autofluorescence imaging to thoroughly characterize sources of heterogeneity. Overall, this work enhances the versatility of metabolic autofluorescence imaging and complementary analysis methods to resolve extensive heterogeneity within the TME and describe the distinct behavior of individual cells.

6.2.2 Novel techniques for evaluating spatial and temporal changes in biological systems

Generally, metabolic autofluorescence imaging offers a critical advantage over standard phenotypic and functional assays by exhibiting sensitivity to spatial and temporal metabolic changes of cell populations infiltrating live 3D TME models[13]. Previous studies of metabolic autofluorescence have assessed cellular metabolism in 3D and *in vivo* models sampled at a single plane[2,8,10,11,16]. This does not fully exploit the advantages of reduced scattering and greater penetration depth offered by multi-photon fluorescence excitation[19,21]. Thus, this dissertation presents work (Chapter 3) demonstrating metabolic autofluorescence imaging as a tool for measuring spatial effects on metabolic heterogeneity. Novel *in vitro*

tumor-macrophage co-culture platforms and *in vivo* mouse models developed in these studies also provide more accurate models and support comprehensive investigation into the evolving TME. Furthermore, endogenous fluorescence captured by metabolic imaging reflects dynamic metabolic activity and supports non-destructive functional measurements over time in live, intact samples[2,8,10,11,14,16]. Metabolic imaging studies have previously reported altered cell metabolism in 3D *in vitro* and *in vivo* systems after sustained exposure to various stimuli (e.g., drug, cytokine treatment), but also ignore the coincident spatial changes in metabolic activity[10,11,16,22]. The studies presented in Chapter 3 are the first to validate metabolic autofluorescence imaging for non-invasive monitoring of cell-level 3D spatial and temporal dynamics of cell populations (i.e., macrophages) in response to the TME.

6.2.3 Improved analytical methods for quantifying functional heterogeneity

Metabolic autofluorescence imaging has enabled significant discovery about heterogeneous function across biological systems, due to considerable advances in image analysis[8,23]. Multivariate classification models based on metabolic autofluorescence measurements have been established to identify heterogeneous non-malignant cell populations and their energy demands[20,24,25]. Additionally, spatial analysis methods have been previously developed to determine spatial relationships within high-SNR images of fluorescent probes within various biological samples, but these perform poorly using weak autofluorescence contrast[26–28]. Chapters 4 and 5 highlight the design of novel algorithms for classifying cell heterogeneity and quantifying spatial relationships in tumor cell cultures by combined metabolic autofluorescence imaging and multivariate statistical methods. Chapter 4 presents the first study to provide a framework for analyzing function-dependent patterns of cellular organization in metabolic autofluorescence images. This method integrated new population clustering methods, per-population descriptive spatial metrics, and multivariate spatial statistics for unique characterization of TME structure. The study presented in Chapter 5 adapted multivariate classification to detect heterogeneous tumor cell populations based on cell-cycle state, providing a novel tool to evaluate tumor cell dormancy contributing to TME heterogeneity. These innovative techniques for analyzing metabolic autofluorescence images

improve the ability to resolve various sources of TME heterogeneity and characterize their dynamic effects on global tumor behavior.

6.3 Future directions

In this dissertation, metabolic autofluorescence imaging is demonstrated as a robust functional imaging technique suitable for probing the TME. Additional progress to improve output and performance of the tools described here and in previous studies is critical to widespread use. Therefore, additional opportunities for advancing this technology are highlighted below.

The combined metabolic autofluorescence imaging and 3D Stacks microscale platform reported in Chapter 3 provides a relevant system to evaluate functional changes affected by tumor-macrophage crosstalk within the TME. Though this model system mimics key components of the TME, it does not fully recapitulate the full TME complexity driving tumor development[29–32]. Integration of additional TME components, such as lymphocytes and other immune cells, stromal cells, and vasculature into these microscale cultures may support more representative measurements of metabolic behavior in macrophages, or other cell types. Additionally, environmental factors (e.g., oxygen and pH gradients) strongly influence cell metabolism, so the effects of these stimuli should be considered within the co-culture platform[22,33–35]. Fluorescent sensors for nutrient diffusion and processing could be used to reflect local environmental conditions in these cultures to correlate with metabolic autofluorescence changes[22]. Furthermore, the composition of the TME is unique across tumor types and for each patient. Recapitulating this within the 3D culture platforms would likely better inform on the significance of inter-tumor and inter-patient heterogeneity to tumor progression and treatment response, as well as the cell-level dynamics regulating this response[36]. These adaptations could provide more comprehensive insight into the dynamic states of the TME.

Metabolic imaging of the *in vitro* TME models described in this dissertation was primarily established for observing the innate tumor-macrophage response within the TME. However, these tools are optimal for studying longitudinal effects of perturbations, due to the high-throughput model design and non-invasive functional imaging capability. These experiments could be modified to evaluate effects of

cancer therapies on TME heterogeneity and the influence of the TME on treatment efficacy. This interactive response has been previously reported using standard functional assays, limiting interpretation of longitudinal changes in response to therapy[37–40]. Integration of metabolic autofluorescence and standard functional measures could better elucidate biological mechanisms driving heterogeneity in cell sensitivity to drug treatment. Thus, metabolic autofluorescence imaging in combination with 3D TME microscale models could serve as a novel drug screening approach to reveal long-term TME function and potency effects from new and existing drugs and drug combinations

Both *in vivo* and 3D *in vitro* models have been widely used to study tumor growth, cancer drug response, and TME dynamics, though few studies examine how these responses differ across models[41]. The studies presented in Chapter 4 demonstrate that functional differences between model systems are apparent in the spatial analysis of metabolic autofluorescence images. However, these comparisons were made between xenografts and 3D organoid cultures that have limited physiological similarity to the *in vivo* TME (e.g., lack immune, stromal components). This similarity was also limited for xenografts as they were not engrafted in the originating tissue associated with the tumor type. As mentioned previously, 3D microscale cultures presented in Chapter 3 can be developed to better represent the TME landscape. Metabolic imaging of more physiologically accurate *in vivo* tumors grown within the natural tissue environment and complex, multi-cellular *in vitro* cultures in parallel could provide more direct functional comparisons between these widely-used models. Development of multiphoton endoscopy utilizing endogenous tissue contrast supports translation of this technique for characterization of the *in vivo* human TME[42-44]. However, limited spatiotemporal resolution of current endoscopic methods suggests metabolic autofluorescence imaging may be best suited for preclinical studies to resolve cell-level heterogeneity within *ex vivo* patient tissue[43-44]. Collectively, these studies could reveal sources of discordance between *in vitro* and *in vivo* treatment studies and inform model selection to improve studies of drug efficacy.

The advancement of analysis tools demonstrated in this dissertation have independently contributed significant findings about TME dynamics and underlying sources of heterogeneity. However, integration of these techniques would support more comprehensive assessment of the TME landscape. For example,

spatiotemporal metabolic changes could be evaluated for multiple cellular compartments while accounting for environmental pressures across the TME. Furthermore, the spatial and metabolic variables provided by these analyses could be used in building more robust classification algorithms and improve discrimination between these populations within complex, intact TME models. The classification models reported here demonstrated high performance in heterogeneous, *in vitro* tumor cell cultures. Due to the unique metabolic autofluorescence differences also observed in heterogeneous macrophage cultures, it would be valuable to evaluate the translation of these models to utilize all metabolic and spatial variables for improved separation of macrophage populations, possibly further highlighting versatility of these methods. However, the power of this analysis would be better evidenced upon validation for classification of diverse cell populations *in vivo.* Thus, additional imaging studies measuring quiescent and proliferative niches in *in vivo* leukemic or other tumor models would reinforce the application of these tools. Ultimately, a fully-integrated analytical framework for quantifying and classifying cell-specific metabolic autofluorescence would be significant for exploring heterogeneity in both normal and diseased tissue environments.

6.4 Final remarks

In summary, the work presented in this dissertation has illustrated substantial innovations in metabolic autofluorescence imaging technologies and analyses for probing TME heterogeneity. Current developments and future translation of these tools may provide better understanding of variable behavior of cellular compartments across the complex TME and how these responses are provoked. This could facilitate new insights into microenvironment-associated effects on tumor evolution and response to therapy and identify novel treatments targeted to tumor heterogeneity. Further advances in coupling these increasingly complex models and computational tools would promote rigorous functional studies of cancer and disease progression. Overall, cell-level metabolic autofluorescence imaging and quantitative analysis of heterogeneity offer a powerful method for exploring diverse function across biological systems that are critical to improving medical diagnoses and treatment.

6.5 References

1. Ramamonjisoa N, Ackerstaff E. Characterization of the Tumor Microenvironment and Tumor-Stroma Interaction by Non-invasive Preclinical Imaging. *Front Oncol*. 2017;7:3. doi:10.3389/fonc.2017.00003

2. Walsh AJ, Cook RS, Manning HC, et al. Optical metabolic imaging identifies glycolytic levels, subtypes, and early-treatment response in breast cancer. *Cancer Res*. 2013;73(20):6164-6174. doi:10.1158/0008-5472.CAN-13-0527

3. Chance B, Schoener B, Oshino R, Itshak F, Nakase Y. Oxidation-reduction ratio studies of mitochondria in freeze-trapped samples. NADH and flavoprotein fluorescence signals. *J Biol Chem*. 1979;254(11):4764-4771.

4. Blacker TS, Marsh RJ, Duchen MR, Bain AJ. Activated barrier crossing dynamics in the non-radiative decay of NADH and NADPH. *Chem Phys*. 2013;422:184-194. doi:10.1016/j.chemphys.2013.02.019

5. Lakowicz JR, Szmacinski H, Nowaczyk K, Johnson ML. Fluorescence lifetime imaging of free and protein-bound NADH. *Proc Natl Acad Sci U S A*. 1992;89(4):1271-1275. doi:10.1073/PNAS.89.4.1271

6. Georgakoudi I, Quinn KP. Optical Imaging Using Endogenous Contrast to Assess Metabolic State. *Annu Rev Biomed Eng*. 2012;14(1):351-367. doi:10.1146/annurev-bioeng-071811-150108

7. Skala MC, Squirrell JM, Vrotsos KM, et al. Multiphoton microscopy of endogenous fluorescence differentiates normal, precancerous, and cancerous squamous epithelial tissues. *Cancer Res*. 2005;65(4):1180-1186. doi:10.1158/0008-5472.CAN-04-3031

8. Walsh AJ, Skala MC. Optical metabolic imaging quantifies heterogeneous cell populations. *Biomed Opt Express*. 2015;6(2):559-573. doi:10.1364/BOE.6.000559

9. Skala MC, Riching KM, Gendron-Fitzpatrick A, et al. In vivo multiphoton microscopy of NADH and FAD redox states, fluorescence lifetimes, and cellular morphology in precancerous epithelia. *Proc Natl Acad Sci*. 2007;104(49):19494-19499.

10. Sharick JT, Jeffery JJ, Karim MR, et al. Cellular Metabolic Heterogeneity In Vivo Is Recapitulated in Tumor Organoids. *Neoplasia*. 2019;21(6):615-626. doi:10.1016/j.neo.2019.04.004

11. Shah AT, Heaster TM, Skala MC. Metabolic Imaging of Head and Neck Cancer Organoids. Sobol RW, ed. *PLoS One*. 2017;12(1):e0170415. doi:10.1371/journal.pone.0170415

12. Blacker TS, Duchen MR. Investigating mitochondrial redox state using NADH and NADPH autofluorescence. *Free Radic Biol Med*. 2016;100:53-65.

13. Kolenc OI, Quinn KP. Evaluating Cell Metabolism Through Autofluorescence Imaging of NAD(P)H and FAD. *Antioxid Redox Signal*. 2019;30(6):875-889. doi:10.1089/ars.2017.7451

14. Smokelin IS, Mizzoni C, Erndt-Marino J, Kaplan D, Georgakoudi I. Optical changes in THP-1 macrophage metabolism in response to pro- and anti-inflammatory stimuli reported by label-free two-photon imaging. *J Biomed Opt*. 2020;25(1):1-14. https://doi.org/10.1117/1.JBO.25.1.014512.

15. Quinn KP, Sridharan G V., Hayden RS, Kaplan DL, Lee K, Georgakoudi I. Quantitative metabolic imaging using endogenous fluorescence to detect stem cell differentiation. *Sci Rep*. 2013;3(1):3432. doi:10.1038/srep03432

16. Walsh AJ, Cook RS, Sanders ME, et al. Quantitative optical imaging of primary tumor organoid

metabolism predicts drug response in breast cancer. *Cancer Res*. 2014;74(18):5184-5194. doi:10.1158/0008-5472.CAN-14-0663

17. Alfonso-García A, Smith TD, Datta R, et al. Label-free identification of macrophage phenotype by fluorescence lifetime imaging microscopy. *J Biomed Opt*. 2016;21(4):46005. doi:10.1117/1.JBO.21.4.046005

18. Szulczewski JM, Inman DR, Entenberg D, et al. In Vivo Visualization of Stromal Macrophages via label-free FLIM-based metabolite imaging. *Sci Rep*. 2016;6(1):25086. doi:10.1038/srep25086

19. Mulligan SJ, Macvicar BA. Two-Photon Fluorescence Microscopy: Basic Principles, Advantages and Risks. https://pdfs.semanticscholar.org/cdf1/24284c19218d3478ceafa77f4c11222c9e3d.pdf. Accessed May 8, 2018.

20. Liu Z, Pouli D, Alonzo CA, et al. Mapping metabolic changes by noninvasive, multiparametric, high-resolution imaging using endogenous contrast. *Sci Adv*. 2018;4(3). doi:10.1126/sciadv.aap9302

21. Pawley JB, Masters BR. Handbook of Biological Confocal Microscopy, Third Edition. *J Biomed Opt*. 2008;13(2):029902. doi:10.1117/1.2911629

22. Ayuso JM, Gillette A, Lugo-Cintrón K, et al. Organotypic microfluidic breast cancer model reveals starvation-induced spatial-temporal metabolic adaptations. *EBioMedicine*. 2018;37:144-157. doi:10.1016/j.ebiom.2018.10.046

23. Heaster TM, Walsh AJ, Landman BA, Skala MC. Density-based clustering analyses to identify heterogeneous cellular sub-populations. In: Skala MC, Campagnola PJ, eds. Vol 10043. International Society for Optics and Photonics; 2017:100430X. doi:10.1117/12.2252499

24. Wang ZJ, Walsh AJ, Skala MC, Gitter A. Classifying T cell activity in autofluorescence intensity images with convolutional neural networks. *bioRxiv*. January 2019:737346. doi:10.1101/737346

25. Walsh A, Mueller K, Jones I, et al. Label-free Method for Classification of T cell Activation. *bioRxiv*. 2019:536813.

26. Stoltzfus CR, Filipek J, Gern BH, et al. CytoMAP: a spatial analysis toolbox reveals features of myeloid cell organization in lymphoid tissues. *CELL-REPORTS-D-19-04536*. 2019.

27. Pécot T, Zengzhen L, Boulanger J, Salamero J, Kervrann C. A quantitative approach for analyzing the spatio-temporal distribution of 3D intracellular events in fluorescence microscopy. Akhmanova A, ed. *Elife*. 2018;7:e32311. doi:10.7554/eLife.32311

28. Biot E, Crowell E, Burguet J, Höfte H, Vernhettes S, Andrey P. Strategy and software for the statistical spatial analysis of 3D intracellular distributions. *Plant J*. 2016;87(2):230-242. doi:10.1111/tpj.13189

29. Montanez-Sauri SI, Sung KE, Berthier E, Beebe DJ. Enabling screening in 3D microenvironments: probing matrix and stromal effects on the morphology and proliferation of T47D breast carcinoma cells. *Integr Biol*. 2013;5(3):631. doi:10.1039/c3ib20225a

30. Montanez-Sauri SI, Beebe DJ, Sung KE. Microscale screening systems for 3D cellular microenvironments: platforms, advances, and challenges. *Cell Mol Life Sci*. 2015;72(2):237-249. doi:10.1007/s00018-014-1738-5

31. McWhorter FY, Smith TD, Luu TU, Rahim MK, Haun JB, Liu WF. Macrophage secretion heterogeneity in engineered microenvironments revealed using a microwell platform. *Integr Biol*

(Camb). 2016;8(7):751-760. doi:10.1039/c6ib00053c

32. Yu J, Berthier E, Craig A, et al. Reconfigurable open microfluidics for studying the spatiotemporal dynamics of paracrine signalling. *Nat Biomed Eng*. 2019;3(10):830-841. doi:10.1038/s41551-019-0421-4

33. Romero-Garcia S, Moreno-Altamirano MMB, Prado-Garcia H, Sánchez-García FJ. Lactate Contribution to the Tumor Microenvironment: Mechanisms, Effects on Immune Cells and Therapeutic Relevance. *Front Immunol*. 2016;7:52. doi:10.3389/fimmu.2016.00052

34. Riemann A, Wußling H, Loppnow H, Fu H, Reime S, Thews O. Acidosis differently modulates the inflammatory program in monocytes and macrophages. *Biochim Biophys Acta - Mol Basis Dis*. 2016;1862(1):72-81. doi:10.1016/J.BBADIS.2015.10.017

35. Ozcelikkale A, Moon H, Linnes M, Han B. *In vitro* microfluidic models of tumor microenvironment to screen transport of drugs and nanoparticles. *Wiley Interdiscip Rev Nanomedicine Nanobiotechnology*. 2017;9(5):e1460. doi:10.1002/wnan.1460

36. Dzobo K, Senthebane DA, Thomford NE, Rowe A, Dandara C, Parker MI. Not everyone fits the mold: Intratumor and intertumor heterogeneity and innovative cancer drug design and development. Omi a J Integr Biol. 2018;22(1):17-34.

37. Ayuso JM, Truttschel R, Gong MM, et al. Evaluating natural killer cell cytotoxicity against solid tumors using a microfluidic model. *Oncoimmunology*. December 2018:1-11. doi:10.1080/2162402X.2018.1553477

38. Christakou AE, Ohlin M, Önfelt B, Wiklund M. Ultrasonic three-dimensional cell culture on chip for dynamic studies of tumor immune surveillance by natural killer cells. 2015.

39. Pavesi A, Tan AT, Koh S, et al. A 3D microfluidic model for preclinical evaluation of TCR-engineered T cells against solid tumors. *JCI insight*. 2017;2(12):e89762. doi:10.1172/jci.insight.89762

40. Adriani G, Pavesi A, Tan AT, Bertoletti A, Thiery JP, Kamm RD. Microfluidic models for adoptive cell-mediated cancer immunotherapies. *Drug Discov Today*. 2016;21(9):1472-1478.

41. Rosa R, Monteleone F, Zambrano N, Bianco R. In vitro and in vivo models for analysis of resistance to anticancer molecular therapies. *Curr Med Chem*. 2014;21(14):1595-1606. doi:10.2174/0929867313209990226

42. Wu C, Gleysteen J, Teraphongphom NT, Li Y, Rosenthal E. In-vivo optical imaging in head and neck oncology: basic principles, clinical applications and future directions. Int J Oral Sci. 2018;10(2):10. doi:10.1038/s41368-018-0011-4

43. Boppart SA, You S, Li L, Chen J, Tu H. Simultaneous label-free autofluorescence-multiharmonic microscopy and beyond. APL Photonics. 2019;4(10):100901.

44. Phipps JE, Bec J, Marcu L. Dual-Modality Fluorescence Lifetime and Intravascular Ultrasound for Label-Free Intravascular Coronary Imaging BT - Multimodality Imaging: For Intravascular Application. In: Zhou Q, Chen Z, eds. Singapore: Springer Singapore; 2020:153-171. doi:10.1007/978-981-10-6307-7_6

APPENDIX

A. SUPPLEMENTARY MATERIAL FOR CHAPTER 3

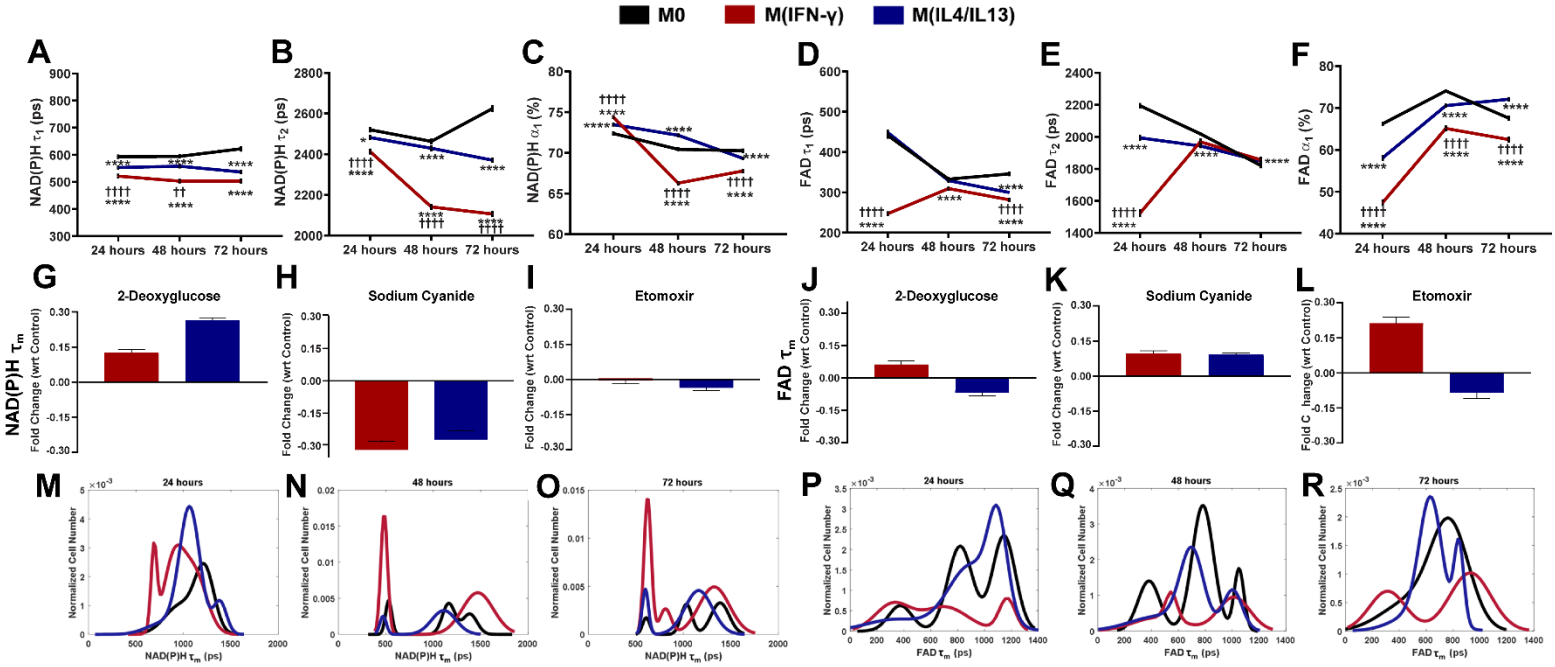

Figure A.1: Fluorescence lifetimes of NAD(P)H and FAD exhibit differences between macrophage polarization states. Quantitative measurement of A) NAD(P)H τ_1, B) NAD(P)H τ_2, C) NAD(P)H α_1, D) FAD τ_1, E) FAD τ_2, F) FAD α_1, illlustrate metabolic differences across 2D cultures of RAW264.7 macrophages polarized to M0, M(IFN-γ), and M(IL4/IL13) over a 72-hour timecourse. Fold change of NAD(P)H τ_m in response to treatment with G) 2-deoxyglucose, H) sodium cyanide, and I) etomoxir and FAD τ_m in response to treatment with J) 2-deoxyglucose, K) sodium cyanide, and L) etomoxir in M(IFN-γ) and M(IL4/IL13) macrophages shows metabolic inhibitor treatment alters NAD(P)H and FAD mean lifetimes of 2D polarized mouse macrophages. Population distribution modeling demonstrates metabolic heterogeneity for single-cell NAD(P)H τ_m over M) 24 hours, N) 48 hours, and O) 72 hours and FAD τ_m over P) 24 hours, Q) 48 hours, and R) 72 hours in macrophages unstimulated (M0) and stimulated to M(IFN-γ) and M(IL4/IL13).

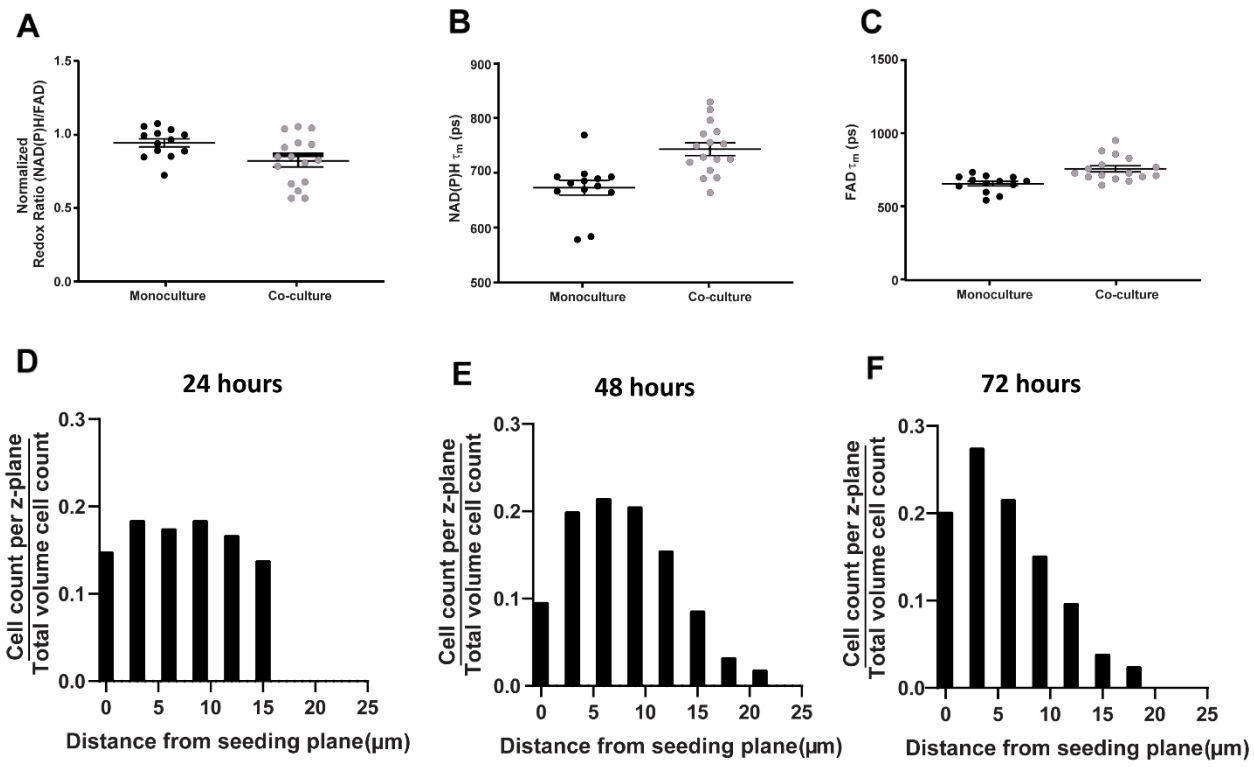

Figure A.2: Assessment of non-specific metabolic and migration effects in 3D Stacks co-cultures. Quantitative measurement of A) redox ratio, B) NAD(P)H τ_m, and C) FAD τ_m across 3D RAW264.7 macrophage monocultures or co-cultures of Polyoma Middle T-virus (PyVMT) breast cancer and RAW264.7 macrophages 1 hour post-seeding. Significant differences were not observed in redox or lifetime measurements between monocultured and co-cultured macrophages, demonstrating metabolic autofluorescence of monoculture and co-cultured moacrophages are similar upon initial seeding. RAW264.7 macrophages were seeded at the top and bottom of 3D ECM layers, and migration was measured at D) 2 hours, E) 48 hours, and F) 72 hours. Migration was quantified from cell counts at each 3 μm slice divided by the total cell count across the entire 3D macrophage layer. RAW264.7+RAW264.7 co-cultures exhibit minimal changes in cell distribution across the collagen layer, suggesting actively-migrating macrophage populations are absent in macrophage-macrophage co-cultures and active migration observed in tumor-macrophage co-cultures is induced by tumor stimuli.

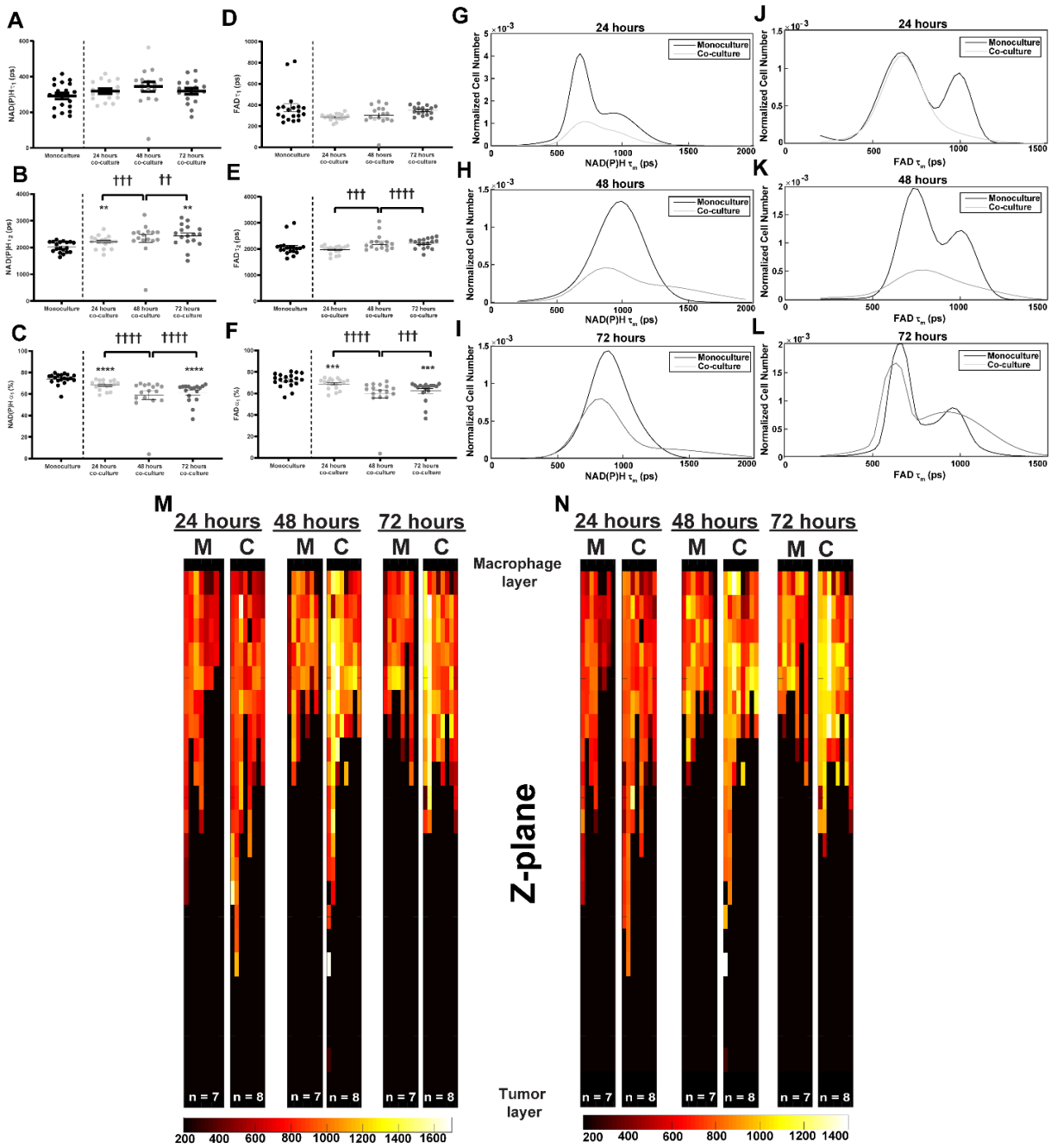

Figure A.3: Prolonged co-culture of mouse breast cancer and macrophages yields heterogeneous NAD(P)H and FAD fluorescence lifetime and migration compared to monoculture. Quantitative measurement of A) NAD(P)H τ_1, B) NAD(P)H τ_2, C) NAD(P)H α_1, D) FAD τ_1, E) FAD τ_2, F) FAD α_1, across 3D RAW264.7 macrophage monocultures or co-cultures of Polyoma Middle T-virus (PyVMT) breast cancer and RAW264.7 macrophages over 24, 48, and 72 hours. Population distribution modeling of single-cell NAD(P)H τ_m at A) 24 hours, B) 48 hours, and C) 72 hours post-seeding and FAD τ_m at D) 24 hours, E) 48 hours, and F) 72 hours post-seeding in monocultures and co-cultures. Representative heatmaps of M) NAD(P)H τ_m and N) FAD τ_m during RAW264.7 macrophage migration in 3D monocultures and co-cultures with PyVMT breast carcinoma. Both monocultured and co-cultured macrophages display increased heterogeneity in NAD(P)H and FAD lifetime, regardless of time and migration distance.

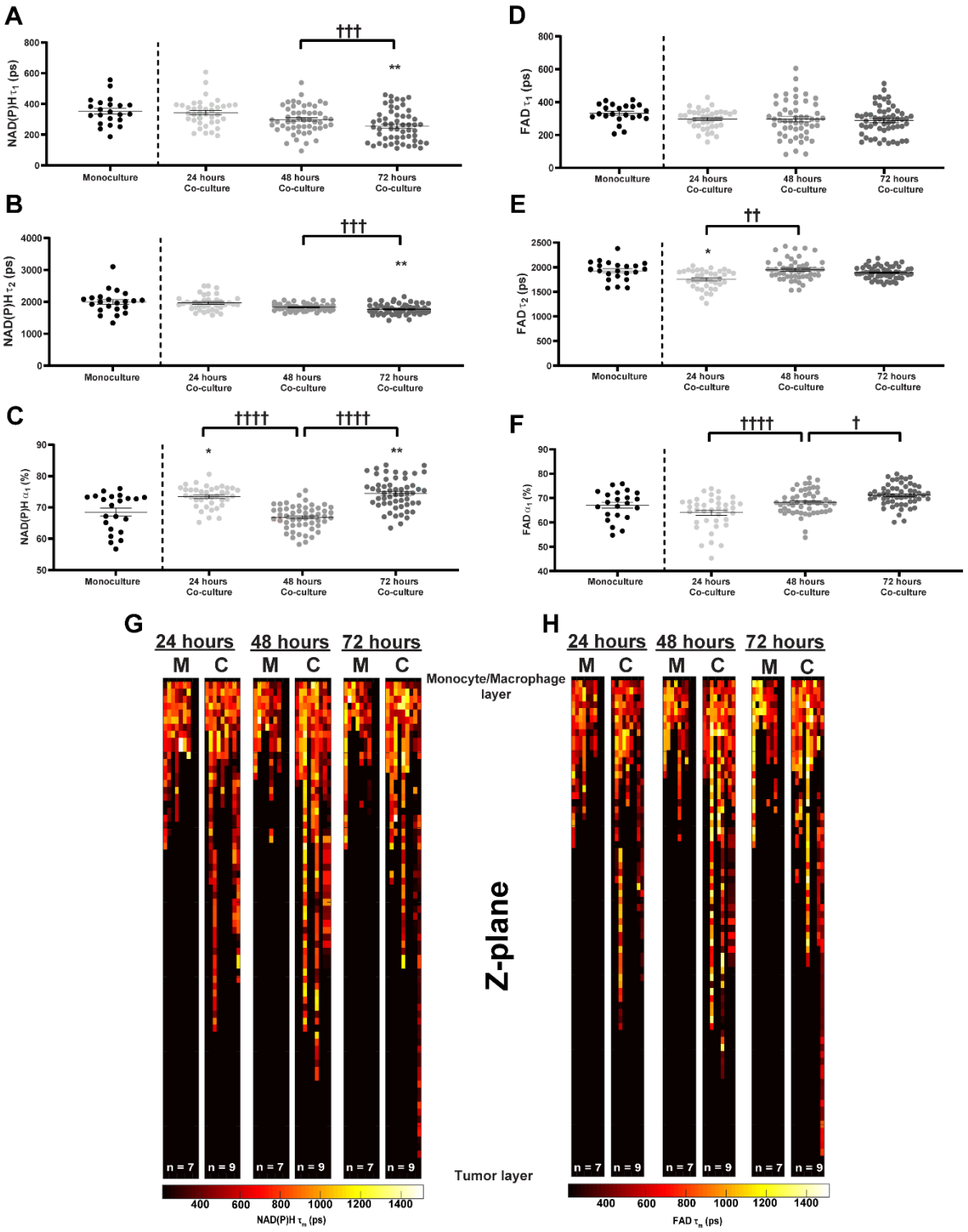

Figure A.4: Primary human tumor cells stimulate changes in NAD(P)H and FAD fluorescence lifetime and cell migration in co-cultured human monocyte-derived macrophages. Quantitative measurement of A) NAD(P)H τ_1, B) NAD(P)H τ_2, C) NAD(P)H α_1, D) FAD τ_1, E) FAD τ_2, F) FAD α_1 across 3D monocultures of human THP-1s or co-cultures of primary breast cancer cells and THP-1s over 24, 48, and 72 hours. Representative heatmaps of G) NAD(P)H τ_m and H) FAD τ_m during THP-1 migration in 3D monocultures and co-cultures with primary breast carcinoma. Both monocultured monocytes and co-cultured monocyte-derived macrophages exhibit substantial heterogeneity in NAD(P)H and FAD lifetime within z-planes across the 3D layer at all timepoints.

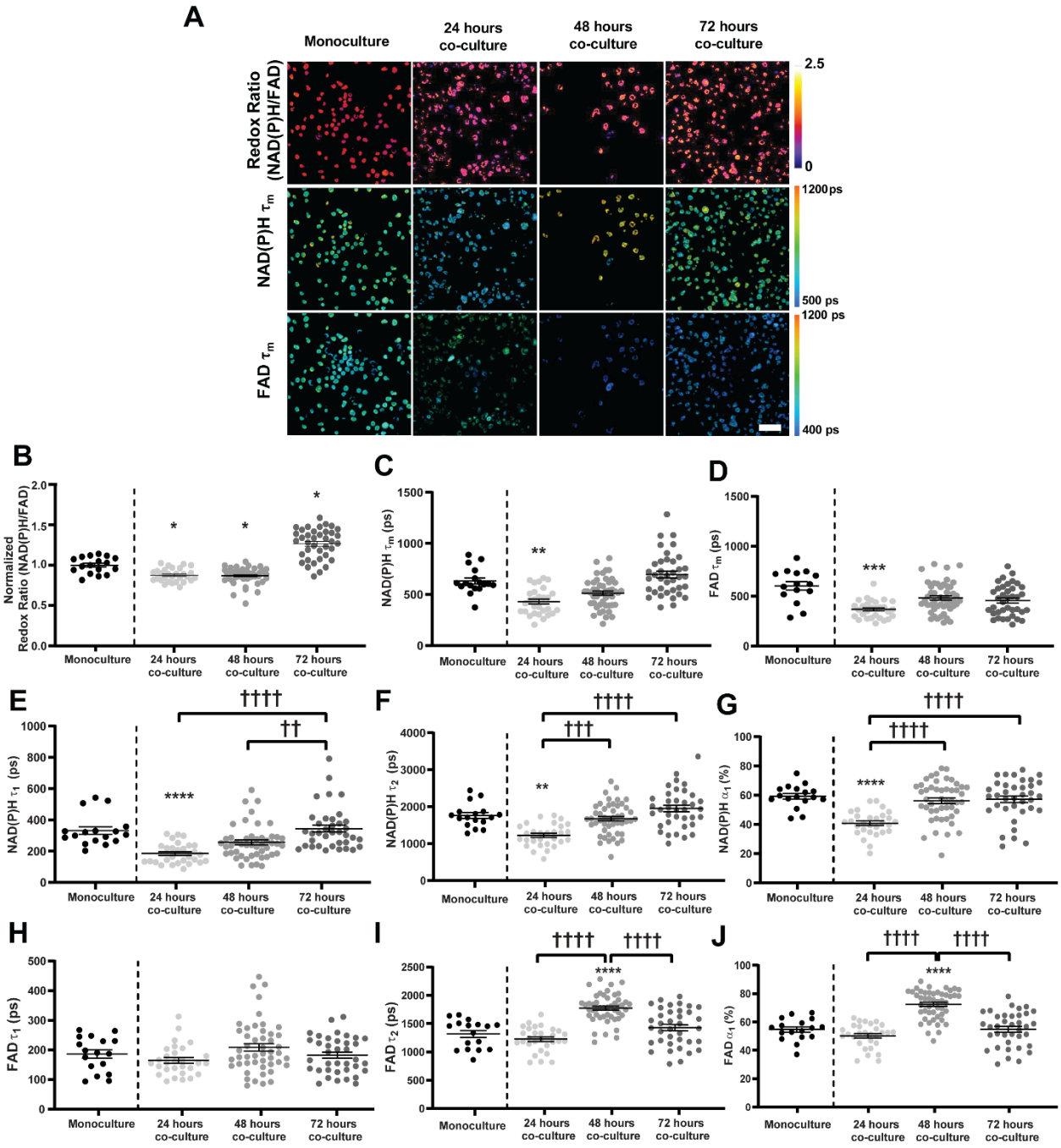

Figure A.5: Metabolic changes in human THP-1s following co-culture with MDA-MB-231 human breast carcinoma. A) Representative autofluorescence images demonstrate qualitative differences in the optical redox ratio, NAD(P)H τ_m, and FAD τ_m in 3D monocultures of human THP-1s or co-cultures of MDA-MB-231 breast cancer and THP-1s. Scale bar = 50 µm. Quantitative trends in B) redox ratio, C) NAD(P)H τ_m, D) FAD τ_m, E) NAD(P)H τ_1, F) NAD(P)H τ_2, G) NAD(P)H α_1, H) FAD τ_1, I) FAD τ_2, and J) FAD α_1 of monocultures or co-cultures over 24, 48, and 72 hours;*,**,*** $p<0.05,0.01,0.001$ vs monoculture.

Table A.1: Significance of redox ratio fold change in inhibitor-treated 2D cytokine-stimulated mouse macrophages

Inhibitor	M(IFN-γ)		M(IL4/IL13)	
	Redox ratio fold change relative to M0	p-value	Redox ratio fold change relative to M0	p-value
2-Deoxyglucose	-0.5030	<0.000001	-0.3283	0.000676
Sodium cyanide	0.5729	<0.000001	0.8256	<0.000001
Etomoxir	0.3084	0.000007	0.6204	<0.000001

Table A.2: Mouse and human macrophage polarization gene panels

Gene Symbol	Refseq #	Official Full Name	Associated Phenotype[76]
Mouse gene panel			
Stat3	NM_011486	signal transducer and activator of transcription 3	M2-like
Vegfa	NM_001025	vascular endothelial growth factor A	M2-like
Ccl5	NM_013653	chemokine (C-C motif) ligand 5	M1-like
Il10	NM_010548	interleukin 10	M2-like
Ptgs2	NM_011198	prostaglandin-endoperoxide synthase 2	M2-like
Ccl2	NM_011333	chemokine (C-C motif) ligand 2	M1-like
Il23a	NM_031252	interleukin 23, alpha subunit p19	M1-like
Ccl22	NM_009137	chemokine (C-C motif) ligand 22	Mixed
Il12b	NM_008352, XM_006532306	interleukin 12b	Mixed
Il1b	NM_008361, XM_006498795	interleukin 1 beta	M1-like
Il6	NM_031168	interleukin 6	Mixed
Nos2	NM_010927, XM_006532446	nitric oxide synthase 2, inducible	Mixed
Cxcl5	NM_009141	chemokine (C-X-C motif) ligand 5	M1-like
Tnf	NM_013693, NM_001278601	tumor necrosis factor	Mixed
Hsp90ab1	NM_008302	heat shock protein 90 alpha (cytosolic), class B member 1	Reference gene
Pgk1	NM_008828	phosphoglycerate kinase 1	Reference gene
Human gene panel			
Vegfa	NM001025366	vascular endothelial growth factor A	M2-like
Il10	NM_000572	interleukin 10	Mixed
Ptgs2	NM_000963	prostaglandin-endoperoxide synthase 2	M2-like
Ccl2	NM_002982	chemokine (C-C motif) ligand 2	M1-like
Ccl22	NM_00990	chemokine (C-C motif) ligand 22	M2-like
Il12b	NM _00187	interleukin 12b	Mixed
Il1b	NM_000576	interleukin 1 beta	M1-like
Il6	NM_000600	interleukin 6	Mixed

Nos2	NM_000625	nitric oxide synthase 2, inducible	Mixed
Tnf	NM_000594	tumor necrosis factor	M1-like
Csf1	NM_000757	colony stimulating factor 1 (macrophage)	Mixed
Tgfb1	NM_000660	transforming growth factor, beta 1	Mixed
Actb	NM_001101	actin, beta	Reference gene
B2m	NM_004048	beta-2-microglobulin	Reference gene

Table A.3: Coefficients of variation (CV) and significance of CV equality for optical redox ratio in 2D cytokine-stimulated mouse macrophages and 3D mouse monocultures and co-cultures

Time	Coefficient of variation			Squared ranks test
	2D culture			
	M0	M(IFN-γ)	M(IL4/IL13)	Test Statistic
24 hours	0.786	1.05	1.23	-4.512 (*)
48 hours	0.963	0.892	1.08	-78.823 (*)
72 hours	1.04	1.11	1.06	-78.609 (*)
	3D culture			
	Monoculture		Co-culture	
24 hours	0.241		0.357	25.654 (*)
48 hours	0.275		0.385	8.997 (*)
72 hours	0.249		0.339	29.400 (*)

(*) **p <0.05**

B. SUPPLEMENTARY MATERIAL FOR CHAPTER 4

A

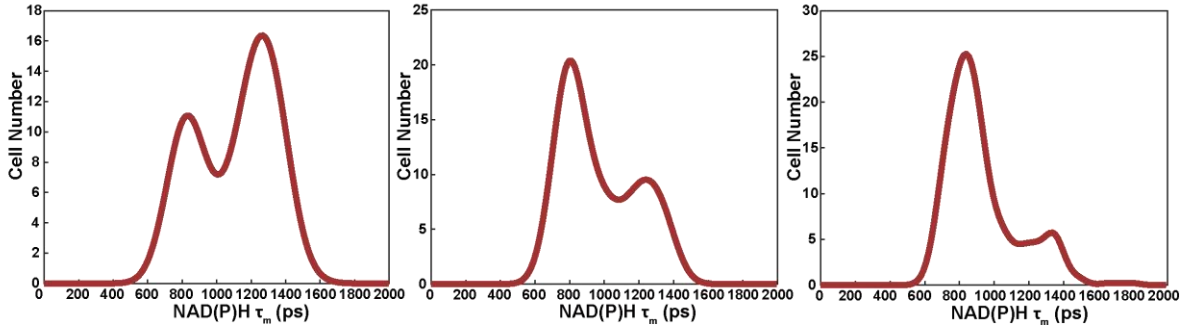

B

Predicted	Actual					
	MDA 30%:SKBR3 70%		MDA 50%:SKBR3 50%		MDA 70%:SKBR3 30%	
	MDA-MB-231	SKBR3	MDA-MB-231	SKBR3	MDA-MB-231	SKBR3
MDA-MB-231	67	3	129	5	220	5
SKBR3	5	92	9	58	7	41
Accuracy	**95.2%**		**93.0%**		**95.6%**	

Figure B.1. Validation of density-based clustering of cell sub-populations. (a) Population density modeling using kernel density estimation visualizes cell sub-populations in breast carcinoma co-cultures plated at known proportions. (b) Classification with density-based clustering analysis demonstrates high accuracy for all co-culture conditions compared to actual classification (manual classification by an expert based on morphology [24]) analysis demonstrates high accuracy for all co-culture conditions compared to actual classification (manual classification by an expert based on morphology [24])

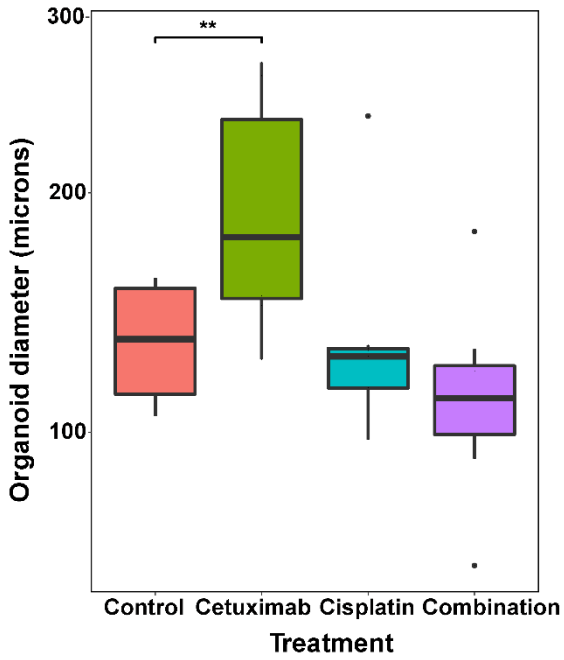

Figure B.2. Organoid diameter measurements across control and treated conditions. Organoid diameter is calculated for each control organoid and cetuximab-, cisplatin- and combination-treated organoids. Control organoids are smaller in diameter compared with cetuximab-treated organoids. Diameter differences between all other treatment conditions lack significance. (**p <0.01; Tukey-HSD test).

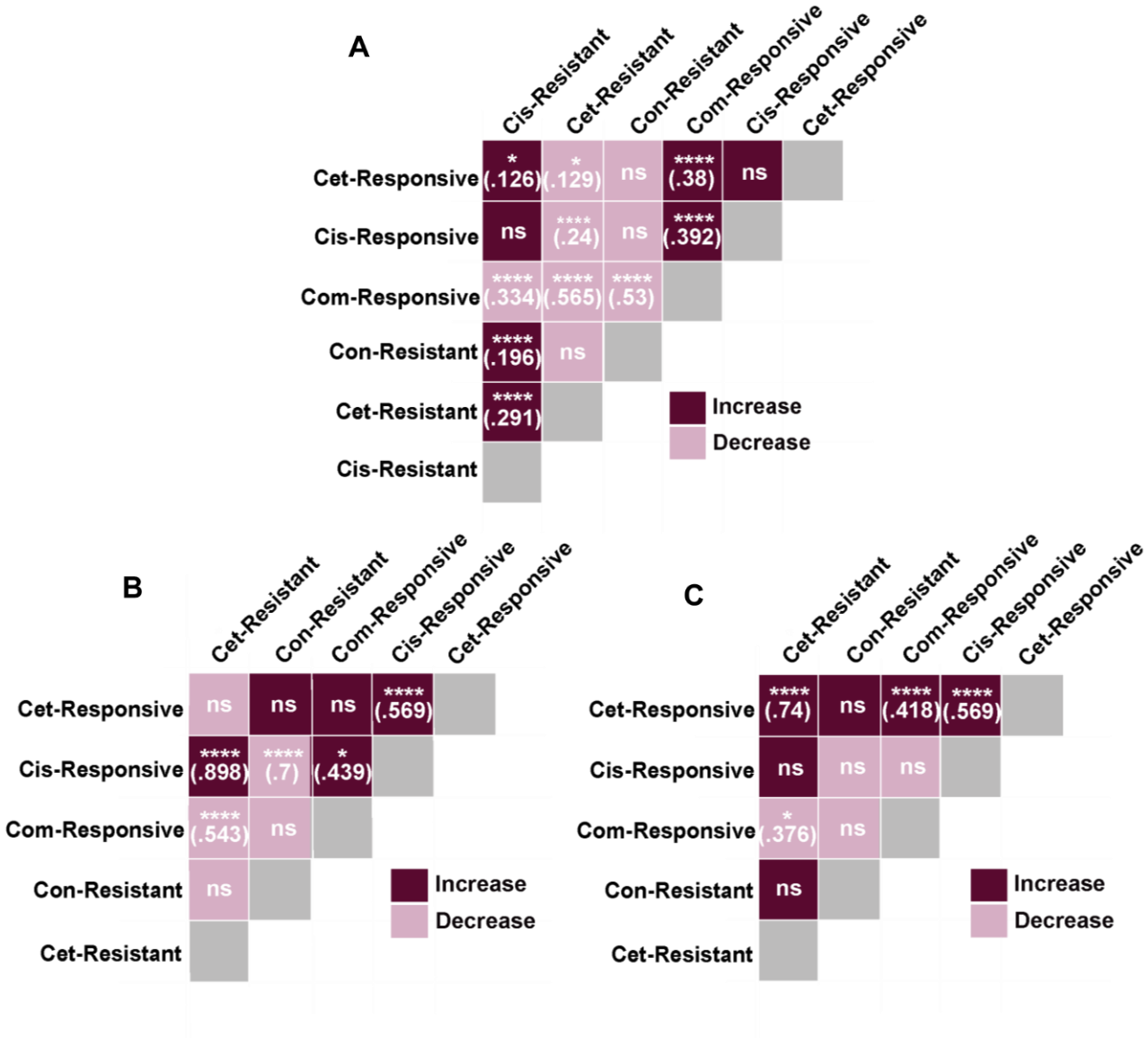

Figure B.3. Significance and effect size heatmaps reveal differences in spatial parameters between responsive and resistant populations in control and treated xenografts and organoids. Heatmaps show the direction of change, significance, and effect size for row conditions with respect to the column conditions. Statistical significance (asterisks) and effect size (notated values) of (a) xenograft intra-population proximity, (b) organoid intra-population proximity, and (c) organoid centricity is calculated between responsive and resistant populations in each treatment condition. (*, ****p <0.05, 0.0001; Tukey-HSD test). Con = control; Cet = cetuximab; Cis = cisplatin; Com = combination.

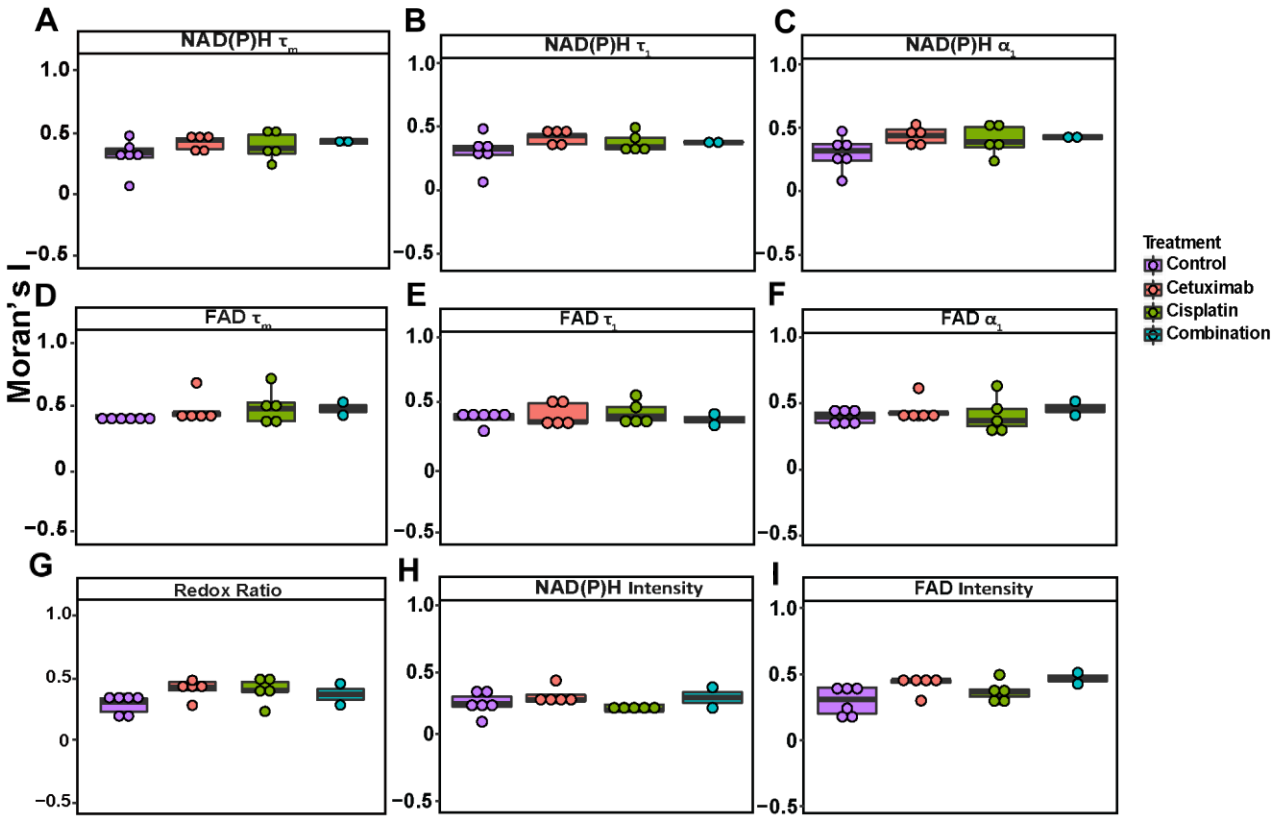

Figure B.4. Global Moran's I for NAD(P)H and FAD intensity and fluorescence lifetime components in control and drug-treated xenografts. Moran's I is calculated for each xenograft across treatment conditions for the following metabolic variables: (a) NAD(P)H τ_m, (b) NAD(P)H τ_1, and (c) NAD(P)H α_1, (d) FAD τ_m, (e) FAD τ_1, (f) FAD α_1, (g) redox ratio, (h) NAD(P)H intensity, and (i) FAD intensity. Positive spatial autocorrelation ($I \gg 0$) is observed for all intensity and lifetime measurements for each treatment condition.

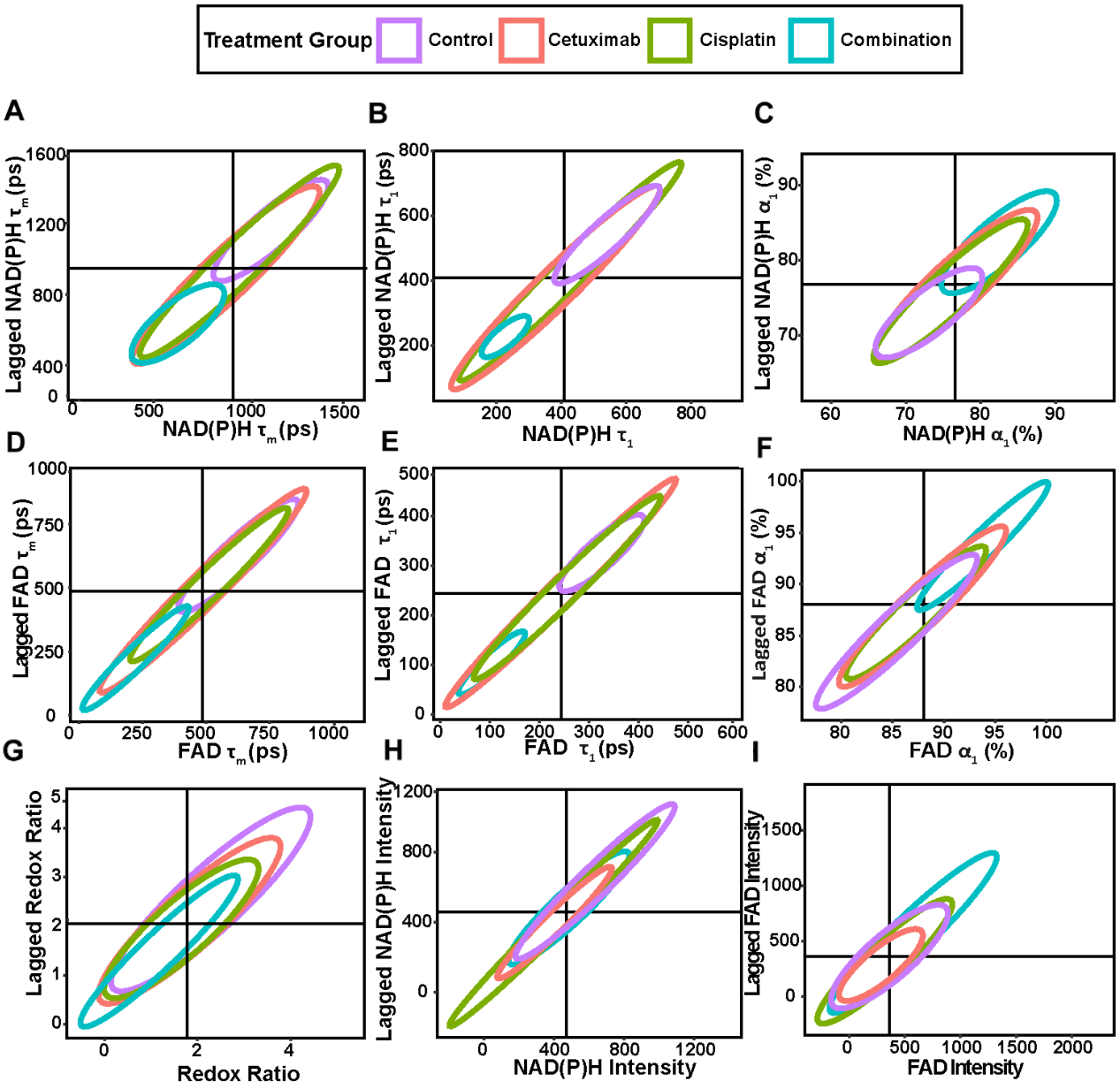

Figure B.5. Local indicators of spatial association (LISA) for NAD(P)H and FAD intensity and lifetime components across xenograft treatment groups. Unique clustering patterns are observed for (a) NAD(P)H τ_m, (b) NAD(P)H τ_1, (c) NAD(P)H α_1, (d) FAD τ_m, (e) FAD τ_1, (f) FAD α_1, (g) redox ratio, (h) NAD(P)H intensity, and (i) FAD intensity measurements between control and cetuximab-, cisplatin-, and combination-treated xenografts.

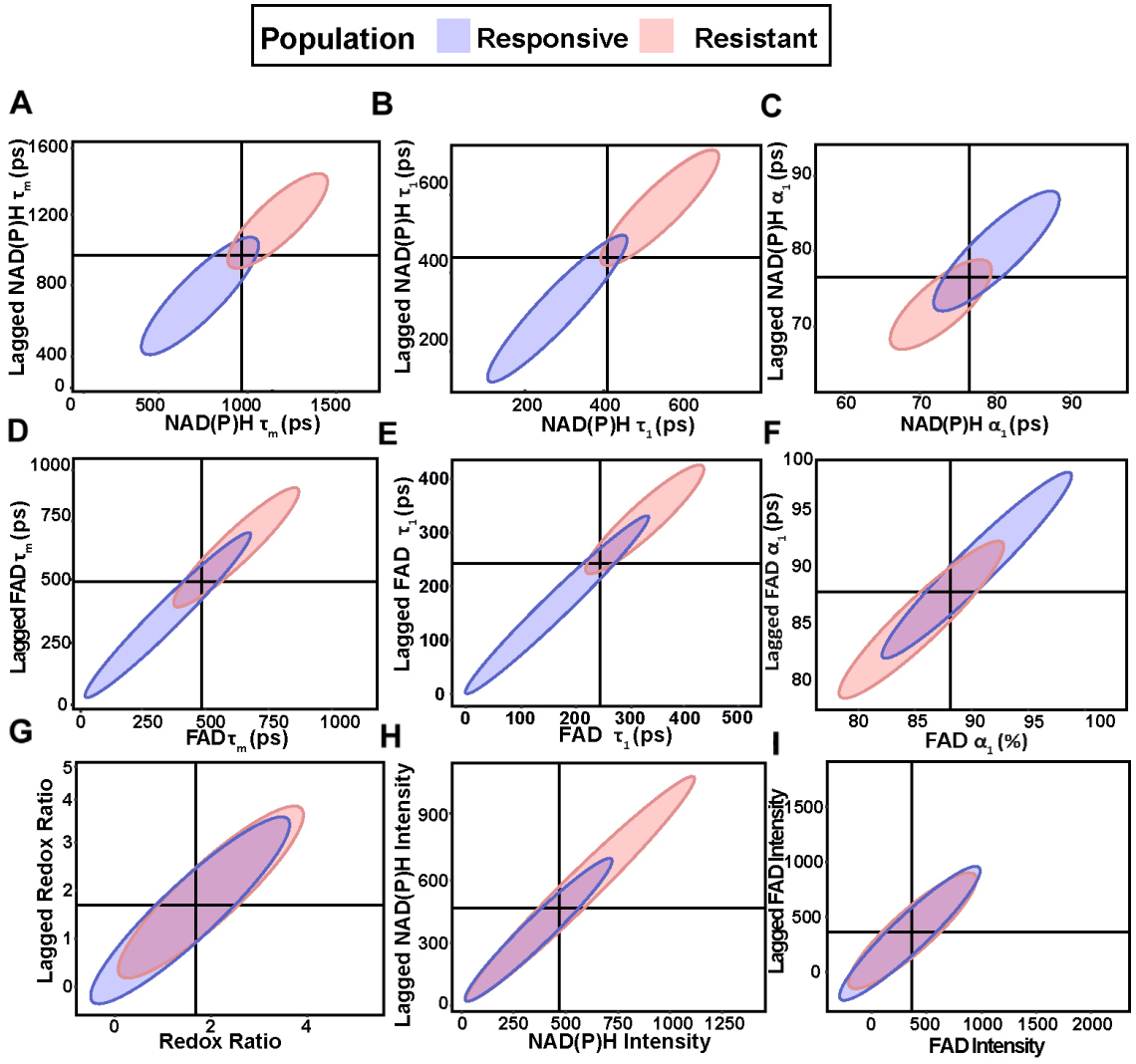

Figure B.6. Local indicators of spatial association (LISA) for NAD(P)H and FAD intensity and lifetime components for responsive and resistant xenograft populations. Clustering patterns for responsive and resistant populations are shown for (a) NAD(P)H τ_m, (b) NAD(P)H τ_1, (c) NAD(P)H α_1, (d) FAD τ_m, (e) FAD τ_1, (f) FAD α_1, (g) redox ratio, (h) NAD(P)H intensity, and (i) FAD intensity measurements.

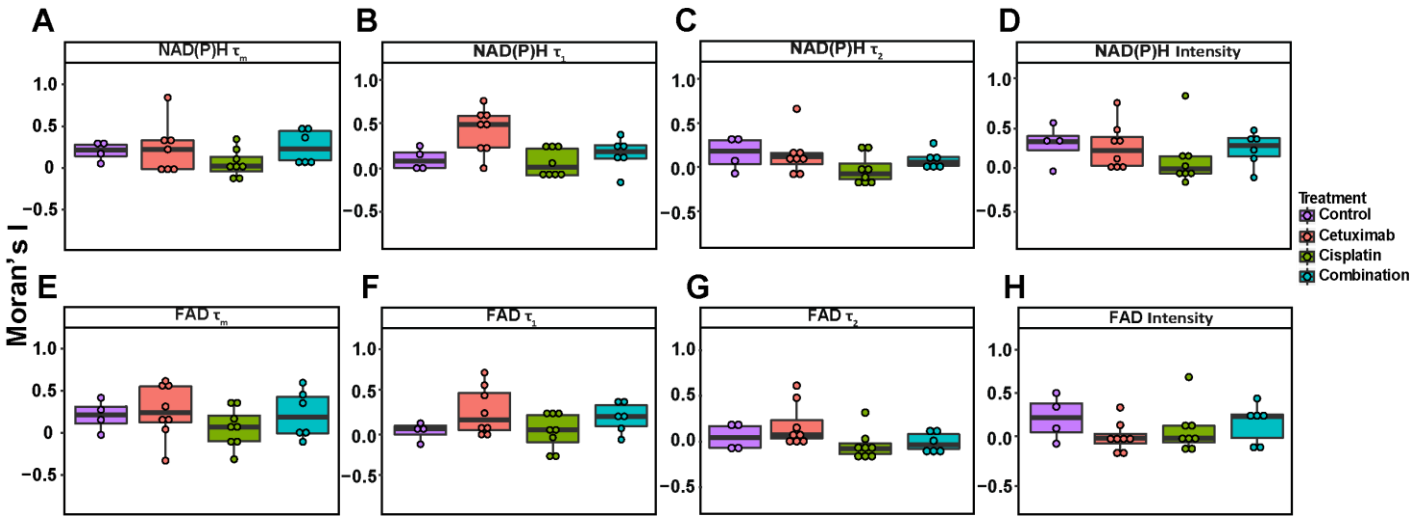

Figure B.7. Global Moran's I for NAD(P)H and FAD intensity and fluorescence lifetime components in control and drug-treated organoids. Organoids across treatment groups exhibit minimal spatial autocorrelation (0.5 > I > 0) for (a) NAD(P)H τ_m, (b) NAD(P)H τ_1, (c) NAD(P)H τ_2, and (d) NAD(P)H intensity measurements, as well as (e) FAD τ_m, (f) FAD τ_1, (g) FAD τ_2, and (h) FAD intensity measurements

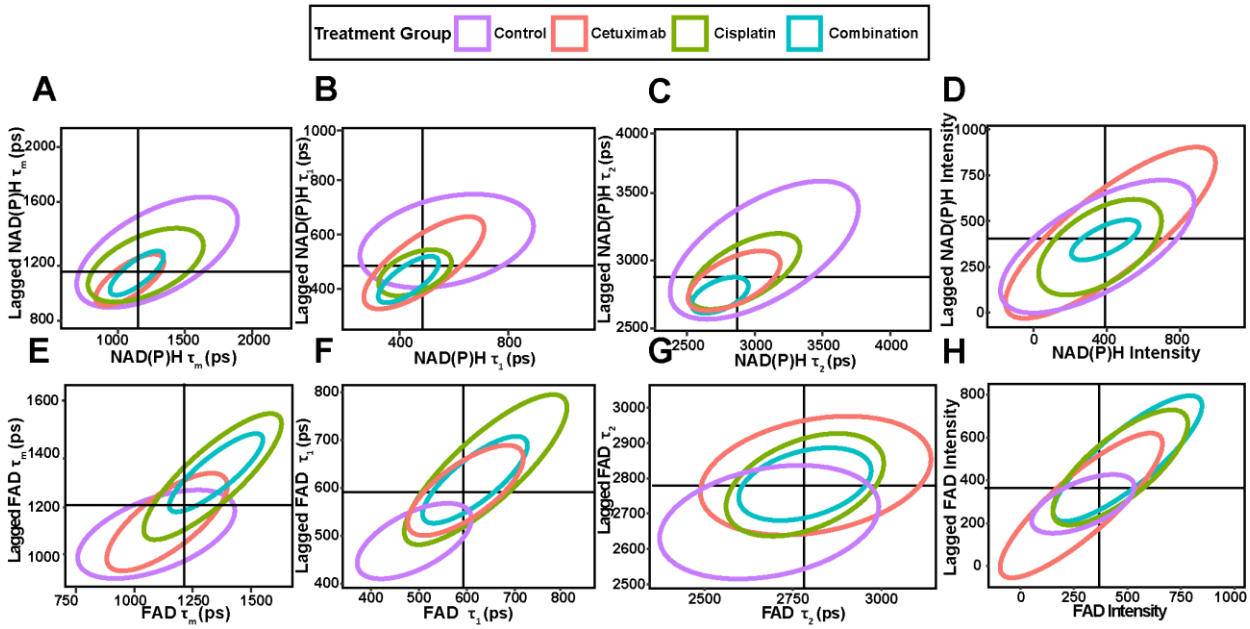

Figure B.8. Local indicators of spatial association (LISA) for NAD(P)H and FAD intensity and lifetime components across organoid treatment groups. Differences in clustering of (a) NAD(P)H τ_m, (b) NAD(P)H τ_1, (c) NAD(P)H τ_2, (d) NAD(P)H intensity, (e) FAD τ_m, (f) FAD τ_1, (g) FAD τ_2, and (h) FAD intensity measurements are observed between control organoids and organoids treated with cetuximab, cisplatin, or their combination.

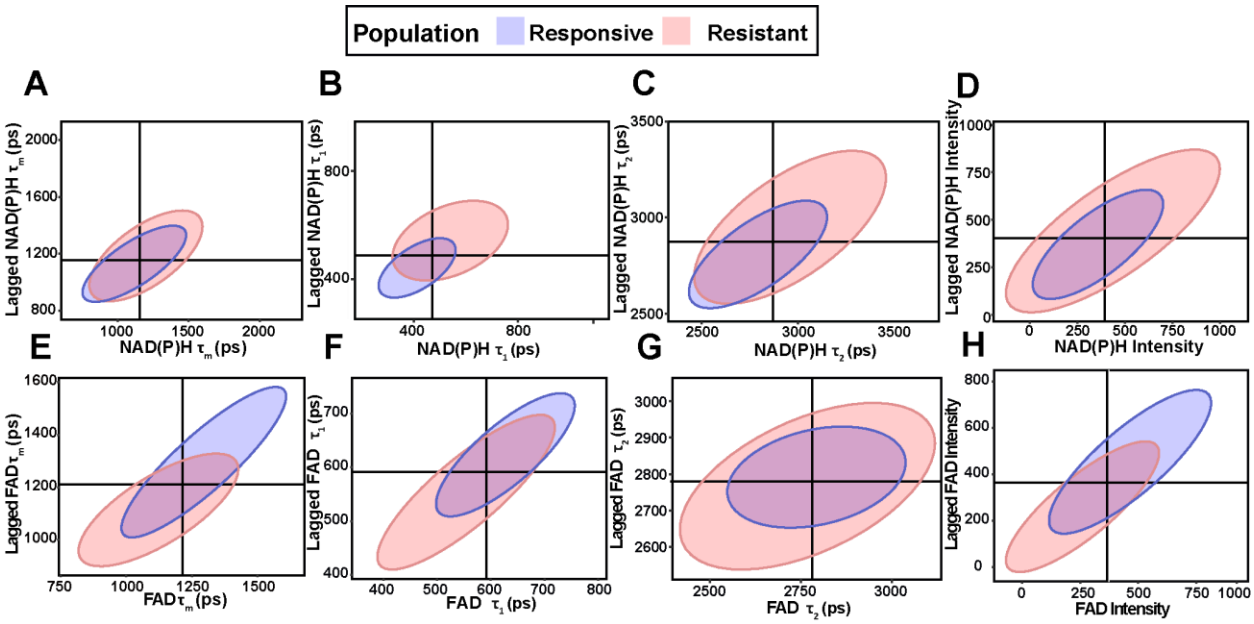

Figure B.9. Local indicators of spatial association (LISA) for NAD(P)H and FAD intensity and lifetime components for responsive and resistant organoid populations. Responsive and resistant populations exhibit characteristic clustering of (a) NAD(P)H τ_m, (b) NAD(P)H τ_1, (c) NAD(P)H τ_2, and (d) NAD(P)H intensity measurements, as well as (e) FAD τ_m, (f) FAD τ_1, (g) FAD τ_2, and (h) FAD intensity measurements.

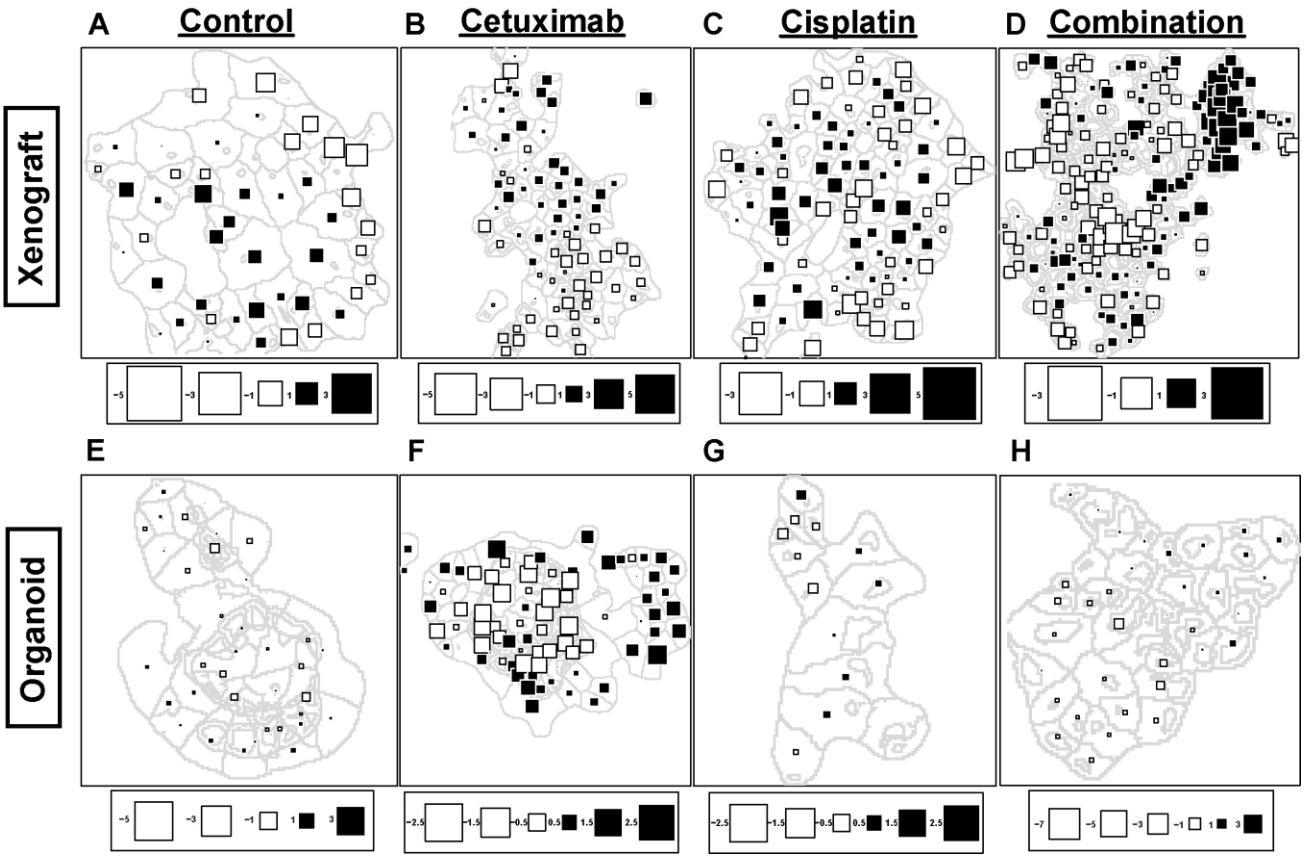

Figure B.10. Representative spatial principal components analysis (SPCA) maps. Individual SPCA scores along the first principal axis are mapped to corresponding cells within xenografts (a-d) or organoid (e-h) images. Square size represents magnitude of the score. Positive scores are color coded black, while negative scores are color coded white.

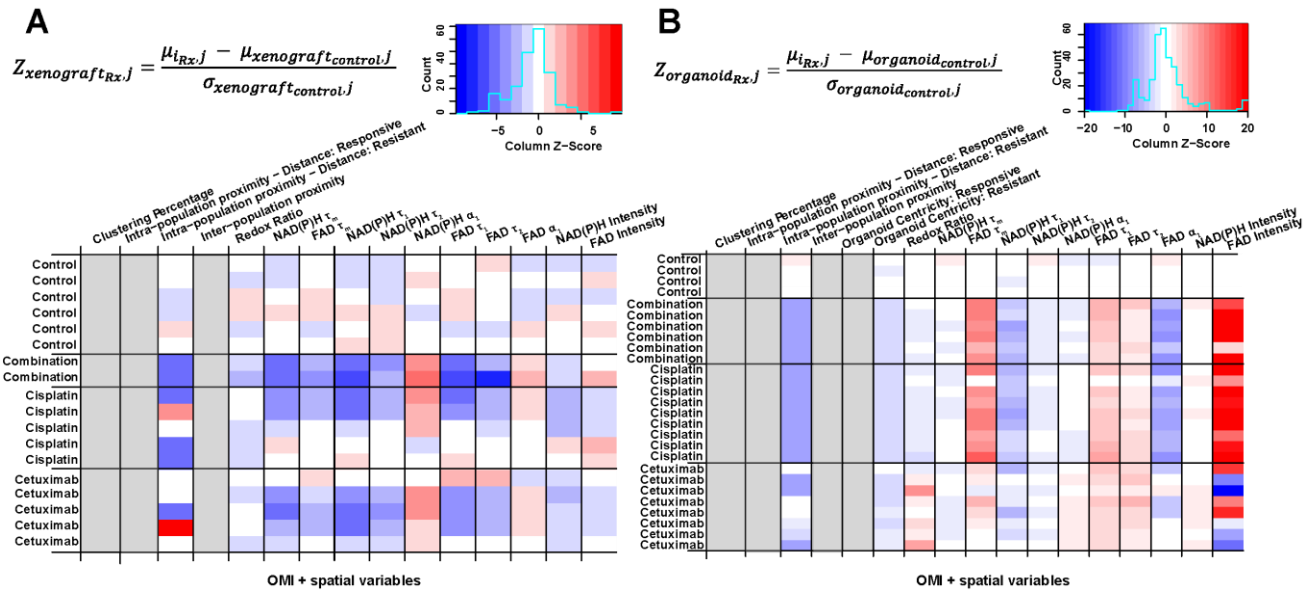

Figure B.11. Assessment of inter-sample variability across treatment groups within xenograft and organoid models. Metabolic and spatial variables for each (a) xenograft and (b) organoid sample were Z-score transformed with respect to the corresponding control sample averages and plotted as heatmaps to visualize relative differences between control and treated samples. Gray boxes indicate samples without a value for a given variable, due to lack of variation across the control samples.

Table B.1: List of abbreviations

Abbreviation	Explanation
OMI	Optical metabolic imaging
FLIM	Fluorescence lifetime imaging
τ_m	Mean lifetime
τ_1	Short lifetime
τ_2	Long lifetime
α_1	Fractional component
$d_{cell\_diameter}$	Average cell diameter
spatial PCA	Spatial principal components analysis
LISA	Local indicators of spatial association